Homeostasis and Functions of Ca^{2+} and Metal Stores in Lysosomes and Lysosome-related Organelles

by

Mingxue Gu

A dissertation submitted in partial fulfillment
of the requirements for the degree of
Doctor of Philosophy
(Molecular, Cellular and Developmental Biology)
In the University of Michigan
2020

Doctoral Committee

Professor Richard Hume, Chair
Professor Robert Fuller
Professor John Y. Kuwada
Professor Yanzhuang Wang

Mingxue Gu

mingxue@umich.edu

ORCID: 0000-0002-7132-7284

DEDICATION

To my family,
For their love, support, and critiques.

ACKNOWLEDGEMENTS

This thesis would not be possible without the help and support of many people throughout my Ph.D. study. I would like to take this opportunity to express my sincere appreciation to all of them.

First, I would like to extend my sincere gratitude to my Ph.D. advisor Dr. Haoxing Xu. As a science mentor, Dr. Xu always provides professional and inspiring instructions and advice, as well as sharp critiques towards my experimental design, data, and scientific writing, enabling the fulfillment of my research projects described in this thesis. Meanwhile, as an experienced senior scientist, Dr. Xu shares useful information and experience on career development as well as self-regulation. His diligence and passion towards science motivates me. The freedom he gave me for my project on lysosomal Ca^{2+} refilling enhanced my abilities as an independent researcher.

I would like to thank Dr. Richard Hume, Dr. Mohammed Akaaboune, and Dr. Wanlu Du for their support in maintaining the lab during the hard times. I would like to thank Dr. Richard Hume, in particular, for his dedication of time and effort in assisting not only lab business, but also the progress of research projects and paper writing.

I would also like to express my sincere thanks to my thesis committee members, Dr. Richard Hume, Dr. Yanzhuang Wang, Dr. John Kuwada, and Dr. Robert Fuller for all the perceptive suggestions, invaluable advice and critiques during the progress of my thesis. I would like to thank Dr. Robert Fuller, who proposed the involvement of yeast Vps13p with membrane contact sites and Ca^{2+} regulation. The VPS13D story would not have been initiated without his suggestions.

I would like to thank Dr. Kenneth Cadigan, in whose lab I did a rotation, and I appreciate his guidance, as well as his help and support through all the difficult times of the lab.

I also want to thank many people in MCDB for making my graduate work possible, especially Mary Carr, who helps in every aspect of graduate life, and Gregg Sobocinski, who always offers solutions towards problems on imaging systems as well as other instruments.

I would also like to thank all the Xu lab members, who have interacted with me. for the engaging scientific conversations and the fun moments. I thank Dr. Xiping Cheng, Dr. Xinran Li, Dr. Abigail Garrity, Dr. Junsheng Yang, Dr. Nirakar Sahoo and Dr. Wanlu Du for the discussions, suggestions, and critiques about my projects. I thank Dr. Wuyang Wang and Dr. Xiaoli Zhang for guiding me on electrophysiology. I thank Dr. Lu Yu, Dr. Ping Li, Dr. Meiqin Hu and Ce Wang for being helpful and supportive as labmates as well as friends all the time. I thank Wei Chen and Qi Geng, two previous rotation students, for the short, but happy time we had in the lab. I thank those who offered help when I was in the hospital last year. Your company made me feel at home. I thank the visiting scholars and all the current and previous undergraduate students, including Meimei Yang, Spring Gao, Kaiyuan Tang, Shiyu Xiao and Prateek Pinchi for helping me with some of the experiments and data analysis.

I thank all my friends here at Michigan, without whom my life wouldn’t be so cheerful.

Finally, to my family, for providing me with their unconditional support and love throughout my life. Even though they do not understand science, they are always there to back me up when I face frustrations and failures in researches. To my father, who challenged himself at the age of 50 to switch from bridge to tunnel engineering, for teaching me that “men struggles upwards”.

PREFACE

The work described in this thesis mainly belongs to three manuscripts written during my stay at the Xu lab. Chapters II was published in Developmental Cell, 2017 May 8;41(3):262-273.e6. Chapter III and IV are currently in preparation.

Contents presented in Chapter I (Introduction) partially originated from my co-first author review papers published in Trends in Biochemical Sciences (Li P, Gu M, Xu H. Lysosomal Ion Channels as Decoders of Cellular Signals. Trends Biochem Sci. 2019;44(2):110-124. doi:10.1016/j.tibs.2018.10.006), my co-first author book chapter currently in press (Zhang X, Gu M, Hu M, Yang Y, Xu H. Endosomal and Lysosomal Electrophysiology. In press.), and my co-authored review paper published in Protein Cell (Yang J, Zhao Z, Gu M, Feng X, Xu H. Release and uptake mechanisms of vesicular Ca^{2+} stores. Protein Cell. 2019;10(1):8-19. doi:10.1007/s13238-018-0523-x). To be more specific, the main body of sections 1.1.1, 1.1.2, 1.1.4 are derived from the Trends in Biochemical Sciences review and the book chapter, parts of the sections 1.3.2.1 and 1.3.5 are derived from the Protein Cell paper, Figure 1.1 and 1.2 are modified from the Trends in Biochemical Sciences review, and Figure 1.4 is updated from the Protein Cell paper. The other parts of the introduction are generated from previously published literatures.

Contents presented in Chapters II originated from a published work "Gastric acid secretion from parietal cells is mediated by a Ca^{2+} efflux channel in the tubulovesicle" in Developmental Cell with authors listed as Nirakar Sahoo, Mingxue Gu, Xiaoli Zhang, Neel Raval, Junsheng Yang, Michael Bekier, Raul Calvo, Samarjit Patnaik, Wuyang Wang, Greyson King, Mohammad Samie,

Qiong Gao, Sasmita Sahoo, Sinju Sundaresan, Theresa M. Keeley, Yanzhuang Wang, Juan Marugan, Marc Ferrer, Linda C. Samuelson, Juanita L. Merchant, and Haoxing Xu. All figures from these chapters, except Figure 2.7J-L, were included in the manuscript. Figure 2.7J-L consists of data obtained in the same study, but not included in the final manuscript. Nirakar Sahoo initiated the project. I designed and carried out all the electrophysiology experiments and generated according data. The other experiments included in Chapter II were designed and carried out mainly by Nirakar Sahoo.

Contents in Chapter III originated from a manuscript currently in preparation, with authors listed as Mingxue Gu, Wei Chen, Meiqin Hu, Meimei Yang, Michael Ryan, Timothy Nold, Prateek Pinchi, Haoxing Xu, and Wanlu Du. Wanlu Du initiated the project. I designed and carried out most of the experiments. Wanlu Du, Michael Ryan and Timothy Nold carried out the CellTiter cell viability assays. Wei Chen and Meiqin Hu generated part of the electrophysiology recording data. Meimei Yang and Prateek Pinchi participated in the PI-based cell death assays and data analysis. Wanlu Du and Haoxing Xu participated in the experiment design, data interpretation, and manuscript preparation.

Contents in Chapter VI originated from a manuscript currently in preparation, with authors listed as Mingxue Gu, Meimei Yang, Richard Hume and Haoxing Xu. I designed and carried out most of the experiments. Meimei Yang participated in Ca^{2+} imaging and data analysis. Haoxing Xu participated in the experiment design, data interpretation, and manuscript preparation. Richard Hume participated in data interpretation and manuscript preparation.

Chapter V aims to provide a comprehensive discussion about the conclusions, limitations, and future directions of the work presented in the three data chapters.

TABLE OF CONTENTS

LIST OF FIGURES

CHAPTER I

CHAPTER II

CHAPTER III

CHAPTER IV

LIST OF TABLES

LIST OF ABBREVIATIONS

2-APB	2-aminoethoxydiphenyl borate
8-Br-cAMP	8-bromoadenosine 3',5'-cyclic adenosine monophosphate
AD	Alzheimer's disease
ALG-2	apoptosis-linked gene 2
ANOVA	analysis of variance
AP	autophagosome
AP-3	adaptor protein complex 3
aSMases	acid sphingomyelinases
ATP	adenosine triphosphate
Baf-A1	bafilomycin A1
BAPTA	1,2-bis(o-aminophenoxy)ethane-N,N,N′,N′-tetraacetic acid
BBB	blood brain barrier
BFP	blue fluorescent protein
BK	big conductance calcium-activated potassium channel
BLI	bioluminescence
BLOC	biogenesis of LRO complex
cAMP	cyclic AMP
CaM	calmodulin
CAMKII	Ca^{2+}/calmodulin-dependent protein kinase II
Cas9	CRISPR-associated protein-9 nuclease
CAX	Ca^{2+}/H^{+} exchanger
CCh	carbachol
CETN3	centrin-3
CLC	chloride channel
CM-H2DCFDA	chloromethyl derivative of 2',7'-dichlorodihydrofluorescein diacetate
CORVET	class C core vacuole/endosome tethering
CRAC	Ca^{2+} release-activated Ca^{2+}
CRISPR	clustered regularly interspaced short palindromic repeats
DAPI	4',6-diamidino-2-phenylindole
DFO	deferoxamine
DMSO	dimethylsulfoxide
DMT1	divalent metal transporter 1
DN	dominant negative
DynlC2	dynein light chain 2
EGFP	enhanced green fluorescent protein
EGFR	epidermal growth factor receptor
EM	electron microscopy
ER	endoplasmic reticulum

ERK	extracellular signal-regulated kinase
ERMES	ER-mitochondria encounter structure
E-Syt	extended synaptotagmin-like protein
ET	electron tomography
FFAT	diphenylalanine in an acidic tract
Fluc	firefly luciferase
FRET	fluorescence resonance energy transfer
FYVE	Fab-1, YGL023, Vps27, and EEA1
GECI	genetically-encoded Ca^{2+} indicator
GPN	gly-phe β-naphthylamide crystalline
Grp75	75-kDa glucose-regulated protein
GWAS	genome-wide association studies
H2R	type 2 histamine receptor
HEK	human embryonic kidney
HD	Huntington's disease
HOPS	homotypic fusion and vacuole protein sorting
hVps41	human vacuolar protein sorting-associated protein 41
IBMX	3-isobutyl-1-methylxanthine
ICA	internal carotid artery
IMM	inner mitochondrial membrane
IP	intraperitoneal
IP3R	inositol trisphosphate receptor
KD	knockdown
KIF5B	kinesin family member 5B
KO	knockout
LAMP1	lysosomal associated membrane protein 1
LD	lipid droplet
LDL	low-density lipoprotein
LE	late endosome
LEL	late endosome and lysosome
LIC	lysosomal ion channel
LL	double leucine
LRO	lysosome-related organelle
LSD	lysosomal storage disease
LTP	lipid transport protein
LY	lysosome
LysoCa/Na/K	lysosomal $Ca^{2+}/Na^{+}/K^{+}$
M6P	mannose-6-phosphate
M6PR	mannose-6-phosphate receptor
MAPK	mitogen-activated protein kinase
MBM	melanoma brain metastases
MCP-1	monocyte chemoattractant protein-1
MCS	membrane contact site
MCU	mitochondrial Ca^{2+} uniporter
Mfn2	mitofusin 2
ML-IV	mucolipidosis type IV

MLN64	metastatic lymph node 64 protein
ML-SA	mucolipin synthetic agonist
ML-SI	mucolipin synthetic inhibitor
mTOR	mammalian target of rapamycin
mTORC	mammalian target of rapamycin complex
MVB	multivesicular body
NAADP	nicotinic acid adenine dinucleotide phosphate
Nec-1	necrostatin-1
NIPR	Na^+-independent cytoplasmic pH recovery
NPC1	Niemann-Pick disease, type C1
NVJ	nuclear-vacuole junction
OG	oregon green
OMM	outer mitochondrial membrane
ORP1L	oxysterol-binding-related protein 1L
ORP5	OSBP-related protein 5
ORD	oxysterol-binding-related domain
OSBP	oxysterol-binding protein
P2X4	P2X purinoceptor 4
PAM	protospacer adjacent motif
PD	Parkinson's disease
PDZD8	PDZ domain-containing protein 8
PI	propidium iodide
PI(3,5)P_2	phosphatidylinositol 3,5-bisphosphate
PI(4,5)P_2	phosphatidylinositol 4,5-bisphosphate
PIKfyve	phosphoinositide kinase, fyve-type zinc finger containing
PKA	protein kinase A
PLA	proximity ligation assay
PLC	phosphoinositide phospholipase C
PM	plasma membrane
PtdIns(3)P	phosphatidylinositol-3-phosphate
PTP1B	protein tyrosine phosphatase 1B
qPCR	quantitative polymerase chain reaction
RFP	red fluorescent protein
RILP	Rab-interacting lysosomal protein
RIP	receptor interacting protein
ROS	reactive oxygen species
RyR	ryanodine receptor
SEM	standard error of the mean
SERCA	sarcoplasmic reticulum (SR)-ER Ca^{2+}-adenosine triphosphatase
SLC38A9	solute carrier family 38 member 9
SLC39	solute carrier family 39
SNARE	soluble N-ethylmaleimide-sensitive fusion protein (NSF) attachment protein receptor
SOCE	store-operated Ca^{2+} entry
SR	sarcoplasmic reticulum
SRM	super-resolution fluorescence microscopy

STARD3	StAR-related lipid-transfer domain containing 3
STARD3NL	STARD3 N-terminal like protein
START	StAR-related lipid-transfer
STED	stimulated emission depletion
STIM	stromal interaction molecule
STX11	syntaxin 11
Syt7	synaptotagmin VII
TFEB	transcription factor EB
TG	thapsigargin
TGN	trans-Golgi network
TIM	translocase of the inner membrane
TKO	triple knockout
TM	transmembrane
TMEM175	transmembrane protein 175
TOM	translocase of the outer membrane
TPC	two-pore channel protein
TPEN	N,N,N′,N′-tetrakis(2-pyridinylmethyl)-1,2-ethanediamine
TRP	transient receptor potential
TRPML/ML	transient receptor potential mucolipin
TV	tubulovesicle
VAC	vacuolar apical compartment
VAMP	vesicle- associated membrane protein
VAP	VAMP-associated protein
vCLAMP	vacuole-mitochondria patch
VDAC	voltage-dependent anion channel
VPS13A/B/C/D	vacuolar protein sorting 13 homolog A/B/C/D
V-ATPase	vacuolar-ATPase
VPS	vacuolar protein sorting-associated protein
WT	wild-type
ZIP	zinc importer protein
ZnT	zinc transporter

ABSTRACT

Lysosomes and lysosome-related organelles (LROs) are involved in many intracellular signaling pathways as well as in a variety types of membrane trafficking processes such as exocytosis and autophagy. These organelles serve as intracellular stores for Ca^{2+}, Zn^{2+} and Fe^{2+}. Impairment of lysosomal Ca^{2+} homeostasis and membrane trafficking has been implicated as a likely cause of lysosomal storage diseases (LSDs), and more broadly in neurodegeneration, and cancer. Lysosomal membrane proteins, particularly ion channels, are crucial for lysosomal Ca^{2+} signaling. This thesis is focused on the establishment and regulation of Ca^{2+} homeostasis in lysosomes and LROs, and their contributions to diseases, but also explores the roles of other lysosomal cations.

The first two data chapters of this thesis focused on the major Ca^{2+} release channel of lysosomes, transient receptor potential mucolipin 1 (TRPML1 or ML1), which regulates various aspects of lysosomal function, including trafficking, fusion, and fission. In chapter II, we studied tubulovesicles, the organelles within parietal cells of the stomach that secrete acid in response to histamine stimulation. We identified TRPML1 as the tubulovesicular Ca^{2+} release channel, and showed that in response to histamine stimulation of parietal cells, TRPML1 is activated by cyclic AMP/protein kinase A (cAMP/PKA). This activation is required for the apical-directed trafficking of tubulovesicles, which results in the delivery of the hydrogen potassium ATPase (H^+/K^+-ATPase) to the apical membrane and an increase in acid secretion. The identification and functional analysis of TRPML1 on tubulovesicles provides a novel target for acid-related gastric diseases.

In chapter III, we showed that in a melanoma cancer model, hyper-activity of TRPML1 leads to elevated cell death of metastatic melanoma cells. Release of Zn^{2+}, instead of Ca^{2+}, is required for elevating cell death, potentially through direct disruption of mitochondrial functions. Collectively, these findings may advance our understanding of the functional roles of lysosomes and LROs as stores for signaling ions such as Ca^{2+} and Zn^{2+}, and how they engage in disease pathologies.

The molecular mechanisms that establish and maintain the 5000-fold Ca^{2+} gradient across the lysosome membrane remains an enigma, but endoplasmic reticulum (ER) Ca^{2+} has been suggested to be critical for lysosomal Ca^{2+} store refilling. In chapter IV, by using a physiological assay which monitors lysosomal Ca^{2+} store refilling, and super resolution imaging to visualize lysosome behavior upon luminal Ca^{2+} release and depletion, we confirmed that ER Ca^{2+} is required for the acute refilling of lysosomes and identified several molecules required for this function. Lysosome Ca^{2+} stores are refilled using membrane contact sites (MCSs) with ER tubules, in which the ER Ca^{2+} releasing channel IP3R participate. VPS13D is recruited to ER-lysosome MCSs sites for MCS formation and stabilization. Such recruitment is supported by a cytosolic Ca^{2+} sensor, potentially CETN3, which was suggested to directly interact with VPS13D in previous literature.

Taken together, the results of this thesis add important new information on the machinery regulating lysosomal [Ca^{2+}], as well as the physiology of Ca^{2+} channeling MCSs. Disruption of lysosomal Ca^{2+} homeostasis is commonly seen in LSDs and neurodegenerative diseases. Therefore, ER to lysosome Ca^{2+} transfer may serve as a potential therapeutic target.

CHAPTER I

Introduction[1]

1.1 Overview of lysosomes and lysosome-like intracellular vesicles

1.1.1 Lysosomal physiology

Lysosomes are traditionally viewed as the macromolecule degradation center of the cell expressing more than 60 types of acidic hydrolases (Kolter and Sandhoff, 2005; Xu and Ren, 2015). A more active role of lysosomes as a signaling hub has been recently demonstrated to self-regulate lysosomal movement, membrane fusion and fission, exocytosis, and proliferation (biogenesis and reformation) (Perera and Zoncu, 2016; Xu and Ren, 2015). The ionic composition of the lysosome lumen plays an essential role in both the "digestive" and the "signaling" functions of the lysosome. Lysosome ionic homeostasis is established and maintained by lysosomal ion channels and transporters that mediate ionic flux across the lysosomal membranes in response to cellular cues derived from the cytoplasm as well as the lysosome lumen (Perera and Zoncu, 2016; Xu and Ren, 2015). In this part of introduction, I will discuss recent advances in the understanding of lysosomal contents, lysosomal channels and function, the signals and signal transducers that regulate lysosomal membrane trafficking, and formation of lysosome-organelle membrane contact sites.

[1] Sections 1.1.1, 1.1.2, 1.1.4 of this Chapter and Figure 1.1, 1.2 are adapted from my co-first author review in Trends in Biochemical Sciences and my co-first author book chapter currently in press. Sections 1.3.2.1 and 1.3.5 and Figure 1.4 are derived from my second author review in Protein Cell.

1.1.1.1 Lysosomal contents

Lysosomes contain degradation cargos, catabolic products, various proteins (luminal enzymes, transmembrane and membrane-associated proteins), ions, water, and membrane lipids. Among these, catabolites often serve as nutrient-sensitive signals that in turn control the duration and rate of degradation (Perera and Zoncu, 2016). Water is the solvent that enables all the reactions. As cytoplasmic-facing structural phosphoinositides ($PI(3,5)P_2$ etc.) regulate lysosomal trafficking and tubulation (Li et al., 2016b), lysosomal luminal lipids, such as cholesterol, participates in cell signaling (Castellano et al., 2017).

1.1.1.2 Lysosome ionic composition

Concentration gradients for H^+, Na^+, K^+, Ca^{2+}, Fe^{2+}, Zn^{2+}, and Cl^- are established between the cytosol and the lysosome lumen (Figure 1.1) (Mindell, 2012; Morgan et al., 2011; Xu and Ren, 2015). With the exceptions of H^+ and Ca^{2+}, luminal concentrations of other ions have not been accurately determined (Xu and Ren, 2015). Under resting and basal states, lysosomes are heterogeneous in ionic compositions (Johnson et al., 2016; Xu and Ren, 2015). Lysosomal positioning may affect the luminal ionic composition, as peripheral lysosomes are less acidic than the perinuclear lysosomes (Johnson et al., 2016). Likewise, primary and terminal lysosomes have a high Na^+ concentration similar to the extracellular space, whereas secondary lysosomes (e.g., the newly formed autolysosomes) may have much lower luminal [Na^+] due to the prior fusion with the cytosol-derived K^+-loaded autophagosomes (Xu and Ren, 2015). Given the size of the lysosome, ion flux mediated by transient openings of organellar channels may be sufficient to cause drastic changes in the luminal ionic composition (Xu et al., 2015; Xu and Ren, 2015).

H^+: The acidic pH, which comes from the 100-1,000 fold concentration gradient for H^+, in the lysosomal lumen vs. cytosol is required for the activity of most lysosome hydrolases (Kolter and Sandhoff, 2005; Mindell, 2012). During endosome maturation, lysosomes are gradually acidified by the V-ATPase to reach a plateau luminal pH of approximately 4.6 (Huotari and Helenius, 2011). Disruption of lysosomal pH gradient using V-ATPase inhibitors (e.g., bafilomycin-A1) or protonophores results in failure of autophagosome-lysosome fusion and accumulation of the endocytic and autophagic cargos (Kawai et al., 2007; Mauvezin and Neufeld, 2015; Padman et al., 2013). On the other hand, the TMEM175 mediated H^+ "leak" conductance functions as the dissipating pathway regulating lysosomal pH homeostasis (Hu et al., personal communication).

Na^+/K^+: Isolated lysosomes are reported to contain high $[Na^+]_{Lumen}$ (100-140mM compared with ~12mM in the cytosol) and low $[K^+]_{Lumen}$ (2-50mM, lower than $[K^+]_{Cytosol}$ of ~150mM) (Koivusalo et al., 2011; Morgan et al., 2011; Wang et al., 2012; Xu and Ren, 2015). Several recent whole-endolysosome patch-clamp studies show the presence of multiple Na^+-selective and K^+-selective channels in the lysosome, including TPC1/2 and the large conductance Ca^{2+}- and voltage- activated K^+ (BK) channel respectively (Cang et al., 2015; Cao et al., 2015b; Wang et al., 2017b; Wang et al., 2012). The ion transporters that establish the lysosomal Na^+ and K^+ gradients are unknown. Disruption of the Na^+/K^+ gradient using Na^+/H^+ and K^+/H^+ ionophores, or genetic approaches to knock out TPC1/2 or BK, may rapidly change lysosome membrane potential ($\Delta\psi$, defined as $\Delta\psi = \psi_{cytosol}-\psi_{lumen}$), which in turn regulates $\Delta\psi$-dependent lysosomal functions, such as catabolite export (Cang et al., 2013) and Ca^{2+} import (Wang et al., 2017b).

Ca^{2+}: Lysosomes serve as mobile intracellular Ca^{2+} stores, with $[Ca^{2+}]_{Lumen}$ ($[Ca^{2+}]_{Ly}$) ~0.5 mM, 5,000-fold higher than $[Ca^{2+}]_{Cytosol}$ ($[Ca^{2+}]_{Cyt}$; ~100nM) (Yang et al., 2018). A putative Ca^{2+}/H^{+} exchanger was proposed to drive lysosomal Ca^{2+} uptake (Christensen et al., 2002; Morgan et al., 2011), but recent studies suggest that ER Ca^{2+} may refill lysosome stores independent of pH (Garrity et al., 2016). Therefore, the lysosomal Ca^{2+} uptake channel/transporter mediating Ca^{2+} exchange from ER remains to be identified. In response to changes in nutrient availability, redox status, and lipid abundance, Ca^{2+}-permeable channels in the lysosome mediate lysosomal Ca^{2+} release (Cao et al., 2015a; Dong et al., 2010; Shen et al., 2012; Xiong and Zhu, 2016; Xu and Ren, 2015; Zhang et al., 2016), regulating most lysosomal functions, including lysosome movement, membrane trafficking, and membrane contact sites formation, through various downstream Ca^{2+} effectors, such as synaptotagmin VII (syt7), apoptosis-linked gene 2 (ALG-2), calcineurin, and calmodulin (Chu et al., 2015; Li et al., 2016a; Li et al., 2016b; Medina et al., 2015). The existence of multiple Ca^{2+} sensors may allow lysosomal Ca^{2+} release to regulate distinct steps of lysosomal membrane trafficking.

Little is known about Ca^{2+} buffering systems in acidic stores such as lysosomes and how they regulate native Ca^{2+} stores (Dickson et al., 2012; Morgan et al., 2011). Some Ca^{2+} chelation occurs in acidic vesicles from abundant phosphate and sulphate groups which are strong acids that can form complexes even at low pH (Dickson et al., 2012; Morgan et al., 2011). Polyanionic matrices, such as polyphosphates and small organic acids (e.g. oxalic acid) are also implicated in acidic granular calcium buffering (Dickson et al., 2012; Morgan et al., 2011; Nguyen et al., 1998). Secretory granules with pH of 5.5-5.9 possess resting Ca^{2+} of ~70μM, while the total Ca^{2+} is usually put in the range of 30-40mM, leading to an effective Ca^{2+} binding ratio (bound/free) as high as 500:1 of the granular Ca^{2+} buffering molecules (Dickson et al., 2012). Such binding affinity

can be significantly reduced with H^+ competition at low pH (Dickson et al., 2012), resulting in higher proportion of free Ca^{2+} and increased Ca^{2+} dynamics.

Zn^{2+} and other metals: Lysosomes are intracellular stores of Fe^{3+}, Fe^{2+}, Zn^{2+}, and Cu^{2+} ions in micromolar concentrations (Kiselyov et al., 2011; Mills et al., 2010). Metals such as Fe^{3+}, Fe^{2+}, and Zn^{2+} ions are liberated via proteolysis of endocytosed or autophagocytosed metal-bound proteins (Cho et al., 2012; Kiselyov et al., 2011; Lee and Koh, 2010), or from the cytoplasm via lysosomal membrane transporters . Proteomic analysis of the lysosomal membrane suggested the presence of ZnT2 and ZnT4 transporters (Bostanci et al., 2014; Falcon-Perez and Dell'Angelica, 2007; Huang and Gitschier, 1997; McCormick and Kelleher, 2012; Murgia et al., 1999; Palmiter et al., 1996). ZIP3 and ZIP8, part of the SLC39 family, are also localized to the lysosome for Zn^{2+} export out of the lysosome (Jeong and Eide, 2013). The permeability of TRPML1 to Fe^{2+} and Zn^{2+} implies it to be another route for the movement of Fe^{2+}/Zn^{2+} that activates signaling pathways (Cheng et al., 2010). While lysosomal Fe^{2+} is required for the Fenton reaction and ROS production (Kiselyov et al., 2011; Mills et al., 2010), lysosomal Zn^{2+} is suggested to be critical for the activity of hydrolases such as acid sphingomyelinases (aSMases) (Schissel et al., 1998). On the other hand, high lysosomal Zn^{2+} inhibits cathepsin activity (Lockwood, 2013). Whether heavy metal release regulates signal transduction or lysosomal trafficking remains unclear.

Cl^-: $[Cl^-]_{Lumen}$ is estimated to be 70-80mM in C. elegans coelomocytes and ~118mM in murine J774A.1 cells and human THP-1 cells using the pH-insensitive probe Clensor (Chakraborty et al., 2017). Lysosome Cl^-, is likely maintained by CLC family Cl^-/H^+ exchangers (Graves et al., 2008;

Jentsch, 2007; Neagoe et al., 2010; Stauber and Jentsch, 2013), and may provide counterions for acidification.

1.1.1.3 Lysosomal ion channels

High-resolution quantitative proteomics suggested a total of 343 lysosomal (membrane-bound and lumen) proteins and a potential of 828 lysosome-associated proteins (Wyant et al., 2018). Despite the more than 60 different types of hydrolases discovered, only ~50 lysosomal membrane proteins have been identified and functionally characterized. These membrane proteins have a wide range of functions including maintaining lysosomal membrane integrity, transport of ions and catabolites, and regulation of fusion and fission events (Lubke et al., 2009; Schroder et al., 2007; Schwake et al., 2013; Xu and Ren, 2015). Still, many of the lysosome membrane constituents remain poorly understood (Wyant et al., 2018).

One major component of lysosomal membrane proteins, the transport proteins, work actively to maintain nutrient and ion homeostasis. These transport proteins consist of transporters importing or exporting metabolites and catabolites from lysosomes and channels/transporters permeable to ions (Xu and Ren, 2015). Identified lysosomal catabolites exporters include the major amino acid transporter SLC38A9 (Wyant et al., 2017), cysteine exporter cystinosin (Kalatzis et al., 2001), and the cholesterol transporter NPC1 (Figure 1.1) (Infante et al., 2008). A huge effort is required to characterize additional lysosomal transporters and their regulatory machineries.

Lysosomal ion channels (LICs) include “committed” lysosomal channels that reside primarily on LELs, e.g. TRPML1-3, TPC1-2, and TMEM175, as well as “non-committed” lysosomal channels that are also plasma membrane channels, i.e. BK channels and P2X4 purinergic receptors/channels (Figure 1.1) (Cang et al., 2015; Cang et al., 2013; Cao et al., 2015a;

Cao et al., 2015b; Cheng et al., 2010; Wang et al., 2017b; Wang et al., 2012; Xiong and Zhu, 2016). Lysosome-targeting trafficking motifs, e.g., double leucine (LL) motifs, are required for the highly specific expression of LICs in the lysosome (Bonifacino and Traub, 2003; Xu and Ren, 2015). Both "committed" and "non-committed" LICs, regardless of their primary locations in the cell, display significant endogenous currents in the lysosome (Xiong and Zhu, 2016).

There exist at least three types of lysosomal channels permeable to Ca^{2+} (LysoCa channels) in mammalian cells. Direct recordings on native lysosomes (Figure 1.1) verified Ca^{2+} currents mediated by TRPML1-3, TPC1-2, and P2X4 under appropriate conditions. Unlike TRPMLs and P2X4 which are non-selective among monovalent cations, TPCs are highly select for Na^+ (Cang et al., 2013; Guo et al., 2017; Wang et al., 2012), and hence are more likely to be involved in direct regulation of lysosomal $\Delta\psi$- and Na^+-dependent functions. Regulation of lysosomal $\Delta\psi$ is also achieved by the characterized K^+ channel BK and the H^+ "leak" channel (also K^+ permeable) TMEM175 (Figure 1.1). The following discussion will focus on the primary lysosomal Ca^{2+} channel, TRPML1. Detailed information of the other above-mentioned channels or additional candidate LysoCa, LysoNa, and LysoK channels that are only inferred by pharmacology or antibodies are not discussed here.

1.1.2 Mucolipin TRP channels (TRPMLs).

The mucolipin subfamily of transient receptor potential (TRP) channels, TRPML1-3, are tetrameric 6 transmembrane (TM, S1-S6) channels that are localized exclusively on endosomes and lysosomes (Cheng et al., 2010) (Figure 1.2). Whereas TRPML1 is ubiquitously expressed, TRPML2 and TRPML3 are more restricted in expression, being found in the thymus, kidney and spleen (Cheng et al., 2010; Xu and Ren, 2015). Although TRPML1 has been most extensively

studied, genetic and cell biological studies of mammalian TRPML2 and TRPML3, as well as non-mammalian, e.g., Drosophila and C. elegans TRPMLs, suggest conserved roles of mucolipin channels in regulating lysosomal functions (Dong et al., 2008; Grimm et al., 2017). Loss-of-function mutations of human TRPML1 cause type IV mucolipidosis (ML-IV), a lysosomal storage disease (LSD) with the symptoms of neurodegeneration and muscular dystrophy (Boudewyn and Walkley, 2018). Two di-leucine motifs at the intracellular N- and C-termini are responsible for the lysosomal localization of TRPML1 (Xu and Ren, 2015). Whole-endolysosome patch-clamp studies reveal that mammalian TRPML1-3 channels are permeable to both Ca^{2+} and Na^{+}, as well as K^{+} and heavy metal ions such as Fe^{2+} and Zn^{2+}, but not H^{+} (Xiong and Zhu, 2016). Under physiological conditions, ML1 mainly releases Ca^{2+}, Fe^{2+} and Zn^{2+} from lysosomal lumen to cytosol. Recent high-resolution structural studies have confirmed that the cationic selectivity is determined by negatively charged amino acid residues in the pore loop formed by S5 and S6 and the luminal pore between S1 and S2, and the activation gate is made of the S6 helices (Chen et al., 2017; Schmiege et al., 2017).

1.1.2.1 Gating of TRPML1

Endogenous agonists: PI(3,5)P_2 and ROS. PI(3,5)P_2 is a late endosome and lysosome (LEL)-specific phosphoinositide that regulates several trafficking steps of lysosomes (McCartney et al., 2014). PI(3,5)P_2 potently activates whole-lysosomal TRPML1-3 and Drosophila TRPML channels by binding to positively-charged amino acid residues in the cytosolic N-terminus in S1, as modelled in the high-resolution structures (Chen et al., 2017; Dong et al., 2010; Hirschi et al., 2017). PI(3,5)P_2 binding may lead to conformational changes in the S2-S3 linker to open the S6 gate (Chen et al., 2017; Hirschi et al., 2017) (Figure 1.2). Whereas cellular PI(3,5)P_2 levels are

shown to change prior to lysosomal trafficking events, in $PI(3,5)P_2$-deficient cells, many lysosomal functions are defective, including retrograde movement, exocytosis, and reformation (McCartney et al., 2014; Xu and Ren, 2015; Zolov et al., 2012). Inhibiting $PI(3,5)P_2$ synthesis genetically or pharmacologically causes lysosomal trafficking defects mimicking ML-IV cells (McCartney et al., 2014). Hence, TRPMLs may serve as an essential signal transducer for lysosomal $PI(3,5)P_2$. Consistently, mutations in the $PI(3,5)P_2$ binding sites of TRPML1 affect $PI(3,5)P_2$-dependent lysosomal functions (Li et al., 2016b). However, other $PI(3,5)P_2$ effectors may also contribute to the regulation of these lysosomal functions (McCartney et al., 2014).

Reactive oxygen species (ROS) are environmental stress signals that regulate a number of cellular functions, including autophagosome and lysosome biogenesis (Ravi et al., 2016; Zhang et al., 2016). ROS levels are elevated upon mitochondrial damage, and this triggers mitophagy to remove damaged mitochondria and excessive ROS, working as a negative feedback mechanism to maintain cellular health (Zhang et al., 2016). ROS induce nuclear translocation of TFEB, a transcriptional regulator of autophagosome and lysosome biogenesis (Settembre et al., 2011), in a TRPML1- and lysosomal Ca^{2+}-dependent manner (Zhang et al., 2016). ROS directly and robustly activate lysosomal TRPML1 channels, suggesting that TRPML1 may function as a signal transducer for ROS to regulate lysosome function (Ravi et al., 2016; Zhang et al., 2016). Consistent with the hypothesis, ROS sensitivity of TRPML1 is shown to be required for ROS-induced TFEB activation and mitophagy (Zhang et al., 2016). Since TRPML1 is activated by more than one cellular cue, to test which activation mechanism is the key to a specific function, it is necessary to introduce knock-in mutations at agonist-specific binding sites.

Endogenous inhibitors: mTOR, PI(4,5)P_2, sphingomyelin, adenosine. mTOR was recently shown to directly phosphorylate and inhibit TRPML1 (Li et al., 2016a; Onyenwoke et al., 2015; Sun et al., 2018). As TRPML1 is activated during amino acid starvation, it is possible that starvation-induced mTOR inhibition serves as a nutrient-derived signal to modulate TRPML1-mediated Ca^{2+} release. Two cell surface lipids reportedly inhibit TRPML1: PI(4,5)P_2 and sphingomyelin (Shen et al., 2012; Zhang et al., 2012). This inhibition is proposed to prevent TRPML1 from being active in non-lysosomal compartments (Shen et al., 2012; Zhang et al., 2012). However, PI(4,5)P_2 was recently reported to be generated on the lysosomal membrane to regulate mTOR-dependent lysosome reformation (Rong et al., 2012), which is a Ca^{2+}-dependent process (Li et al., 2016b), implying the involvement of PI(4,5)P_2 inhibition of TRPML1 in the process. Lysosomal PI(4,5)P_2 and sphingomyelin levels are aberrantly elevated in some LSD cells (De Leo et al., 2016; Shen et al., 2012). Likewise, in adenosine deaminase-deficient cells, luminal adenosine accumulation may inhibit TRPML1 to cause lysosomal dysfunction (Zhong et al., 2017). Hence, pathogenic TRPML1 inhibition may underlie the trafficking defects in many LSDs.

Other modulators: luminal acidic pH and cAMP/PKA. Luminal pH modulates the channel activities of TRPML1 and TRPML3 (Miao et al., 2015). Hence, cellular cues affecting lysosome acidification may regulate lysosome functions via TRPML-dependent mechanisms. In uro-epithelial cells, pathogen invasion induces lysosome alkalization to trigger TRPML3- and Ca^{2+}-dependent exosome release (Miao et al., 2015). cAMP signaling is known to regulate lysosome acidification and function, but the underlying mechanisms are not clear (Rahman et al., 2016). In parietal cells, PKA increases the activity of TRPML1 that is localized in the tubulovesicles (Sahoo

et al., 2017; Vergarajauregui et al., 2008b). Future studies may reveal whether cAMP/PKA signaling regulates lysosome function through TRPML1.

TRPML-specific synthetic agonists and inhibitors. Small-molecule synthetic modulators have been used to probe TRPML-dependent lysosomal functions (Li et al., 2013b; Shen et al., 2012). ML-SA (synthetic agonist) compounds, by binding to a hydrophobic pocket above the S5-S6 gate (Schmiege et al., 2017) (Figure 1.2), specifically activate whole-lysosomal TRPMLs, but not other lysosomal ion channels. Binding mutations were reported to selectively abolish ML-SA1 activation without interfering with $PI(3,5)P_2$ activation (Schmiege et al., 2017). Hence, synthetic agonists may provide a powerful tool to acutely activate and inhibit TRPML1, linking channel activity with specific lysosomal functions. For example, ML-SA activation of TRPML1 is sufficient to trigger lysosomal exocytosis, TFEB activation, and retrograde transport, and the effects were abolished in TRPML1 knockout (KO) cells (Li et al., 2016b; Wyant et al., 2017; Zhang et al., 2016). Moreover, many lysosomal functions mediated by endogenous activation of TRPML1 are blocked by ML-SIs (synthetic inhibitors) (Li et al., 2016b; Zhang et al., 2016).

1.1.2.2 Physiology of TRPML1

Metal export. As a non-selective cation channel, TRPML1 exports Fe^{2+} and Zn^{2+} from the lysosomal lumen to the cytosol (Dong et al., 2008; Eichelsdoerfer et al., 2010). ML1 KO cells show lysosomal Fe^{2+} and Zn^{2+} overload phenotypes, which lead to iron-deficiency anaemia in ML-IV patients (Dong et al., 2008).

Membrane trafficking. Multiple lines of evidence suggest that because it is the primary Ca^{2+} release channel of lysosomes, in response to various cellular cues, TRPML1 regulates membrane trafficking including lysosomal fusion, fission, motility, positioning, and exocytosis (Cheng et al., 2010; Xu and Ren, 2015). Accumulation of enlarged late endosomes (LE) and autophagosomes (AP) in both ML1-deficient mouse and Drosophila models indicate impaired LE-lysosome and AP-lysosome fusion (Dong et al., 2008; Venkatachalam et al., 2008). Retrograde trafficking of lactosylceramide from LEL to the trans-Golgi network (TGN) is defective in ML-IV cells (Chen et al., 1998; Pryor et al., 2006; Thompson et al., 2007). Given that LE-lysosome fusion and membrane fission are Ca^{2+}-dependent processes, ML1 likely plays a role in both lysosomal fusion, fission and reformation (Luzio et al., 2007a; Luzio et al., 2007b). However, as most cellular assays do not directly measure vesicle fusion or fission, these cellular defects may also be secondary effects of lysosomal storage or defects in another cellular processes. Membrane fusion and fission may coordinately regulate each other. Thus, super-resolution imaging monitoring fusion and fission events in real time are needed.

Motility and positioning of lysosomes was recently shown to be driven by ML1 activity (Li et al., 2016b). TRPML1 activity is required to promote Ca^{2+}-dependent centripetal movement of lysosomes towards the perinuclear region (where autophagosomes accumulate) following autophagy induction (Li et al., 2016b). While the peripheral mobilization of lysosome has not been implicated as Ca^{2+}-regulated, TRPML1 regulates lysosome tubulation by tuning the balance between minus-end and plus-end motility (Li et al., 2016b).

TRPML1 regulates lysosomal exocytosis in a Ca^{2+}-dependent manner. Overexpression of a gain-of-function mutation of ML1 boosted lysosomal exocytosis in HEK293T cells (Dong et al., 2009; Medina et al., 2011). Lysosomal exocytosis induced by TFEB overexpression is abolished

in ML-IV fibroblasts (Medina et al., 2011). The muscular dystrophy phenotype in ML1 KO mice is caused by impaired lysosomal exocytosis and membrane repair (Cheng et al., 2014; Yu et al., 2020). In Duchenne muscular dystrophy mouse models, activation of ML1 with ML-SAs elevated lysosomal exocytosis, protecting muscle cells from membrane damage (Yu et al., 2020). Therefore, ML1 is both necessary and sufficient for lysosomal exocytosis.

Signal transduction. Lysosome transduces downstream signals with Ca^{2+} released through TRPML1 via different Ca^{2+} effectors. Calcineurin is activated upon ML1 opening, dephosphorylating TFEB for downstream autophagic and lysosomal gene transcription events (Medina et al., 2015). Recently, multiple publications demonstrated ML1's positive role in regulating mTOR activity through calmodulin (Li et al., 2016a; Sun et al., 2018; Wong et al., 2012). Since mTOR inhibits ML1 activity by direct phosphorylation (Onyenwoke et al., 2015; Sun et al., 2018), the two molecules form a negative feedback loop and together with TFEB, constitute a sophisticated regulatory network in lysosomal adaptation to nutrient depletion.

Several Ca^{2+} sensors participate in regulating lysosomal membrane trafficking. ALG-2, a cytosolic sensor with five EF-hand motifs, directly interacts with ML1 in a Ca^{2+}-dependent manner (Vergarajauregui et al., 2009). Upon activation of the TRPML1-ALG-2 pathway, the dynactin-dynein motor protein complex is recruited to drive minus-end-directed motility of lysosomes (Li et al., 2016b). Syt7 seems to be the most important Ca^{2+} sensor in lysosomal exocytosis (Samie et al., 2013). Inhibition of syt7 either by antibody or dominant negative form diminished lysosomal exocytosis (Samie et al., 2013). Mice macrophages knockout of syt7 showed impaired lysosomal exocytosis and particle uptake (Samie et al., 2013). Since lysosomal exocytosis was not completely abolished in KOs (Samie et al., 2013), additional Ca^{2+} sensors are present in compensation.

1.1.3 Transport of Lysosomal Contents to Lysosomes

Newly synthesized lysosome proteins from the rough ER are targeted to the lysosome through two pathways. The TGN to endosome pathway carries receptor targeted substrates, typically hydrolases, directly to the endocytic pathway for subsequent lysosome delivery (Braulke and Bonifacino, 2009; Kornfeld and Mellman, 1989; Saftig and Klumperman, 2009; Trivedi et al., 2020) 117. An indirect pathway also exists that includes transport to the plasma membrane and subsequent endocytic delivery (Coutinho et al., 2012; Rijnboutt et al., 1991a; Rijnboutt et al., 1991b). The TGN pathway tags newly made proteins with mannose-6-phosphate residues that are recognized and bound by two different mannose-6-phosphate receptors (M6PRs) in the TGN (Doray et al., 2002; Kornfeld, 1992; Pohlmann et al., 1995; Sohar et al., 1998). Clathrin coated vesicles from the TGN containing M6PRs transfer hydrolases to endosomes (Sachse et al., 2002), where hydrolases dissociate from M6PRs due to endosomal acidity, and are further fed into lysosomes through the endosome maturation process (Figure 1.3, Pathway ①) (Saftig and Klumperman, 2009). Some lysosome membrane proteins like LAMPs arrive at the lysosome through a more direct, clathrin-independent pathway, where non-clathrin coated vesicles that originated in the Golgi fuse directly with late-endosomes using SNARE machinery VAMP7 and hVps41 for delivery (Figure 1.3, Pathway ②) (Pols et al., 2013b). This suggests that lysosomal membrane proteins are delivered at progressive stages of endosome maturation to ensure precision of vesicular specificity as well as to avoid endosomal sorting processes (Pols et al., 2013b).

Component exchange may also employ the non-vesicular, inter-organelle material exchange pathways at lysosome-organelle membrane contact sites (Figure 1.3, Pathway ③). Lysosomes form membrane contact sites with all types of organelles, including ER, mitochondria, and peroxisomes (Eisenberg-Bord et al., 2016; Wong et al., 2018). Free cholesterol can be exported

from lysosomes to the ER and peroxisomes through lysosome-ER (Hoglinger et al., 2019; Infante et al., 2008; Zhao and Ridgway, 2017) and lysosome-peroxisome membrane contact sites (Chu et al., 2015), while lysosomal Ca^{2+} stores may be acutely refilled by ER Ca^{2+} at ER-lysosome membrane contact sites (Garrity et al., 2016).

1.1.4 Lysosome-associated diseases

Lysosome-associated diseases include classic lysosomal storage disease (LSDs) as well as other diseases that are tightly linked to lysosome functions, such as common neurodegenerative diseases and cancer, many of which show lysosomal storage phenotype or can be ameliorated through manipulation of lysosomal proteins.

1.1.4.1 Lysosomal storage diseases

Lysosomal storage diseases describe over 50 inherited rare diseases characterized by accumulation of lysosomal materials, typically caused by mutations in catabolic enzymes, membrane channels and transporters, and proteins regulating lysosomal degradation, export, and trafficking (Boustany, 2013; Dong et al., 2010; Parenti et al., 2015; Parkinson-Lawrence et al., 2010; Schulze and Sandhoff, 2011; Vitner et al., 2010). Although each LSD is rare, combined the prevalence adds up to around 1 in 8000 live births (Parenti et al., 2015). Typical clinical manifestations of LSDs include neurological, skeletomuscular, and visceral (hepatosplenomegaly) abnormities (Parenti et al., 2015). Other organs, including kidney, blood system, heart, respiratory tracts and lungs, skin, stomach and intestines, can all be affected (Parenti et al., 2015).

Commonalities of LSDs include accumulation of un-degraded materials, impaired lipid trafficking, disturbed ER Ca^{2+} homeostasis, and enhanced cellular stress responses (Boustany,

2013; Lieberman et al., 2012; Lim et al., 2015; Walkley and Vanier, 2009). Mutations in NPC1 cause Niemann-Pick type C disease (NPC), a neurodegenerative LSD with cholesterol/sphingolipid accumulation (Lloyd-Evans et al., 2008; Shen et al., 2012). Excessive sphingomyelin accumulation in the lysosome inhibits TRPML1 (Shen et al., 2012). Likewise, mutations in PIKfyve, the PI(3,5)P2-synthesizing enzyme, and OCRL, a PI(4,5)P2 phosphatase, also cause LSD-like symptoms (Dong et al., 2010; Schmiege et al., 2017). Loss-of-function mutations in TRPML1 gene cause ML-IV (Boudewyn and Walkley, 2018). Thus, reduced lysosomal TRPML1 activity may underlie or contribute to trafficking defects and lysosome dysfunction in many LSDs.

A variety of therapies have been proposed and tested in many different LSDs. Enzyme replacement therapies, substrate reduction therapies, and pharmacological chaperones are currently being used with varying degrees of success while technical barriers still exist (Boustany, 2013; Brady, 2006; Parenti et al., 2015). Gene therapy by transducing the non-mutated gene using virus seems to be most promising, especially with CRISPR/Cas9 technology (Parenti et al., 2015). Clinical trials for gene therapy in a wide range of LSDs are already in progress (Nagree et al., 2019; Parenti et al., 2015). Compared with costly enzyme replacement or gene therapy for individual LSD, targeting TRPML1 is attractive as it appears to play a key role in multiple diseases (Medina et al., 2015). With the potent small molecule agonists and antagonists, ML1 may be a potential therapeutic target for treating LSDs and lysosome-associated diseases at low cost (Grimm et al., 2017). In NPC cells, overexpression of ML1 and ML-SA1 ameliorate cholesterol storage, suggesting ML1 activation facilitates lysosomal function (Shen et al., 2012; Zou et al., 2015). However, off-target effects could exist as ML1 is involved in a wide range of signaling cascades.

1.1.4.2 Neurodegenerative diseases

Because they are heavily reliant on autophagy and intracellular trafficking, neurons are especially sensitive to lysosome and autophagy defects (Appelqvist et al., 2013; Bellettato and Scarpa, 2010). Recent studies have revealed connections between LSDs and neurodegenerative diseases. About two-thirds of LSD patients show neurological impairment, especially childhood neurodegeneration (Parenti et al., 2015). Amyloid peptides, the pathological hallmark in Alzheimer's disease (AD), are found accumulated intracellularly in NPC cells (Nixon, 2004). Whereas impaired TRPML1 signaling may contribute to AD (Bae et al., 2014; Lee et al., 2015), genome-wide association studies (GWAS) have identified a link between TMEM175 and PD (Chang et al., 2017). TMEM175-deficient neurons are susceptible to α-synuclein aggregation ((Jinn et al., 2017); Hu et al., personal communication). Deregulated autophagic flux in mice results in pathological neurodegeneration (Nixon, 2013).

Lysosomes have been proposed as a potential target for treating neurodegeneration (Lie and Nixon, 2019). For instance, genetic and pharmacological activation of TFEB decreased aggregated α-synuclein in PD cell and mouse models through autophagic-lysosomal pathway (Decressac et al., 2013; Kilpatrick et al., 2015). Similarly, studies in AD and Huntington's disease (HD) have also revealed TFEB activation helps clearance of protein aggregation and improves neurological function in AD and Huntington's disease (HD) (Polito et al., 2014; Tsunemi et al., 2012; Xiao et al., 2014).

1.1.4.3 Cancer

Lysosomes have several different roles in cancer. Due to their high energy demand, cancer cells step up their catabolic capabilities, e.g., by boosting autophagy and facilitating lysosomal

degradation, to promote tumor progression (Hamalisto and Jaattela, 2016; Kallunki et al., 2013; Kroemer and Jaattela, 2005). An acidic tumor microenvironment has been shown to cause redistribution of lysosomes to the cell periphery (Ji et al., 2019), which may enhance proliferation through increased mTORC1 and mTORC2 signaling (Korolchuk et al., 2011). Upon exosome release or lysosomal exocytosis, the degradation products, i.e., nutrients, are also taken up by neighboring cancer cells to sustain their growth (Goldsmith et al., 2014; Kroemer and Jaattela, 2005). Release of lysosomal enzymes by exocytosis can digest the extracellular matrix and enable cancer progression and metastasis (Kirkegaard and Jaattela, 2009). Given the heavy dependence on lysosomal machinery for their survival, cancer cells are particularly sensitive to lysosome disruption (Groth-Pedersen and Jaattela, 2013; Ostenfeld et al., 2005; Petersen et al., 2013). Lysosome inhibitors and/or inducers of lysosome membrane permeability are reportedly effective in triggering cancer cell death (Amaravadi et al., 2016; Piao and Amaravadi, 2016). Inhibition of lysosomal exocytosis through interruption of SNARE-associated synaptotagmin proteins has been shown to inhibit cell migration and cancer invasion (Machado et al., 2015; Meng and Wang, 2015; Naegeli et al., 2017).

By mediating lysosomal Ca^{2+} signaling and thus regulating lysosomal exocytosis and autophagy, TRPML1 possesses protumorigenic functions. TRPML1 was recently reported to be upregulated in melanoma (Kasitinon et al., 2019), and a high expression level of ML1 may serve as a prognostic marker for several different types of cancer (https://www.proteinatlas.org/ENSG00000090674-MCOLN1). Several loss-of-function studies suggest that ML1 inhibition or knock-down may reduce cancer cell proliferation (Jung et al., 2019; Xu et al., 2019). Therefore, TRPML1 may act as a potential target for anti-cancer therapies.

1.2 Physiology of lysosome-related intracellular organelles

Lysosome-related organelles (LROs), including pigment cell melanosomes, platelet dense and alpha granules, and neuronal presynaptic vesicles are compartments sharing features with endosomes and lysosomes, while harboring unique morphology, cell type-specific contents, and diverse functions in specialized cells, to fulfill specific physiological needs (Bowman et al., 2019; Delevoye et al., 2019; Marks et al., 2013). General characteristics of LROs include an acidic luminal pH and Ca^{2+} storage (Bowman et al., 2019). LROs require specific endosomal effectors and molecular mechanisms for their biogenesis, maturation, transport, and release (Bowman et al., 2019).

Most LROs develop from endosomal precursors but some originate from the secretory pathway (Delevoye et al., 2019). Melanosomes, for example, are derived from the endosome system, maturing from sorting endosomes, followed by fusion with lysosomes and the import of melanogenic enzymes and transporters via transport carriers from early/recycling endosomes or the TGN (Delevoye et al., 2019; Marks et al., 2013; Raposo and Marks, 2007). Thus, the membrane constitutes and luminal contents of LROs are predominantly derived from the early and/or late endosomal system and lysosomes, sharing membrane proteins such as LAMP1.

For melanosomes and platelet dense granules, two highly studied LROs, maturation requires the functions of four groups of proteins: the adaptor protein complex 3 (AP-3) as a protein sorting machinery to facilitate LRO maturation, such as OCA2 to melanosomes (Bowman et al., 2019; Dell'Angelica, 2009; Dell'Angelica et al., 1999; Kantheti et al., 1998); homotypic fusion and vacuole protein sorting (HOPS) and the class c CORe vacuole/endosome tethering (CORVET) complexes (HOPS/CORVET) that function as endosomal tethers and SNARE regulators (Balderhaar and Ungermann, 2013; Bowman et al., 2019; Nickerson et al., 2009; Peplowska et al.,

2007; Pols et al., 2013a); biogenesis of LRO complex (BLOC)-1 which localizes to and is required for formation of the endosomal tubular transport carriers that fuse with melanosomes to deliver cargo (Cullinane et al., 2011; Di Pietro et al., 2006; Setty et al., 2008; Setty et al., 2007), and BLOC-2 that facilitates tubular cargo transport carrier targeting (Dennis et al., 2015); BLOC-3 and the Rab GTPase targets of BLOC-3 function Rab32 and Rab38 (Gerondopoulos et al., 2012), which may play a primary role in retrograde transport of cargoes from melanosomes to the endosome system (Dennis et al., 2016).

Most, if not all, LROs undergo secretion to release luminal contents into the extracellular space in response to signaling cues (Marks et al., 2013). This requires the assistance of actin/myosin-based motors (Nightingale et al., 2011), and the stimulus-dependent fusion machinery with the plasma membrane (PM) (Al Hawas et al., 2012; Ye et al., 2012). One essential component of the molecular machinery that allows for melanosome docking at the cell periphery is Rab27A, which functions as a component in the Rab27A-myosin VA-melanophilin complex to tether LROs to cortical actin (Hume et al., 2001; Wu et al., 2001; Wu et al., 2002). Munc13-4, a Ca^{2+}-binding effector of Rab27A , is a SNARE interacting protein functioning in granule secretion as a tether (Chicka et al., 2016; Elstak et al., 2011), directly regulating SNARE-dependent fusion at the plasma membrane together with STX11 and Munc18 (Boswell et al., 2012; Dieckmann et al., 2015; Spessott et al., 2017). While presumably similar mechanisms exist for all other LROs, the specific molecular components involved might differ. For example, Rab27 is absent in platelet alpha granules, and whether CD63, a common sorting protein on LRO membranes, is present on presynaptic vesicles remains unknown (Delevoye et al., 2019).

As intracellular Ca^{2+} stores, LROs house Ca^{2+}-permeable channels that may regulate their own secretion. In T-cells, TPCs localize to lytic granules, which are identified as the target

organelles for the Ca^{2+} mobilizing messenger NAADP to promote secretion (Davis et al., 2012). P2X4 is found in lamellar bodies of alveolar cells (Miklavc et al., 2011; Miklavc et al., 2013).

New LRO family members may be present in organelles with features that differ from conventional endolysosomes (Delevoye et al., 2019). Tubulovesicles have been long proposed as acidic vesicular Ca^{2+} stores that undergo exocytosis, bringing H^+/K^+-ATPase proton pumps to the apical membranes of parietal cells for acid secretion in the stomach upon histamine stimulation (Forte and Zhu, 2010; Yao and Forte, 2003). Derived by endocytosis and then fusion with early endosomes, pre-tubulovesicles undergo vesicular maturation into recycling endosomes, where sorting and budding events take place for tubulovesicular reformation (Forte and Zhu, 2010). The adapter protein AP-1 and sorting protein CD63 have been shown to localize on tubulovesicles (Duffield et al., 2003; Okamoto et al., 2000). With fusion signals, tubulovesicles undergo fusion with the PM utilizing the v-SNARE machinery requiring Munc18 (Liu et al., 2007). With the identification of lysosomal TRPML1 as a membrane resident protein (see Chapter II for details), tubulovesicles may meet the criteria of LROs, being cell type-specific and containing endolysosomal contents.

1.3 Membrane contact sites between lysosomes and intracellular organelles

1.3.1 Physiology of organellar membrane contact sites

Until recently, the exchange of signals and metabolites between cellular compartments was thought to occur primarily by two broad mechanisms: diffusion or active transport through the cytoplasm, and vesicular trafficking, but recent studies, suggest that a third mechanism, exchange of signals and metabolites at regions where organelles are in direct contact also has a role. As a ubiquitous way for organellar communication and activity integration, functional contacts play

widespread roles in cell physiology and cellular stress responses. All organelles form functional contacts with at least one other and often more than one organelle (Shai et al., 2018; Valm et al., 2017).

Membrane contact sites (MCS) are classically defined as areas of close apposition between the membranes of two organelles with the actual distance depending on the proteomics and function (see below). Both homotypic (between identical organelles) and heterotypic (between two different organelles or two different membrane types) contact sites have been reported. Heterotypic contacts involve a wide range of organelles including ER-mitochondria/ PM/Golgi/peroxisomes/lipid droplets (LDs), LDs-peroxisomes, mitochondria-vacuoles/endosomes/PM/LDs/peroxisomes, lysosome-mitochondria/ER/peroxisomes, etc. (Eisenberg-Bord et al., 2016). Homotypic contact sites, that are not fusion intermediates, have been described between different parts of the ER (Wang et al., 2016) or two peroxisomes (Schrader et al., 2000; Zaar et al., 1984) and potentially other multicopy organelles. In some cases, MCSs appear to form between three organelles. For example, the mitochondria-ER-cortex tether functions in the distribution and inheritance of mitochondria in yeast (Lackner et al., 2013).

To differentiate membrane contacts from organellar fusion and general organelle juxtaposition, a typical MCS should possess the following features:

Specific function: MCS must fulfill a specific function, which in general can be summarized into three categories: i) Metabolite transfer: to bidirectionally transport specific molecules such as Ca^{2+}, lipids, amino acids, and metals (Burgoyne et al., 2015; Lahiri et al., 2015; Sheftel et al., 2007). ii) Organelle dynamics regulation: to transmit signaling information or physical force important for remodeling activities, such as organelle biogenesis, positioning, motility and fission (Friedman et

al., 2013; Hamasaki et al., 2013; Raiborg et al., 2015; Rowland et al., 2014). iii) Signaling: to serve as signaling hubs or facilitating signaling, for example, Ca^{2+} and ROS signaling at the ER-mitochondria MCSs (Booth et al., 2016; Muallem et al., 2017; Yoboue et al., 2018). That MCSs are functional indicates the existence of regulatory mechanisms for individual MCS. Organelles can form more than one type of functionally distinct MCSs. Multiple ER-mitochondria MCSs exist with different functions composed by separate sets of proteins (Phillips and Voeltz, 2016).

Tethering: Contact sites are tethered areas of proximity between two bi- or mono-layer membrane-bound organelles. The distance between the two organelles may vary depending on diffusion characteristics of transported metabolites or functional characterization. ER-mitochondria contacts are usually in the range of 10-80 nm, with loose contacts formed with rough ER membranes 50-80nm, tight contacts for lipid exchange formed with smooth ER <10nm, and contacts functioning in mitochondrial fission ~30nm (Csordas et al., 2010). Typically, the IP3R-Grp75-VDAC mediated ER-mitochondria contact for mitochondrial Ca^{2+} uptake is at 12-24nm (Csordas et al., 2010). Close MCSs of <5nm exists in lysosome-mitochondria contact for mitochondria fission (Wong et al., 2018). However, as cases of much larger value (over 300nm in Num1-anchored mitochondria-PM contacts) exist (Ping et al., 2016), distance cannot be the sole measure to be define a contact site. Instead, the presence of tethering forces from protein-protein or protein-lipid interactions in all cases reported to date makes it the preferred biomarker for MCSs.

Defined proteome: An ideal MCS should have proteins and/or other membrane components required for: tethering, function, regulation, and the maintenance of the architecture. Based on current knowledge, MCS are composed of four classes of proteins: structural proteins

(tether/spacer), functional proteins, sorter proteins, and regulatory proteins (Scorrano et al., 2019). Tethers physically establish/maintain the connection between the two membranes while spacers keep the two membranes at a defined distance to inhibit fusion. Tethers are often directly anchored to one of the two membranes through a transmembrane domain or by a lipid modification, and interact with proteins and/or lipids on the partner membrane via a second domain (Chung et al., 2015; Giordano et al., 2013). Thus, "public" tethers may exist based on the property of its proteins/lipid interacting domain. Vesicle- associated membrane protein (VAMP)-associated proteins (VAPs), a general tether involved in various ER MCSs interacts with diphenylalanine in an acidic tract (FFAT) motif containing partner proteins (Di Mattia et al., 2018; Johnson et al., 2018). Importantly, pairs of molecules functioning at contacts can also drive tethering and the sum of the forces exerted by all these pairs ultimately tethers the two organelles (Manford et al., 2012). Generally, most contacts have multiple tethering molecules so that deleting any singular tethering pair appears ineffective in abolishing a contact.

Functional proteins fulfill functions, such as metabolite transfer by channels/transporters. The functions often benefit from dense concentrations of specific proteins in the contact forming membranes, limiting the events local so that the bulk cytosol is not altered (especially for material transfer) (Csordas et al., 2010; Prakriya and Lewis, 2015). This is achieved by sorting and recruitment proteins, which work to define the MCS proteome and lipidome. Sorting can occur by direct binding to proteins for active recruitment, or indirectly by altering lipids or the proteins themselves (e.g. post-translational modifications), or by repelling non-residents of contact sites (Scorrano et al., 2019).

Regulatory proteins coordinate contacts to maintain homeostasis. These include proteins that regulate the contact site itself (Honscher et al., 2014), as well as the functional proteins in the

contacts. For example, p53 changes the redox state of the sarcoplasmic reticulum (SR)-ER Ca^{2+}-adenosine triphosphatase (SERCA) pumps at the ER, leading to an excessive Ca^{2+} load, thus altering ER-mitochondria tethering (Giorgi et al., 2015).

The characterization of contact-site proteins is largely immature. Many proteins have several capacities in the same molecule such as tethers that are also lipid transporters or regulators (Scorrano et al., 2019).

Whether contacts have a unique lipidome remains elusive, but fractionation of ER-mitochondria contacts suggests the presence of ceramides and sterols-enriched rafts (Garofalo et al., 2016; Poston et al., 2011). Also, palmitoylation may serve as a signal to enrich proteins at mitochondria-ER MCSs (Lynes et al., 2012).

The duration of time that a contact persists is flexible, depending on its function, regulation, and cell type. Indeed, dynamic and transient contacts exist as well as stable ones that are maintained over long periods. Dynamic contacts of <10s have been described during ER-endosome contacts that control endosome motility following depletion of Ca^{2+} from ER stores or increase of intracellular Ca^{2+} (Raiborg et al., 2015), while more stable contacts between lysosome and mitochondria may last for 2min or more (Wong et al., 2018). Some specialized ER-PM MCSs in muscle cells may persist for the lifespan of the cell (Dickson, 2017). Presumably, the average contact time of MCSs not only varies regarding its functional property and quantity of metabolites transferred, but also largely relies on the regulation of tether formation and dissociation.

1.3.2 Metabolic channeling at MCSs

MCSs allow metabolites to be efficiently transferred between cellular compartments. The most characterized metabolites are Ca^{2+} and lipids. MCSs may allow a form of substrate

channeling that occurs when metabolites are passed directly between channels/enzymes. This prevents metabolites from being consumed by off-pathway reactions, and also increases reaction rates by reducing the transfer time. Driven by specific organellar cues and mediated by distinct proteome, such exchange at MCSs is organelle- or enzyme-specific (Prinz et al., 2020).

1.3.2.1 Channeling of Ca^{2+}

A key aspect of the regulation of Ca^{2+} signaling is the compartmentalization of Ca^{2+} in various cytoplasmic organelles that act as intracellular Ca^{2+} stores. Whereas Ca^{2+} release from the large-volume Ca^{2+} stores, such as the ER, is extensively involved in signal transduction, Ca^{2+} release from the small-volume individual vesicular stores such as lysosomes may be more useful in local regulation, such as membrane fusion and individualized vesicular movements (Li et al., 2013a; Li et al., 2016b). Conceivably, these two types of Ca^{2+} stores may be established, maintained, or refilled via distinct mechanisms.

MCSs have been found to be involved in regulating this important signaling pathway by means of concentrating and directing Ca^{2+} transfer. ER stores are maintained by the well characterized process of store-operated Ca^{2+} entry (SOCE), which requires the collaborative interaction of stromal interaction molecule (STIM), an ER luminal Ca^{2+} sensor, and the PM calcium release-activated calcium modulator Orai1 (Liou et al., 2005; Park et al., 2009; Prakriya et al., 2006). Upon ER Ca^{2+} store depletion, Ca^{2+} dissociates from the luminal EF-hand domain of STIM1 and STIM2, leading to their oligomerization and translocation to the ER-PM MCSs (Stathopulos et al., 2008; Zhou et al., 2013). Orai1 channels in turn accumulate at MCS spots on the PM, and are activated upon direct binding with STIM proteins, resulting in a sustained Ca^{2+} influx from the extracellular space (Stathopulos and Ikura, 2017). The imported Ca^{2+} is taken up

from the nearby cytosol by the SERCA pump in the ER (Clapham, 2007). The channeling of Ca^{2+} via this mechanism allows the Ca^{2+} to directly enter the ER without increasing the Ca^{2+} concentration in the cytoplasm outside the vicinity of the MCS.

Maintenance and refilling of smaller intracellular Ca^{2+} stores has been shown to be ER Ca^{2+}-dependent. The IP3R are the primary Ca^{2+} releasing channels on ER. Opening of IP3R leads to a local increase in Ca^{2+} concentration, which diffuses and significantly decreases by approximately 100nm away from the channels. Moreover, Ca^{2+} uptake of organelles such as mitochondria require high $[Ca^{2+}]_{Cyt}$. Driven by a large negative $\Delta\psi$ in the inner membrane, mitochondrial Ca^{2+} uptake through mitochondrial Ca^{2+} uniporters (MCU) requires a large, localized Ca^{2+} concentration due to its low affinity. Therefore, the release of Ca^{2+} from the ER to other organelles is expected to be much more efficient at tight contacts.

ER-mitochondria MCSs play a central role in regulating mitochondrial Ca^{2+} levels by modulating Ca^{2+} movement from the ER lumen to the mitochondrial matrix. The efficient ER-to-mitochondria transfer of Ca^{2+} requires the enrichment of IP3Rs at ER-mitochondria MCSs, creating local Ca^{2+} spikes much higher in concentration than the bulk cytoplasm, exceeding 10μM (Csordas et al., 2010). Ca^{2+} is funneled to the voltage dependent anion-selective channel (VDAC) in the outer mitochondrial membrane (OMM) (Rizzuto et al., 1998; Szabadkai et al., 2006) and further translocates across the inner mitochondrial membrane (IMM) into the matrix utilizing MCU (Baughman et al., 2011; De Stefani et al., 2011). The cytoplasmic chaperone 75-kDa glucose-regulated protein (Grp75) serves as a tether and a cytosolic regulator of the IP3R-VDAC complex, promoting interaction between the channels to increase mitochondrial Ca^{2+} uptake efficiency (Szabadkai et al., 2006). Additional regulators of Ca^{2+} transfer have been identified at ER-mitochondrial MCSs. The OMM protein dynamin-related family member mitofusin 2 (Mfn2)

is one proposed tether regulating inter-organelle linkage at Ca^{2+}-transfer sites (de Brito and Scorrano, 2008). Recently, an ER membrane protein, PDZD8, was also implicated in ER-dependent mitochondrial Ca^{2+} homeostasis (Hirabayashi et al., 2017).

1.3.2.2 Channeling of lipids

MCSs play important roles in intracellular lipid trafficking by serving as sites of non-vesicular lipid exchange between organelles. Non-vesicular transport of lipids at MCSs requires a machinery that can extract a lipid molecule out of the original membrane, shelter it from the cytosolic aqueous environment in a hydrophobic pocket, close the cytosolic gap between the opposing membranes to enable the transfer of the molecule, and finally insert it into the outer layer of the target membrane (Phillips and Voeltz, 2016). It is generally facilitated by lipid transport proteins (LTPs), which have domains that can bind one or more lipid monomers in hydrophobic pockets or grooves and transfer the lipids between membranes. Many LTPs bind MCS-localized membrane proteins such as VAPs in the ER (Wong et al., 2019). Generally, lipid consumption at target membrane (Kumagai and Hanada, 2019) and lipid (Kannan et al., 2017; Kim et al., 2011) or LTP enrichment (Maeda et al., 2013) at MCSs may all drive the channeling of lipids .

Aside from the biosynthetic route that originates at ER, organelles of the late secretory pathway mostly receive cholesterol from low-density lipoprotein (LDL) endocytosed to the late endosome/lysosome (LEL) (Litvinov et al., 2018), making LELs the central connector in cholesterol-transferring MCSs. ER-resident oxysterol-binding protein (OSBP)-related protein 5 (ORP5) is capable of binding sterol in a conserved pocket and co-immunoprecipitates with lysosomal NPC1 (Suchanek et al., 2007). This led to a model that the two proteins form functional

MCSs to transfer sterol from LELs to the ER membrane (Du et al., 2011). Depletion of NPC1 or ORP5 resulted in sterol accumulation on the late endosome membrane (Du et al., 2011).

VPS13 proteins are large, evolutionarily conserved MCS proteins with a single orthologue (Vps13p) in the yeast Saccharomyces cerevisiae and four orthologues in humans (VPS13A-D). Each of the four human VPS13 genes is associated with a genetic disorder: chorea acanthocytosis with VPS13A, Cohen syndrome with VPS13B, an early onset form of Parkinson's disease with VPS13C, and a form of ataxia with spasticity with VPS13D (De et al., 2017). Knockout (KO) of VPS13D in mice is maternal lethal (https://www.jax.org/strain/017386). Yeast Vps13p localizes to two MCSs: the vacuole-mitochondria patch (vCLAMP) and the nuclear-vacuole junction (NVJ) (Gao and Yang, 2018). In mammalian cells, VPS13A is found to primarily localize to ER-mitochondria contacts, whereas VPS13C localizes to ER-LEL MCSs, interacting with VAPs (Kumar et al., 2018). Drosophila VPS13D colocalize with lysosomal LAMP1 proteins (Anding et al., 2018). The VPS13 family are LTPs defined by sequence homology of the ~120 N-terminal amino acids, or the chorein_N motif (Lees and Reinisch, 2020). The purified yeast Vps13α region binds glycerophospholipids (Gao and Yang, 2018). Indeed, yeast Vps13p appears to function in parallel with the ER-mitochondria encounter structure (ERMES), which tethers the ER to mitochondria and mediates lipid transfer (Gao and Yang, 2018). Thus, VPS13 proteins may play direct roles in the transport of glycerophospholipids at MCSs.

1.3.3 Regulation of membrane dynamics

MCSs generate subdomains within organelle membranes that regulate many membrane-based processes including organelle fission and fusion, as well as the trafficking and intracellular positioning.

Several organellar fission events are dependent on MCSs. Endosomal fission is ER-endosome MCS regulated, with the ER being recruited to endosome fission sites potentially by VPS35 (Rowland et al., 2014). Assembly of ER-endosome MCS at the base of the budding domain is followed by rearrangement of ER tubules around the base of the bud, accompanied by bud fission (Rowland et al., 2014). A similar mechanism exists for ER mediating mitochondrial fission (Friedman et al., 2011). Recently, lysosomes have been implied in marking mitochondrial fission sites via contacts promoted by active GTP-bound lysosomal Rab7 GTPase (Wong et al., 2018).

The formation of the MCSs has been implicated in regulating the trafficking and localization of endosomes. During the maturation process of endosomes trafficking along microtubules from the plasma membrane to final fusion with lysosomes, approximately 53% of all early endosomes, and a staggering 99% of LE, remain in contact with the ER during the long distance trafficking (Friedman et al., 2013). Once bound, the endosomes appear to be tightly tethered to the ER, even 'dragging' ER tubules with them, suggesting the binding of MCS proteins to certain motors (Friedman et al., 2013).

Cholesterol levels affect the composition of ER-LE MCSs, and in turn affects late endosome trafficking and positioning. This mechanism is mediated by a cholesterol-sensing protein, oxysterol-binding-related protein 1L (ORP1L). Containing an oxysterol-binding-related domain (ORD) capable of binding sterols and a FFAT domain, ORP1L localizes to the surface of late endosomes but also possesses the ability to interact with ER VAPs (Rocha et al., 2009). When the ORP1L ORD domain senses cholesterol in the late endosome membrane, ORP1L interacts with a complex includes RAB7 GTPase, Rab-interacting lysosomal protein (RILP), the HOPS late endosome tethering complex, and the dynactin (p150Glued)-dynein motor complex, resulting in minus-end-directed late endosome trafficking (Rocha et al., 2009). Conversely, at low cholesterol

levels, ORP1L undergoes a conformational change that causes its disengagement from dynactin and interaction with VAPs, forming ER-LE MCSs, reducing dynein-facilitated trafficking towards microtubule minus ends (Rocha et al., 2009). Similarly, StAR-related lipid-transfer (START) domain containing 3 (STARD3), with its conserved START protein domain capable of binding to cholesterol and an FFAT motif recruiting ER, senses sterol at ER-late endosome MCSs and provides position regulation of late endosomes (Alpy et al., 2013). Overexpression of STARD3 results in accumulation of late endosomes at the perinuclear region while STARD3 knockdown results in late endosome scattering to the cell periphery (Alpy et al., 2013).

Another protein functions at ER-LEL MCSs to regulate late endosome trafficking is protrudin, an ER transmembrane protein interacting with VAP (Shirane and Nakayama, 2006). It binds to Rab7 (Raiborg et al., 2015) as well as phosphatidylinositol-3-phosphate (PtdIns(3)P) (Shirane and Nakayama, 2006), a lipid enriched on the endosomal membrane, through a FYVE domain. Protrudin promotes plus-end-directed trafficking of LEs by recruiting kinesin-1 to contact sites, followed by transfer of this motor onto FYVE and coiled-coil domain-containing protein (FYCO1), which localizes to the late endosome membrane via Rab7 and PtdIns(3)P, thus functioning as an adaptor to link kinesin-1 to late endosomes (Raiborg et al., 2015). Overexpression of protrudin and Rab7 leads to LE accumulation in the cell periphery as well as ER wrapping around LEs (Raiborg et al., 2015). Conversely, protrudin depletion results in perinuclear accumulation of LEs (Raiborg et al., 2015).

1.3.4 Current techniques in Studying Organellar Membrane Contact Sites

Being transient and abundant, MCSs are hard to visualize, purify, understand their functions and study how environmental and genetic perturbations affect them. It remains

challenging to unequivocally identify a contact and its components, determine its function and monitor its changes upon regulatory signals.

Current approaches to study MCSs can be briefly classified into the following categories: global mapping by proximity-dependent biotinlation and cell fractionation; visualization by super-resolution fluorescence microscopy (SRM), electron microscopy (EM) and electron tomography (ET); identification by proximity-driven fluorescent signal generation such as proximity ligation assay (PLA) and fluorescence resonance energy transfer (FRET) (Huang et al., 2020; Scorrano et al., 2019).

One major challenge lies in the confirmation of a real functional contact. Proteins residing in distinct organelle membranes might be in close contact to each other for many reasons. For example, components of the TOM complex, the translocase of the outer mitochondrial membrane, and the TIM23 complex, the main translocase of the inner membrane, can be crosslinked to each other modulated by incoming precursor proteins to allow direct handover of substrate proteins (Dudek et al., 2013). Stochastic interactions between compartments also introduces a large number of false-positives, especially considering that most contact durations last less than one minute. Functional KO of candidate proteins may not be effective due to the high redundancy (Prinz et al., 2020).

Study of MCSs requires techniques offering both high spatial and temporal resolution. Although offering the best resolution to access nanometer-size MCSs, the fixation and dehydration procedures of EM tend to disrupt the intact architecture MCSs. Also, the dynamics of MCSs in living cells cannot be accessed with EM and ET. SRM offers a unique window with super temporal and spatial resolution in living cells for MCSs, but is limited to visualization without functional examination. While PLA detects protein-protein interactions with endogenous expression levels,

excluding the possibility that fluorescence-tags may disrupt normal protein tethering/function, the fixation process renders it to monitor MCS dynamics. Therefore, a combination of approaches is needed to carefully characterize a specific MCS.

1.3.5 Lysosome contact sites

Over the past few years, an increasing number of lysosome-organelle contacts have been identified and implicated as having important functional consequences (Table 1) (Eisenberg-Bord et al., 2016; Gatta and Levine, 2017). MCSs channeling lipid transfer between lysosome and other organelles are most well studied. In addition, several proteins at LY-organelle MCSs have been implicated in the regulation of lysosome/organellar membrane trafficking, in some cases in response to changes in cholesterol or PtdIns3P levels.

Table 1. Summary of lysosome-organelle MCSs

	Proteome	**Proposed Function**
Vacuole-Mitochondria	VPS13-MCP-1	Phospholipid transport
	Ypt7-VPS39-Tom40	Phospholipid transport
	VPS39-HOPS	Vesicular transport
LY-mitochondria	Rab7	Mitochondrial fission
	MLN64	Cholesterol transport
	VDAC1/DMT1	Mitochondrial Fe^{2+} uptake
LEL-ER	VPS13C	Phospholipid transport
	PDZD8	Ca^{2+} transport
	NPC1-OSBP5	LEL to ER cholesterol transport
	ORP1L-VAP	Endolysosomal trafficking
	STARD3(NL)-VAP	Endolysosomal trafficking
	Rab7-Protrudin	Endolysosomal trafficking
	Annexin A1-EGFR- PTP1B	ER to MVB cholesterol transport
LY-peroxisome	Syt7-PI(4,5)P_2	LY to peroxisome cholesterol transport

The channeling of lysosomal Ca^{2+} is less understood. Several lines of evidence suggest that the ER-LEL interface is a dynamic site for Ca^{2+} crosstalk between these organelles, with Ca^{2+}

being released from both LELs and the ER (Atakpa et al., 2018; Garrity et al., 2016; Kilpatrick et al., 2017). LELs can release Ca^{2+} stores through both TRPs and TPCs. It has been shown that TPC1 localizes to ER-endosome MCSs, tempering EGF receptor (EGFR)-mediated signaling (Kilpatrick et al., 2017). Both NAADP or TPC1 inhibition disrupted contact formation, prolonging EGFR phosphorylation, enhancing downstream signaling through both ERK and PLCγ (Kilpatrick et al., 2017). Therefore, ER-endosome MCS may emerge as Ca^{2+}-dependent hubs for signaling. However, despite its emerging role as a Ca^{2+} signaling center, the establishment, maintenance, and refill of lysosomal Ca^{2+} store remains an enigma. The refilling mechanisms of ER and mitochondrial Ca^{2+} give the hint that lysosomes may refill their Ca^{2+} stores through ER-LY contacts. Indeed, results shown in Chapter IV demonstrate that the ER Ca^{2+} store is essential for lysosomal Ca^{2+} refiling. Depletion of ER Ca^{2+} or inhibition of IP3Rs abolished lysosomal Ca^{2+} refiling, indicating a potential Ca^{2+} channeling MCS with IP3R involved.

Based on the current model that ER store refills wherein ER Ca^{2+} release triggers ER-PM functional coupling via STIM and Orai proteins, lysosomal refilling may be considered as a regulated, three-step process (Figure 1.4): 1) triggering, by increased peri-lysosomal Ca^{2+} and/or decreased $[Ca^{2+}]_{Ly}$; 2) docking, involving the formation of ER-lysosome MCSs; and 3) fueling, wherein Ca^{2+} is transported from the ER to lysosomes through functional ER-lysosome MCSs.

ER-lysosome MCS formation requires several tethering proteins to keep the two opposing membranes in apposition, which may be local Ca^{2+}-dependent. MCS gaps could be reduced, from 20-30 nm to within 5-15 nm, to provide a functional conformation highly amenable to Ca^{2+} exchange (Phillips and Voeltz, 2016), depending on the size of cytosolic domain of the tethering protein. Several E-Syts (extended synaptotagmin-like proteins) have been confirmed to act as tethers at ER-PM MCSs (Giordano et al., 2013; Min et al., 2007). E-Syts have an N-terminal β-

hairpin embedded in the ER membrane and multiple C2 domains in the C-terminal, which contains binding sites for both Ca^{2+} and phospholipids (Giordano et al., 2013; Min et al., 2007). Similar Ca^{2+} sensor proteins may play equivalent roles in ER-lysosome MCSs. Both $PI(4,5)P_2$ and $PI(3,5)P_2$ have been observed in lysosomes (Xu and Ren, 2015). Thus, upon Ca^{2+} release from lysosomes, a Ca^{2+}- and phospholipid-dependent interaction between the two membranes may, in addition to the pre-existing tethers, help bring ER and lysosomes even closer, further supporting the functionality of ER-lysosome MCSs.

After docking, a steep gradient between the Ca^{2+}-loaded ER and Ca^{2+}-depleted lysosomes can drive the transfer of Ca^{2+} from the ER to lysosomes. This process involves the coordinated actions of IP3R-mediated Ca^{2+} release from the ER and lysosomal Ca^{2+} uptake via a putative uptake channel or transporter (Figure 1.4). Although accumulation of IP3Rs through lateral diffusion in ER-lysosome MCSs has not yet been demonstrated directly, constitutive Ca^{2+} release mediated by local enriched IP3Rs has been reported on ER-mitochondrial MCSs (Cardenas et al., 2010; Szabadkai et al., 2006). Because IP3Rs are constitutively active, refilling is plausible given very high local Ca^{2+} concentrations in MCSs, without a widespread Ca^{2+} release (Rizzuto et al., 1998).

In summary, metabolic cross-talk between the endolysosomal system and other organelles appears to be of major biomedical importance in the understanding of lysosome-associated diseases like NPC. Effluxes of metabolites generated by lysosomes to other organelles, possibly through MCSs, could be potential targets for LSDs featured by accumulation of lysosomal contents.

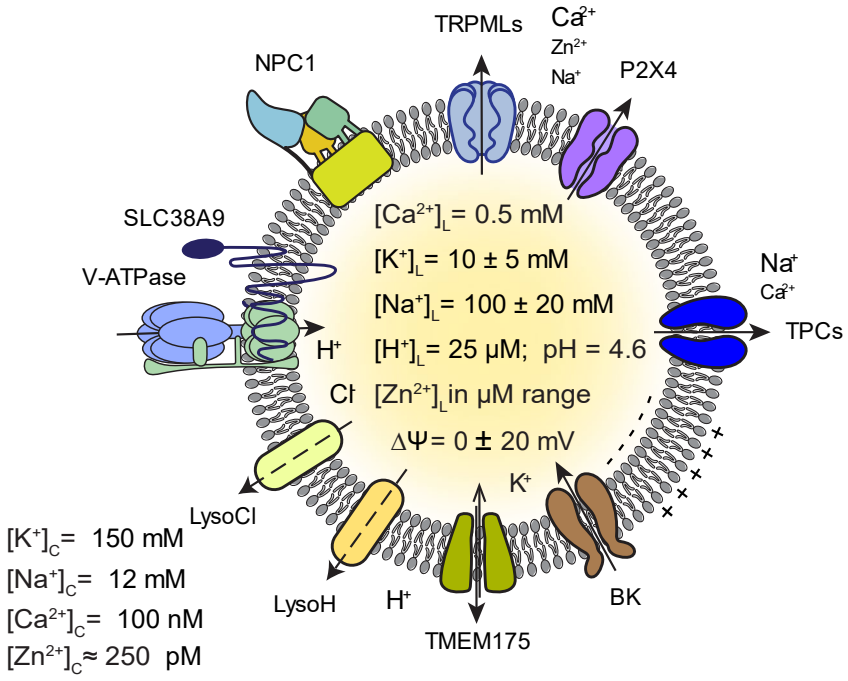

Figure 1.1 Lysosomal ionic composition, ion channels and transporters.
Compared with cytoplasm, the lysosome lumen contains high H^+, Ca^{2+}, Zn^{2+} and Na^+, but low K^+. At resting conditions, lysosomal $\Delta\psi$ is close to 0 mV. Lysosomal channels that have been characterized using lysosomal patch-clamp include Na^+/Ca^{2+}-permeable TRPMLs, P2X4, and TPCs, K^+-selective channel BK, and H^+-selective K^+-permeable channel TMEM175. V-ATPase is the proton pump that acidifies lysosomes. The molecular identities of lysosomal Cl^- conductance is not yet known. SLC38A9 is the lysosomal arginine sensor and transporter; NPC1 is the lysosomal cholesterol transporter. Modified from Figure 2 from Li and Gu et al., 2019.

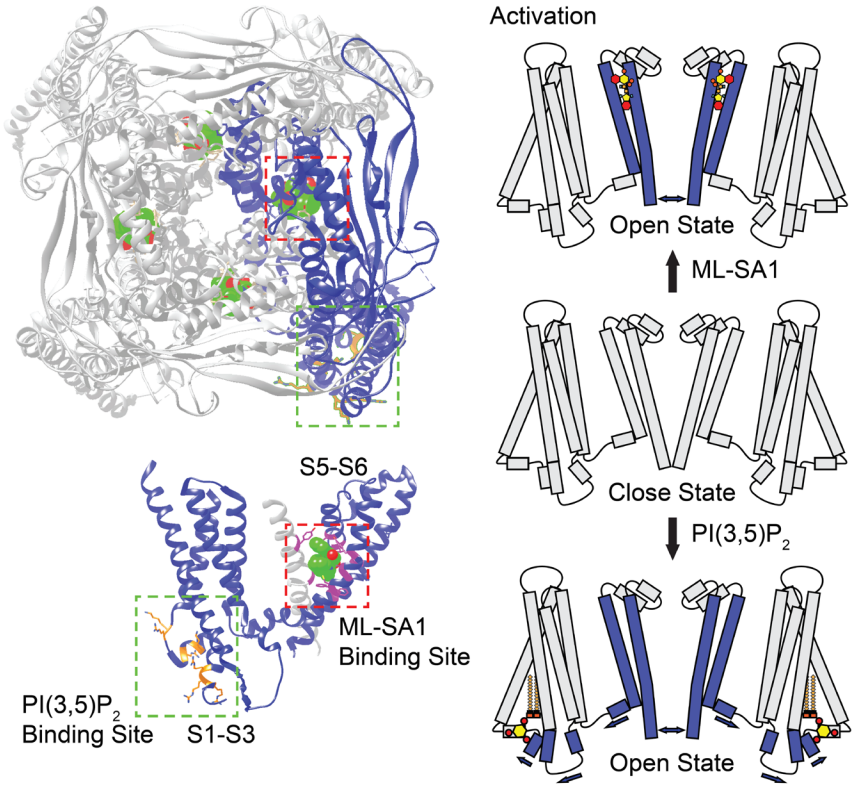

Figure 1.2 Structural mechanisms of ligand-dependent activation of lysosomal TRPML. High-resolution structures of TRPML1. The upper left panel shows a top view of TRPML1 in the tetrameric assembly. Red and green boxes indicate the ML-SA1 and $PI(3,5)P_2$ binding sites, respectively. The lower left panel illustrates the ML-SA1 and $PI(3,5)P_2$ binding sites in a TRPML1 subunit. The right panels are illustrations of ligand-induced channel opening. Modified from Figure 4 from Li and Gu et al., 2019.

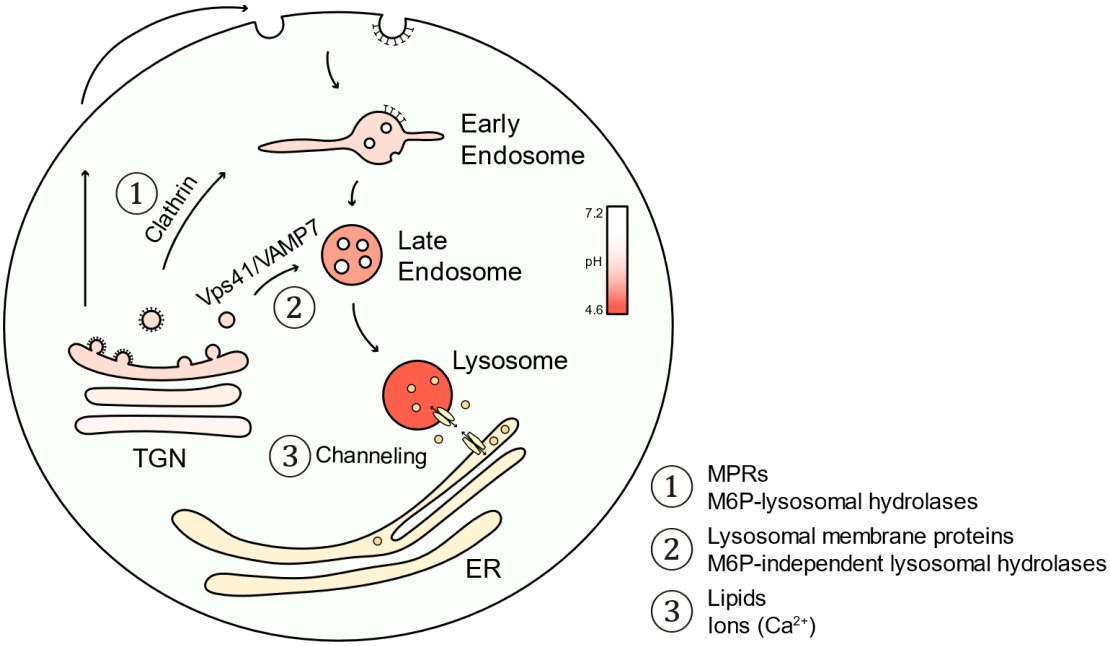

Figure 1.3 Three major pathways to transport materials to lysosomes.
From the TGN, two major pathways mediate transport to the endolysosomal system: ① Clathrin-coated M6PR containing vesicles transport M6P-containing hydrolases to the endosomes which finally mature into lysosomes; ② Non-clathrin-coated vesicles fuse directly with late endosomes utilizing Vps41/VAMP7 SNARE machinery. ③ On the other hand, MCSs between ER and lysosomes transport lipids and ions to the lysosomal lumen via a vesicle-independent pathway. Note that MCS between lysosomes and other organelles form but metabolite transfer events to lysosomes have only been seen in ER-lysosomes MCSs so far.

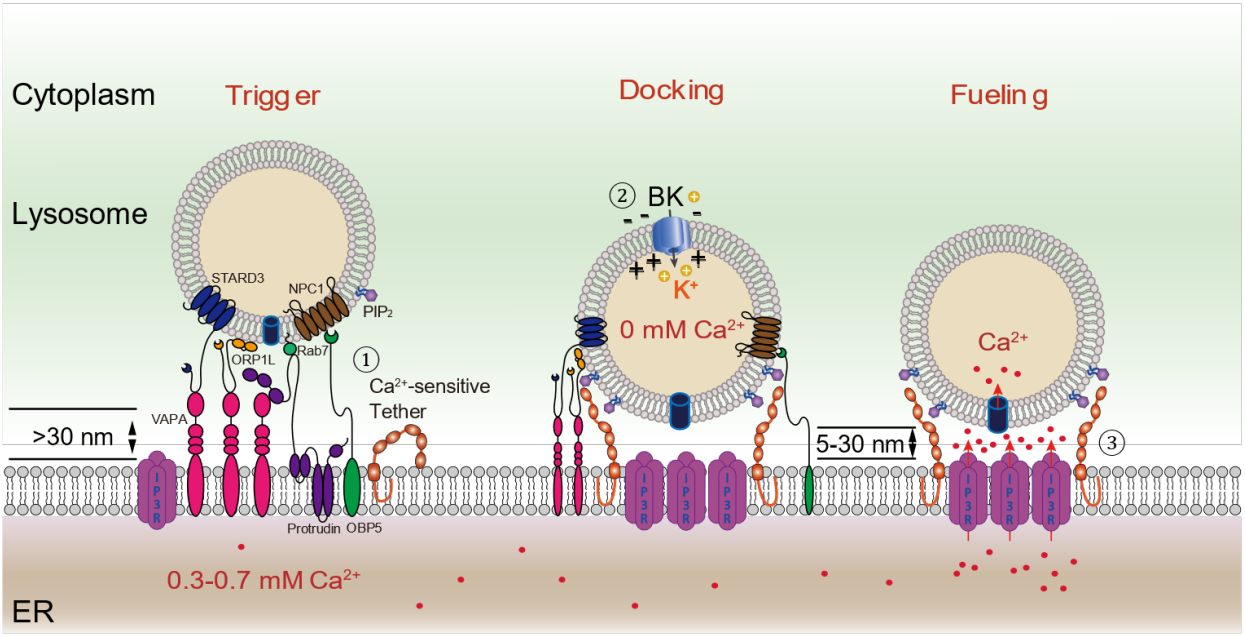

Figure 1.4 A three-step working model of lysosomal Ca^{2+} refilling.
Current known ER-LY MCSs tethers include endolysosome-localized ORP1L, STARD3, Protrudin, NPC1, and ER-localized ORP5, and VAP. Lysosome Ca^{2+} stores are depleted upon cellular stimulation triggering lysosomal Ca^{2+} release. An increase in juxta-lysosomal $[Ca^{2+}]_{Cyt}$ or a decrease in $[Ca^{2+}]_{Ly}$ triggers refilling, requiring Ca^{2+}-sensitive tethering proteins. In the docking step, MCSs are formed mainly by putative Ca^{2+}-sensitive tethers (e.g., E-syt1). In the fueling step, ER and lysosomal membranes are brought closer (< 30nm). Meanwhile, both IP3Rs and putative uptake channel/transporters are enriched in ER-lysosome MCSs. Ca^{2+} is then released from the ER via IP3Rs, causing a steep Ca^{2+} gradient that drives the influx of Ca^{2+} via an unidentified lysosomal uptake channel/transporter. Modified from Figure 2 from Yang et al., 2019.

CHAPTER II

Ca^{2+} Release From ML1 in Tubulovesicles Regulates Vesicular Trafficking and Gastric Acid Secretion[2]

Abstract

Gastric acid secretion by parietal cells requires trafficking and exocytosis of H^+-K^+-ATPase-rich tubulovesicles (TVs) toward lumen-facing apical membranes. Histamine is the primary trigger of this process via cAMP elevation. Here, we found TRPML1 as a tubulovesicular Ca^{2+} channel essential for TV exocytosis and acid secretion. Whereas ML-IV patients are reportedly achlorhydric, transgenic overexpression of ML1 in mouse parietal cells induced constitutive acid secretion. Gastric acid secretion was blocked and stimulated by ML1 inhibitors and agonists, respectively. Organelle-targeted Ca^{2+} imaging and direct patch-clamping of apical vacuolar membranes revealed that ML1 mediates a PKA-activated conductance on TV membranes that is required for histamine-induced Ca^{2+} release from TV stores. Hence, we demonstrated that ML1, acting as a Ca^{2+} channel in TVs, links transmitter-initiated cyclic nucleotide signaling with Ca^{2+}-dependent TV exocytosis in parietal cells, providing a regulatory mechanism that could be targeted to manage acid-related gastric diseases.

[2] Adapted with modifications from my second author paper in Development Cell (Sahoo N, **Gu M**, Zhang X, et al. Gastric Acid Secretion from Parietal Cells Is Mediated by a Ca^{2+} Efflux Channel in the Tubulovesicle. Dev Cell. 2017;41(3):262-273.e6. doi:10.1016/j.devcel.2017.04.003).

Introduction

Acid secretion in the stomach is mediated by parietal cells that are filled with vesicular and tubular TVs, which carry the H^+/K^+-ATPase responsible for H^+ pumping (Hersey and Sachs, 1995; Yao and Forte, 2003). Upon stimulation with gastric transmitters (secretagogues), parietal cells undergo striking morphological changes, including SNARE dependent membrane remodeling and actin-dependent cytoskeleton reorganization (Forte and Zhu, 2010). Subsequently, TVs are translocated to fuse with apically-directed canaliculi, resulting in a large, deeply-invaginated secretory surface that is connected to the stomach lumen (Hersey and Sachs, 1995). The primary secretagogue is histamine, produced by enteroendocrine cells, which activates the Gs-coupled type 2 histamine (H2) receptor to initiate a cAMP-dependent signaling cascade (Chew et al., 1980; Malinowska et al., 1988). Although some types of regulated exocytosis, including synaptic neurotransmitter release, are Ca^{2+}-dependent (Thorn et al., 2016), it remains uncertain whether Ca^{2+} is involved in histamine-triggered TV exocytosis (Chew and Brown, 1986; Negulescu et al., 1989; Yao and Forte, 2003). Acetylcholine, which also acts as a gastric secretogogue, has been shown to induce large releases of Ca^{2+} from endoplasmic reticulum Ca^{2+} stores (Forte and Zhu, 2010; Negulescu et al., 1989). Meanwhile, histamine has been reported to induce very small Ca^{2+} increases in the gastric parietal cells of some species, and no detectable Ca^{2+} responses in other species (Chew and Brown, 1986; Courtois-Coutry et al., 1997; Negulescu et al., 1989; Yao and Forte, 2003). In other processes for which Ca^{2+}-dependence has been debated, organelle-targeted Ca^{2+} imaging methods with very high detection sensitivity have implicated non-ER Ca^{2+} stores as essential for the cellular response (Xu and Ren, 2015).

TRPML1 is the principle Ca^{2+} release channel in the lysosome; it regulates membrane fusion/fission and the transport of lysosomes in response to cellular cues (Xu and Ren, 2015).

Notably, ML-IV possesses gastric phenotype of constitutive achlorhydria, which is recapitulated in ML1 KO mice (Chandra et al., 2011; Schiffmann et al., 1998; Venugopal et al., 2007).

The aim of the present study was to investigate whether ML1 has a direct role in gastric acid secretion. To address this question, we examined how gastric acid secretion is altered in genetically engineered mouse models and affected by direct, pharmacological manipulations of ML1 channel activity.

Methods

ML1 mouse lines

ML1 KO mice were developed in a B6:129 mixed genetic background and their phenotype has been characterized as described elsewhere (Venugopal et al., 2007). The GCaMP3- ML1 *ROSA-lSl* mice were generated in a C57BL/6J genetic background, as described in *Figures S2A and S2B* and crossed with an ATP4B *Cre* line (Syder et al., 2004) to generate the ML1 *ROSAlSl*:ATP4B *Cre* ($ML1^{PC}$) mice, in which the GCaMP3-ML1 transgene is selectively expressed in parietal cells. Prior to most experiments, mice were fasted overnight with free access to water. Both sexes of mice were used under an approved animal protocol following the Institutional Animal Care Guidelines at the University of Michigan.

Gastric gland isolation

Gastric glands were isolated as described previously (Pasham et al., 2013). Briefly, mice were fasted overnight with free access to tap water. After the animals were euthanized, their stomachs were isolated and sliced longitudinally to separate the forestomach, antrum, and corpus regions. The corpus tissues were sliced into small sections and digested in collagenase at 37°C for

1 h. The digested samples were then filtered through 40 μm filters and pelleted by light centrifugation at the speed of 50 x*g* for 8 min. Isolated gastric glands were plated on Matigel (BD Biosciences)-coated cover slips and incubated at 37˚C in a culture medium (Medium A, pH 7.4) containing: DMEM, 20 mM HEPES, 1 mM glutamine supplement, 10 mM glucose, 0.2% BSA, 50ng/ml EGF, 5% selenite-insulin-transferrin liquid medium, 50 U/ml penicillin/streptomycin, 200 μg/ml gentamycin, and 50 μg/ml novobiacin.

Primary parietal cell isolation and culture

After mucosal digestion of isolated glands, supernatants were pelleted by centrifugation at 200 x*g*, washed three times with HEPES-MEM, and re-suspended in Medium A. Approximately 70% of the total gastric cells suspended in Medium A were parietal cells. The cells were plated onto Matrigel-coated 18-mm round coverslips or 35-mm dishes and incubated at 37˚C.

NIPR measurement

In isolated glands and cultured parietal cells, NIPR (Figure 4A) was measured with a pH-sensitive BCECF dye (Pasham et al., 2013). Briefly, glands and cells were loaded with 10 μM BCECF-AM (Thermo-Fisher, USA) for 15 min at 37˚C. Acid loading was achieved by a brief application of NH_4Cl (20 mM). NIPR was triggered upon Na^+ removal (0 Na^+). A linear fit, within 5 min of reaching peak acidity, was used to determine the rate of pH recovery (ΔpH/min) during re-alkalization. BCECF fluorescence was recorded by an EasyRatio Pro system (PTI) at 440-nm and 490-nm wavelengths. The fluorescence ratio (F_{490}/F_{440}) was used to calculate cytoplasmic pH values based on a standard calibration curve constructed for a range of pH 5 to 8.5 with K^+-H^+ ionophore nigericin (Pasham et al., 2013). The standard 145 Na^+ solution contained (in mM): 125

NaCl, 3 KCl, 1 $CaCl_2$, 1.2 $MgSO_4$, 5 glucose, and 32.2 HEPES (pH 7.4). The 0 Na^+ solution contained (in mM): 125 NMDG-Cl, 3 KCl, 1 $CaCl_2$, 1.2 $MgSO_4$, 5 glucose, 32.2 HEPES (pH 7.4). For the NH4Cl application, 10 mM NMDG-Cl was replaced with 20 mM NH_4Cl. The high K^+ solution used for calibration contained (in mM): 105 KCl, 1 $CaCl_2$, 1.2 $MgSO_4$, 32.2 HEPES, 10 mannitol, and 10 μg/ml nigericin (pH 7.0).

Immuno-electron microscopy

Ultrathin sections (60-80 nm) were etched in 10% H_2O_2 and 5% sodium metaperiodate for 10 min. After several washes and blocking with 1% BSA in PBS, the sections were incubated overnight with rabbit anti-GFP antibody (Life technologies, USA) at 4˚C. After several washes, the sections were then incubated with anti-rabbit IgG secondary antibody conjugated with 10-nm colloidal gold particles (Sigma, USA) for 2–3 h at room temperature. The sections were washed and contrasted with uranyl acetate and then examined with a Philips CM10 transmission electron microscope.

Biochemistry

Standard western blotting analyses were performed (Zhang et al., 2016). The lysis buffer contained 1% NP-40, 0.25% Na-deoxycholate, 1 mM NaF, 150 mM NaCl, 1 mM Na_3VO_4, 0.5 mM $CaCl_2$, and 50 mM Tris-HCl (pH 7.4). For the immunoprecipitation experiments, after a 10-s sonication, whole-cell lysates were centrifuged at 14,000 ×*g* for 10 min. Supernatants were incubated with primary antibodies at 4°C for 1 h, followed by overnight incubation with Protein A/G plus-agarose. Western blot analyses were performed with rabbit anti-ML1 (1:200, Life technologies, USA), anti-HK-α, and anti-HK-β (1: 1,000) antibodies.

Immunohistochemistry

$ML1^{PC}$ parietal cells were fixed in 4% paraformaldehyde in PBS, permeabilized with 0.1% Triton X-100 plus 1% BSA for 10 min, followed by blocking with 1% BSA for 1 h. The cells were incubated with various antibodies, including mouse anti-HK-α or β (1: 1,000; MBL international), anti-ML1, and anti-GFP (1:200; Life technologies, USA). The sections were then incubated with anti-mouse or anti-rabbit IgG secondary antibodies conjugated with Alexa Flour 488 or 546 (Life Technology) for 2 h. F-actin rich apical vacuole immunolabeling was performed with phalloidin-TRITC (1:1000; ECM Bioscience). The sections were mounted with Fluoromount-G (Southern Biotechnology Associates, Inc.).

Cellular fractionation

Subcellular membrane fractions were obtained from corpus glands as described previously (He et al., 2011; Wang et al., 2012). Briefly, tissues were homogenized in PBS supplemented with 10 mM sucrose and 1 mM EDTA (pH 7.2) in a Potter-Elvehjem homogenizer. The homogenates were then subjected to sequential centrifugation steps to produce pellets 1–3 (P1–3): P1 (3,200 x*g* for 10 min, plasma membrane fraction), P2 (20,000 x*g* for 10 min, lysosome fraction), and P3 (100,000 x*g* for 1 h, TV fraction).

Confocal imaging

Time-lapse imaging was conducted on an Olympus spinning-disk confocal microscope equipped with a temperature controller. GCaMP3 fluorescence was monitored at an excitation wavelength of 480 nm (F480) by an EasyRatio Pro imaging system (PTI). Cells were bathed in Tyrode's solution containing 145 mM NaCl, 5 mM KCl, 2 mM $CaCl_2$, 1 mM $MgCl_2$, 10 mM

Glucose, and 20 mM HEPES (pH 7.4). TV Ca^{2+} release was monitored in a zero Ca^{2+} solution containing 145 mM NaCl, 5 mM KCl, 3 mM $MgCl_2$, 10 mM glucose, 1 mM EGTA, and 20 mM HEPES (pH 7.4). Free Ca^{2+} concentration was estimated by Maxchelator software (http://maxchelator.stanford.edu/). Images were analyzed with MetaMorph Advanced Imaging acquisition software v.7.7.8.0 (Molecular Devices) and Image J (NIH).

STED microscopy

STED microscopy was performed using the STED module of a Leica TCS SP8 STED 100X microscope (Leica Microsystems) on paraffin-embedded tissue sections. Hybrid detectors were used to detect signals at a certain time gate after a laser excitation pulse with a pixel size of ~20 nm. The images were further de-convolved with the Huygens Professional Software (Scientific Volume Imaging).

Whole-endolysosome electrophysiology

Isolated enlarged endolysosomes were subjected to whole-endolysosomal electrophysiology by a modified patch-clamp method (Dong et al., 2010; Wang et al., 2012). Briefly, cells were treated with 1 μM vacuolin-1 overnight to increase selectively the size of late endosomes and lysosomes (Cerny et al., 2004). Enlarged vacuoles were released into the dish by mechanical disruption of the cell membrane with a finetip glass electrode. Unless otherwise indicated, vacuoles were bathed continuously in an internal (cytoplasmic) solution containing 140 mM K^+-gluconate, 4 mM NaCl, 1 mM EGTA, 2 mM Na_2-ATP, 2 mM $MgCl_2$, 0.39 mM $CaCl_2$, 0.1 mM GTP, and 10 mM HEPES (pH adjusted to 7.2 with KOH; free $[Ca^{2+}]_i$ ~ 100 nM calculated by MaxChelator software). The pipette (luminal) solution contained 145 mM NaCl, 5 mM KCl, 2

mM $CaCl_2$, 1 mM $MgCl_2$, 10 mM HEPES, 10 mM MES, and 10 mM glucose (pH adjusted to 4.6 with NaOH). The whole-endolysosome configuration was achieved as described previously (Wang et al., 2012). After formation of a gigaseal between the patch pipette and an enlarged endolysosome, voltage steps of several hundred millivolts with a millisecond duration were applied to break into the vacuolar membrane (Wang et al., 2012). All bath solutions were applied via a fast perfusion system that produced a complete solution exchange within a few seconds. Data were collected via an Axopatch 2A patch clamp amplifier, Digidata 1440, and processed in pClamp 10.0 software (Axon Instruments). Whole-endolysosome currents were digitized at 10 kHz and filtered at 2 kHz. All experiments were conducted at room temperature (21-23˚C) and all recordings were analyzed in pCLAMP10 (Axon Instruments) and Origin 8.0 (OriginLab).

Whole-VAC electrophysiology

Whole-VAC patch-clamp was performed on apical vacuoles isolated from parietal cells, as illustrated in Figure 6A. Briefly, cultured parietal cells were treated with 50-100 μM histamine + 20 μM IBMX for 30-40 min to induce VAC formation in WT parietal cells. $ML1^{PC}$ parietal cells contained large VACs. Large VACs were released into the dish by mechanical disruption of the cell membrane with a fine-tip glass electrode. Subsequently, whole-VAC and cytoplasmic-side-out recordings were performed in a manner similar to that of endolysosomal recordings (Wang et al., 2012).

Data analysis

Data are presented as means ± standard errors of the mean (SEMs). Statistical comparisons were performed with one-way analyses of variance (ANOVAs) with Bonferroni's posthoc analysis or Student's t-tests. P values < 0.05 were considered statistically significant.

Results

Localization of ML1 proteins in the TVs

To investigate the subcellular localization of ML1, cultured parietal cells from wild-type (WT), ML1 KO, and parietal cell-specific ML1-overexpressing ($ML1^{PC}$) mice were used. Parietal cells were isolated from corpus glands in stomachs. To generate the parietal cell-specific ML1 transgenic mouse model, a floxed (fl) allele carrying the GCaMP3-ML1 transgene (Shen et al., 2012) was integrated into the ROSA26 locus behind a *loxSTOPlox* cassette (Figure 2.1A). Crossing ROSA-*loxSTOPlox*-GCaMP3-ML1 (abbreviated ML1 *ROSA lSl*) mice with a parietal-cell-specific Cre line (ATP4B *Cre*) (Syder et al., 2004) generated parietal cell-specific ML1 overexpression (ML1 *ROSA-lSl*:ATP4B *Cre* or $ML1^{PC}$) mice (Figures 2.1B). We observed multifold increases in both basal and ML-SA-activated ML1 currents, relative to WT levels, in $ML1^{PC}$ parietal cells (Figures 2.1C, 2.1D). Corpus glands from ML1 KO mice exhibited no detectable expression of ML1 proteins in electrophysiology (Figure 2.1E).

With dual-STED super resolution imaging, double immunohistochemistry analyses revealed that ML1 was co-localized mostly (>80%) with α or β subunits of H^+/K^+-ATPase, which are TV markers (Figure 2.2A). TVs are generally smaller than late endosomes and lysosomes, and Lamp1 and H^+/K^+-ATPase are rarely co-localized (Chandra et al., 2011). The subcellular localization of GCaMP3-ML1 was confirmed by immuno-gold electron microscopy wherein a

predominance of gold particles was observed in the TVs of $ML1^{PC}$ cells (Figure 2.2B). In TV fractions isolated by cellular fractionation (Suda et al., 2011), which are enriched with H^+/K^+-ATPase but devoid of LAMP1, endogenous ML1 proteins were detected readily in WT cells (Figure 2.2C). Moreover, in co-immunoprecipitation analyses, endogenous ML1 proteins interacted directly with α or β subunits of H^+/K^+-ATPase (Figures 2.2D). Collectively, these results suggest that ML1 is targeted partially to in Lamp1-resident late endosomes and lysosomes, while predominantly to the TVs of parietal cells.

Activation of ML1 induces Ca^{2+} release from TVs

Like lysosomes, TVs are also intracellular Ca^{2+} stores (Tsunoda et al., 1988). In GCaMP3-ML1-expressing parietal cells isolated from $ML1^{PC}$ mice, application ML-SA1 or ML-SA5 (1-10 μM) in a "zero" Ca^{2+} external solution (free $[Ca^{2+}] < 10$ nM) evoked robust Ca^{2+} release evidenced by GCaMP3 fluorescence changes ($\Delta F/F_0$; Figure 2.3A, 2.3E). ML-SA5-induced Ca^{2+} release was also observed in GCaMP3-ML1-transfected HEK293 cells (Figures 2.3C, 2.3E). However, when cells were pretreated with GPN, a membrane permeable dipeptide that depletes lysosome Ca^{2+} stores (Berg et al., 1994), ML-SA5-induced Ca^{2+} responses were abolished in HEK293 cells, but preserved in parietal cells (Figures 2.3B, 2.3D, 2.3E). Hence, unlike other cell types wherein ML1 is localized exclusively to lysosomes, in parietal cells, ML1 is expressed in GPN-inaccessible TVs. Taken together, these results establish TVs as intracellular Ca^{2+} stores in which ML1 is functionally present.

Synthetic inhibitors of ML1 block gastric acid secretion

As a quantitative measure of H^+/K^+-ATPase-dependent proton secretion, we determined the rate of Na^+-independent cytoplasmic pH (pH_c) recovery (NIPR) by measuring the fluorescence intensity of the pH-sensitive dye BCECF (Pasham et al., 2013) (Figure 2.4A). NIPR was virtually absent under resting conditions (Figures 2.4B, 2.4F) in both WT (0.006 ± 0.003 ΔpH/min, n = 29 cells) and ML1 KO parietal cells. Histamine stimulation increased NIPR by ~1,400% to 0.084 ± 0.009 ΔpH/min (n = 24) in WT cells, but did not affect NIPR in ML1 KO parietal cells (0.008 ± 0.005 ΔpH/min, n = 28, Figures 2.4C, 2.4E, 2.4F). Strikingly, brief exposure of WT parietal cells to ML-SI3 or ML-SI4 (10-20 μM), two structurally-independent ML1 inhibitors (Zhang et al., 2016), also abolished histamine-induced NIPR (Figures 2.4D, 2.4F). This suggests that ML1 functions as a direct physiological regulator of gastric acid secretion and provide counterevidence to the prior suggestion that secondary or developmental defects underlie the achlorhydria phenotype of ML1 KO mice and ML-IV patients (Chandra et al., 2011).

ML1 agonism induces gastric acid secretion independent of histamine

Incubation of WT parietal cells with the ML1 agonist ML-SA5 (Shen et al., 2012; Zhang et al., 2016) resulted in an NIPR in that was ~1,000% of that observed in untreated WT cells (Figures 2.4G, 2.4I). Conversely, ML-SA treatment did not affect NIPR in ML1 KO parietal cells (Figure 2.4H, 2.4I), suggesting that ML1 activation is sufficient to induce acid secretion both *in vitro* and *in vivo*.

Notably, a high NIPR rate was observed in $ML1^{PC}$ parietal cells even under resting conditions without histamine (0.076 ± 0.010 ΔpH/min, n = 22; Figures 2.4J, 2.4L). This constitutive NIPR, which was as large as histamine-stimulated NIPR in WT cells, was blocked

completely by ML-SIs (Figures 2.4K, 2.4L). Taken together, these results suggest that the hyperchlorohydric phenotype of $ML1^{PC}$ mice is caused by histamine-independent acid secretion induced by ML1 upregulation.

ML1 channel activity is necessary and sufficient for TV exocytosis

In cultured parietal cells, upon secretagogue stimulation, apical canalicular membranes are engulfed into the cell to form multiple actin-wrapped vacuoles known as vacuolar apical compartments (VACs), which remain separate from the basolateral membrane and free TVs in the cytosol (Nakada et al., 2012). Cellular cues such as histamine promote polarized trafficking of TVs to apical membranes for H^+/K^+-ATPase insertion. Hence, total VAC membrane area provides a quantitative measurement of TV exocytosis (Nakada et al., 2012). In resting WT cells, small (diameter < 2μm) VACs were observed occasionally with a total surface area < $10\mu m^2$ (Figures 2.5A, 2.5B). VACs formed within 10-20 min after bath application of histamine and then fused together to generate one or a few large VACs (up to 8μm in diameter; total VAC surface area > $50\mu m^2$; Figures 2.5A, 2.5B). Histamine-stimulated VAC formation was abolished by ML-SIs (Figures 2.5A, 2.5B). No histamine-induced VAC formation was observed in ML1 KO parietal cells (Figures 2.5C). Hence, ML1 was found to be necessary for histamine-dependent TV exocytosis.

On the other hand, ML-SA5 treatment was sufficient to induce VAC formation in WT cells (Figures 2.5A, 2.5B). Furthermore, large VACs were observed in resting $ML1^{PC}$ parietal cells, but their presence was decreased sharply by ML-SI4 (Figures 2.5D, 2.5E). Taken together, these results suggest that ML1 plays an essential role in TV exocytosis.

ML1 promotes polarized trafficking of TVs to apical, but not basolateral, membranes

Consistent with the hypothesis that histamine induces trafficking and fusion of TVs towards apical canalicular membranes (Forte and Zhu, 2010), our immunofluorescence analysis of cultured parietal cells revealed that the α subunit of H^+/K^+-ATPase accumulated in VAC membranes, but was absent from basolateral membranes (Figure 2.5A). ML1 protein was also selectively accumulated in VAC membranes (Figure 2.5D).

To further probe TV trafficking, we developed a patch-clamp method to record directly from VAC membranes isolated from $ML1^{PC}$ cells or histamine-stimulated WT cells (whole-VAC recording; Figure 2.6A). Native VAC membranes are comprised of both apical membranes and TV membranes (Nakada et al., 2012) (Figure 2.6A). Conversely, the plasma membranes of cultured parietal cells consist exclusively of basolateral membranes, which can be subjected to whole-cell recording (Figure 2.6A). In the whole-VAC patch configuration, inwardly rectifying ML1-like currents were observed in histamine-treated WT cells (basal I_{ML1} = 33 ± 11 pA/pF, n = 7) and $ML1^{PC}$ cells (Figures 2.6B, 2.6C, 2.6F), and these currents were potentiated by ML-SA5 (149 ± 45 pA/pF, n = 7; Figures 2.6B, 2.6C, 2.6F). Substantial I_{ML1} was detected even in VAC-cytosolic-side-out patches (Figures 2.6G, 2.6H). Whole-cell I_{ML1} was not detected in histamine stimulated WT cells (1± 0.5 pA/pF, n = 8) or $ML1^{PC}$ cells (Figures 2.6D, 2.6E). These results implicate ML1 in polarized trafficking and exocytosis of TVs towards apical membranes.

ML1 mediates histamine-induced PKA- and ATP-dependent Ca^{2+} release from TV stores

Histamine-dependent activation of parietal H2 receptors activates cAMP-dependent PKA to phosphorylate multiple target proteins required for TV exocytosis (Forte and Zhu, 2010). Two PKA phosphorylation sites, Ser^{557} and Ser^{559}, on TRPML1 C-terminal tail facing cytosol have been

predicted but functionally undetermined (Vergarajauregui et al., 2008a). The Ca^{2+}- and cAMP/PKA-dependences of TV exocytosis and acid secretion suggest that ML1, as a TV Ca^{2+} release channel, is regulated, directly or indirectly, by cAMP/PKA signaling.

In WT cells that were pretreated with 8-Br-cAMP, basal and ML-SA-activated whole endolysosomal ML1 currents (I_{ML1}) were increased significantly (Figures 2.7A, 2.7B). These increases were not seen in the presence of PKA inhibitors (Figures 2.7A, 2.7B), indicating that I_{ML1} in partial cells is potently upregulated by PKA signaling. In Ca^{2+} imaging assay, bath application of histamine produced robust Ca^{2+} release, as well as small Ca^{2+} oscillations (Figures 2.7C). Such Ca^{2+} release in $ML1^{PC}$ parietal cells was blocked by ML-SI4 or PKA inhibitor H-89 (20μM; Figures 2.7D-F). The membrane-permeable cAMP analogue 8-Br-cAMP induced spontaneous Ca^{2+} oscillations in a zero-Ca^{2+} external solution, and these spontaneous oscillations were largely diminished in the presence of ML-SI4 (10μM; Figures 2.7G-I). Together, these results suggest that histamine induces ML1-mediated TV Ca^{2+} release through cAMP and PKA signaling.

Interestingly, whole-VAC ML1 currents were potentiated with application of ATP (Figures 2.7J, 2.7K). Such activation of ML1 was not seen in whole-endolysosomal patches in ML1 overexpressing COS1 cells (Figures 2.7L). Parietal cells possess highly elevated number of mitochondria to balance the large amount of ATP consumption by H^+/K^+-ATPases. This may lead to the assumption that ML1 in TVs obtain cell-type specific regulation by ATP.

Discussion

In the present study, we used pharmacological and genetic manipulation methods to recognize missing links between histamine and acid secretion in gastric parietal cells. Utilizing the newly developed tubulovesicular patch clamp technique, along with GCaMP-based genetic Ca^{2+}

indicator and other supporting methodologies, we identified ML1 as a functional Ca^{2+} releasing channel localized on TV membrane. Our results indicate that ML1 channels expressed on parietal-cell TVs provide a PKA-sensitive Ca^{2+} release machinery that triggers Ca^{2+}-dependent fusion of TVs with apically-directed canalicular membranes, resulting in apical localization of the H^+/K^+-ATPases that pump H^+ into the gastric lumen (Figure 2.8). The putative Ca^{2+}-dependence of TV fusion had been controversial because conventional Ca^{2+} imaging studies had not shown consistent increases in response to histamine treatment, as was demonstrated finally in the current study. Using organelle-targeted Ca^{2+} probes and super-resolution imaging, we showed unequivocally here that TV trafficking and exocytosis are dependent on Ca^{2+} release from TVs mediated by ML1 proteins, which are in turn regulated by histamine-stimulated PKA signaling. Our demonstration of ML1 expression in TVs has provided an answer to a longstanding puzzle as to why the achlorhydric phenotype is only seen in ML-IV, but not any other LSDs (Chandra et al., 2011; Xu and Ren, 2015).

Though not officially indicated as an LRO, TVs possess multiple characteristics resembling lysosomes, including acidic pH, Ca^{2+} storage, endosomal derivative, and common proteomics such as ML1 which is demonstrated in the present research. The TRPML protein family has been implicated in a variety of organelles related to the endosomal system such as ML1 in lysosomes and potentially LROs, ML2 in endosomes, lysosomes and LROs (Grimm et al., 2012), raising the possibility that TRPMLs serve as the primary Ca^{2+} releasing channel not only on lysosomes, but also other endosome-derived acidic Ca^{2+} stores. The expression of TRPMLs on various LROs provides opportunities in identifying physiological agonists/antagonists regulating channel functions, as exampled by the discovery of cAMP/PKA and ATP regulation of TV ML1 in this study. While the cAMP/PKA regulation of ML1 appears to be ubiquitously possessed by

several different cell types, the ATP activation is more TV-specified, indicating cell-type- or organellar-specific modification of the channel.

It is likely that additional regulators of this ML1 pathway remain to be discovered. Indeed, a number of TV-localized channels and transporters, including K^+ channels, have been reported to regulate acid secretion (Forte and Zhu, 2010; Lambrecht et al., 2005). Some of them may affect TV membrane potential and thus ML1-mediated Ca^{2+} release, which is strongly voltage-dependent (Xu and Ren, 2015). The Ca^{2+} effector associated with TV fusion is not yet known. However, Ca^{2+}-sensing proteins, such as apoptosis-linked gene 2 and Syt7 proteins, have been shown to link ML1-mediated lysosomal Ca^{2+} release with retrograde transport and membrane fusion of lysosomes (Li et al., 2016b), making them candidates for this role in TVs. Given the well-established roles of gastric acids in stomach homeostasis and gastric biology (Forte and Zhu, 2010; Hersey and Sachs, 1995), our identification of ML1 as the first known TV Ca^{2+} channel may lead to the development of new therapeutic approaches to treat acid-related gastric diseases.

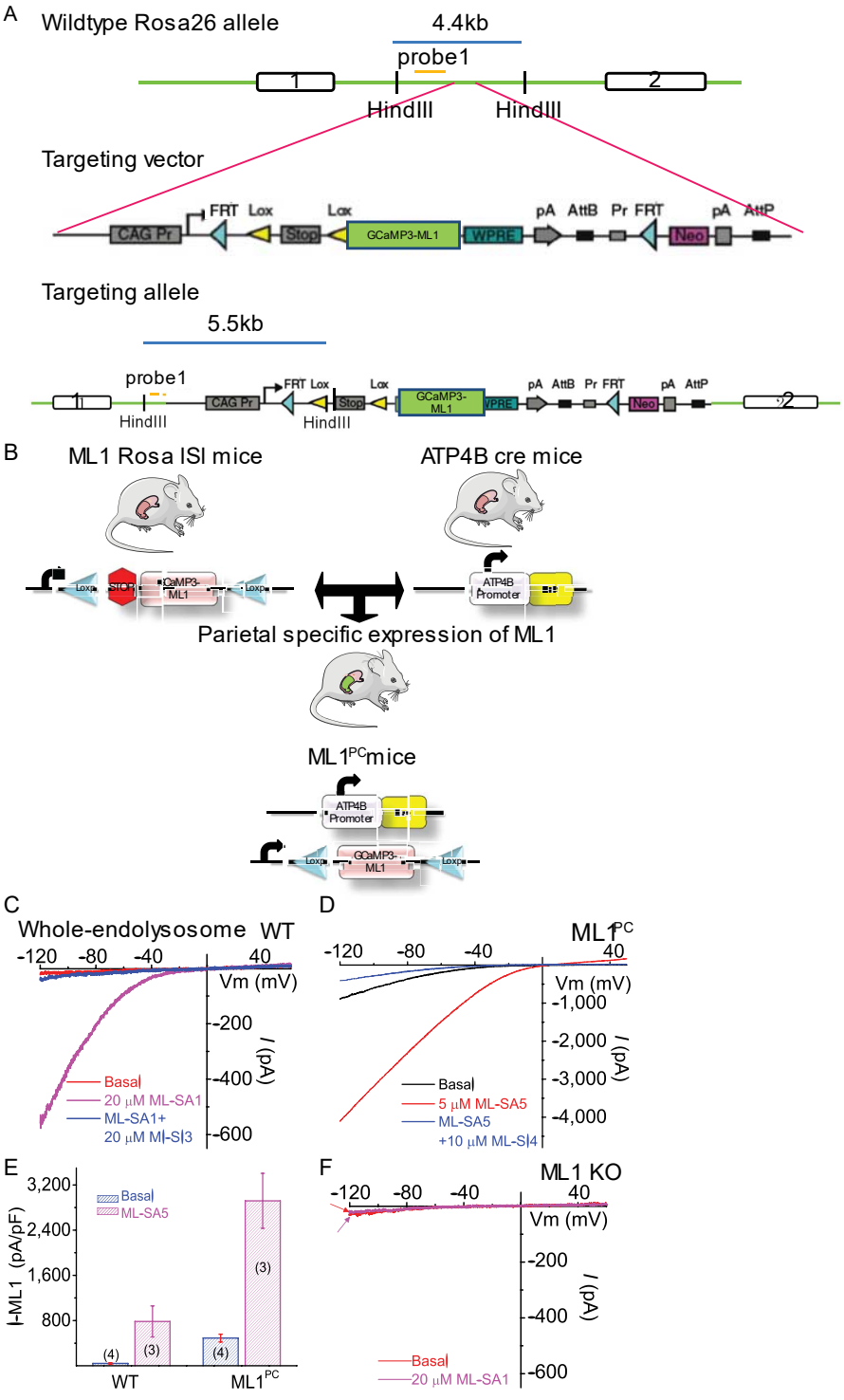

Figure 2.1 Generation of parietal-cell-specific ML1^{PC} mice and characterization of ML1^{PC} and ML1 KO mice.

(A) Targeted generation of GCaMP3-ML1 loxP-loxP mice. A *LoxSTOPlox* cassette carrying a GCaMP3-ML1 transgene was inserted between exon 1 and 2 of the ROSA 26 allele. (B) ROSA-*loxSTOPlox*-GCaMP3-ML1 (abbreviated as ML1 *ROSA-lSl*) mice were crossed with ATP4BCre mice to generate progeny mice with parietal cell-specific expression of GCaMP3-ML1 (ML1

ROSA-lSl:ATP4B *Cre* or $ML1^{PC}$). Expression of ATP4B-promoter-driven Cre recombinase led to excision of the *loxSTOPlox* cassette, enabling the expression GCaMP3-ML1 specifically in the parietal cells of the $ML1^{PC}$ mice. (C) Whole-endolysosomal I_{ML1} was activated by TRPML agonists (ML-SA1/3/5; 1-20 μM) and inhibited by ML1 antagonists ML-SI3/4 (10-20 μM) in WT parietal cells. (D) Whole-endolysosome I_{ML1} in $ML1^{PC}$ parietal cells. (E) I_{ML1} current densities in WT and $ML1^{PC}$ parietal cells. (F) Whole-endolysosome I_{ML1} in ML1 KO cells.

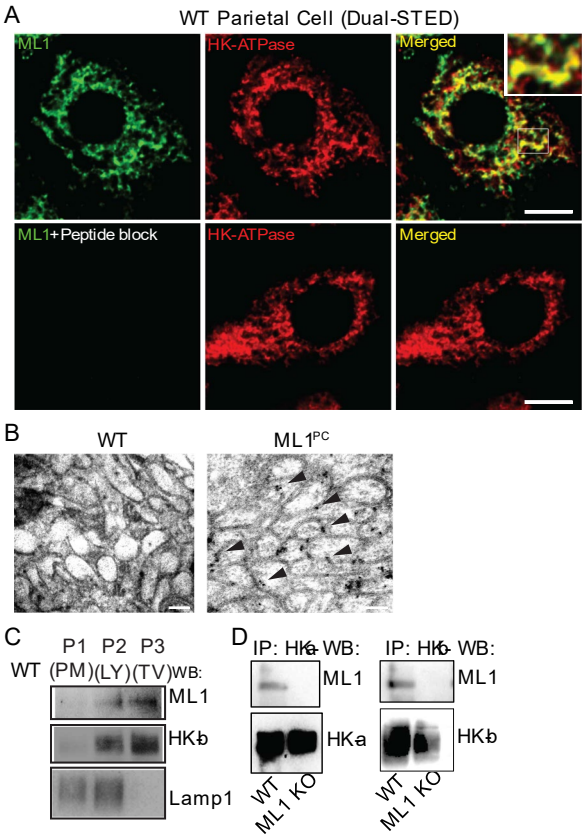

Figure 2.2 ML1 is localized in TVs.
(A) Dual-STED images of WT corpus tissues immunolabeled with anti-HK-α and anti-ML1. A pre-incubation of anti-ML1 with ML1 epitope peptide confirmed the specificity of the ML1 antibody. Scale bar, 5 μm. (B) Immunogold electron microscopy images of WT and ML-SI4-treated (to prevent constitutive TV exocytosis) $ML1^{PC}$ parietal cells. Scale bar, 0.1 μm. (C) Gradient centrifugation purification of TVs from WT parietal cells. P1 (3,200 xg), P2 (20,000 xg), and P3 (100,000 xg) pellets represent plasma membrane (PM)-rich, lysosome/mitochondria (LY), and H^+/K^+-ATPase-rich fractions (TV), respectively. (D) Co-immunoprecipitations of ML1 with HK-α and HK-β in WT and ML1 KO corpus glands cell lysates.

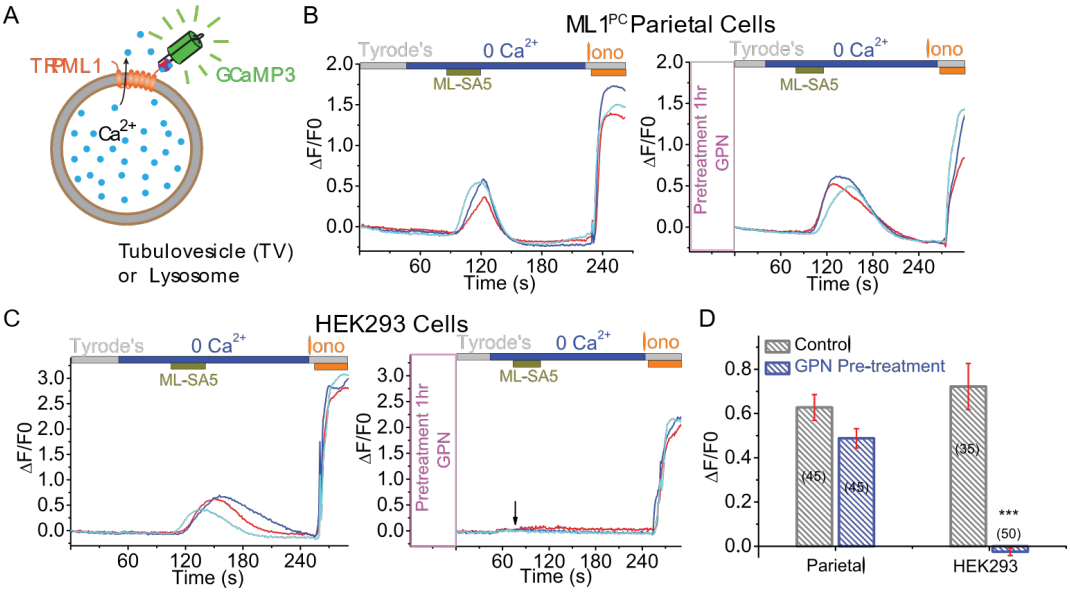

Figure 2.3 TV-localized ML1 mediates Ca^{2+} release from TVs.
(A) Genetically-encoded Ca^{2+} indicator that detects Ca^{2+} release from lysosomes and TVs. Illustration of a TV/lysosome-targeted genetically-encoded Ca^{2+} sensor, in which GCaMP3 is fused directly to the N terminus of ML1. (B and C) Effects of GPN pretreatment on ML-SA5-induced Ca^{2+} release (GCaMP3 fluorescence, F_{480}, in zero Ca^{2+} solution) from $ML1^{PC}$ parietal cells (B) or GCaMP3-ML1-transfected HEK293 cells (C). Cells were pretreated with ML-SI4 for 30 min to prevent TV exocytosis. Downward arrow (C) indicates the time point at which ML-SA5 was applied. (D) Quantitation of ML-SA5-induced GCaMP3 Ca^{2+} responses under control and GPN-pretreated conditions (mean ± SEM, n = 30-50 cells from %4 coverslips/experiment). ***$p < 0.001$, Student's t test.

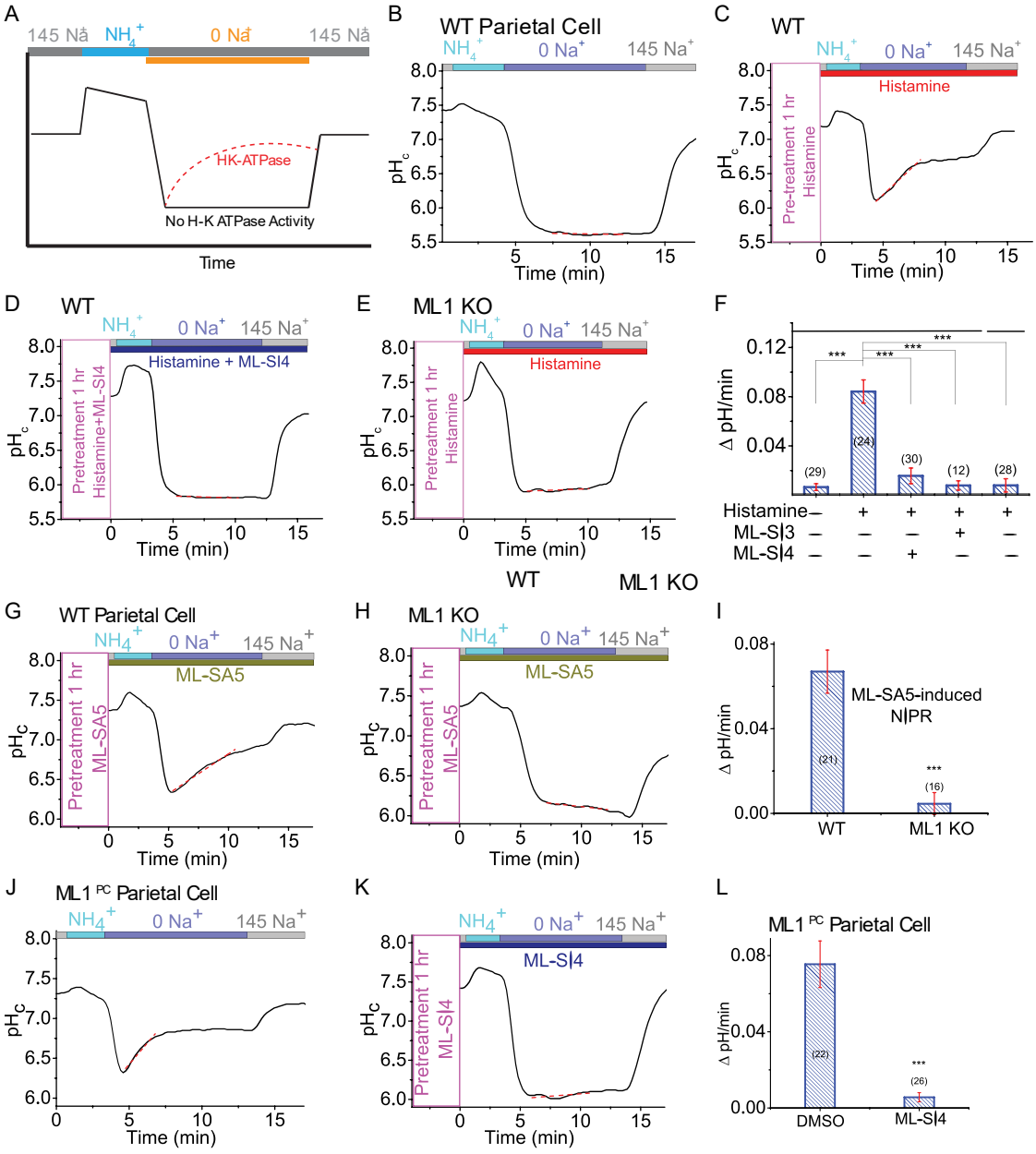

Figure 2.4 ML1 is necessary and sufficient to induce histamine-stimulated acid secretion. (A) Schematic diagram of the NIPR (Na^+-independent pH recovery) assay. After H^+-loading cells with NH_4Cl (20 mM), NIPR was triggered by replacement of all extracellular Na^+ with NMDG+ ("0" Na^+). In the absence of Na^+, Na^+/H^+ exchangers are not operative and any cytoplasmic pH (pH_c) changes are thus under H^+/K^+-ATPase control (Pasham et al., 2013). (B-E) Histamine (100 µM + 20 µM IBMX) and ML-SI4 (10 mM) effects on proton secretion, indexed by NIPR observed while pH_c was under H^+/K^+-ATPase control relative to responses in 0 Na^+ (red dotted lines). (F) NIPR rates (n = 10-30 cells) under resting and histamine-stimulated conditions. (G and H) ML-SA5 (10 µM, applied 1 hr prior) potentiation of NIPR in WT (G), but not ML1 KO (H) parietal cells. A linear fit (red dotted line) was used to determine the rate of pH recovery during re-alkalization. (I) NIPR of ML-SA5-treated WT and ML1 KO parietal cells. (J and K) ML-SI4 (10

μM) annulment of constitutive NIPR in $ML1^{PC}$ parietal cells. (L) ML-SI4 effects on $ML1^{PC}$-cell NIPR.

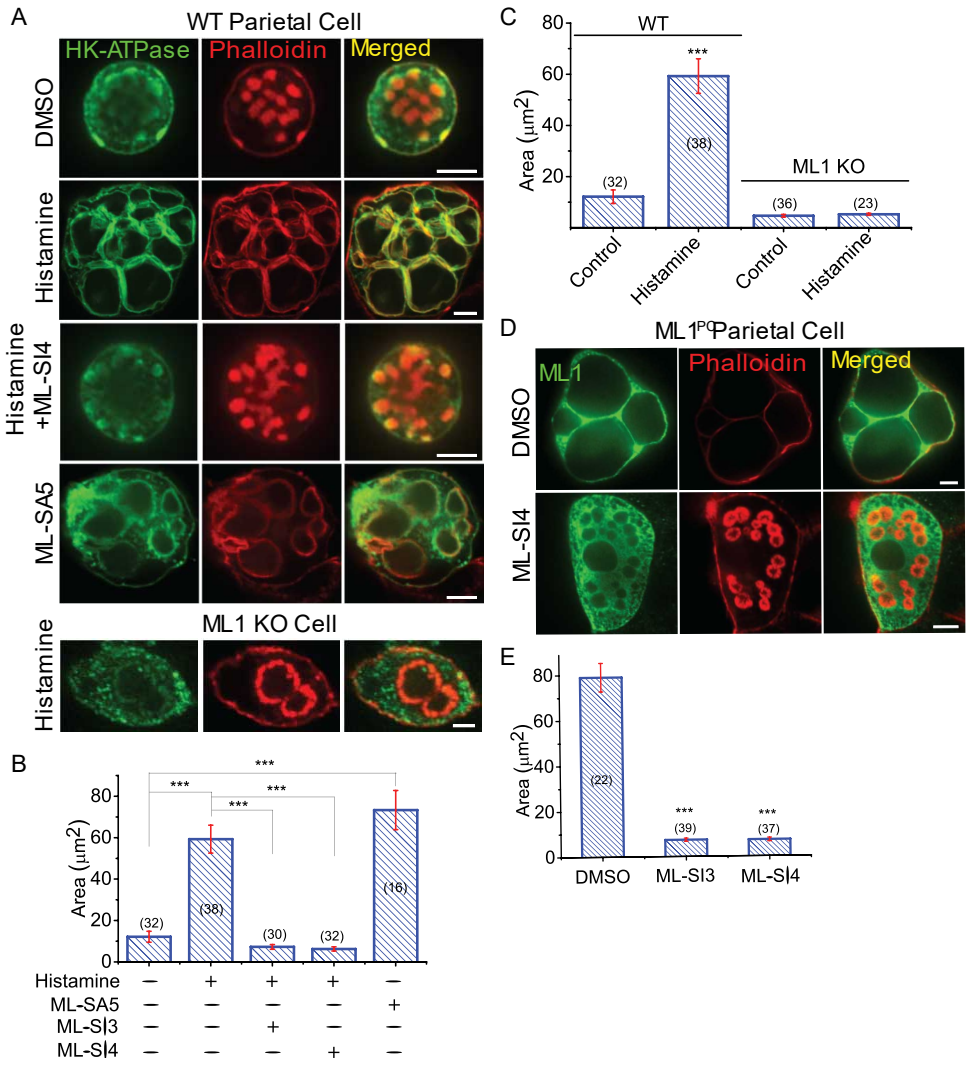

Figure 2.5 ML1 is necessary and sufficient to trigger TV exocytosis.
(A) Anti-HK-α immunocytochemistry with phalloidin-labeled F-actin. Cells were treated with ML-SA5 (10 μM) or histamine (50μM + 10 μM IBMX) in the presence or absence of ML-SI3 (20 μM) or ML-SI4 (10 μM) for 30 min at 37°C. Scale bar, 10 μm. Blue and white arrows indicate basolateral and apical membranes, respectively. (B) VAC total surface area, an index of TV exocytosis associated with gastric acid secretion, under various treatment conditions (average of 3–6 z-plane sections/cell). Mean ± SEM from R3 experiments. ***p < 0.001, one-way ANOVA, Bonferroni's post hoc analysis. (C) Summary of the effects of histamine on VAC formation in WT and ML1 KO parietal cells. ***P < 0.001 one-way ANOVA with Bonferroni's post-hoc analysis. (D) ML-SI4 (10 μM) effects on constitutive VAC formation in $ML1^{PC}$ parietal cells. Scale bar, 10 μm. Blue and white arrows indicate basolateral and apical membranes, respectively. (E) ML-SI effects on VAC total surface area. Mean ± SEM from R3 experiments. ***p < 0.001, one-way ANOVA, Bonferroni's post hoc analysis.

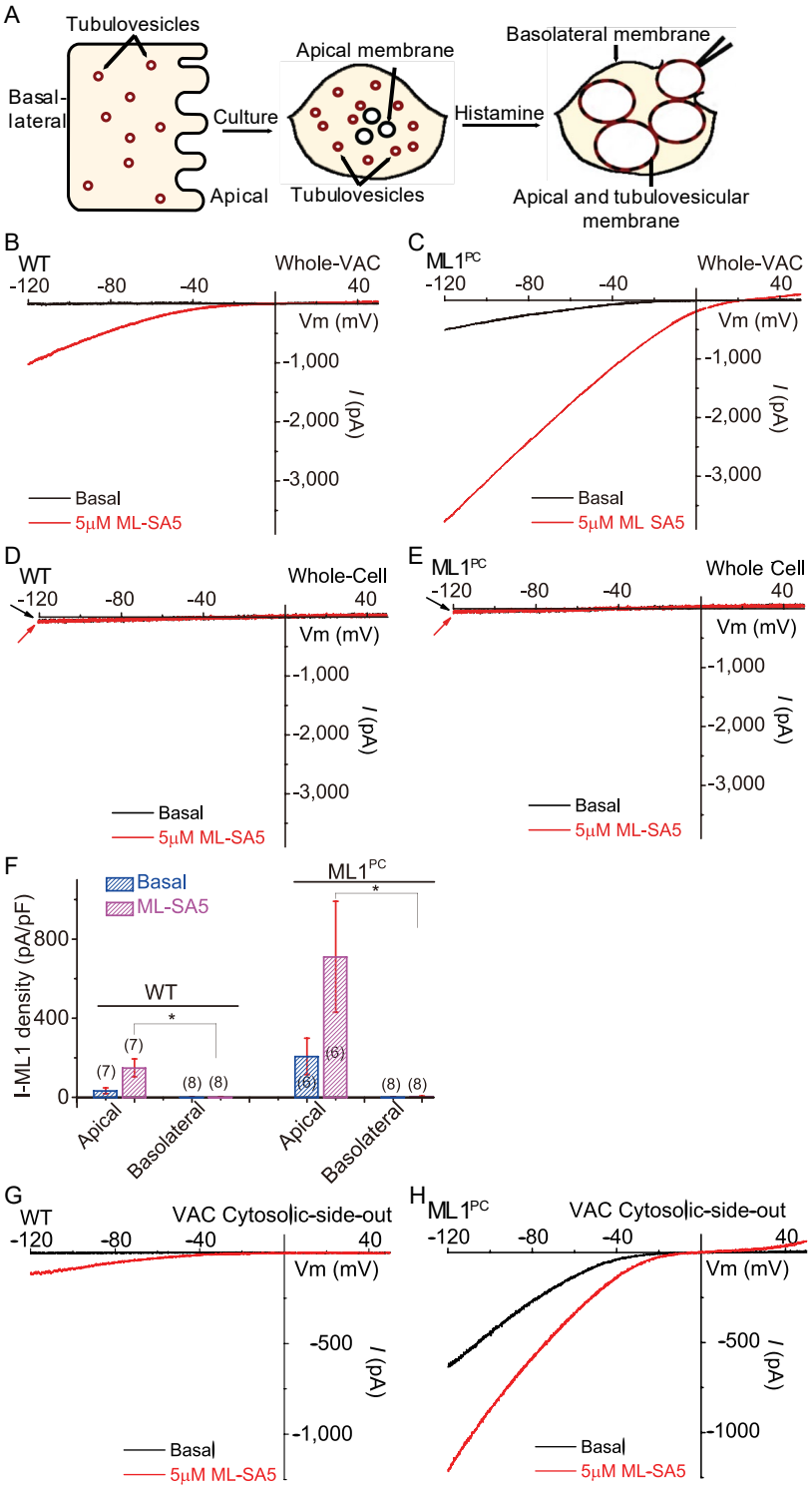

Figure 2.6 ML1 Promotes Polarized TVs Trafficking toward Apical Membranes.
(A) Patch-clamp recording from basolateral (standard whole-cell recording) or apical (lyse cell to expose VACs before whole-VAC recording) membranes. Note that the extracellular side of the apical membrane is facing the VAC lumen. (B and C) Representative whole-VAC (apical membrane) recordings of ML1-like currents in histaminestimulated WT (B) and ML1^{PC} (C)

parietal cells. (D and E) Representative whole-cell (basolateral membrane) detection of IML1 in WT and $ML1^{PC}$ cells. (F) Group averages of data from experiments shown in (B)-(E) (n = 3-5 patches/condition). Mean ± SEM from R3 experiments. *$p < 0.05$, one-way ANOVA, Bonferroni's post hoc analysis. (G and H) Representative cytoplasmic-side-out recordings of VACs revealed I_{ML1} in histamine stimulated WT and and $ML1^{PC}$ parietal cells.

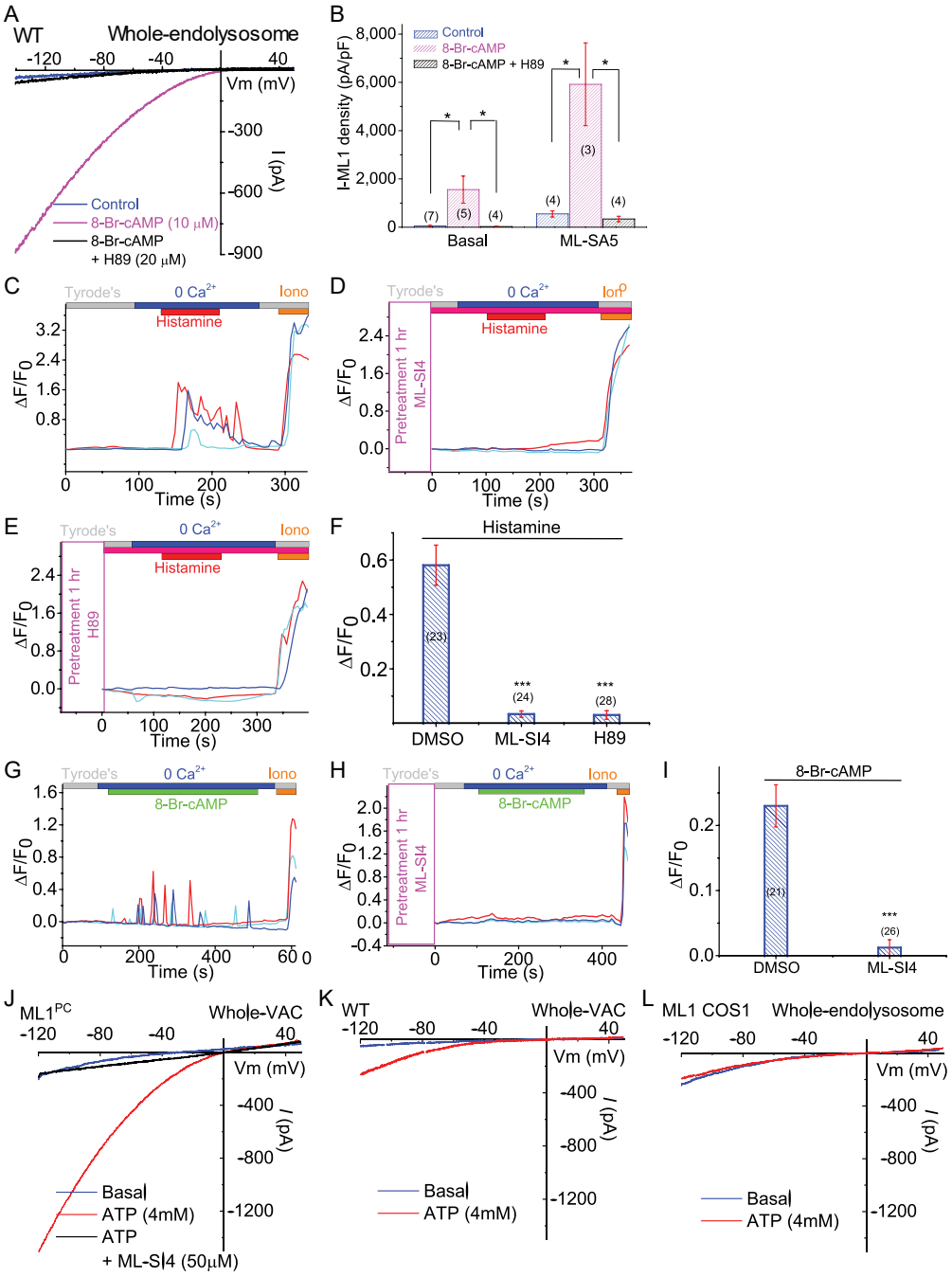

Figure 2.7 cAMP/PKA and ATP regulation of TV-localized ML1.
(A) Whole-endolysosomal I_{ML1} in WT parietal cells with and without 8-Br-cAMP (20 μM) and H89 (20 μM). (B) Mean current densities under treatments shown in (P). Mean ± SEM from R3 experiments. (C-F) Histamine (50 μM)-induced TV Ca^{2+} release in GCaMP3-ML1-expressing $ML1^{PC}$ cells was blocked by ML-SI4 (10 μM) (D) or H89 (20 μM) (E). Experimental averages are shown in (F). (G-I) ML-SI4 (10 μM) (H) blocked 8-Br-cAMP (20 mM)-induced Ca^{2+} oscillations (G) in $ML1^{PC}$ cells. Experimental averages are shown in (I). (J-L) Whole-VAC I_{ML1} in WT (J) and $ML1^{PC}$ (K) parietal cells, and whole-endolysosomal I_{ML1} (L) in ML1 transfected COS1cells with ATP (4 mM).

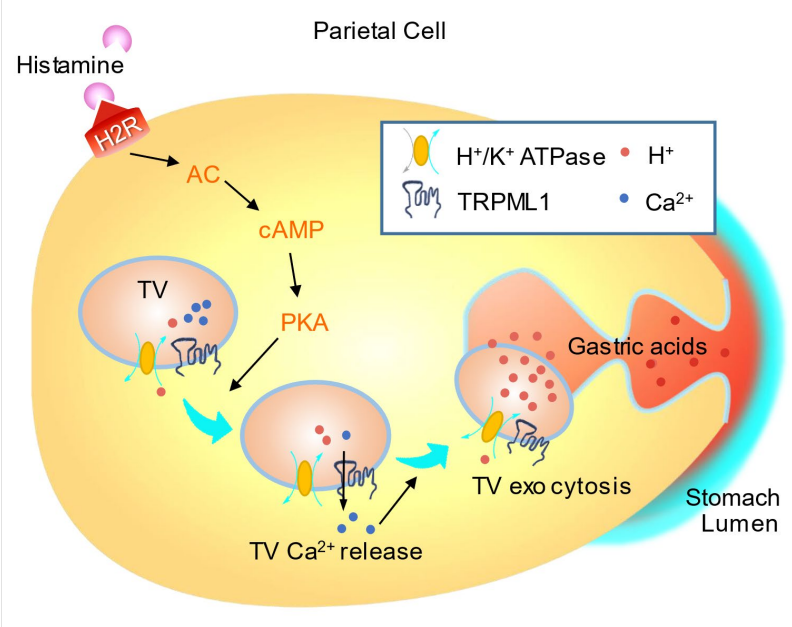

Figure 2.8 Signaling pathways that mediate histamine-stimulated ML1-dependent TV exocytosis and acid secretion.

Activation of type 2 histamine receptor (H2Rs) in parietal cells by histamine induces cAMP-dependent PKA activation. Localized on TVs, ML1 may mediate a PKA-sensitive Ca^{2+} release pathway to trigger Ca^{2+}-dependent fusion of TVs with each other and with apical membranes. Histamine induced exocytosis of H^+/K^+-ATPase-enriched TVs toward lumen-facing apical membranes in a cAMP/PKA-dependent manner.

CHAPTER III

Zn^{2+} Release From ML1 in Lysosomes Eradicates Metastatic Melanoma

Abstract

In cancer cells, the function of lysosomes is often up-regulated to match the high energy demand required for tumorigenesis and tumor progression. Mucolipin TRP channel 1 (TRPML1) is a Ca^{2+} and Zn^{2+} release channel in the late endosome and lysosome that regulates lysosomal degradation, trafficking, and biogenesis. An elevated expression of TRPML1 reportedly serves as a prognostic marker for several types of cancer. Here we show that at nanomolar concentrations, small-molecule TRPML1-specific synthetic agonists (ML-SAs) induced catastrophic and irreversible melanoma cell death within hours after drug administration while completely sparing normal cells. Both genetic and pharmacological inhibition of ML1 readily blocked ML-SA-induced cell death. Compared with normal cells, vesicular Zn^{2+} stores are also dramatically up-regulated in metastatic melanoma cells. Activation of lysosomal TRPML1 channels in metastatic melanoma cells induce excessive lysosomal Zn^{2+} release to cause mitochondrial dysfunction and cellular ATP depletion. In addition, ML-SAs show promising therapeutic efficiency in an *in vivo* model of advanced melanoma. Hence, targeting lysosomal machinery by ML-SAs can selectively eradicate metastatic tumor cells both *in vitro* and *in vivo*.

Introduction

The lysosome is an essential cellular organelle and plays an indispensable role in cell survival and growth (Xu and Ren, 2015). Besides the general roles in protein degradation,

recycling, and nutrient signaling (Xu and Ren, 2015), lysosomes are also actively involved in cancer progression, such as cell proliferation and survival via providing nutrients by lysosome digestion (Amaravadi et al., 2016; Goldsmith et al., 2014), drug resistance by endocytosis and degradation of exogenous chemicals (Zhitomirsky and Assaraf, 2016), and cancer cell metastases by secreting lysosomal hydrolases and digest extracellular matrix (Hamalisto and Jaattela, 2016). To meet the high demands of metabolic requirement, lysosome functions are adaptively up-regulated in many tumors compared to adjacent normal tissues (Kallunki et al., 2013; Kroemer and Jaattela, 2005; Serrano-Puebla and Boya, 2016). Upregulated lysosomal hydrolase activities have been demonstrated at the boarder of the metastatic tumor area in patient samples (Piao and Amaravadi, 2016). Previous study has reported that lysosomes are hypertrophic and more susceptive to destabilizing treatments that induce lysosomal membrane permeabilization in oncogene transformed cells compared with normal cells (Groth-Pedersen and Jaattela, 2013; Ostenfeld et al., 2005; Petersen et al., 2013). In addition, vulnerability of lysosomes is closely associated with both necrosis and apoptosis, making cancer cell's lysosome an ideal target for anti-cancer therapies (Amaravadi et al., 2016; Piao and Amaravadi, 2016). However, the precision targeting of the lysosomes of cancer cells is quite difficult because of the need to spare basal lysosomal functions in non-cancerous cells (Bonam et al., 2019; Hamalisto and Jaattela, 2016; Piao and Amaravadi, 2016).

TRPML1 (ML1) is a Ca^{2+} and Zn^{2+} permeable cation channel exclusively located in late endosomes and lysosomes (LEL) and loss-of-function mutations in ML1 cause the neurodegenerative disease mucolipidosis IV (ML-IV) (Cheng et al., 2010). In ML-IV patients' cell, zinc accumulation has been demonstrated in large lysosomes, suggesting a functional link between ML1 and zinc homeostasis (Blaby-Haas and Merchant, 2014; Eichelsdoerfer et al., 2010;

Falcon-Perez and Dell'Angelica, 2007; Kukic et al., 2013). Zinc has been implicated in pathological damage in strokes and neurodegenerative disorders. Upon such pathological conditions, increases in cytosolic Zn^{2+} have been reported to cause massive neuronal cell death (Bossy-Wetzel et al., 2004). ML1 was recently reported to be up-regulated in melanoma, and high expression level of ML1 may serve as a prognostic marker for several types of cancer (Kasitinon et al., 2019). Because the activation state of ML1 channels in melanoma cells is unknown, plausible scenarios can be imagined in which either ML1 agonist or antagonist treatment could enhance or deter the cancerous behavior of these cells. We therefore hypothesize that the adapted lysosome machinery, especially ML1, in melanoma cells can be pharmacologically targeted to induce cancer cell death.

In the present study, we report that over-stimulation of ML1 by ML1-specific synthetic agonists (ML-SAs) induces catastrophic and irreversible necrosis in metastatic melanoma cells, while completely sparing normal cells. Such cell death can be prevented by ML1-specific synthetic inhibitors (ML-SIs), Zn2+ chelator, or ML1 knock-down, and is associated with mitochondria swelling and rapid cellular ATP depletion. Further, ML-SAs demonstrate potent therapeutic efficiency and survival benefit in *in vivo* advanced melanoma models.

Methods

Molecular biology

ML1 siRNA constructs were purchased from Sigma Aldrich (EHU062561). GZnP3-TRPML1 and GZnP3-Rab7 plasmids were obtained from Dr. Yan Qin from University of Denver. All constructs were confirmed by DNA sequencing and western blotting.

Melanoma mouse models

Athymic nude mice (females, 8 weeks old, Charles River Laboratories, Wilmington, MA) weighing between 18g and 22g were used in the study. Mice were housed in standard cages at 21°C with a 12h light-12h dark cycle and had access to food (standard laboratory chow) and water ad libitum. For experimental procedures, mice were anesthetized by 2% isoflurane inhale. For subcutenous (s.c.) tumor model, MeWo-FmC cells ($1x10^6$ tumor cells/mouse) were suspended in 100µl PBS and s.c. injected into immunocompromised nude mice. ML-SA5 (dissolved in 10% DMSO, 40% PEG300, and 50% PBS) was administered to mice (5mg/Kg) by intraperitoneal injection 3 times a week for 5 weeks. For brain tumor model: M12-FmC cells were implanted stereotactically into nude mice brains (0.5×10^5 tumor cells/mouse) in the following co-ordinates: 2.2 mm lateral from bregma, 2.5 mm ventral from dura on the cranial suture. ML-SA5 (10mM/5 µl) was administered by intratumoral injection. Mice were imaged for the success of tumor cell injection post-implantation and then periodically for tumor progress by *in vivo* Bioluminescent imaging (BLI) as described previously (Du et al., 2017). All *in vivo* procedures were approved by animal protocol following the Institutional Animal Care Guidelines at the University of Michigan.

Mammalian cell lines

HEK293 cells were cultured in Dulbecco's Modified Eagle Medium (DMEM, Thermo Fisher Scientific) with 10% fetal bovine serum (FBS, Atlanta Biologicals) and 1x MycroZap (Lonza). Transfection was done using Lipofectamine 2000 (Invitrogen). Melanocytes were kindly provided by D. Fisher (MGH, Boston) and cultured in Ham's F-10 Nutrient Mix (F-10, Thermo Fisher Scientific) with 10% FBS. MeWo and M12 were provided by J. Sarkaria (Mayo Clinic,

Rochester) and cultured in DMEM with 10% FBS. All cells were used at low passages without further authentication or testing for mycoplasma contamination.

Immunohistochemistry.

Cells were fixed with 100% (v/v) methanol for 8 min in -20˚C. After blocking with PBS + 2% BSA for 1 h, samples were incubated with primary antibodies overnight and then secondary antibodies for 1 h. After 10 min DAPI counterstaining, coverslips were mounted with Fluoromount-G (Southern Biotechnology Associates, Inc.). The antibodies used included: anti-LAMP1 (DSHB, cat. H4A3, 1:200) and Rabbit anti-mouse Texas Red (Invitrogen, cat. T862, 1:1000).

Confocal imaging.

Fluorescence imaging and time-lapse imaging were conducted in a spinning-disk confocal imaging system composed of an Olympus IX81 inverted microscope, 10x, 20x and 60x Olympus objectives, a CSU-X1 scanner (Yokogawa), an iXon EM-CCD camera (Andor), a temperature controller (Tokai Hit), and MetaMorph Advanced Imaging acquisition software v.7.7.8.0 (Molecular Devices). For PI fluorescence time-lapse imaging, cells were challenged with DMEM supplemented with 10 μM ML-SA5 and 10 μg/mL PI, and images were taken at an interval of 10 min. For MitoTracker live imaging, cells were treated with ML-SAs and loaded with MitoTracker Green (Invitrogen, M7514) staining 1 h before imaging. Inhibitors were pretreated for 30 min. Images were analyzed with MetaMorph Advanced imaging acquisition software v.7.7.8.0 (Molecular Devices) and Image J (NIH).

PI staining assay

Cells were washed twice with respective culture medium before being loaded with 10 μg/mL PI along with drug treatments. To be specific, MeWo, melanocyte, and HEK293 cells were loaded with PI for 6h while M12 cells 3h before they were imaged using an Olympus IX81 inverted fluorescence microscope, 10X. Images were analyzed with Image J.

CellTiter cell viability assay

Cells (0.5×10^4/well) were seeded in 96-well plates and incubated with drug treatments for indicated duration. Cell viability was measured by a quantitative luminescence assays using an ATP-dependent luminescent reagent (CellTiter-Glo, Promega, Madison, WI) according to the manufacturer's instructions.

RNA extraction and RT-qPCR

Total RNA was extracted and purified from the cultured human fibroblasts using E.Z.N.A. HP total RNA kit (Omega Bio-tek, Georgia, USA). The cDNA was then synthesized using a Superscript III RT kit (Thermo Fisher Scientific, New York, USA). PCR mixture was prepared with PowerUp SYBR green 2X master mix (Thermo Fisher Scientific, New York, USA) using the following primers: GAPDH, forward (fw): 50-tgcaccaccaactgcttagc-30, reverse (rev): 50-ggc atggactgtggtcatgag-30; TRPML1, fw: 50-gagtgggtgcgacaagtttc-30, rev: 50-tgttctcttcccggaatgtc-30. Real time qPCR was performed with ABI StepOnePlus RealTime PCR System.

Western blotting

Cells were lysed with ice-cold RIPA buffer (Boston BioProducts, Massachusetts, USA) in the presence of 1×protease inhibitor cocktail (Sigma, Missouri, USA) and phosphatase inhibitor cocktail 2 (Sigma, Missouri, USA), NaF (1 mM), and Na_3VO_4 (1 mM). Protein samples (10–100μg) were then loaded and separated on 4% to 12% gradient sodium dodecyl sulfate (SDS) polyacrylamide electrophoresis gels (Thermo Fisher Scientific, New York, USA) and transferred to polyvinylidene difluoride membranes. The membranes were blocked with 1% bovine serum albumin or 5% milk in PBS supplemented with 0.1% Tween20 for 1 h and then incubated with primary antibodies against ML1 (Alomone Labs, cat. ACC-081, 1:200), LAMP1 (DSHB, H4A3, 1:200) and β-actin (Sigma, A5316, 1:200). Bound antibodies were detected with IRDye 680RD goat anti-mouse or 800CW goat anti-rabbit IgG secondary antibody (LI-COR, 926-68070, 926-32211, 1:5,000) and enhanced chemiluminescence reagents (Thermo Fisher Scientific, New York, USA). Protein levels were quantified with ImageJ (NIH) software.

Whole-endolysosome and whole-cell electrophysiology

Experiments were performed in mechanically isolated endolysosomes as described previously. In brief, cells were treated with 1μM vacuolin-1 overnight to increase the size of late endosomes and lysosomes selectively [49]. Unless otherwise indicated, vacuoles were bathed continuously in an internal (cytoplasmic) solution containing 140 mM K^+-gluconate, 4 mM NaCl, 1 mM EGTA, 2 mM $MgCl_2$, 0.39 mM $CaCl_2$, and 20 mM HEPES (pH adjusted with KOH to 7.2; free $[Ca^{2+}]_i$ approximately equal to 100 nM). The pipette (luminal) solution contained 145 mM NaCl, 5 mM KCl, 2 mM $CaCl_2$, 1 mM $MgCl_2$, 10 mM glucose, 10 mM HEPES, and 10 mM MES (pH adjusted to 4.6 with NaOH). The whole-endolysosome configuration was achieved as

described previously. After formation of a giga-seal between the patch pipette and an enlarged endolysosome, voltage steps of several hundred millivolts with a millisecond duration were applied to break into the vacuolar membrane. All bath solutions were applied via a fast perfusion system that produced a complete solution exchange within a few seconds.

Whole-cell ML1 currents were measured using a pipette/cytosolic solution that contained (in mM): 145 mM NaCl, 5 mM KCl, 2 mM $CaCl_2$, 1 mM $MgCl_2$, 10 mM glucose, and 10 mM HEPES (pH adjusted to 7.4 with NaOH). The bath/extracellular solution contained (in mM): 30mM $ZnCl_2$, 110 Mm NaCl, 10 mM HEPES and 10 mM MES (pH 4.6 adjusted with HCl). Patch pipettes had a resistance of 2-4 mΩ.

Data were collected via an Axopatch 2A patch clamp amplifier, Digidata 1440, and processed with pClamp 10.0 software (Axon Instruments, Molecular Device, California, USA). Currents were digitized at 10 kHz and filtered at 2 kHz. All experiments were conducted at room temperature (21˚C-23˚C), and all recordings were analyzed in pCLAMP10 (Axon Instruments, Molecular Device, California, USA) and Origin 8.0 software.

Zn^{2+} imaging

FluoZinTM-3, AM was loaded into cells by placing the dye (5μM) in the culture medium at 37°C for 30min, followed by a 5-min wash with the culture medium. Fluorescence imaging using the spinning-disk confocal imaging system was performed at 37°C. The cell permeant AM-ester is expected to be present at all locations in the cytoplasm. The genetically encoded Zn^{2+} sensor GZnP3 was fused to a cytosolic N-terminus of TRPML1 (GZnP3-TRPML1) to create a sensor that detects juxta-lysosomal [Zn^{2+}] or to Rab7 (GZnP3-Rab7) to create a control sensor which has its greatest expression in early endosomes, although there is also some expression in

lysosomes (Minckley et al., 2019). Cells were transiently transfected and the fluorescence intensity of GZnP3 at 488 nm was recorded with an EasyRatioPro system (Photon Technology International, Inc. New Jersey, USA).

Reagents

FluoZin^{TM}-3, AM was purchased from Thermo Fisher Scientific (cat. F24195). Propidium iodide (cat. P4864) was purchased from Sigma-Aldrich. Other reagents used in the study included: BAPTA-AM (Invitrogen, cat. B6769); TPEN (Sigma Aldrich, cat. P4413); Nec-1 (Cayman Chemical, cat. 11658); DFO (Sigma Aldrich, cat. D9533); z-VAD (R&D Systems, cat. FMK001); Vacuolin-1 (Millipore Sigma, cat. 673000); GPN (Santa Cruz, cat. Sc-252858). ML-SA and ML-SI compounds were identified initially by Ca^{2+} imaging-based high-throughput screening conducted at the National Institutes of Health (NIH)/National Center for Advancing Translational Sciences Chemical Genomics Center (https://pubchem.ncbi.nlm.nih.gov/bioassay/624414), and their potencies were improved by medicinal chemistry. All ML-SA and ML-SI compounds are available upon request under material transfer agreement with the University of Michigan.

Data analysis

Average data are presented as means ± standard errors of the mean (SEMs). Statistical comparisons were performed with one-way analyses of variance (ANOVAs) with Bonferroni's *post hoc* analysis or with paired and unpaired Student's t-tests where appropriate. *P* values < .05 were considered statistically significant.

Results

ML1 channel activity is up-regulated in metastatic melanoma cells

RNA-seq of human cancer samples from 17 types of cancer in the Cancer Genome Atlas (TCGA) project of Genomic Data Commons (GDC) demonstrated that ML1 mRNA expression level is the highest in melanoma among tested cancer types (https://www.proteinatlas.org/ENSG00000090674-MCOLN1/pathology). Based on this information, we performed real-time qPCR and western blotting experiments that showed a more than two-fold increase in ML1 mRNA and protein level in metastatic melanoma cells (MeWo and M12) compared with non-cancerous human melanocytes (Figures 3.1A-C). To further confirm the up-regulation of ML1 channel activity on lysosomes, whole-lysosomal ML1-mediated currents (I_{ML1}) activated by ML1-specific synthetic agonists (ML-SAs) were recorded (Figures 3.1D-G). Specificity of ML-SAs has been confirmed using ML1 knockout (KO) cells in previous publications (Shen et al., 2012). I_{ML1} was on average 75-fold and 30-fold higher in MeWo and M12 cells, respectively, compared with normal melanocytes (Figure 3.1G).

Consistent with the role of ML1 in TFEB-dependent lysosome biogenesis, the protein level of endogenous LAMP1, a common lysosome marker, was detected by western blotting increased by more than two folds in both lines of metastatic melanoma cells (Figures 3.1B, 3.1C), and immunofluorescence analysis of LAMP1 signal showed an approximately 30% increase in lysosome density in MeWo and M12 cells than melanocytes (Figure 3.1H). Together, these results suggest that ML1, as well as lysosome biogenesis were functionally upregulated in metastatic melanoma cells.

Selective cytotoxic effects of ML-SAs on metastatic melanoma cells

SA5 and SA8 are potent agonists of ML1 (EC_{50} 290±150 nM and 80±14 nM respectively) with independent structures that induce the flow of all permeable ions. Both activators triggered catastrophic and irreversible cell death in MeWo and M12 cells, while completely sparing melanocytes (Figures 3.2A, 3.2B). Within 0.5~2 h, ML-SA-treated M12 and MeWo cells exhibited obvious morphological changes characteristic of cell death, e.g., rounding-up and swelling (Figure 3.2A), followed by reduced cytosolic ATP levels as measured by CellTitre-Glo ATP assay (Figure 3.2C) and loss of membrane integrity as detected by propidium iodide (PI) staining (Figure 3.2A). Likewise, a human breast-to-brain metastatic cancer cell line MDA231-BrM2 was also sensitive to ML-SAs (Figure 3.2C). In contrast, normal melanocytes and common mammalian cell lines, e.g., HEK293 cells, HeLa, and primary human fibroblasts, displayed no obvious vulnerability to ML-SA treatment (Figure 3.2C). While MeWo cells possess higher lysosomal ML1 channel activity (Figure 3.1E-G), the death rate of MeWo cells upon ML-SA treatments was ~30% lower than that of M12 cells (Figure 3.4B, 3.4C), the onset of cell death was about 1h later, and the time required to reach maximum cell death was around 2-times longer in MeWo cells (Figure 3.3B), potentially due to difference in other factors downstream in the pathway.

By conducting time-dependence (Figures 3.3A, 3.3B) and dose dependence (Figures 3.4A-C) analysis using PI staining assay with supplement of CellTitre-Glo ATP assay, we set the treatment dose of SA5 and SA8 to 3μM and 1μM, in consistence with the drug potency data, and treatment time of MeWo and M12 cells 6h and 3h respectively to reach an 80% effect for later experiments.

The cytotoxic effects of ML-SAs were completely prevented by co-treatment of independent ML1-specific synthetic inhibitors (ML-SIs) SI3 and SI4 in both PI staining and

CellTitre-Glo ATP assays (Figures 3.5A-C), suggestive of ML-SAs' specificity. Dominant-negative (DN)-ML1-expressing M12 cells exhibit significantly reduced ML-SA-induced cell death (Figure 3.5D). Two ML-SAs resistant cell clones were developed by long-term selection of M12 cells upon gradually increased SA5 or SA8 doses respectively, named herein as $M12R^{SA5}$ and $M12R^{SA8}$. $M12R^{SA5}$ was also resistant to SA8 challenge and vice versa (Figure 3.5E), indicating the specificity of resistance is through ML1-dependent pathways. ML1 channel activity assessed using electrophysiology was unaffected in the resistant lines compared with WT M12 cells (data not shown), suggesting that the resistance was conferred by alterations in downstream pathways. Collectively, these results suggest that metastatic melanoma cells are uniquely sensitive to ML1 over-activation.

Roles of Zn^{2+} in ML-SA-induced melanoma cell death

To explore the cell death mechanism for ML-SA-evoked melanoma cell death, we tested inhibitors for various cell death pathways, a pan-caspase inhibitor (z-VAD-FmK), a necroptosis inhibitor (necrostatin-1) and an iron chelator deferoxamine (DFO). None of them inhibited ML-SA-caused cell death (Figures 3.6A-C), suggesting that the ML-SA-induced metastatic melanoma cell death is independent of apoptosis, RIP1-regulated necroptosis and ferroptosis.

ML1 is permeable to Ca^{2+}, Na^{+} and K^{+}, as well as to heavy metal ions such as Fe^{2+}. Application of BAPTA-AM (a Ca^{2+} chelator, Figures 3.6D-F) or DFO (a Fe^{2+} chelator, Figures 3.6C) had no effect on ML-SA mediated cell death, but TPEN, a commonly used Zn^{2+} chelator, completely blocked ML-SA-induced melanoma cell death (Figures 3.6D-G), suggesting the involvement of Zn^{2+} in ML-SA-triggered cell death.

As compared to the currents present in control Tyrode's solution, whole-cell patch clamp recordings of ML1 overexpressing HEK293 cells in response to SA1 stimulation showed a positive shift in reversal potential when switched to a high Zn^{2+} bath solution, confirming that ML1 is Zn^{2+} permeable (Figure 4.7A). The efflux of Zn^{2+} from lysosomes could also be detected in MeWo cells overexpressing GZnP3 (a genetically-encoded Zn^{2+} indicator) fused to the cytosolic N-terminal of ML1 (Figures 3.7B, 3.7D). Upon ML-SA activation, an increase in GZnP3 signal was observed, indicating Zn^{2+} efflux from the lysosomes into the cytosol (Figures 3.7B). There was no fluorescence increase in MeWo cells expressing GZnP3-Rab7 in response to SA1 (Figures 3.7C, 3.7D), suggesting that the cytosolic Zn^{2+} increase seen in GZnP3-ML1-expressing cells reflected lysosomal Zn^{2+} efflux.

Using FluoZin™-3AM, a cell-permeant Zn^{2+}-sensitive fluorescent dye (K_d=15nM), to measure cellular Zn^{2+} distribution, we found that intracellular Zn^{2+} stores largely colocalized with LysoTracker positive vesicles (Figure 3.7E), indicating lysosomes as intracellular Zn^{2+} stores in MeWo and M12 cells. Interestingly, in melanocytes, most of the FluoZin-positive puncta were LysoTracker-negative, suggesting that in these cells most of the Zn^{2+} is in non-lysosomal pools (Figure 3.7A). A rapid reduction of fluorescence in FluoZin-labelled (Zn^{2+}-positive) lysosomes in melanoma cells after ML-SA application was not seen (data not shown), probably due to the low dissociation rate of the dye. In the future, the cell-permeant Newport Green DCF Diacetate, a Zn^{2+}-specific dye with lower affinity ($K_d \approx 1\mu M$) (Sumner et al., 2002) could be used to assess cellular Zn^{2+} distribution after ML1 activation in melanoma cells. Newport Green DCF has also been used in conjunction with Texas Red 10000 MW dextran to create a ratiometric fluorescent PEBBLE nanosensor for real-time measurements of intra- and intercellular free Zn^{2+} (Sumner et al., 2002).

ML1 channel activity is necessary and sufficient for metastatic melanoma cell death

To further confirm that the activation of ML1 triggered selective cell death, we challenged HEK293 cells overexpressing ML1-GFP with ML-SAs. Both SA5 and SA8 induced massive cell death in GFP-positive HEK293 cells compared with internal none-transfected control cells (Figures 3.8A, 3.8B, 3.8D) Additionally, such cell death was blocked by ML-SI and TPEN, but not BAPTA-AM, suggesting that ML1 overactivation induced cell death via ML1-mediated Zn^{2+} efflux (Figures 3.8A, 3.8C, 3.8D). ML1 activation insensitive HEK293 cells were used in overexpression assays because melanocytes were susceptible to Lipofectamine transfection.

Conversely, knockdown (KD) of ML1 utilizing siRNA in both MeWo and M12 cells significantly reduced ML-SA-induced cell death (Figures 3.9A, 3.9B). Knockdown efficiency was confirmed by whole-endolysosomal patch clamp recordings (Figure 3.9C). Taken together, ML1 overactivation in metastatic melanoma cells facilitates Zn^{2+}-overload-mediated cell death.

Zn^{2+} mediated mitochondrial dysfunction

Previous publication suggested a role of cytosolic Zn^{2+} overload in producing mitochondrial dysfunction (Bossy-Wetzel et al., 2004; Dineley et al., 2003; Sheline et al., 2000; Skulachev et al., 1967). MitoTracker staining of MeWo and M12 cells showed swelling and fragmented mitochondria 1h post ML-SA treatment, compared with melanocyte controls (Figures 3.10A, 3.10B). Such mitochondrial morphological change were largely inhibited by ML1 inhibition (ML-SAs) or Zn^{2+} chelation (TPEN) (Figures 3.10C, 3.10D), suggesting the specific roles of ML1 and Zn^{2+} in the process. Cytosolic ROS level was also significantly increased in MeWo and M12 cells 1h post ML-SA treatment (Figure 3.11A), and application of ML-SIs and TPEN reversed this increase (Figure 3.11B).

In vivo efficacy of ML-SAs in an advanced mouse melanoma model

To evaluate the therapeutic efficacy of ML-SAs *in vivo*, we engineered MeWo cells to stably express both the fluorescent protein mCherry and the bioluminescent protein firefly luciferase (Fluc). These modified MeWo cells, referred to as MeWo-FmC cells, exhibited normal cell morphology, proliferation, migration, and drug sensitivity compared with their parental cells. A similar strategy was used to generate M12-FmC cells. In a subcutaneous xenograft tumor model, *in vivo* bioluminescence (BLI) imaging was performed weekly to monitor tumor growth. In tumor-bearing mice that were randomly separated into vehicle- vs. ML-SA-treated groups, intraperitoneal (IP) injections of SA5 (5 mg/kg, treatment started one week post tumor cell inoculation) resulted in much reduced tumor growth *in vivo* (Figures 3.12A-C, 3.12E, 3.12F) and improved survival (Figure 3.12G). In a second MBM mouse model established by injecting M12-FmC cells ($2x10^5$ cells in 100 µl PBS) via the right internal carotid artery (ICA) injection into immunocompromised nude mice, i.c.v. injection of SA5 (5mM/5µl, single injection one week after tumor cell inoculation) significantly diminished tumor growth without causing obvious systemic toxicities (Figure 3.12D).

Discussion

TRPML1 has been suggested to be a positive regulator of cancer progression as it regulates mTOR and TEFB signaling, and sustains several cancer hallmarks, including proliferation and autophagy. Typically, ML1 is preferentially required for the survival and proliferation of melanoma cells through negative regulation of MAPK and mTORC1 signaling to promote micropinocytosis (Kasitinon et al., 2019). Loss of ML1 function impairs the growth of patient-derived melanomas in culture and in xenografts (Kasitinon et al., 2019). Here, we identified

hyperactive ML1 as a negative regulator of metastatic melanoma cell growth. Using both *in vitro* and *in vivo* cell death and tumor growth experiments, we demonstrated a link between Zn^{2+} release, the ML1 channel, and cancer cell death; hyperactivation of ML1 via ML1-specific agonists results in cytosolic Zn^{2+} overflow, leading to robust and specific melanoma cell death. Under physiological conditions, non-cancer cells such as melanocytes possess low $[Zn^{2+}]_{Ly}$ as well as modest lysosomal ML1 protein expression, while in metastatic melanoma cells, lysosome biogenesis, ML1 expression, and lysosomal Zn^{2+} concentration are all upregulated. Activation of ML1 in metastatic melanoma cells, but not in the non-cancer cells, induced massive Zn^{2+} release into the cytosol, causing Zn^{2+}-induced cell toxicity. Therefore, ML1 activity in melanoma cells requires strict regulation and both hypo- and hyper-activation of ML1 disrupts cellular functions (Figure 3.13). This work suggests that manipulating lysosomal ML1 activity as well as Zn^{2+} release may be viable approaches to treat advanced melanoma.

In live imaging, mitochondrial swelling starts 10min post SA5 or SA8 application in M12 cells and 30min in MeWo cells, significantly ahead of their average cell death time, suggesting that the mitochondrial dysfunction may act as primary phenotypes downstream of cytosolic Zn^{2+} overload. In this case, mitochondrial Zn^{2+} transporters could be targeted to see whether ablating mitochondrial Zn^{2+} responses rescues melanocytes from ML-SA-induced cell death. However, Zn^{2+} has been accepted as a second messenger that is able to activate many signaling pathways within a few minutes of an extracellular stimulus by release of Zn^{2+} from intracellular stores, such as inhibiting a multitude of tyrosine phosphatases (Maret, 2017; Murakami and Hirano, 2008). Therefore, mitochondria may not be the first site to reach in this cell death pathway.

Unlike the cytosol, which keeps the free Zn^{2+} concentration as low as 0.1nM, intracellular vesicles such as endosomes and lysosomes contain micromolar to millimolar concentrations of

Zn^{2+}, acting as vesicular Zn^{2+} stores (Bozym et al., 2010; Han et al., 2018). Zn^{2+} is transported into lysosomes via Zn^{2+} transporter ZnT2 and ZnT4 (Falcon-Perez and Dell'Angelica, 2007; Kukic et al., 2013), or through other pathways such as endocytosis and autophagy . Although cytosolic Zn^{2+}, as an essential trace element, is required for normal cellular functions, excessive Zn^{2+} release from Zn^{2+} stores reportedly inhibits mitochondrial functions, e.g., mitochondrial aconitase in the Krebs cycle and cytochrome c reductase activities in the electron transfer chain, to cause cellular energy failure and subsequent cell death (Costello et al., 1997; Kuznetsova et al., 2005). Generally speaking, inhibition of crucial enzymes by Zn^{2+} may become significant when free cytosolic [Zn^{2+}] reaches above 10 nM (Dineley et al., 2003). Hence, Zn^{2+} release channels and transporters such as ML1, must be tightly regulated in normal cells.

Dysregulated Zn^{2+} homeostasis is associated with many cancers (Chandler et al., 2016; Hwang et al., 2010; Serra et al., 2020). Cancer cells usually obtain less cytosolic Zn^{2+}, as normal physiological concentrations of Zn^{2+} inhibit cancer cell proliferation and migration (Pan et al., 2017). Indeed, nuclear p53 protein expression was increased with Zn^{2+} deficiency along with an increase in the binding activity of transcription factors involved in regulating cell proliferation and apoptosis (Franklin and Costello, 2009; Reaves et al., 2000). Such $[Zn^{2+}]_{Cyto}$ decrease can be achieved by either inhibiting Zn^{2+} uptake, or by Zn^{2+} export out of the plasma membrane or into intracellular Zn^{2+} stores. On one hand, in pancreatic cancer tissues, all Zn^{2+} importer ZIP proteins with the exception of ZIP4 are downregulated, leading to low intracellular Zn concentrations, and increased resistance of the malignant cells to Zn^{2+} cytotoxic effects (Pan et al., 2017). On the other hand, the Zn^{2+} exporter ZnT7 gene expression is up-regulated in esophageal cancer. ZnT1 and ZnT2 expression increases in highly aggressive and metastatic basal breast cancer compared to low-invasive luminal, relating [Zn^{2+}] with aggressiveness (Serra et al., 2020). Notably, breast

biopsies from breast cancer patients contain significantly higher Zn^{2+} levels compared with normal breast tissue (Margalioth et al., 1983). Epidemiological studies have established a relationship between high breast tissue Zn^{2+} levels and development of breast cancer (Cui et al., 2007). Expression of lysosomal Zn^{2+} transporter ZnT2 has been shown elevated in breast cancer, leading to the hypothesis that Zn^{2+} is highly accumulated in lysosomal stores in breast cancer cells (Hwang et al., 2010). It has been shown in FluoZin-3 imaging that MDA-MB-231 cells overexpressing ZnT2 showed Zn^{2+} accumulation in vesicular compartments, potentially lysosomes (Chandler et al., 2016). In general, cancer cells exhibit high metabolism and an increased turnover of metal-binding macromolecules, leading to accumulation of heavy metal ions including Fe^{2+} and Zn^{2+} in endolysosomal compartments (Serra et al., 2020). However, whether the accumulation of intracellular zinc pools or the Zn^{2+} secretion is the driving force for carcinogenesis is still unknown. Nonetheless, targeting intracellular Zn^{2+} stores such as lysosomes might serve as a new treatment for cancer.

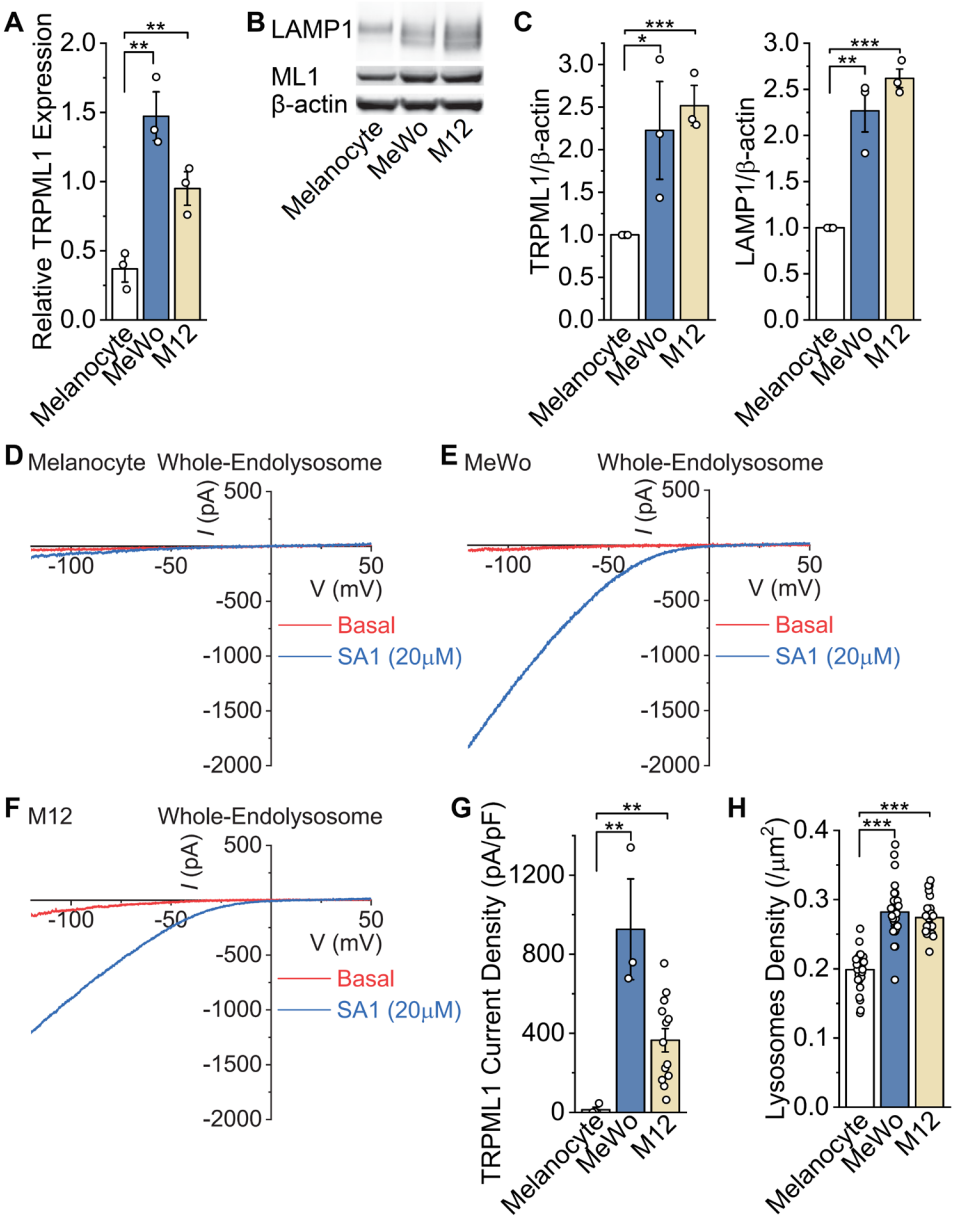

Figure 3.1 Upregulation of ML1 channel activity in metastatic melanoma cells.
(A) Relative ML1 mRNA expression level of Melanocyte, MeWo, and M12 cells. (B) Western blotting of endogenous ML1 and LAMP1 protein expression in melanocyte, MeWo, and M12 cells. β-actin served as the loading control. (C) Quantitation of Western blotting results in B. (D-F) Typical basal and 20μM SA1-induced traces of whole-endolysosome patch clamp of Melanocyte (D), MeWo (E), and M12 (F) ML1 current. SA1 is a specific ML1 agonist. Currents were characterized with a ramp voltage protocol from -120 to +50 mV. (G) ML1 Current density of Melanocyte, MeWo, and M12 cells. (H) LAMP1 density analysis of endogenous LAMP1 immunostaining of Melanocyte, MeWo, M12 and HEK293 cells.

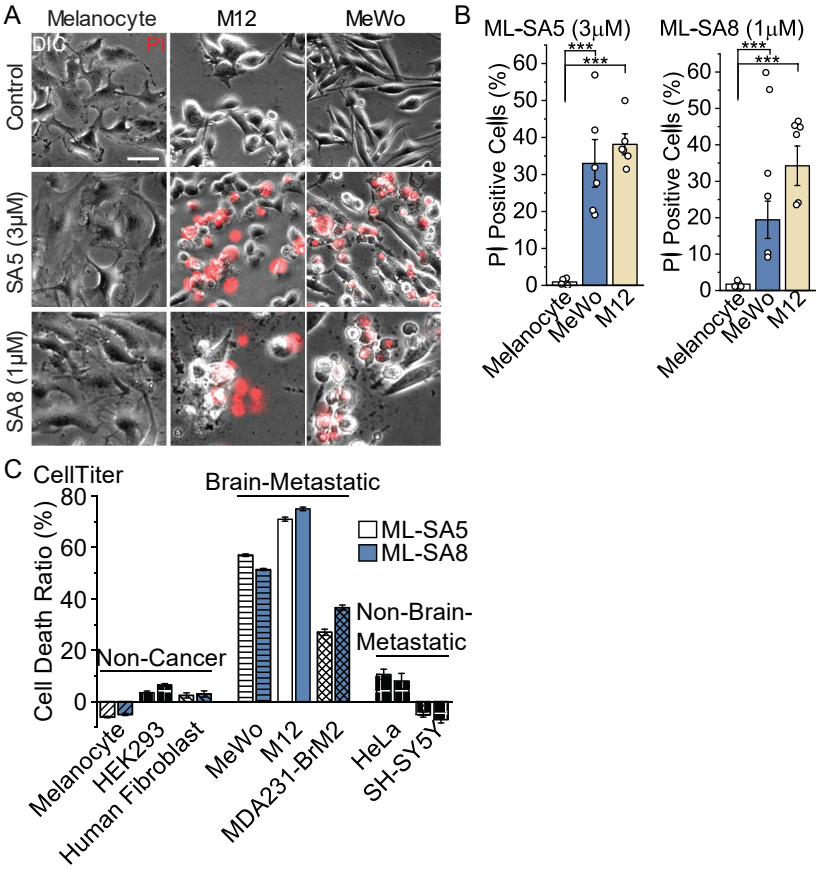

Figure 3.2 Activation of ML1 channel activity exhibit cytotoxic effects on metastatic melanoma cells.

(A) Typical PI staining images of Melanocyte, MeWo, and M12 cells post DMSO (upper panel) or 3μM SA5 (middle panel) or 1μM SA8 (lower panel) treatment. Melanocyte and MeWo cells were treated for 6h; M12 cells were treated for 3h. SA5 and SA8 are specific ML1 agonists. Scale bar: 50μm. (B) Analysis of the percentage of PI positive cells post SA5 or SA8 application in the three cell types in A. (C) CellTiter cell viability analysis of melanocyte, HEK293, human fibroblast, MeWo, M12, MDA231-BrM2, HeLa, and SH-SY5Y cells treated with 3μM SA5 or 1μM SA8 for 12h.

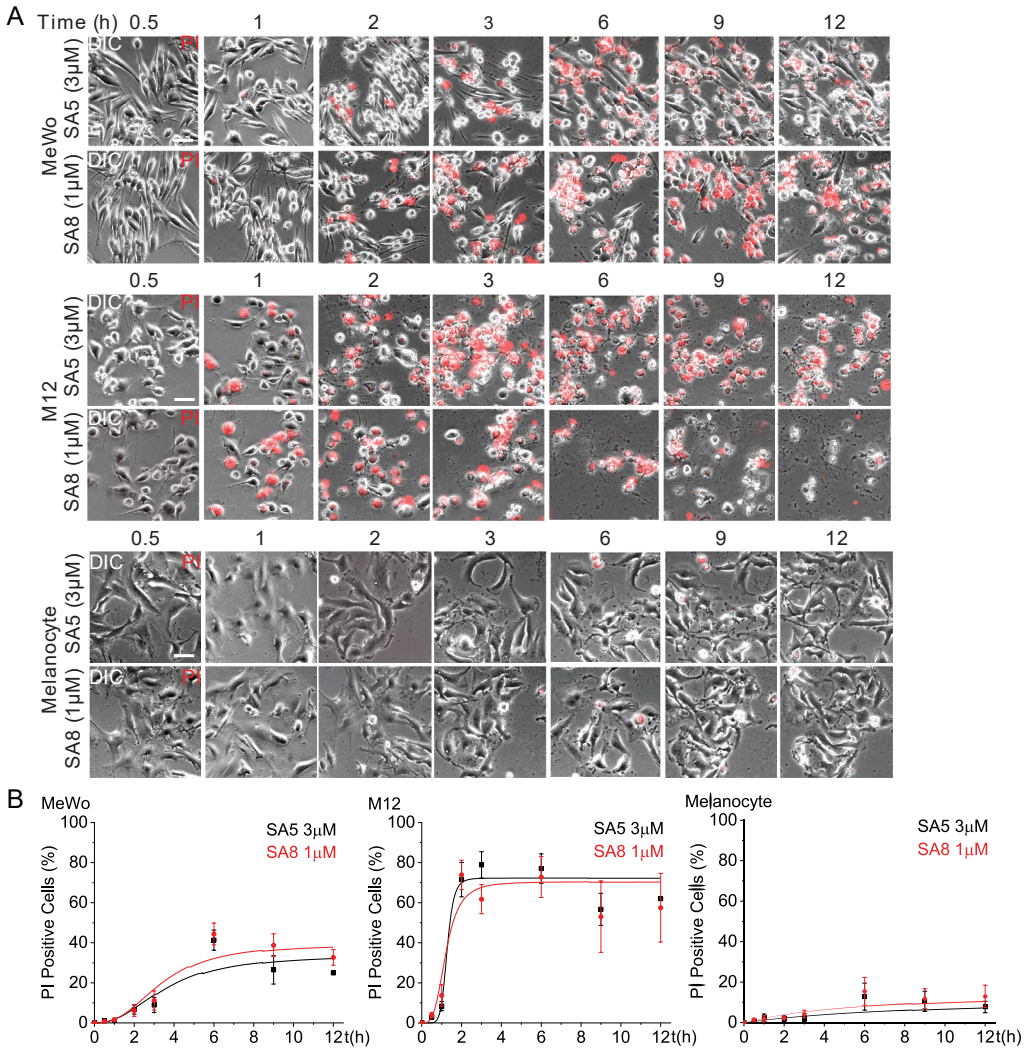

Figure 3.3 Time dependence of ML-SA-induced metastatic melanoma cell death.
(A) Time dependence of SA5 and SA8 on MeWo and M12 cell death. Typical PI staining images of MeWo, M12, and melanocytes cells post 3μM SA5 or 1μM SA8 treatment. Cells were treated with increasing time from 30min to 12h. Scale bar: 50μm. (B) Fitted time dependence curve of MeWo (left), M12 (middle), and melanocyte (right) cell death under SA5 (black) and SA8 (red) treatment.

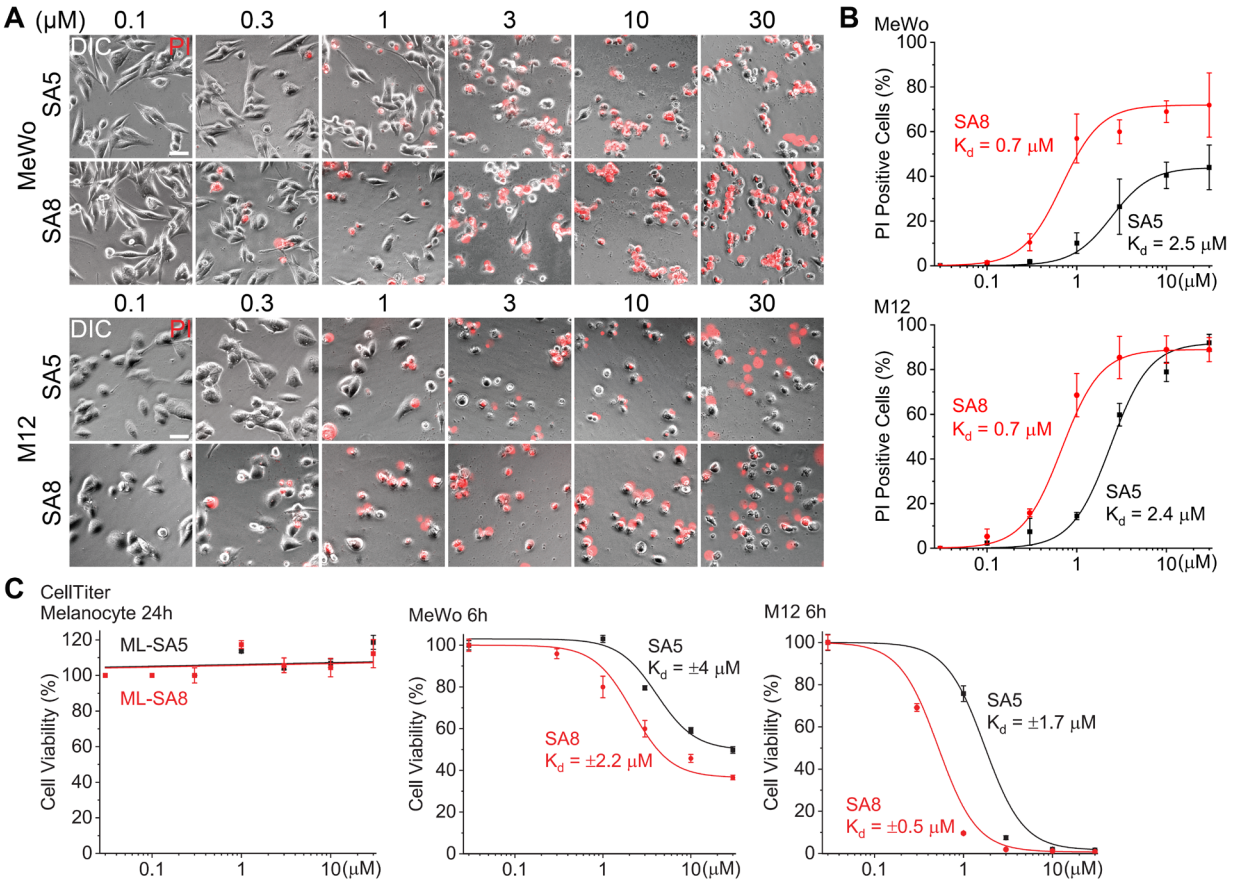

Figure 3.4 Dose dependence of ML-SA-induced metastatic melanoma cell death.
(A) Dose dependence of SA5 and SA8 on MeWo and M12 cell death. Typical PI staining images of MeWo and M12 cells post SA5 or SA8 treatment. Cells were treated with increasing dose of agonists from 0.1 to 30μM. MeWo cells were treated for 6h and M12 cells were treated for 3h. Scale bar: 50μm. (B) Fitted dose dependence curve of MeWo (upper panel) and M12 (lower panel), cell death under SA5 (black) and SA8 (red) treatment. (C) CellTiter cell viability fitting of melanocyte, MeWo, and M12 cells treated with increasing dose (0.01, 0.3, 1, 3, 10, 30 μM) of SA5 (black) or SA8 (red).

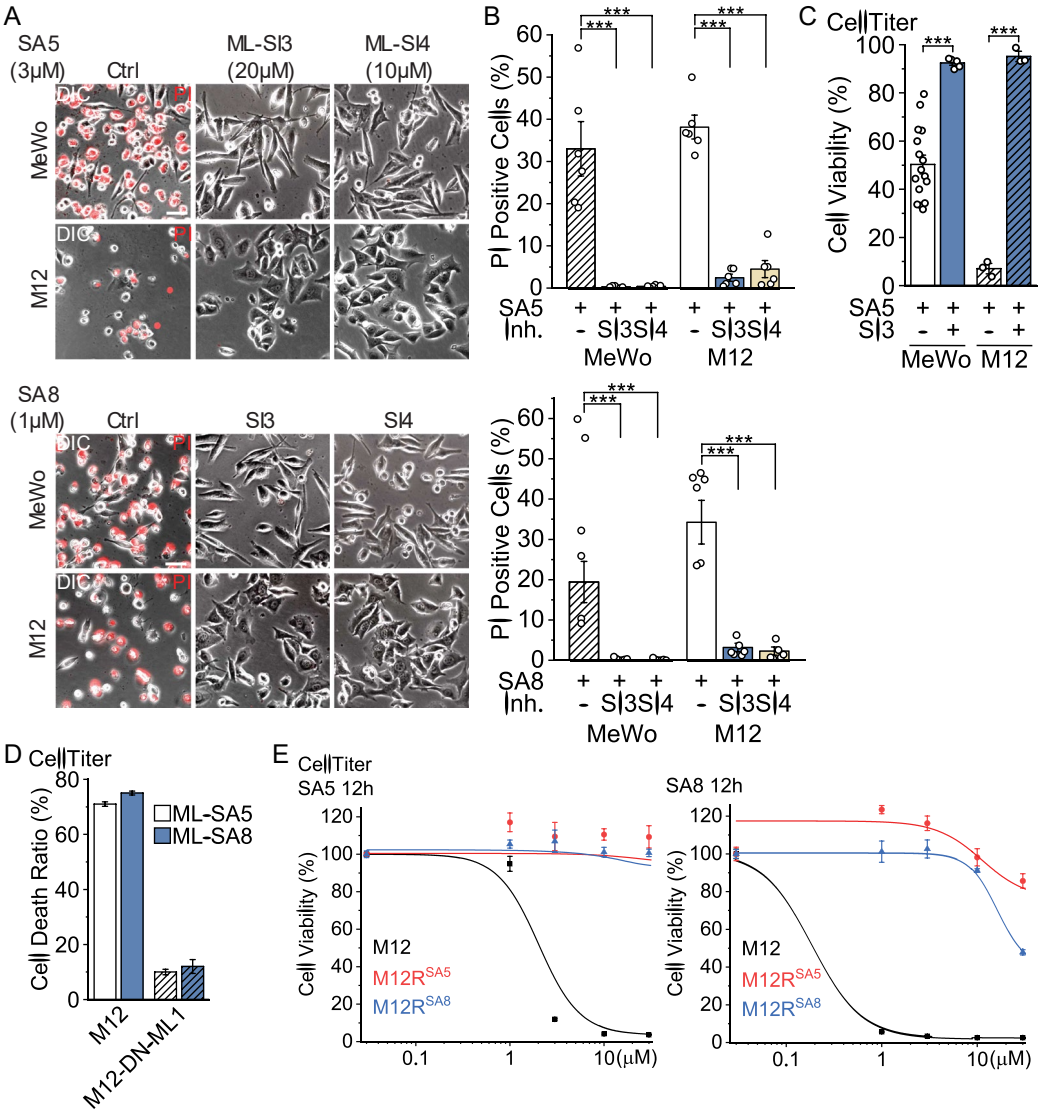

Figure 3.5 Cytotoxic effects on metastatic melanoma cells are ML1-specific.
(A) Typical PI staining images PI staining of MeWo and M12 cells under 3μM SA5/SA8 (left panel), or SA5/SA8 along with SI3 (middle panel) or SI4 (right panel) treatment. SI3 and SI4 are specific ML1 antagonists. Scale bar: 50μm. (B) Analysis of the percentage of PI positive cells post SA5/SA8 or SA5/SA8 and inhibitors treatment in MeWo and M12 cells in A. (C) CellTiter cell viability analysis of MeWo and M12 cells treated with 3μM SA5 or 3μM SA5 and 10 μM ML-SI3 for 6 and 3h respectively. (D) CellTiter cell viability analysis of M12 cells overexpressing WT ML1 or DN-ML1 treated with 3μM SA5 or 1μM SA8 for 3h. (E) CellTiter cell viability fitting of M12, M12R^{SA5}, and M12R^{SA8} cells treated with increasing dose (0.01, 1, 3, 10, 30 μM) of SA5 (left panel) or SA8 (right panel).

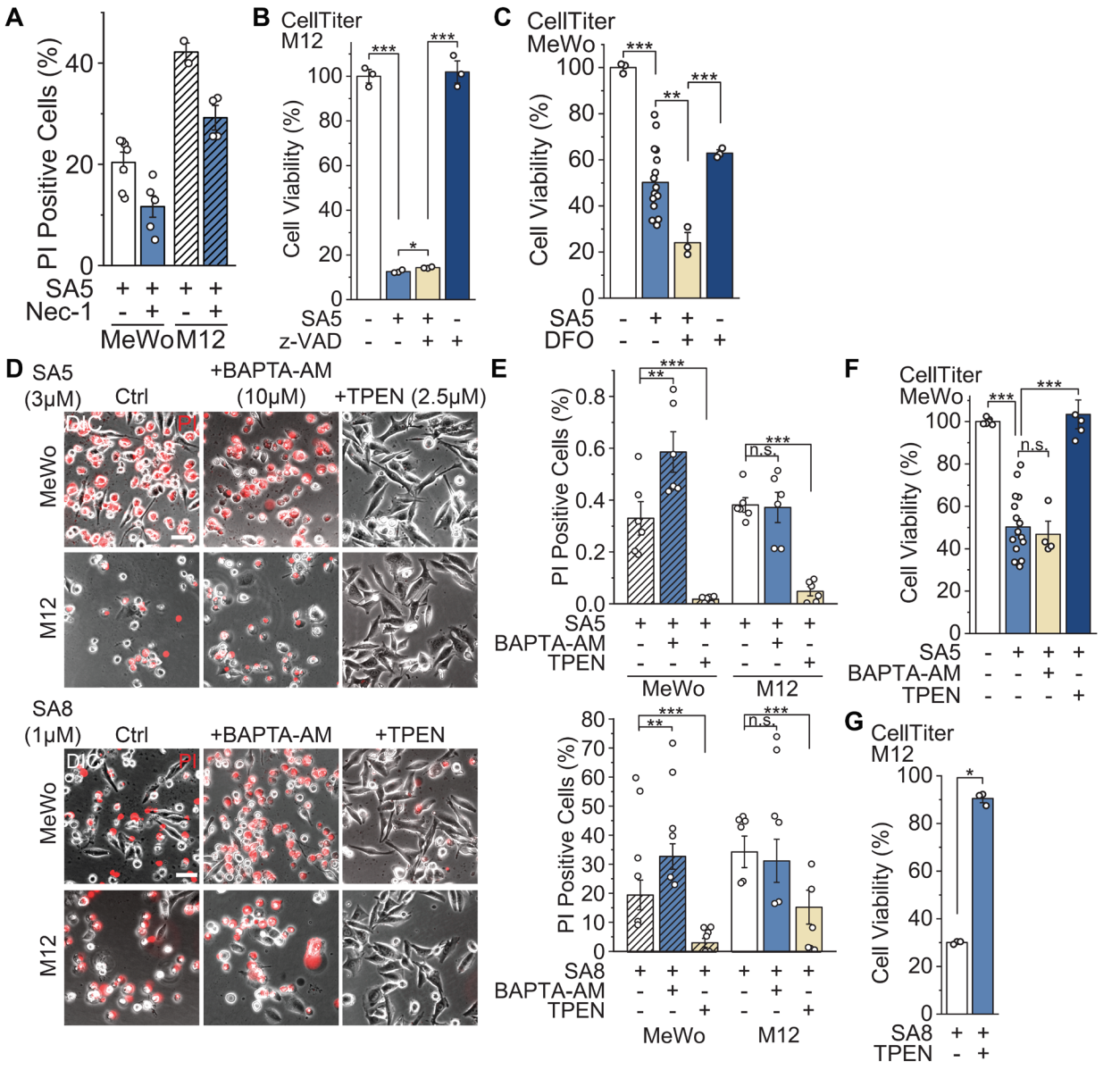

Figure 3.6 Selective cytotoxic effects on metastatic melanoma cells is Zn^{2+} dependent.
(A) PI cell death analysis of MeWo and M12cells treated with 3μM SA5, or 3μM SA5 and 10 μM Necrostatin-1. (B) CellTiter cell viability analysis of M12 cells treated with 3μM SA5, or 3μM SA5 and 20μM z-VAD. (C) CellTiter cell viability analysis of MeWo cells treated with 3μM SA5, or 3μM SA5 and 100 μM DFO. (D) Typical PI staining images of MeWo and M12 cells under 3μM SA5 or 1μM SA8 (left panel), or SA5/SA8 along with 10μM BAPTA-AM (middle panel) or 2.5μM TPEN (right panel) treatment. Cells were pretreated with BAPTA-AM and TPEN for 30min before SA5/SA8 application. MeWo cells were treated for 6h and M12 cells were treated for 3h. Scale bar: 50μm. (E) Analysis of the percentage of PI positive cells post drug application in A. (F) CellTiter cell viability analysis of MeWo cells treated with DMSO, 3μM SA5, 3μM SA5 and 10 μM BAPTA-AM, or 3μM SA5 and 2.5μM TPEN for 6h. (G) CellTiter cell viability analysis of M12 cells treated with 1μM SA8, or 1μM SA8 and 2.5μM TPEN for 6h.

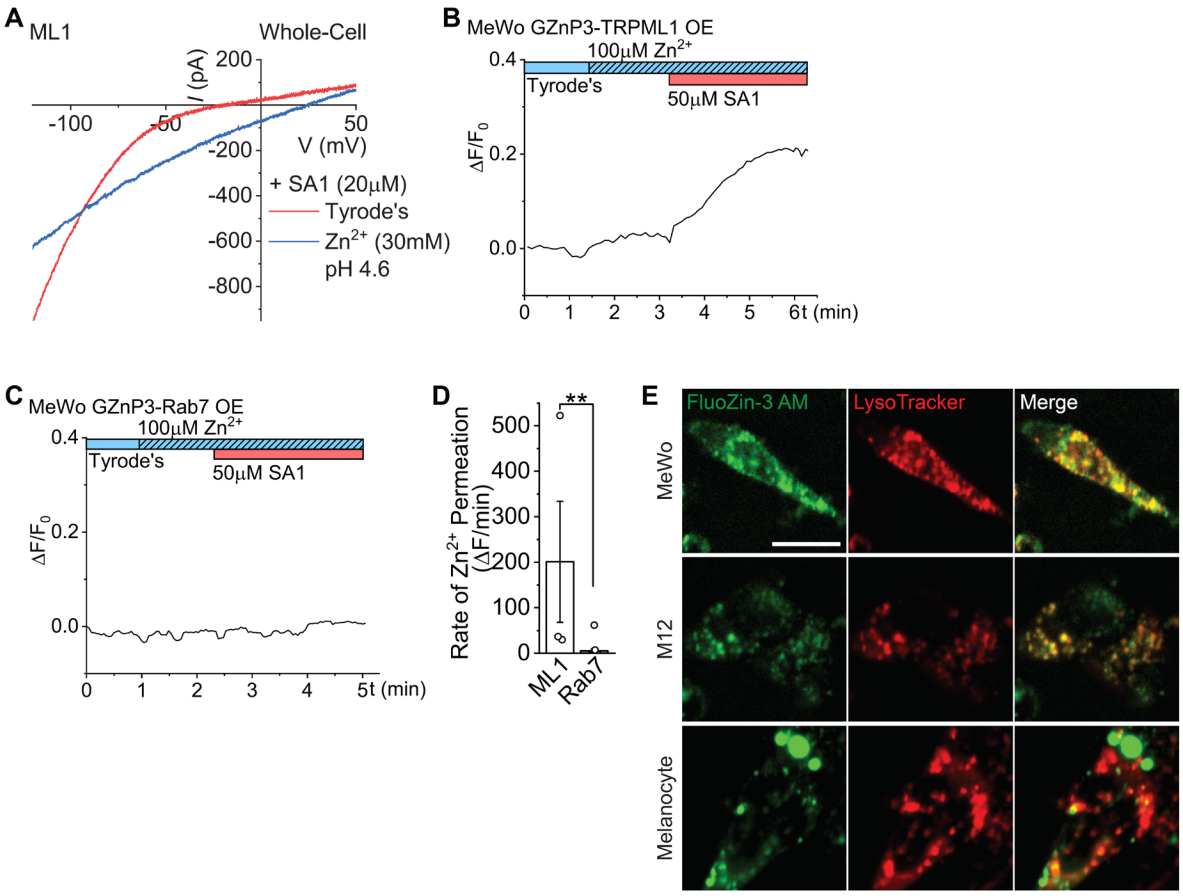

Figure 3.7 Zn^{2+} release from Lysosomes through TRPML1.
(A) Whole-cell patch clamp of EGFP-ML1 overexpressing HEK293 cells. ML1-mediated Zn^{2+} currents were recorded in high Zn^{2+} (30mM) external solution along with ML1 agonist SA1 (20μM). Currents were characterized with a ramp voltage protocol from -120 to +50 mV. (B) SA1-induced cytosolic Zn^{2+} increase, measured with GZnP3 imaging, in MeWo cells overexpressing GZnP3-ML1. (C) GZnP3 imaging in MeWo cells overexpressing GZnP3-Rab7. (D) Analysis of B and C. (D) Live spinning-disk confocal imaging of MeWo (upper penal), M12 (middle panel) and melanocyte (lower panel) cells loaded with FluoZin-3 AM (left penal) and LysoTracker (middle panel). Merged images (right panel) are for indication of colocalization. Scale bar: 20μm.

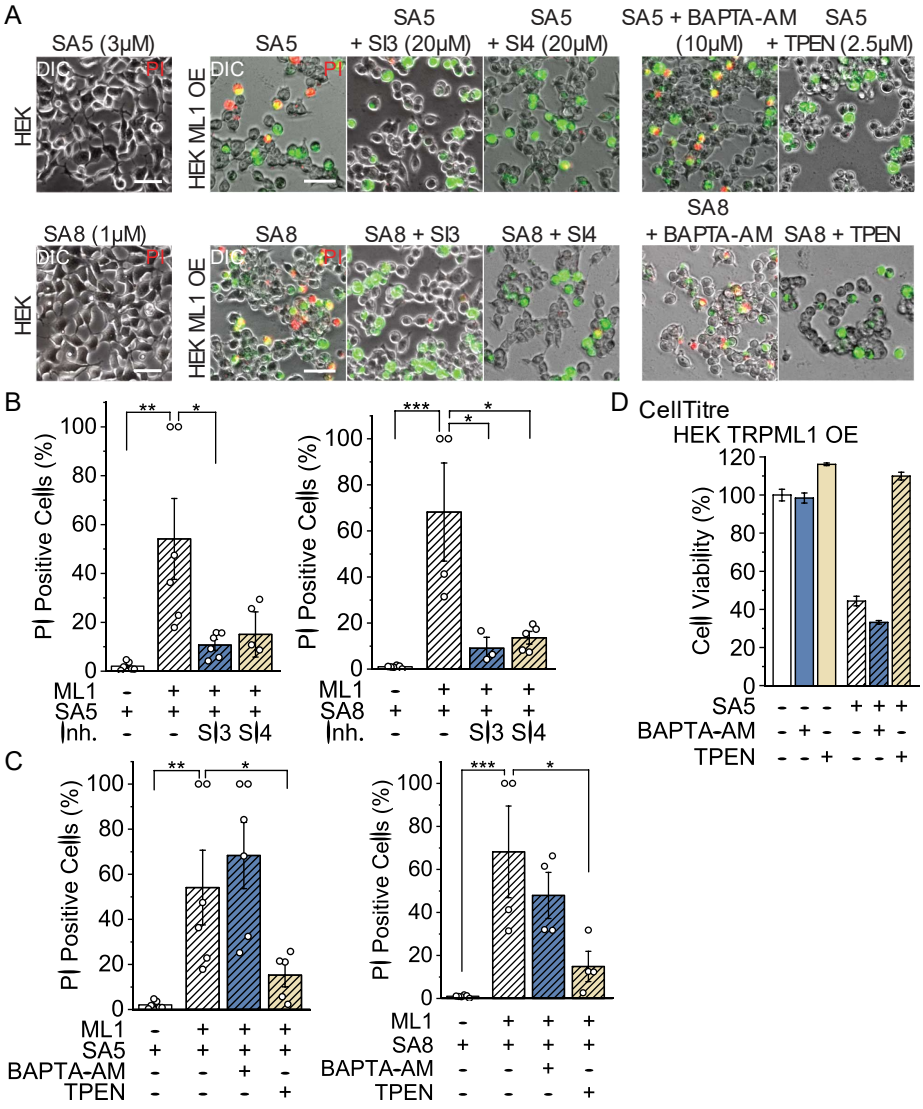

Figure 3.8 ML1 channel activity is sufficient to induce selective cytotoxic effects on metastatic melanoma cells.

(A) Typical PI staining images of control HEK293 cells (left) and HEK293 cells overexpressing EGFP-ML1 (middle left) under 3μM SA5 or 1μM SA8 treatment, HEK293 cells overexpressing EGFP-ML1 treated with SA5/SA8 along with ML-SIs, and SA5/SA8 along with BAPTA-AM or TPEN (right) for 6h. Cells were pretreated with BAPTA-AM and TPEN for 30min before SA5 application. Scale bar: 50μm. (B and C) Analysis of the percentage of PI positive HEK293 cells with or without ML1 overexpression, and post drug application in A. (D) CellTiter cell viability analysis of ML1 overexpressing HEK293 under 3μM SA5, and SA5 with 10μM BAPTA-AM or 2.5μM TPEN treatment for 6h.

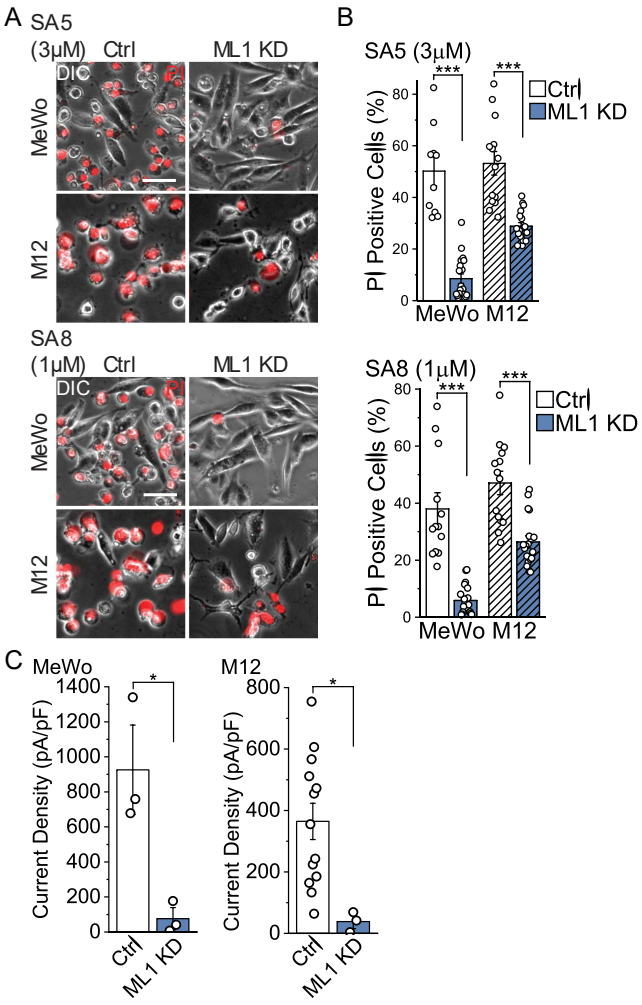

Figure 3.9 ML1 channel activity is necessary to induce selective cytotoxic effects on metastatic melanoma cells.

(A) Typical PI staining images of MeWo (upper panel) and M12 (lower panel) cells with vehicle (left panel) or ML1 shRNA (right panel) transfection under 3μM SA5 or 1μM SA8 treatment. MeWo cells were treated for 6h and M12 cells were treated for 3h. Scale bar: 50μm. (B) Analysis of the percentage of PI positive cells post SA5 application in control versus ML1 KD cells in A. (C) Analysis of whole-lysosomal ML1 current density of MeWo, ML1 KD MeWo, M12, and ML1 KD M12 cells.

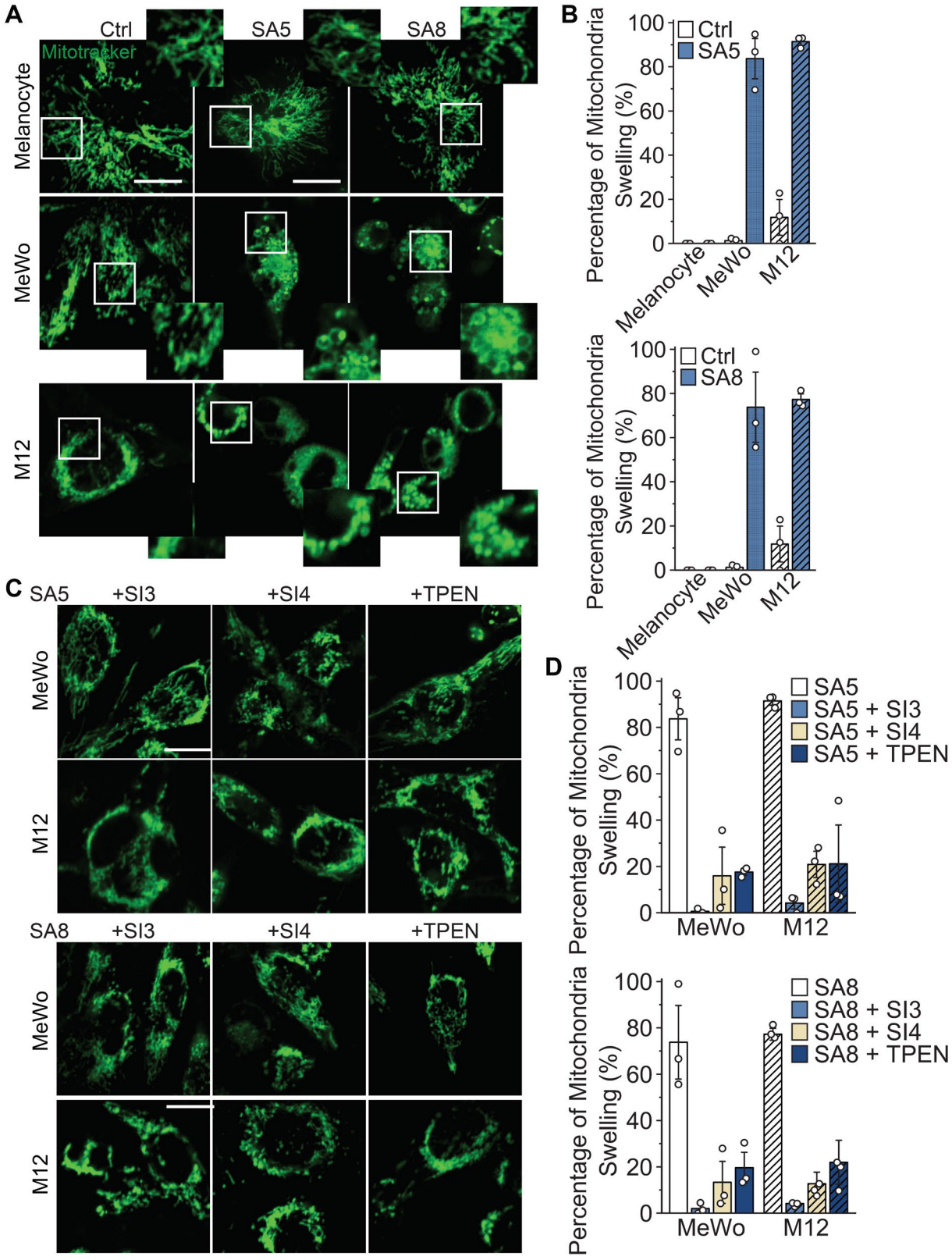
A
Ctrl
SA5
SA8
Mitotracker
Melanocyte
MeWo
M12
B
Percentage of Mitochondria Swelling (%)
Ctrl
SA5
SA8
Melanocyte
MeWo
M12
C
SA5
+SI3
+SI4
+TPEN
SA8
D
SA5 + SI3
SA5 + SI4
SA5 + TPEN
SA8 + SI3
SA8 + SI4
SA8 + TPEN

Figure 3.10 Activation of ML1 channel activity induces mitochondrial swelling in metastatic melanoma cells.
(A) Live imaging of Melanocyte (upper penal), MeWo (middle panel) and M12 (lower panel) cells loaded with MitoTracker under DMSO (left panel), 3μM SA5 (middle panel), or 1μM SA8 (right panel) treatment for 1h. Scale bar: 20μm. (B) Analysis of percentage of cells with swelling mitochondria in A. (C) Live imaging of MeWo (upper penal) and M12 (lower panel) cells loaded with MitoTracker under 3μM SA5 or 1μM SA8 and inhibitor (20μM SI3, 10μM SI4, and 2.5μM TPEN) treatment for 1h. Scale bar: 20μm. (D) Analysis of percentage of cells with swelling mitochondria in C.

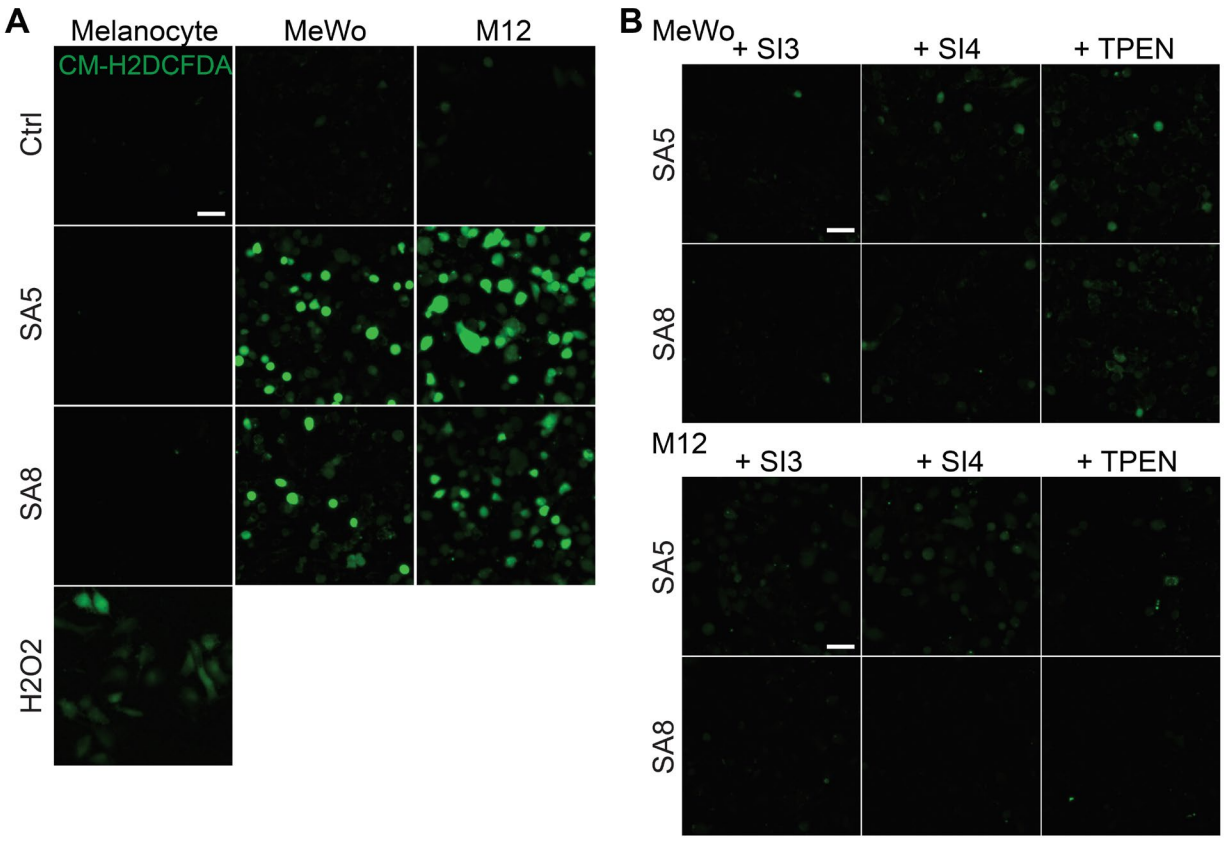

Figure 3.11 Activation of ML1 channel activity induces ROS production in metastatic melanoma cells.
(A) Effect of SA5 and SA8 on cytosolic ROS level of MeWo and M12 cells measured by CM-H2DCFDA (green) imaging. Scale bar: 50μm. (B) Effect of SI3, SI4, and TPEN on cytosolic ROS level of MeWo and M12 cells along with SA5 or SA8 application measured by CM-H2DCFDA (green) imaging. Scale bar: 50μm.

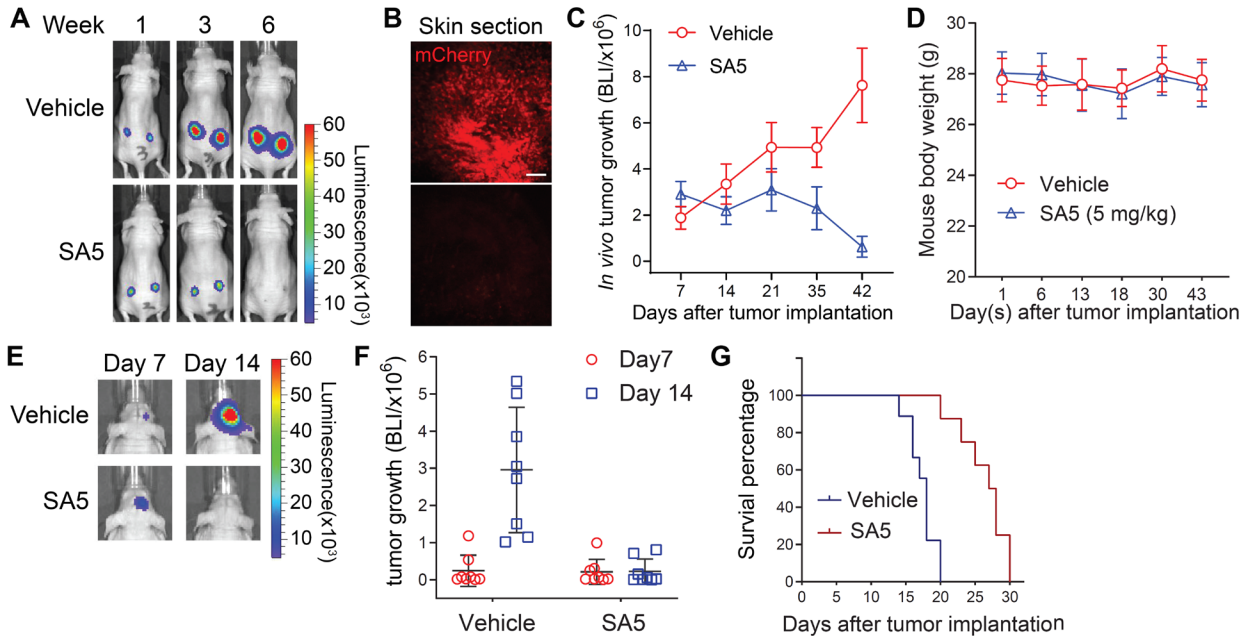

Figure 3.12 The effects of ML-SA5 i.p. injection on subcutaneous tumor growth *in vivo*. (A) Representative BLI imaging of subcutaneous MeWo tumor bearing mice that received daily i.p. injection of ML-SA5 at a dose of 5mg/kg. (B) mCherry fluorescence of tumor skin sections from vehicle- and SA5-treated mice. Scale bar, 100μm. (C) Time-dependent effects of SA5 treatment on tumor progression. (D) The effect of daily ML-SA5 IP injection on mice body weight. (E) Representative BLI imaging of intracranial M12 tumor bearing mice that received daily ICA injection of SA8 at a dose of 1mg/kg. (F) Effects of ML-SA8 treatment on tumor growth at day 7 and day 14. (G) Time-dependent survival rate of vehicle versus SA8 injected M12 tumor bearing mice.

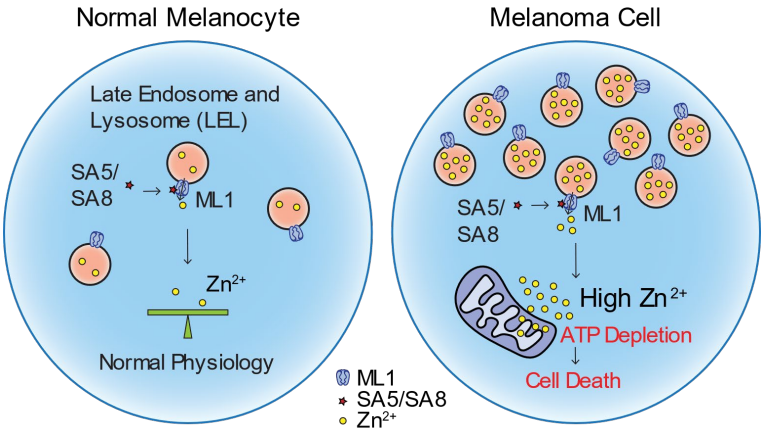

Figure 3.13 ML1 hyperactivity induces metastatic melanoma cell death through Zn^{2+}-dependent cell death pathways.
In normal melanocytes, lysosomes serve as the less predominant intracellular Zn^{2+} stores. Upon activation of ML1 by agonists, few Zn^{2+} ions are released and will not disrupt cellular physiology. Metastatic melanoma cells exhibit elevated lysosome biogenesis and ML1 expression. Lysosomes also serve as the predominant Zn^{2+} store in this case. Therefore, activation of ML1 lead to a flush of Zn^{2+} into the cytosol to cause disruption of mitochondrial function and finally cell death.

CHAPTER IV

Membrane Contact Sites Between Lysosomes and Endoplasmic Reticulum Refills Lysosomal Ca^{2+} Stores

Abstract

Recent imaging studies of intracellular Ca^{2+} dynamics suggest that Ca^{2+} exchange may occur between the intracellular stores of different types of organelles at specific membrane contact sites (MCSs). The endoplasmic reticulum (ER), the largest intracellular Ca^{2+} store, often serves as the donor at these sites. We used super resolution imaging techniques to show that the number of MCSs between lysosomes and the ER increases significantly when Ca^{2+} is released from the lysosome lumen and identified the protein VPS13D as essential for maintaining the Ca^{2+} release-induced ER-lysosome MCSs. Knockdown of VPS13D not only disrupted ER-lysosome MCS formation, but also greatly decreased lysosome Ca^{2+} refilling. Treatment with W-7, which inhibits a broad spectrum of calmodulin-like proteins completely abolished lysosome Ca^{2+} refilling. The target of W-7 may be the EF-hand containing protein CETN3 as its yeast homolog is known to bind and activate the yeast homolog of VPS13D, and knockdown of CETN3 showed significantly reduced lysosome Ca^{2+} refilling. These data suggest a model in which a CTEN3 dependent cytosolic Ca2+ sensing mechanism responds to lysosome Ca2+ store depletion, recruiting VPS13D onto the lysosome membrane, triggering the formation of ER-lysosome MCSs that allow Ca2+ transfer into the lysosomes.

Introduction

Ca^{2+}, as a common second messenger in cells, signals extensive aspects of cellular life in a spatially and temporally regulated manner (Berridge, 2012; Clapham, 2007). A transient change in $[Ca^{2+}]_{Cyt}$, locally or globally, mediates Ca^{2+} signaling, with the extracellular environment or intracellular Ca^{2+} stores providing Ca^{2+} to the cytosol. Under resting conditions, cytosolic Ca^{2+} concentration ($[Ca^{2+}]_{Cyt}$) is low (~100nM) (Clapham, 2007). The concentration of Ca^{2+} is more than three thousand times higher in the extracellular environment (~2mM) and in the lumen of organelles, such as the ER (0.3-0.7mM) (Berridge et al., 2000). Membrane-bound organelles interconnected and continuous in their lumens provide a large storage capacity, serving as intracellular Ca^{2+} stores. Well studied Ca^{2+} storage organelles include the ER, the largest intracellular Ca^{2+} storage site in the cell, the Golgi apparatus and mitochondria (Phillips and Voeltz, 2016; Pizzo et al., 2011). Intracellular vesicles are also Ca^{2+} store organelles, but their roles are much less understood. With the recent development of organelle-targeted genetically-encoded Ca^{2+} indicators (GECIs) (Dong et al., 2008; Morgan et al., 2015; Shen et al., 2012), and the identification of the membrane Ca^{2+} release channel TRPML1 (Dong et al., 2008), lysosomes are emerging as a new Ca^{2+} signaling center for example regulating mTOR activation and TFEB signal transduction (Medina et al., 2015). Calibration experiments employing lysosome-targeted, pH-corrected luminal Ca^{2+} indicators (e.g., Fura-Dextran dyes) have indicated that the Ca^{2+} concentration in the lysosome lumen ($[Ca^{2+}]_{Ly}$) is about 0.5 mM, comparable to $[Ca^{2+}]_{ER}$ (Christensen et al., 2002; Lloyd-Evans et al., 2008). This lysosomal Ca^{2+} store plays a key role in various aspects of lysosomal signaling transduction as well as lysosomal physiology, including lysosomal membrane trafficking and vesicular movements (Xu and Ren, 2015). Therefore, the establishment, maintenance, and refilling of the Ca^{2+} store is of biological significance.

The initial filling and the refilling of lysosomal Ca^{2+} stores are poorly understood. One hypothesis proposes that a Ca^{2+}/H^{+} exchanger (CAX) may drive pH-dependent Ca^{2+} uptake into lysosomes (Christensen et al., 2002; Morgan et al., 2011). Using both cytosolic and luminal Ca^{2+} dyes, researchers have shown that manipulations that cause lysosomal pH dissipation, such as V-ATPase inhibition, lead to lysosomal Ca^{2+} release (Christensen et al., 2002; Lloyd-Evans et al., 2008; Shen et al., 2012), while restoration of the acidic luminal pH is accompanied by Ca^{2+} store replenishment (Christensen et al., 2002). However, such observations might be secondary, as lysosomal pH elevation is also known to affect $[Ca^{2+}]_{Ly}$ or its measurement via affecting the chromophore fluorescence and Ca^{2+}-binding affinity of the luminal Ca^{2+} dyes (Dickson et al., 2012; Morgan et al., 2015). In contrast, a more recent study found that dissipation of the proton gradient in the lysosome (e.g., by V-ATPase inhibitors) had little impact on basal Ca^{2+} stores or their refilling. Instead, depletion of ER Ca^{2+} stores by SERCA inhibitors was shown to abolish lysosomal Ca^{2+} refilling (Garrity et al., 2016). Furthermore, inhibition of IP3Rs, but not RyRs, on the ER membrane blocked refilling (Garrity et al., 2016). Another independent study monitoring lysosomal luminal Ca^{2+} also found that lysosomal Ca^{2+} was not refilled if SERCA activity was inhibited (Ronco et al., 2015). A more recent study showed that inhibition of lysosomal V-ATPase potentiates carbachol (CCh) induced cytosolic Ca^{2+} signals evoked by IP3Rs in HEK cells (Atakpa et al., 2018). Using lysosome membrane attached Ca^{2+} sensors, they argued that IP3Rs deliver Ca^{2+} directly to lysosomes (Atakpa et al., 2018). Taken together, these studies employing both juxta- and intra-lysosomal Ca^{2+} sensors/dyes suggest that lysosome stores are refilled with Ca^{2+} from the ER.

The identity of the lysosomal Ca^{2+} uptake transporter/channel, related regulatory proteins and mechanisms are unknown. ER stores are refilled through sustained Ca^{2+} influx at ER-plasma

membrane (PM) MCSs (Saheki and De Camilli, 2017). ER stores are known to participate in the refilling of mitochondrial Ca^{2+} via ER-mitochondria MCS consisting of the ER Ca^{2+} release channel IP3R, the mitochondria Ca^{2+} uptake channel VDAC1, and the tethering protein Grp75 (Wu et al., 2018). Given that several publications suggest the participation of ER IP3R in lysosomal Ca^{2+} refilling, it is reasonable to hypothesize that lysosome Ca^{2+} is refilled through a similar mechanism as mitochondrial Ca^{2+}.

Methods

Molecular biology

The genetically-encoded Ca^{2+} indicator GCaMP7 was fused directly to the N-terminus of ML1 (GCaMP7-ML1) as described previously. The VPS13D-I-GFP construct was a kind gift from Dr. Eric Baehrecke (University of Massachusetts Medical School). The Sec61β-GFP and Sec61β-BFP plasmids were obtained from Addgene. Lamp1-mCherry was made by fusing mCherry with the C terminus of Lamp1. The VPS13D and VPS13C constructs were purchased from Sigma Aldrich (cat. SHCLNG-NM_015378 and cat. SHCLNG-NM_017684); RFP labeled VPS13D, VPS13C, and CETN3 shRNA construct were bought from Dharmacon (cat. RHS4696-200772749, cat. RHS4696-201895728, and cat. RHS4696-201895728).

Generation of VPS13D knockout cells

VPS13D knockout (KO) HEK-GCaMP7-ML1 cells were engineered by the Crispr-Cas9 system. The designed guide RNA (gRNA) targeting exon 16 (5'-CATACAGCATCTCAAAAAC G-3') was cloned into pSpCas9 (BB)-2A-Puro (PX459) V2.0 vector (Addgene, 62988) and transfected into target cells using Lipofectamine 2000 (Invitrogen). After puromycin (Millipore

Sigma, P8833) selection for 48 hours, the remaining cells were trypsin-digested and limiting diluted into 96-well plates to obtain monoclonal cell populations. The frameshift in KO cells were confirmed with PCR amplification and Sanger sequencing. Singles clones that remained with a heterozygous genome sequence were used as controls.

Mammalian cell culture

Immortalized cell lines (HEK293 and Cos-1) were purchased from ATCC and cultured following standard culture protocols. IP3R Null cells were purchased from Kerafast (EUR030). HEK 293 cells stably expressing GCaMP7-ML1 (HEK-GCaMP7-ML1 cells) were generated using the Flip-In T-Rex 293 cell line (Invitrogen). All these cells were authenticated for mycoplasma contamination. All cells were cultured in a 37°C incubator with 5% CO_2. Tet-On HEK293 cells stably expressing GCaMP7-ML1 (HEK-GCaMP7-ML1 cells), Cos-1 cells, and IP3R Null cells were cultured in DMEM F12 (Invitrogen) supplemented with 10% (vol/vol) FBS or Tet-free FBS. HEK-GCaMP3-ML1 cells, and Cos-1 cells were transfected using Lipofectamine 2000 (Invitrogen). All cells were used for experiments 24-48hr after transfection. We noted that lysosomal Ca^{2+} store refilling was often compromised in high-passage or poorly-maintained cell cultures. New cells were used after we saw a reduction in lysosomal Ca^{2+} refilling under control conditions.

Time Lapse imaging of lysosome-ER contact sites

Live imaging of cells in which the ER and lysosome membrane were labeled was performed at 37˚C on a heated and humidified stage using a Leica SP8 inverted STED microscope (Leica Microsystems) with 100x objective (numerical aperture 1.51), which provides spatial

resolution down to 30 nm. The duration of individual time-lapse imaging sequences was typically 5min with images acquired every 3s. Images were de-convolved with Huygens Professional Software (Scientific Volume Imaging), and Fuji (Image J) and CellProfiler software were used for image analysis.

The colocalization index was obtained using previously established colocalization analysis pipeline with CellProfiler (McQuin et al., 2018). Each image was masked to outline the individual lysosomes or ER tubules, and calculation of the number of lysosomes overlapping with the ER was run. The lysosomes and the ER were considered to be in apposition when the two signals overlap by even down to one single pixel.

For the dynamic analysis, the duration of an interaction between a lysosome and the ER was calculated based on the time difference between the first and last frames showing the interaction. Two factors affected the precision of the estimation. First, the samples were taken every 3 seconds, therefore the true duration could have been underestimated by as much as 6 seconds. Second, some vesicles were already in contact at the first frame sampled, and others still in contact at the last frame sampled, thus, the true contact time was very likely longer than the imaging sequence revealed. Because the difference between the duration of interactions in wild type and treated cells differed by more than 10-fold, this level of uncertainty would have no effect on the conclusions drawn from this analysis.

GCaMP7-ML1 Ca^{2+} imaging

GCaMP7-ML1 expression was induced in Tet-On HEK-GCaMP7-ML1 cells 12-24h prior to experiments using 0.01µg/mL doxycycline. GCaMP7-ML1 fluorescence was monitored at an excitation wavelength of 470 nm (F470) using a EasyRatio Pro system (PTI). Cells were bathed

in Tyrode's solution at room temperature containing 145mM NaCl, 5mM KCl, 2mM $CaCl_2$, 1mM $MgCl_2$, 10mM Glucose, and 20mM Hepes (pH 7.4). Lysosomal Ca^{2+} release was measured with bath application of the ML1 channel agonist ML-SA1 (20 μM, ~1min) in a zero Ca^{2+} solution containing 145mM NaCl, 5mM KCl, 3mM $MgCl_2$, 10mM glucose, 1mM EGTA, and 20mM HEPES (pH 7.4). Ca^{2+} concentration in the nominally free Ca^{2+} solution is estimated to be 1-10μM. With 1 mM EGTA, the free Ca^{2+} concentration is estimated to be <10nM in the zero Ca^{2+} solution based on the Maxchelator software (http://maxchelator.stanford.edu/). ML-SA1 was then washed out for ~1 min followed by a 5-min refilling phase of Ca^{2+} using Tyrode's bath solution. Repeated applications of ML-SA1 were used to access the extent of lysosomal Ca^{2+} refilling. Experiments were carried out 6-12hr after plating at room temperature. Because baseline drift was usually present during the course of the experiment (up to 30 min), we typically set F_0 based on the value that was closest to the lowest point. Except for Figure 4.1, individual traces in the figures represent the average from at least 30-40 cells in one single experiment, and the respective data analysis was calculated from at least 3 independent repeats. The data were normalized to the ionomycin maximum.

Fura-2 Ca^{2+} imaging

Cells were loaded with Fura-2, AM (3μM) and Plurionic-F127 (3μM) in the culture medium at 37°C for 30 min. Fluorescence was recorded using the EasyRatio Pro system (PTI) at two different wavelengths (340 and 380nm) and the ratio (F_{340}/F_{380}) was used to calculate changes in intracellular [Ca^{2+}]. All experiments were carried out at room temperature 6 to 12 hr after plating. An individual trace was averaged from at least 30-40 cells in one single experiment, and the respective data analysis was calculated from at least 3 independent repeats.

Oregon green 488 BAPTA-1 dextran imaging

Cells were loaded by placing Oregon Green 488 BAPTA-1 dextran (100μg/ml) in the culture medium at 37°C for 8-12 hr (pulse), and then chased for additional 12-16 hr in medium without the indicator to allow endocytosis and trafficking to the lysosomes. Fluorescence imaging was performed at 37°C.

Reagents

Reagents were dissolved and stored in DMSO or water depending on their water solubility, and then diluted in Tyrode's and 0 Ca2+ solutions for experiments. 2-APB (D9754), ATP (A8937), Doxycycline (D9891) were from Sigma; GPN (CAS 21438-66-4) was from Santa Cruz; Fura-2 (F1221), Plurionic F-127 (P3000MP) were from Invitrogen; ML-SA1 was from Chembridge; Oregon Green 488 BAPTA-1 dextran (O6798) was from Invitrogen. ML-SI compounds were identified from a Ca^{2+}-imaging-based highthroughput screening conducted at NIH/NCATS Chemical Genomics Center (NCGC; https://pubchem.ncbi.nlm.nih.gov/bioassay/624414#section=Top). ML-SI compounds are available upon request.

Statistical analysis

Data are presented as mean ± SEM. All statistical analyses were conducted using Origin. Paired t-tests were used to compare the average of three or more experiments between treated and untreated conditions. A value of $p<0.05$ was considered statistically significant.

Results

Physiological properties of the lysosome Ca^{2+} refilling process

We assessed lysosomal Ca^{2+} stores using a tool that detected juxtra-lysosomal Ca^{2+} by using the specific, membrane-permeable synthetic TRPML1 agonist ML-SA1 and HEK293 cell lines stably-expressing GCaMP7-ML1 (HEK-GCaMP7-ML1 cells) (Figure 4.1A). The genetically coded single-wavelength Ca^{2+} indicator GCaMP7 was engineered to the cytoplasmic amino terminus of TRPML1. With its low dissociation constant (<102nM) (Muto et al., 2013; Muto et al., 2011), this sensor produces a local response at the locations where there is Ca^{2+} efflux through open lysosomal TRPML1 channels.

The assay used to assess refilling after lysosomal Ca^{2+} store depletion is shown schematically and with typical data for wild type cells in Figure 4.1. Under basal conditions, the Ca^{2+} concentration in the lysosome lumen is high. Activation of the lysosomal Ca^{2+} channel TRPML1 through bath application of ML-SA1 in a 'zero' (free $[Ca^{2+}]$ <10 nM) Ca^{2+} external solution produced lysosomal Ca^{2+} release measured by an increase in GCaMP7 fluorescence (F_{480}). Lysosomal Ca^{2+} stores were largely depleted after the release of the initial, 'naïve' Ca^{2+} store upon first application of ML-SA1, and it required 5min of Tyrode's perfusion between consecutive applications for maximal second response to ML-SA1 (Garrity et al., 2016). All ML-SA1 responses were measured in the 'zero' Ca^{2+} external solution to make sure that the ML-SA1-induced Ca^{2+} responses are exclusively intracellular and lysosomal. Refilling was assessed by comparing the amplitude of the 1st response to the 2nd and 3rd responses.

The analytical process began by obtaining GCaMP7 fluorescence signals for every cell in the field (Figure 4.1B). The traces first had their baseline intensity subtracted, then their amplitude was normalized to the maximal response produced by extracellular application of ~5μM

ionomycin when 2 mM extracellular Ca^{2+} was present (Figure 4.1C) and then all traces were averaged (Figure 4.1D). Finally, the average peak response to each ML-SA1 (or ATP) application was calculated. For wild type cells, the second and third rapid lysosomal Ca^{2+} responses to ML-SA1 were significantly larger than the first basal naïve response (Figure 4.1E).

The published conclusion that the refilling process is extracellular Ca^{2+} dependent, was confirmed by substituting Ca^{2+} with Ba^{2+} in the external Tyrode's perfusion solution (Figure 4.2A-F). GCaMP7 imaging as well as Fura-2-based imaging was used because it has been shown that Ca^{2+} sensors structurally similar to GCaMP7 do not bind Ba^{2+} (Viviano et al., 2016) while Fura-2 responds to both Ca^{2+} and Ba^{2+} (Condrescu et al., 1997). As predicted, adding either Ca^{2+} or Ba^{2+}-containing Tyrode's solution produced an increase in the GCaMP7 and the Fura-2 signal (Figure 4.2A, 4.2B, 4.2D, 4,2E), reflecting the entry of these cations into the cytosol through plasma membrane proteins. In contrast, the second responses to ML-SA1 were significantly increased comparing with the first when Ca^{2+} was present between pulses, but refilling was nearly completely abolished when Ba^{2+} was present (Figure 4.2A-F).

One potential explanation for the greatly attenuated second responses when Ba^{2+}-containing Tyrode's was present could be that a failure of ER Ca^{2+} level maintenance resulted in the lysosomal Ca^{2+} refilling defect. To test this idea, ER Ca^{2+} release was stimulated repetitively by ATP (which acts via P2Y receptors, G proteins and IP3 production) with the Ba^{2+}-containing "Tyrode's" solution present in between each application. Eventually, a loss of ATP responsiveness was seen, indicating ER depletion of Ca^{2+} (Figure 4.2D). However, the ATP-induced ER Ca^{2+} transients remained substantial for the first few applications even though no external Ca^{2+} was present (Figure 4.2D), suggesting that total loss of ER Ca^{2+} is not the primary cause of the inability of lysosomes to refill when Ca^{2+} cannot enter the cell from the extracellular space. One alternative

hypothesis is that plasma membrane proteins may participate in forming MCSs involving three organelles: ER, lysosome, and PM. Orai as well as other plasma membrane Ca^{2+} channels or transporters are likely involved.

The finding that nigericin, a K^+/H^+ antiporter inhibitor, stops lysosomal refilling is suggestive of a role for K^+ in store maintenance or refilling (Garrity et al., 2016). Consistent with this idea, inhibiting the Ca^{2+} activated K^+ channel BK with its specific antagonist paxilline significantly reduced lysosomal Ca^{2+} refilling (Figures 4.2E, 4.2F). However, since both plasma membrane and lysosomal BK channels would be expected to be affected by this treatment, further tests using membrane impermeable BK inhibitors are required to differentiate the contribution of lysosomal versus PM BK. Nevertheless, an interesting hypothesis is that regulation of lysosomal $\Delta\psi$ may be required for Ca^{2+} store refilling of lysosomes. It was reported recently that membrane potential can affect phosphoinositide dynamics (Zhou et al., 2015); and phosphoinositides are known to influence the interaction of lysosomes with other organelles, including peroxisomes and the ER (Chu et al., 2015; Raiborg et al., 2015). Hence, the lysosome-localized BK channels may function as a Ca^{2+} effector in triggering lysosomal Ca^{2+} refilling.

ER refills lysosomal Ca^{2+} store through IP3R-containing membrane contact sites

Considerable evidence suggests that lysosomes refill Ca^{2+} using the ER Ca^{2+} store. Blocking the ER SERCA pump with Thapsigargin (TG) or cyclopiazonic acid completely inhibited lysosome Ca^{2+} refilling (Garrity et al., 2016). Furthermore, the IP3R specific antagonist Xestospongin-C greatly diminished refilling, suggesting the participation of IP3R in the process (Garrity et al., 2016). We confirmed the role of ER IP3R in lysosome Ca^{2+} store refilling by using IP3R1, 2, 3 triple knockout (TKO) cells. IP3R Null HEK-293 cells overexpressing GCaMP7-ML1

showed a normal or larger than normal naïve (first) lysosome Ca^{2+} response compared to WT controls, but refilling was nearly abolished (Figure 4.3A-D). This indicates that prompt lysosome Ca^{2+} refilling upon depletion is probably derived from ER Ca^{2+} released through IP3Rs, However, some other pathways must contribute to the naive lysosome Ca^{2+} store. Since it has been reported that TG application did not directly affect the naive lysosome Ca^{2+} store (Garrity et al., 2016), these results suggest that some lysosomal Ca^{2+} comes either from other intracellular compartments or from the extracellular space.

Live imaging at high spatial and temporal resolutions was used to visualize the movement of lysosomes (vesicles positive for LAMP1 labelled with mCherry) relative to the ER (regions expressing Sec61β-GFP, which is present in both rough and smooth ER domains) (Lynes and Simmen, 2011; Shibata et al., 2008). While some LAMP1-positive vesicles moved substantial distances without overlapping with ER throughout the 5-min imaging sequence, most vesicles in untreated wild type cells remained in place or moved along ER tubules for several imaging frames before eventually detaching from the ER (Figure 4.4A; Ctrl). We quantified these images by two metrics, the proportion of vesicles in apparent apposition to the ER in each frame and the length of time each vesicle remained in contact at a specific point on the ER (Figure 4.4D, 4.4E, see Methods for criteria used to estimate these parameters). As compared to untreated wild type cells, we found that acute depletion of lysosomal Ca^{2+} content by application of GPN or ML-SA1 induced a dramatic increase in the proportion of lysosomes interacting with ER tubules (from 69.8±1.0% to 89.2±0.6% under GPN treatment and 89.7±0.7% in application of ML-SA5) (Figure 4.4A, 4.4B, 4.4D), and the average interaction duration of individual lysosomes with the ER increased from 7.0±0.6s to 132.7±12.2s with GPN and 71.2±12.8s with ML-SA5 treatment (Figure 4.4A, 4.4B, 4.4E). The substantial increase in static lysosomes with these two treatments suggests

that lysosome Ca^{2+} release triggers the formation of more stable lysosome-ER membrane contact sites. In support of this idea, the number of lysosomes interacting with ER tubules and the duration of the contacts did not differ when acute application of the ML1 antagonist ML-SI4, or pretreatment of the V-ATPase inhibitor Baf-A1, and non-specific IP3R inhibitor 2-APB was performed. This suggests that ER-lysosome MCS formation is independent of ML1 activity, lysosomal pH, and IP3R activity (Figure 4.4A, 4.4C-E).

VPS13D is required for ER-lysosome Ca^{2+} exchange MCSs formation

To identify molecules required for lysosomal Ca^{2+} refilling, we screened potential lysosomal membrane proteins (both integral and membrane associated) with unknown functions using the standard calcium imaging assay for refilling. This screen had the potential to identify: i. the lysosomal Ca^{2+} uptake transporter/channel; ii. ER-lysosome membrane contact tethering proteins. One-time experiments of shRNA knockdowns (KDs) were first analyzed and Crispr/Cas9 KOs were generated and further tested to rule out false-positives.

Among the screened 41 candidates, VPS13D was the only positive hit. KD of VPS13D to ~40% of normal mRNA levels (determined by qPCR) inhibited both the naïve lysosome Ca^{2+} store and refilling by ~90% (Figure 4.5A-E). VPS13D belongs to the VPS13 protein family which has been implicated in other organellar MCSs (Gao and Yang, 2018). The effect was specific, because shRNA KD of VPS13C, which is presumed to be localized at ER-endosome/lysosome membrane contact sites and is a member of the same protein family as VPS13D (Kumar et al., 2018), had no effect on lysosome Ca^{2+} refilling (Figure 4.5F, 4.5G). The ER Ca^{2+} store was unaffected in VPS13D KD cells (Figure 4.5H). This effect was confirmed by KD of VPS13D utilizing an independent shRNA (shRNA #2), the vector of which expressed a TurboRFP fluorescent reporter

that allowed visual tracking of shRNA expression. RFP positive VPS13D KD cells showed impaired Ca^{2+} refilling as compared with internal non-transfected control cells as well as the VPS13C KD cells (Figure 4.5I-K). To further confirm that lysosome Ca^{2+} refilling was depleted under VPS13D KD, Oregon Green 488 BAPTA-1 Dextran was used to indicate the concentration of luminal lysosomal Ca^{2+}. In RFP-positive VPS13D KD COS-1 cells, lysosomal luminal Ca^{2+} indicated by Oregon Green fluorescence intensity was significantly lower (~75% of control) than non-transfected controls (Figure 4.5L, 4.5M). The sensitivity of Oregon Green 488 BAPTA-1 Dextran towards lysosomal luminal Ca^{2+} concentration was confirmed by application of GPN, which depleted the Oregon Green fluorescence (Figure 4.5N). Finally, generation of two independent lines of Crispr/Cas9-based VPS13D KO HEK293 cells stabling expressing GCaMP7-ML1 (Figure 4.6A) confirmed the depletion of lysosomal Ca^{2+} refilling (Figure 4.6C-E), while the heterozygous control cell line (Figure 4.6B, 6E) remained unaffected.

Approximately 65% of the VPS13D KD cells showed enlarged lysosomes, many of which accumulated in the perinuclear region (Figure 4.7A, 4.7B). Moreover, lysosomal trafficking was nearly completely ablated in KD cells (Figure 4.7C, 4.7D). Lysosomal Ca^{2+} homeostasis has been implicated in lysosomal storage-related diseases (Kiselyov et al., 2010). Therefore, the Ca^{2+} storage and refilling defects in VPD13D KD cells are likely the primary causes of the abovementioned lysosomal storage-like phenotypes.

VPS13D was found to be located to lysosomes in Drosophila (Anding et al., 2018) while no reports of the cellular localization in any vertebrate have been published. To further explore the role of VPS13D in lysosome Ca^{2+} refilling, we examined the location of the protein using imaging of a version of VPS13D tagged internally (in between exon 40 and 41) with GFP (VPS13D-I-GFP). In cells transiently transfected with VPS13D-I-GFP, imaging demonstrated labeling on

lysosomal membranes as well as expression on other non-early-endosomal-puncta (Figure 4.8A, 4.8C). The co-localization ratio of VPS13D and LAMP1 was significantly increased within 5min of acute application of GPN and ML-SA1 (Figure 4.8A, 4.8B), while 2-APB showed no effect on VPS13D-lysosome colocalization (Figure 4.8A, 4.8B), indicating that VPS13D localizes to lysosomes upon lysosomal Ca^{2+} depletion. KD of VPS13D prevented the increase of ER-lysosome MCS upon ML-SA5 application (Figure 4.8D, 4.8E), suggesting that VPS13D might be required for the formation/stabilization of lysosomal Ca^{2+}-induced ER-lysosome MCS.

A calmodulin-related Ca^{2+} sensor is required for lysosome Ca^{2+} refilling

To identify potential regulatory pathways controlling lysosomal Ca^{2+} refilling, a second screen for conditions disrupting lysosomal Ca^{2+} refilling tested specific inhibitors of several signaling pathways. We found that application of W-7, a pan calmodulin and calmodulin-like protein blocker that interacts with their target binding pockets (Osawa et al., 1998), completely abolished lysosome Ca^{2+} store and refilling, while other treatments such as nutrient starvation and blocking lysosome trafficking, were ineffective (Figure 4.9A; Table 2). Ca^{2+} imaging results showed that pretreatment with 50μM W-7 for 1h abolished ML-SA1-induced lysosomal Ca^{2+} release (Figure 4.9A, 9D), but not ATP induced ER Ca^{2+} release (Figure 4.9E). Fura-2 was used to rule out the possibility that W-7 inhibited GCaMP7 fluorescence. Compared with controls (Figure 4.9B), 50μM W-7 1h pretreatment eliminated the ML-SA1-induced Fura-2 fluorescence increase (Figure 4.9C). Furthermore, during the refilling phase, W-7 acute application along with Tyrode's perfusion transiently diminished the following ML-SA1-induced Ca^{2+} response (Figure 4.9F, 9G). Acute application of W-7 resulted in an increase in the proportion of lysosomes interacting with ER tubules, as well as the duration of the interactions (Figure 4.9H-J), thus

reducing lysosomal motility. Preliminary data showed that Ca^{2+} refilling in dominant negative calmodulin (mCherry-CaM1,2,3,4) expressing cells was not significantly different from the non-transfected WT controls (data not shown), suggesting that calmodulin may not be directly involved in the refilling process. Based on these results, a W-7 sensitive Ca^{2+} sensing mechanism participates in regulating lysosome Ca^{2+} store refilling. Therefore, a calmodulin-like protein is likely involved.

Table 2. Summary of regulations of physiological events on lysosomal Ca^{2+} store and refilling

Conditions		**Lysosomal Ca^{2+}**	
		Store	**Refilling**
mTOR Activity	Torin-1	Unaffected	Unaffected
	Rapamycin	Unaffected	Unaffected
	EBSS Starvation	Unaffected	Unaffected
Cholesterol Accumulation	U18666A	Unaffected	Unaffected
	NPC Mouse Fibroblasts	Unaffected	Unaffected
FYVE-domain-Containing Protein Inhibition	Wortmannin	Unaffected	Unaffected
Lysosomal Positioning	DynlC2-DN Overexpression	Unaffected	Unaffected
	KIF5B-DN	Unaffected	Unaffected
Ca^{2+} Sensing	**Calmodulin Inhibitors**	**Abolished**	**Abolished**
	CAMKII Inhibitor	Unaffected	Unaffected
	Calcineurin Inhibitors	Reduced	Reduced
Lysosome Trafficking	Microtubule Polymerization Inhibitor	Unaffected	Unaffected

VPS13p, the yeast homolog of the mammalian VPS13A, B, C, D family interacts with a Ca^{2+}-binding protein, cdc31p, in yeast membrane contact sites (De et al., 2017). CETN3, the human homolog of cdc31p, is a calmodulin-like Ca^{2+} binding protein with 4 EF-hands. Knockdown of CETN3 in HEK293 cells stably expressing GCaMP7-ML1 to ~30% of normal

mRNA levels significantly reduced the naïve lysosome Ca^{2+} store and refilling (Figure 4.9M, 9N). Therefore, CETN3 may function as a Ca^{2+} sensor in the refilling process, but a detailed mechanism for how it might act is still to be determined.

Discussion

Membrane contact sites provide physical platforms for material exchange between organelles via a direct, non-fusion mechanism. Although ER-lysosome MCSs are well documented, their functional significance for moving Ca^{2+} or other ions is not clear. In comparison, ample evidence supports the involvement of ER-PM and ER-mitochondrial MCSs in Ca^{2+} exchange (Wu et al., 2018). Generally speaking, the short (<30 nm) distance between the ER and lysosomal membranes in MCSs should enable ER-to-lysosome Ca^{2+} transport without causing global $[Ca^{2+}]_{Cyt}$ increases. This is supported by the structurally intimate localization of the ER and lysosomes at ER-lysosome MCSs (Phillips and Voeltz, 2016). Using pharmacological tools and genetic approaches to manipulate lysosomal Ca^{2+} release, and super-resolution imaging to visualize ER-lysosome interaction, we obtained results consistent with a model (Figure 4.10) in which lysosome luminal Ca^{2+} is refilled from the ER in a ER-lysosome MCSs-dependent manner, and that among the players in this process are the ER Ca^{2+} release channel IP3R, the lysosome membrane associated protein VPS13D, the putative Ca^{2+} sensor CETN3 and an unknown lysosomal Ca^{2+} uptake channel/transporter (referred to as $Ly_{Ca}C$ in the following text).

The role of VSP13D is supported by knockdown and knock out experiments. The observation that two independent shRNA KD lines and two KO lines showed the same defective phenotype while internal and VPS13C controls remained normal (Figure 4.5D-G, 4.5I-K) provides strong evidence that VPS13D is involved in lysosomal Ca^{2+} refilling. However, we were unable

to successfully rescue lysosomal Ca^{2+} refilling in VPS13D KO cells through overexpression of exogenous wild type VSP13D to reinforce our conclusions. One explanation for the failed attempt at VPS13D rescue was that it was due to the large size of the protein (489kDa), which resulted in an extremely low expression level. Alternatively, since the GFP is internal, rather than at the N or C terminal, even though it appeared to localize correctly, the VPS13D-I-GFP fusion protein may be dysfunctional in regulating Ca^{2+} refilling. This construct did rescue the mitochondrial morphological defects in HeLa cells (Anding et al., 2018), but different functional domains might be required for the distinct functions of VPS13D. While visualization of colocalization of VPS13D protein, ER tubule and lysosomal LAMP1 using STED imaging (Figure 4.8A, 4.8B) is not sufficient to prove the formation of functional MCSs, the observation that knockdown of VPS13D resulted in reduced colocalization of lysosomes to ER under ML-SA5 treatment (Figure 4.8E) serves as additional evidence that the recruitment of VPS13D to lysosomes promoted MCSs formation. To further confirm that VPS13D is critically involved in ER-lysosome MCSs, super resolution imaging showing VPS13D localized to ER-lysosome MCSs is required. IP3R could be used as a MCS marker on the ER side. Quantitative electron microscopy could be used to analyze the size and component of individual MCS, but unless serial reconstructions are made, the result is highly dependent on the cutting of the semithin sections, therefore is random and may not reflect the real situation. Also, membrane contacts can be hard to preserve at the EM level.

VPS13 protein family members in other organellar MCSs have been implicated in lipid transfer (Kumar et al., 2018). Our results showing that ablation of VPS13D resulted in lysosomal Ca^{2+} refilling defects suggest an additional role of VPS13D in Ca^{2+} channeling MCS. Though the possibility that VPS13D affects lysosomal Ca^{2+} refilling through lipid-involving pathways could not be ruled out, the observation that disrupting lysosomal cholesterol and phosphoinositide

compositions had no effect on its Ca^{2+} store and refilling (Table 2) suggests that lysosomal Ca^{2+} refilling may not be regulated by lipid-dependent mechanisms. Though VPS13D is associated with mitochondrial morphology defects and mitophagy, and knockdown of VPS13D lead to mitochondrial fragmentation and dysfunction, overexpression of VPS13D in Drosophila is predominantly colocalized with LAMP1 signals (Anding et al., 2018). Our confocal data also revealed that under normal conditions, the localization is punctate in a pattern that is unlikely to be mitochondrial (or only at membrane contact sites). However, VPS13D is not exclusively localized at ER-lysosome MCSs, but rather seems to translocate to ER-lysosome MCSs upon lysosomal Ca^{2+} depletion, suggesting additional functions of VPS13D other than ER-lysosome MCS formation.

An interesting and testable hypothesis is that lysosomal Ca^{2+} refilling is triggered directly by lysosomal Ca^{2+} release and involves Ca^{2+}-dependent regulation of ER-lysosome interactions. Indeed, universal inhibition of Ca^{2+} sensing calmodulin and calmodulin-like proteins with W-7 depleted lysosomal Ca^{2+} store and refilling. Furthermore, knockdown of the Ca^{2+} sensor CETN3 showed reduced refilling. In yeast, Vps13p, the only homolog of the VPS13 protein family in humans, functions in complex with cdc31p, a homolog of CETN3, to regulate transport from the trans-Golgi network (TGN) to the late endosome/prevacuolar compartment (PVC) and for TGN homotypic fusion. Cdc31p was detected in fractions from Vps13p purifications on calmodulin Sepharose. TGN–PVC transport and TGN homotypic fusion in a cdc31 mutant background were complemented by addition of purified Vps13p, while Vps13p purified from cdc31 mutant cells were defective for complementation. The presumptive Vps13p-Cdc31p complex eluted from calmodulin Sepharose actively enhanced TGN-PVC transport in both vps13 and cdc31 mutant backgrounds. Thus, Vps13p is required to be in a complex with functional Cdc31p to be active

(De et al., 2017). Cdc31p contains one Ca^{2+}/Mg^{2+}-mixed-binding site in the N terminus and two low-affinity Ca^{2+}-binding sites in the C-terminal domain (Miron et al., 2011). The crystal structure of Cdc31p-Sfi1p (yeast spindle pole body protein) reveals interactions similar to the binding of calmodulin and myosin V (Li et al., 2006). Cdc31p regulates Vps13p function in response to changes in calcium concentrations. Cell-free TGN homotypic fusion was strongly inhibited by treatment of the rapid Ca^{2+} chelator BAPTA, while the slower chelator EGTA had no effect, suggesting a role for transient changes in Ca^{2+} levels during the event (Brickner et al., 2001). Therefore, it is reasonable to hypothesize that CETN3 functions in a local Ca^{2+} increase-dependent manner to regulate VPS13D activity in ER-lysosome MCSs formation. However, the lack of specific human VPS13D antibodies makes it difficult to study the endogenous interaction between VPS13D and CETN3.

Dysregulation of lysosome Ca^{2+} homeostasis causes LSDs and lysosome-related diseases. ML-IV is associated with impaired lysosomal Ca^{2+} release (Kiselyov et al., 2010). Additionally, lysosomal Ca^{2+} stores have been reported to be reduced in Niemann-Pick, type C cells (Lloyd-Evans et al., 2008) and common neurodegenerative diseases, such as familial Alzheimer's disease (Coen et al., 2012; Lee et al., 2015). A recent report showed that Parkinson disease patients' cells with GBA1 or LRRK2 mutations (common risk factors of the disease) exhibit dysregulated lysosomal Ca^{2+} stores (Hockey et al., 2015; Kilpatrick et al., 2016a; Kilpatrick et al., 2016b). The VPS13D KD cells exhibited lysosomal storage (Figure 4.7A, 4.7B). Manipulating ER Ca^{2+} reduces lysosome storage in NPC1 cells and Gaucher patient-derived fibroblasts (Mu et al., 2008; Platt and Lachmann, 2009; Yu et al., 2012). Thus, ER and lysosomal Ca^{2+} homeostasis might serve as potential therapeutic targets.

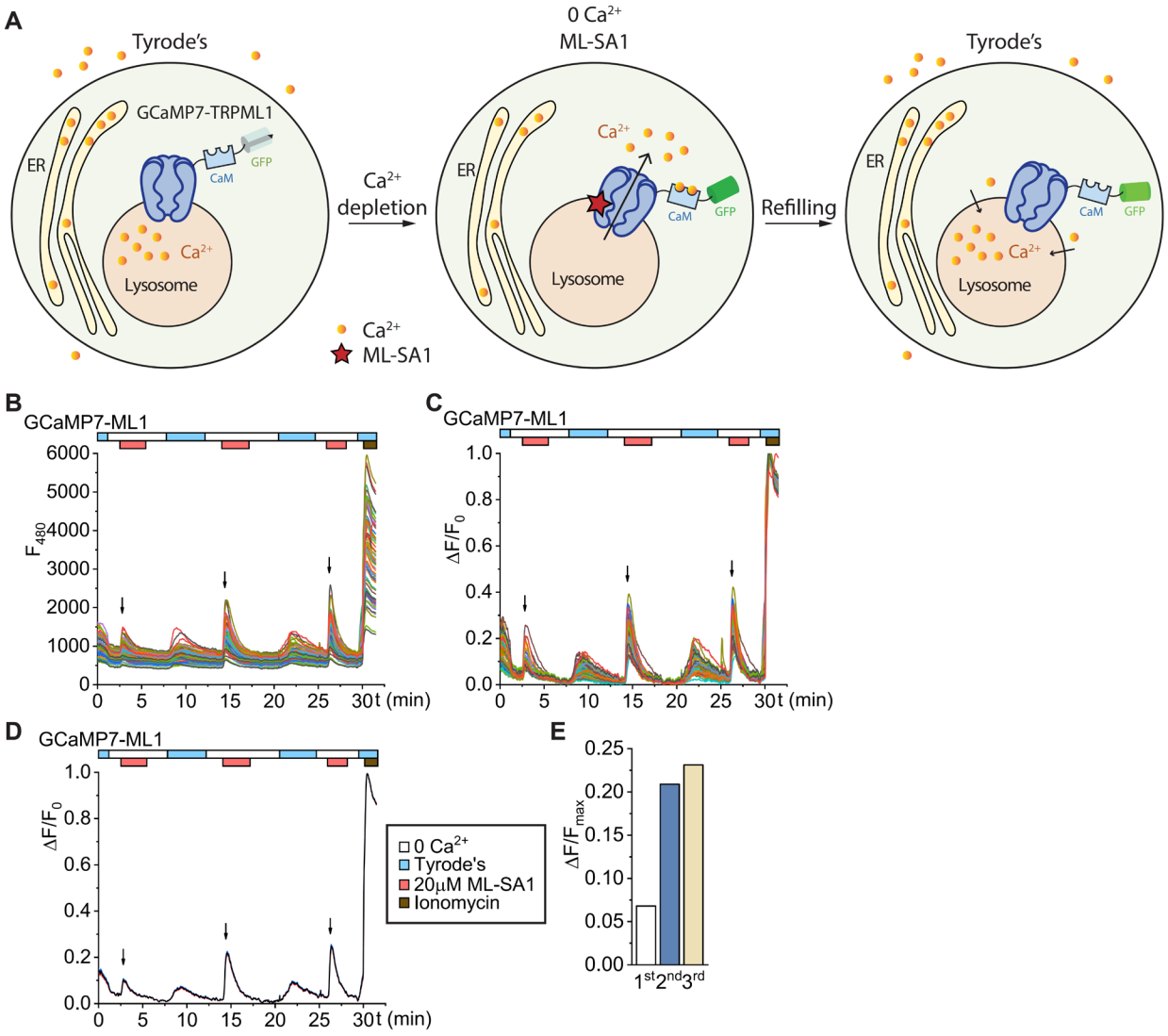

Figure 4.1 The protocol for the lysosomal Ca^{2+} refilling assay.
(A) Schematic of the Ca^{2+} refilling assay. (B) Traces of GCaMP7 fluorescence signals for all cells on the coverslip used in a single experiment. The Tyrode's peaks (below the cyan bars) represents the entry of Ca^{2+} into the cytosol across the plasma membrane. Arrows indicate the ML-SA1-induced responses. The legend next to panel D shows the contents of the solutions used in all panels. (C) The normalized GCaMP7 fluorescence signals in B. (D) Average of all traces in C. (E) Quantification of first, second, and third ML-SA1-induced GCaMP7 fluorescence peaks in D. GCaMP7 fluorescence increases were normalized to ionomycin responses.

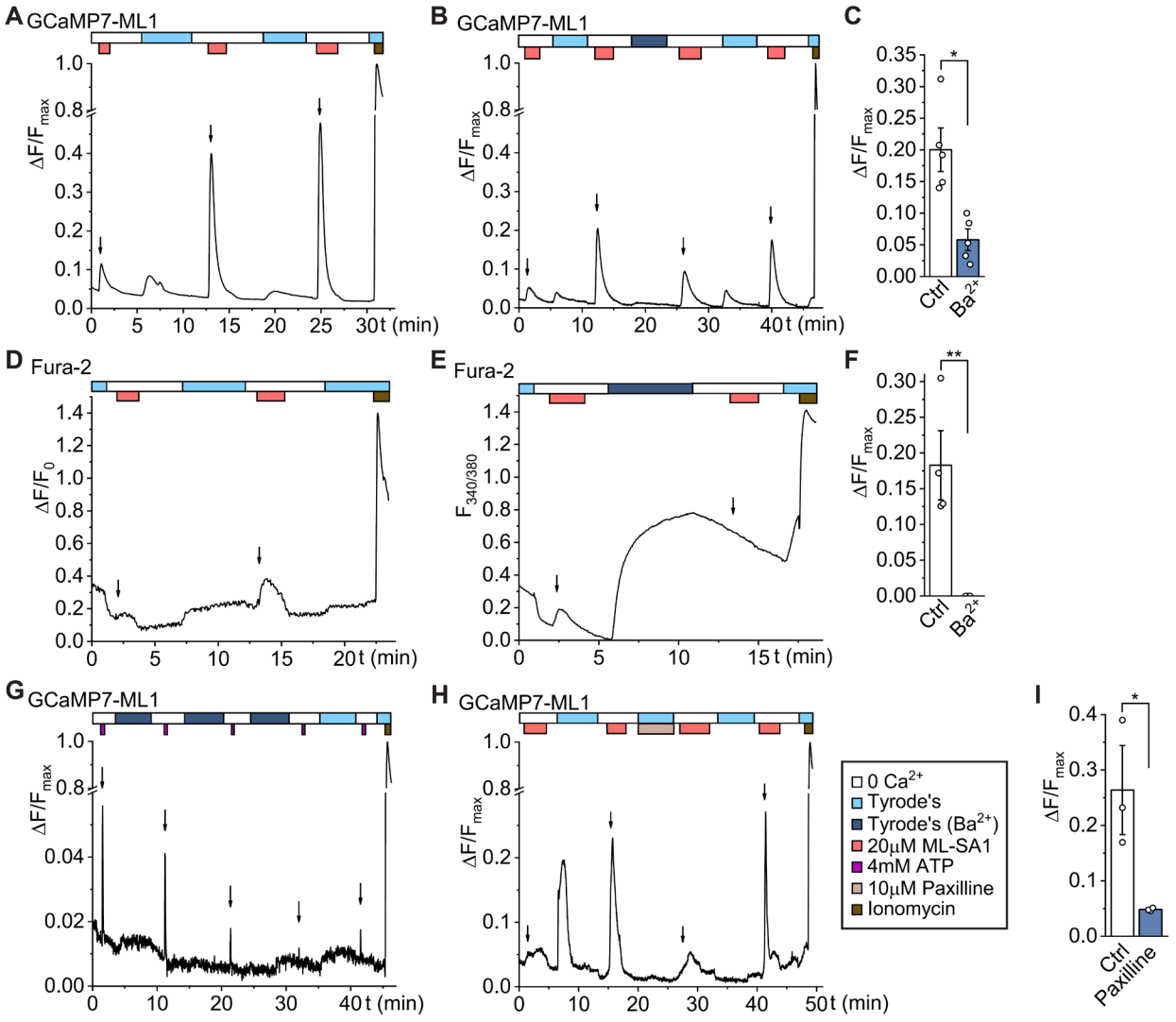

Figure 4.2 Lysosomal Ca^{2+} refilling is external Ca^{2+} and K^+ dependent.
(A) Typical Ca^{2+} imaging trace of refilling of WT GCaMP7-ML1-HEK293 cells. The trace represents the average of ~50 cells. Arrows indicate the ML-SA1-induced responses. The legend next to panel F shows the contents of the solutions. (B) Effect of substituting Ca^{2+} with Ba^{2+} in the Tyrode's bath solution on Ca^{2+} refilling in GCaMP-based Ca^{2+} imaging assay. (C) Quantification of ML-SA1-induced refilling peaks in HEK-GCaMP7-ML1 cells before and after Ba^{2+} substitution. GCaMP7 fluorescence increases were normalized to ionomycin responses (n=5 biological replicates, each includes 30-50 cells). Data are means ± s.e.m. (***P < 0.0001, paired two-tailed t-test). (D) Fura-2-based Ca^{2+} imaging trace of refilling of GCaMP7-ML1-HEK293 cells. (E) Effect of substituting Ca^{2+} with Ba^{2+} in the Tyrode's bath solution on Ca^{2+} refilling assessed with Fura-2-based Ca^{2+} imaging assay. (F) Quantification of ML-SA1-induced refilling peaks before and after Ba^{2+} substitution in Fura-2-based Ca^{2+} imaging assay. Fura-2 fluorescence increases were normalized to ionomycin responses (n=3 biological replicates, each includes 30-50 cells). (G) Effect of substituting Ca^{2+} with Ba^{2+} in the Tyrode's bath solution on ER Ca^{2+} responses to 4mM ATP. (H) Effect of acute application of 10μM Paxilline on Ca^{2+}

refilling. (I) Quantification of ML-SA1-induced refilling peaks in HEK-GCaMP7-ML1 cells before and after paxilline application (n=3).

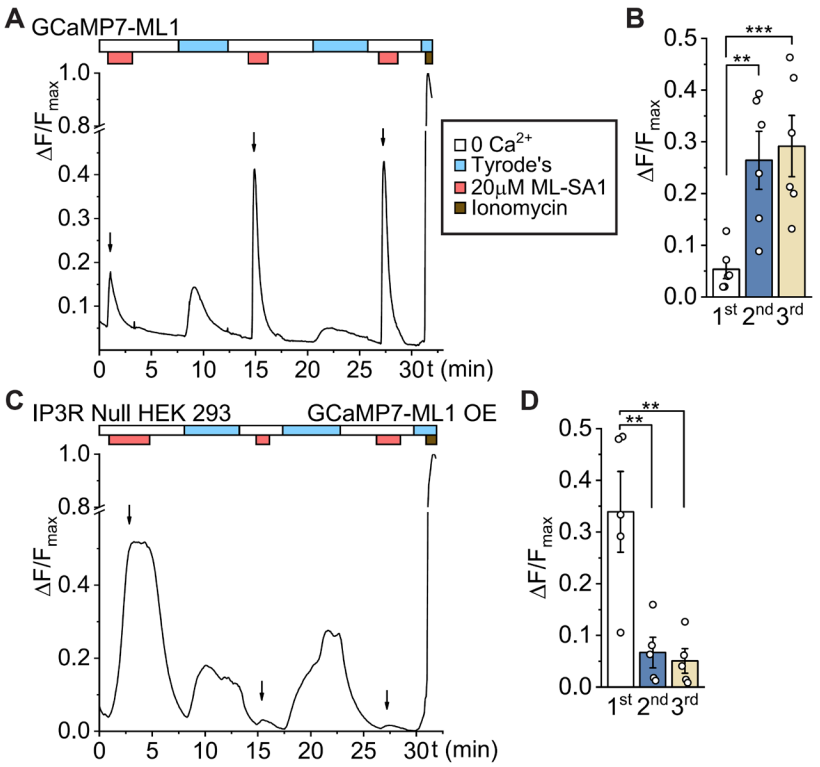

Figure 4.3 Rapid lysosomal Ca^{2+} refilling is IP3R-dependent.
(A) Control GCaMP7-ML1-HEK293 cells show repetitive responses towards ML-SA1. Arrows indicate the ML-SA1-induced responses. The legend next to panel A shows the contents of the solutions. (B) Quantification of first, second, and third ML-SA1-induced GCaMP7 fluorescence peaks in HEK-GCaMP7-ML1 cells. GCaMP7 fluorescence increases were normalized to ionomycin responses (n=6 biological replicates, each includes 30-50 cells). Data are means ± s.e.m. (***P < 0.0001, paired two-tailed t-test). (C) Ca^{2+} refilling of IP3R1,2,3 TKO HEK293 cells overexpressing GCaMP7-ML1. (D) Quantification of first, second, and third ML-SA1-induced GCaMP7 fluorescence peaks in GCaMP7-ML1-overexpressing IP3R1,2,3 TKO HEK293 cells (n=5).

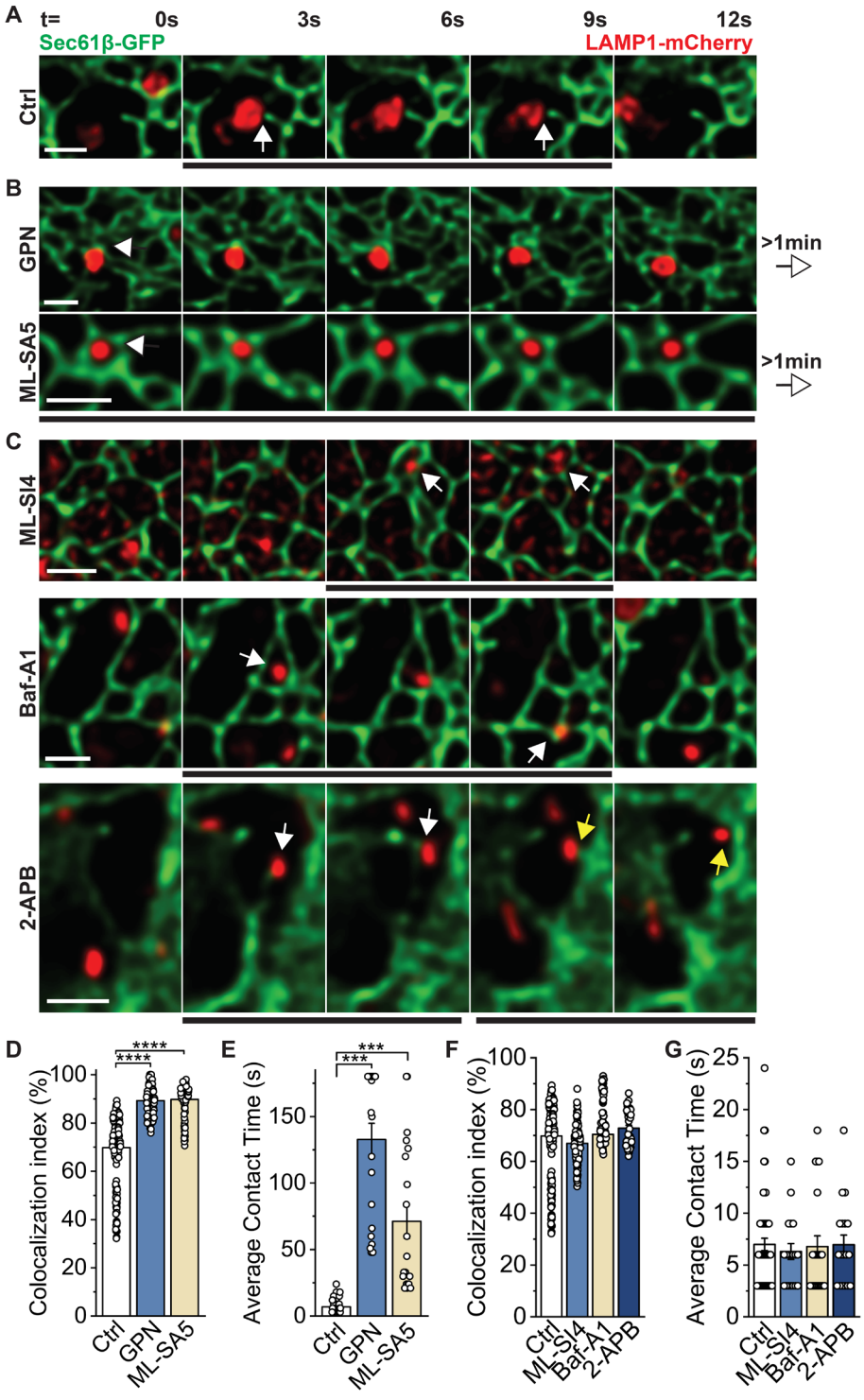

Figure 4.4 Lysosomal Ca^{2+} release induces the formation/stabilization of ER-LY MCSs. (A-C) Representative time-lapse super resolution confocal images showing the dynamics of ER-lysosome contact (arrow) in live COS1 cells expressing Sec61β-GFP (ER) and LAMP1-mCherry (lysosome). 400μM GPN, 10μM ML-SA5 (B), and 20μM ML-SI4 (C) were applied 15min before imaging, and 5μM Baf-A1 and 50μM 2-APB (C) were pre-applied for 1h. Each pair of

arrows in the same color mark the entire process of one specific contact event. The black lines below each sequence run from the first frame to wither the last frame that the contact was present, or to the end of the panel if the contact persisted for more than 12 s, in which case the duration of the contact is indicated to the right. Scale bars, 1μm. (D, E) Quantification of percentage of lysosomes contacting ER (D) and duration of ER-lysosome contacts (E) from confocal time-lapse images (n=30 examples from 5 cells) in A-C. Measurement of interaction duration is limited to the length of the live imaging length. Data are means ± s.e.m. (***P < 0.0001, unpaired two-tailed t-test).

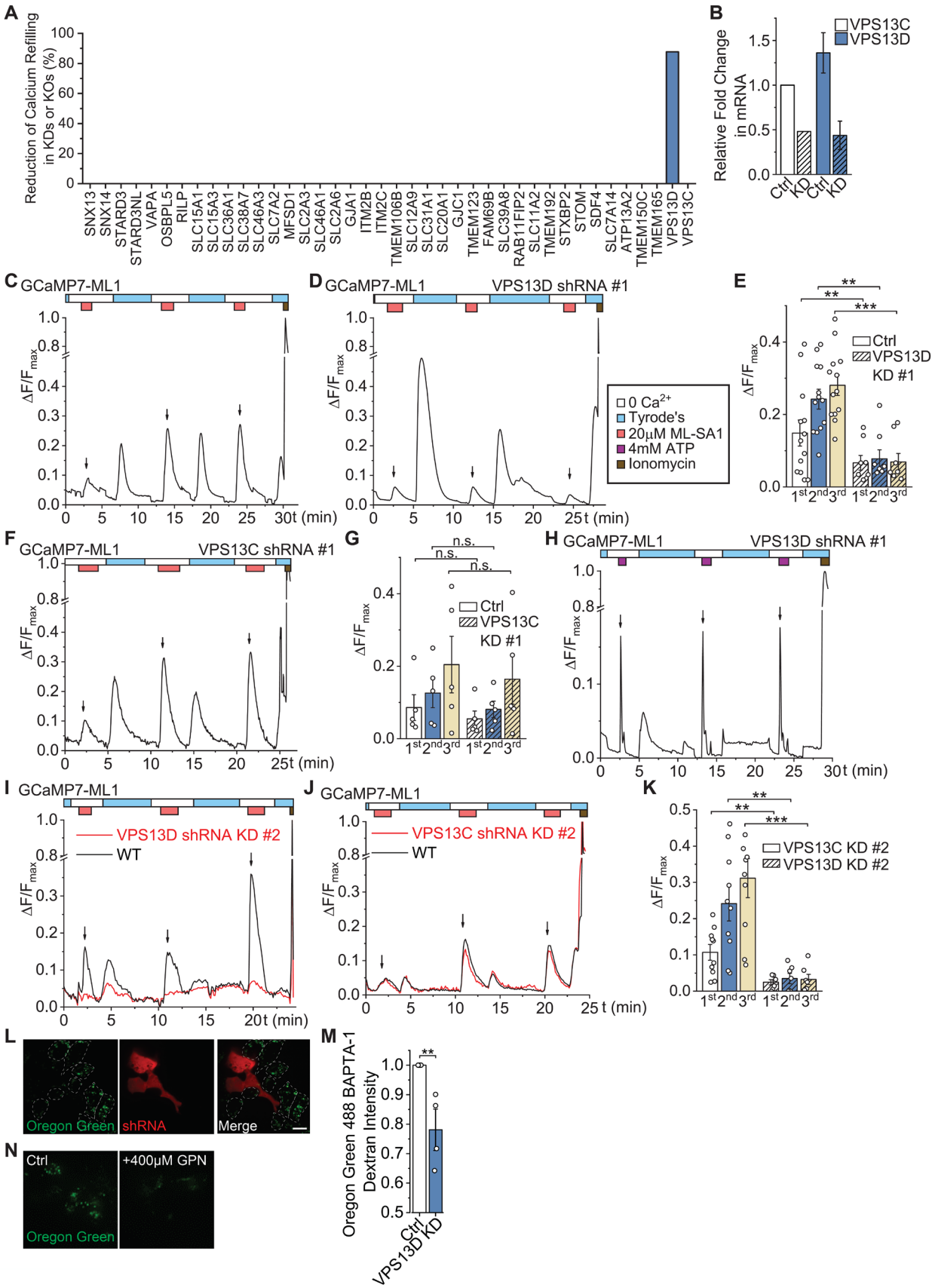
A
Reduction of Calcium Refilling in KDs or KOs (%)
SNX13
SNX14
STARD3
STARD3NL
VAPA
OSBPL5
RILP
SLC15A1
SLC15A3
SLC36A1
SLC38A7
SLC46A3
SLC7A2
MFSD1
SLC2A3
SLC46A1
SLC2A6
GJA1
ITM2B
ITM2C
TMEM106B
SLC12A9
SLC31A1
SLC20A1
GJC1
TMEM123
FAM69B
SLC39A8
RAB11FIP2
SLC11A2
TMEM192
STXBP2
STOM
SDF4
SLC7A14
ATP13A2
TMEM150C
TMEM165
VPS13D
VPS13C
B
Relative Fold Change in mRNA
VPS13C
VPS13D
Ctrl
KD
Ctrl
KD
C
GCaMP7-ML1
ΔF/Fmax
30t (min)
D
GCaMP7-ML1
VPS13D shRNA #1
25t (min)
0 Ca2+
Tyrode's
20μM ML-SA1
4mM ATP
Ionomycin
E
Ctrl
VPS13D KD #1
1st 2nd 3rd 1st 2nd 3rd
F
GCaMP7-ML1
VPS13C shRNA #1
25t (min)
G
n.s.
Ctrl
VPS13C KD #1
H
GCaMP7-ML1
VPS13D shRNA #1
30t (min)
I
GCaMP7-ML1
VPS13D shRNA KD #2
WT
20t (min)
J
GCaMP7-ML1
VPS13C shRNA KD #2
WT
25 t (min)
K
VPS13C KD #2
VPS13D KD #2
L
Oregon Green
shRNA
Merge
M
Oregon Green 488 BAPTA-1 Dextran Intensity
Ctrl
VPS13D KD
N
Ctrl
+400μM GPN
Oregon Green

Figure 4.5 VPS13D is required for lysosomal Ca^{2+} refilling.
(A) One-time Ca^{2+} imaging-based candidate for proteins potentially involved in lysosome refilling. The Y axis shows the extent of reduction of the second and third ML-SA1-induced responses in comparison to the amplitude expected in none-transfected controls. (B) Relative mRNA expression level of VPS13C or VPS13D in control versus KD cells. (C) Control GCaMP7-ML1-HEK293 cells show repetitive responses towards ML-SA1. Arrows indicate the ML-SA1-induced responses. The legend next to panel D shows the contents of the solutions. (D) Ca^{2+} refilling of VPS13D KD HEK-GCaMP7-ML1 cells. (E) Quantification of first, second, and third ML-SA1-induced GCaMP7 fluorescence peaks in between WT and VPS13D KD HEK-GCaMP7-ML1 cells. GCaMP7 fluorescence increases were normalized to ionomycin responses (n=10 biological replicates, each includes 30-50 cells). Data are means ± s.e.m. (***$P < 0.0001$, unpaired two-tailed t-test). (F) Ca^{2+} refilling of VPS13C KD HEK-GCaMP7-ML1 cells. (G) Quantification of ML-SA1-induced GCaMP7 fluorescence peaks in between WT and VPS13C KD HEK-GCaMP7-ML1 cells (n=5). (H) ER Ca^{2+} responses to 4mM ATP of VPS13D KD HEK-GCaMP7-ML1 cells. (I, J) Effect of KD of VPS13C (J) or VPS13D (I) on Ca^{2+} refilling. shRNA #2 targeting a different sequence from #1 in D and F was used. Vector of shRNA #2 encoded TurboRFP for indication of shRNA expression. (K) Quantification of first, second, and third ML-SA1-induced GCaMP7 fluorescence peaks in between VPS13C and VPS13D KD HEK-GCaMP7-ML1 cells (n=10). (L) Representative images showing OG-BAPTA-dextran fluorescence in VPS13D KD HEK-ML1 stable cells (RFP-positive) and WT internal control cells (as circled out by dash lines). Scale bar =20μm. (M) Quantification of OG-BAPTA-dextran fluorescence intensity in L (n=4 images, each includes 3-5 VPS13D KD cells and 3-5 control cells). Data are means ± s.e.m. (***$P < 0.0001$, paired two-tailed t-test). (N) Representative images showing the effect of GPN treatment in OG-BAPTA-dextran loaded HEK-ML1 stable cells.

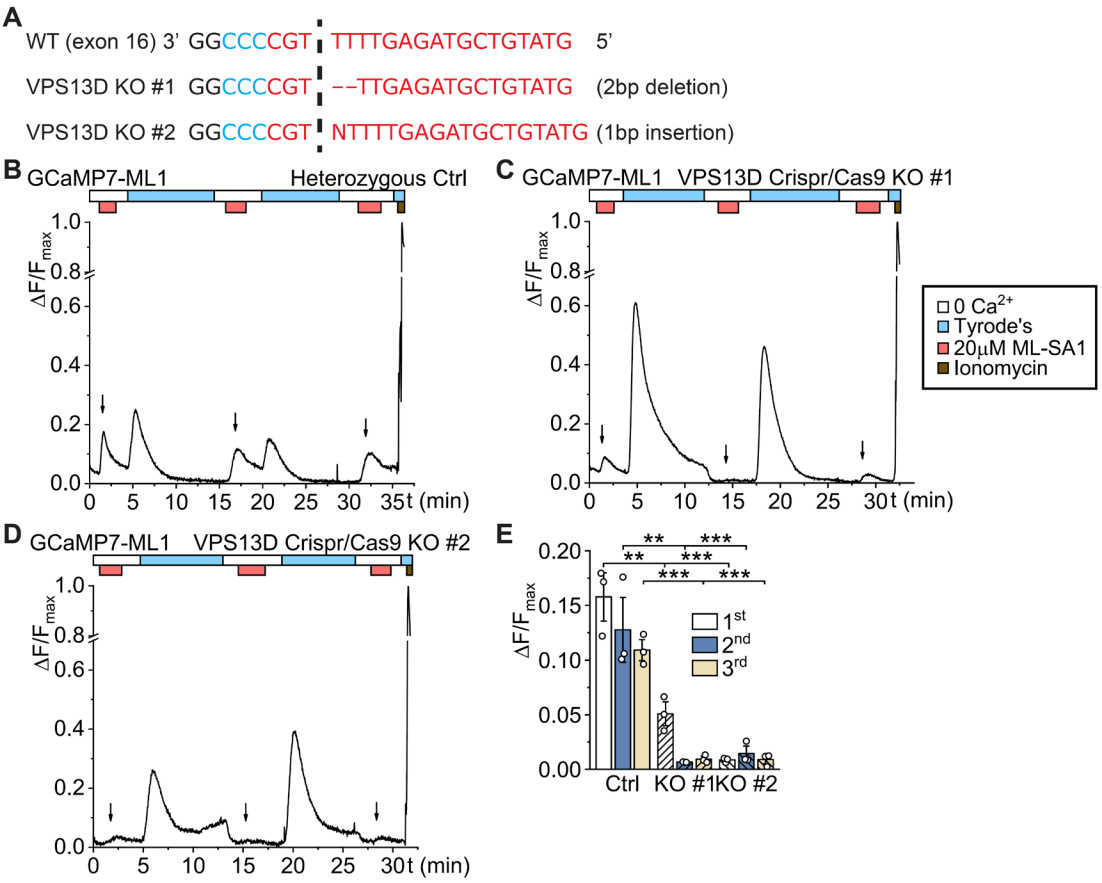

Figure 4.6 Crispr/Cas9-based KO of VPS13D leads to impaired lysosomal Ca^{2+} stores and depleted refilling.

(A) The genomic sequence in Exon 16 of VPS13D is shown. Guide RNA (gRNA) sequence and protospacer adjacent motif (PAM) motif are highlighted in red and blue. Frameshift was detected in diploid HEK-GCaMP7-ML1 cells by Sanger sequencing. (B-D) Ca^{2+} refilling of control (B) and two lines of VPS13D KO HEK-GCaMP7-ML1 cells (C, D). Arrows indicate the ML-SA1-induced responses. The legend next to panel C shows the contents of the solutions. (E) Quantification of first, second, and third ML-SA1-induced GCaMP7 fluorescence peaks in between WT, VPS13D KO #1, and VPS13D KO #2 HEK-GCaMP7-ML1 cells. GCaMP7 fluorescence increases were normalized to ionomycin responses (n=3 biological replicates, each includes 20-50 cells). Data are means ± s.e.m. (***P < 0.0001, unpaired two-tailed t-test).

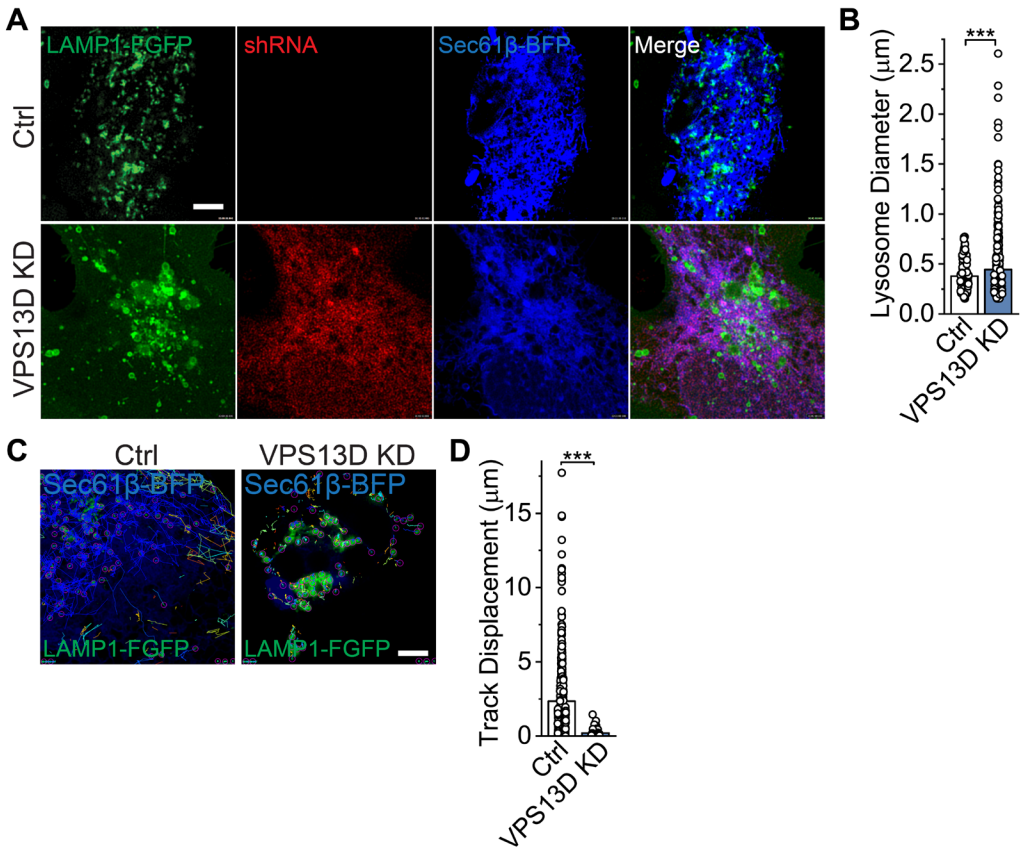

Figure 4.7 VPS13D knockdown lead to lysosomal storage-like phenotypes in cells.
(A) Representative super resolution confocal images of COS1 cells expressing LAMP1-EGFP and Sec61β-BFP showing enlarged and aggregated lysosomes in VPS13D KD COS1 compared with WT. Scale bar, 6μm. (B) Quantification of lysosome diameter in WT and VPS13D KD (red) COS1 cells (n=10 cells). Data are means ± s.e.m. (***P < 0.0001, unpaired two-tailed t-test). (C) Tracking of lysosome mobility in super resolution confocal images of WT and VPS13D KD COS1 cells. Each trace represents a complete track of lysosomal movement. VPS13D KD cells showed significant trafficking defect. Scale bar, 6μm. (D) Quantification of track displacement of individual lysosomal movement in WT and VPS13D KD COS1 cells (n=10 cells).

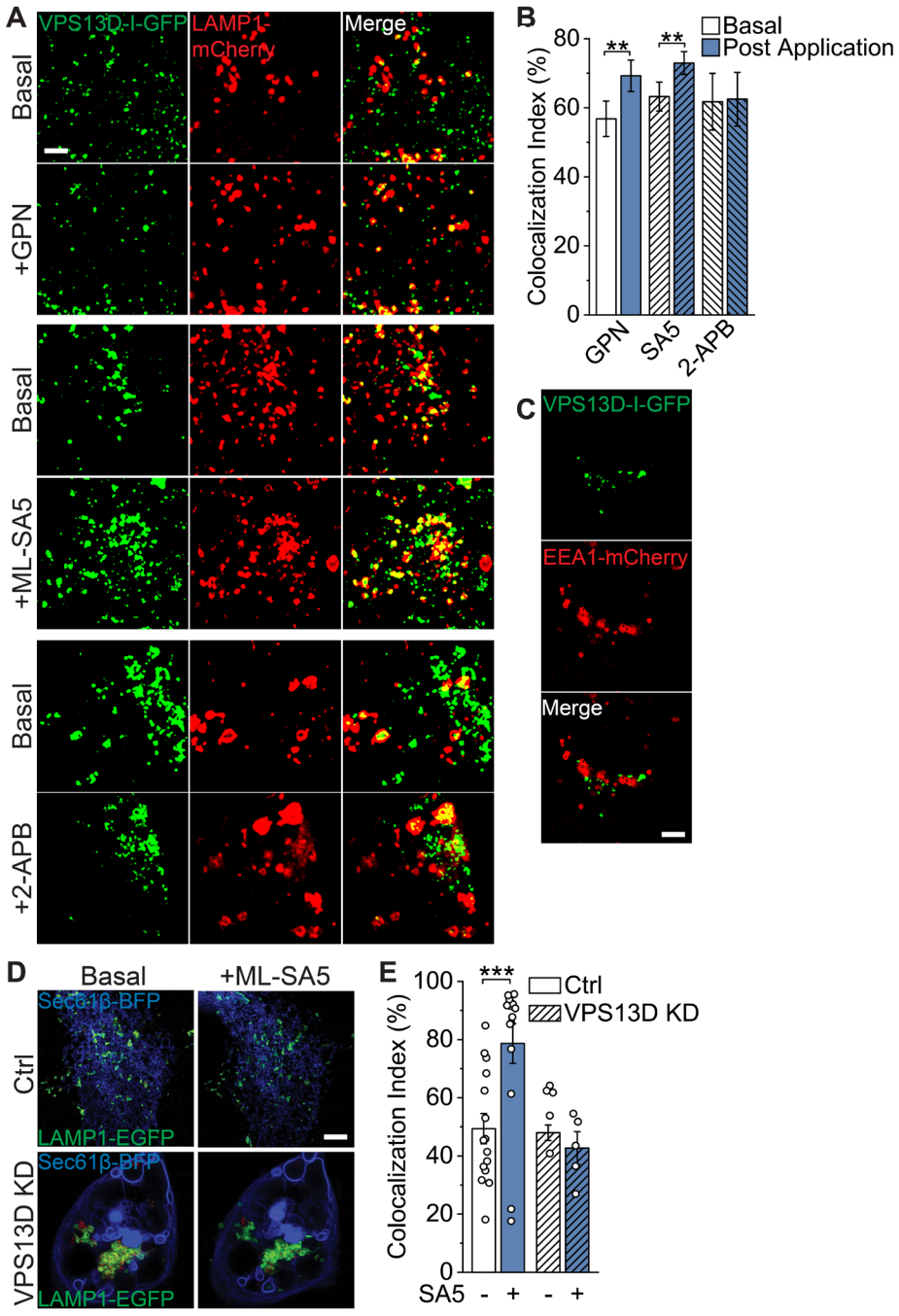

Figure 4.8 VPS13D localizes to lysosomes upon lysosomal Ca^{2+} depletion and is required for ER-LY MCS formation.

(A) Super resolution confocal images of WT COS1 cells expressing VPS13D-I-GFP and LAMP1-mCherry (lysosome) to assess the extent of colocalization of VPS13D with lysosomes with or without 400μM GPN, 10μM ML-SA5, and 50μM 2-APB acute application. Scale bar, 6μm. (B) Quantification of the percentage of lysosomes colocalize with VPS13D in A (n=10 examples from 10 cells). Data are means ± s.e.m. (***P < 0.0001, paired two-tailed t-test). (C) Super resolution confocal images of COS1 cells expressing VPS13D-I-GFP and EEA1-mCherry

(early endosome) to assess the extent of colocalization of VPS13D with early endosomes. Scale bar, 6μm. (D) Super resolution confocal images of WT or VPS13D KD COS1 cells expressing LAMP1-EGFP (lysosome) and Sec61β-BFP (ER) to assess the extent of colocalization of lysosomes with ER with or without 10μM ML-SA5 acute application. Scale bar, 6μm. (E) Quantification of the percentage of lysosomes colocalize with ER in D (n=10 examples from 10 cells).

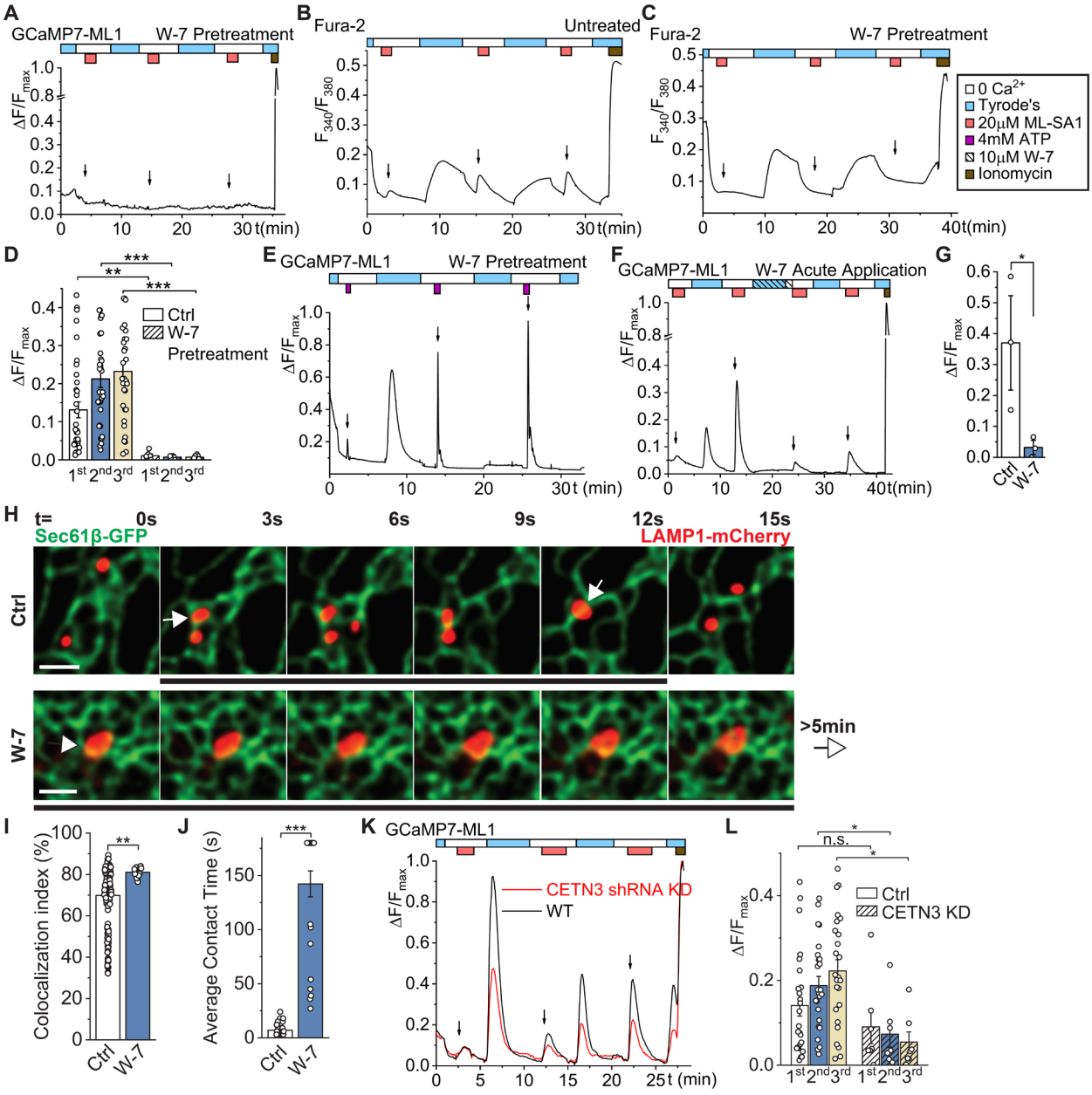

Figure 4.9 W-7 abolishes lysosome calcium refilling and blocks formation/stabilization of ER-LY MCS.

(A) Effect of 1h pretreatment with 50μM W-7 on lysosomal Ca^{2+} refilling in GCaMP-based Ca^{2+} imaging assay. Arrows indicate the ML-SA1-induced responses. The legend next to panel C shows the contents of the solutions. (B) Fura-2-based Ca^{2+} imaging trace of refilling. (C) Effect of 1h pretreatment with 50μM W-7 on Ca^{2+} refilling assessed with Fura-2-based Ca^{2+} imaging assay. (D) Quantification of first, second, and third ML-SA1-induced GCaMP7 fluorescence peaks in control or W-7 pretreated HEK-GCaMP7-ML1 cells based on experiments link panel A. GCaMP7 fluorescence increases were normalized to ionomycin responses (n=20 biological repplicates, each includes 30-50 cells). Data are means ± s.e.m. (***P < 0.0001, unpaired two-tailed t-test). (E) Effect of 1h pretreatment with 50μM W-7 on ER Ca^{2+} release in response to

4mM ATP. (F) Effect of acute application of 50μM W-7 on Ca^{2+} refilling. (G) Quantification of ML-SA1-induced refilling peaks in HEK-GCaMP7-ML1 cells before and after W-7 application (n=3). (H) Representative time-lapse super resolution confocal images showing the dynamics of ER-lysosome contact (arrow) in live COS1 cells expressing Sec61β-GFP (ER) and LAMP1-mCherry (lysosome) with or without 50μM W-7 treatment for 15min. White arrows mark lysosomes before or after contact tethering to ER tubule. Each pair of arrows in the same color mark the entire process of one specific contact event. The black lines below each sequence run from the first frame to wither the last frame that the contact was present, or to the end of the panel if the contact persisted for more than 12 s, in which case the duration of the contact is indicated to the right. Scale bars, 1μm. (I, J) Quantification of percentage of lysosomes contacting ER (I) and duration of ER-lysosome contacts (J) from confocal time-lapse images (n=30 examples from 5 cells) in H. (K) Effect of RFP-labeled shRNA KD of CETN3 on lysosomal Ca^{2+} refilling comparing with WT internal controls. (L) Quantification of first, second, and third ML-SA1-induced GCaMP7 fluorescence peaks in control or CETN3 KD HEK-GCaMP7-ML1 cells (n=10).

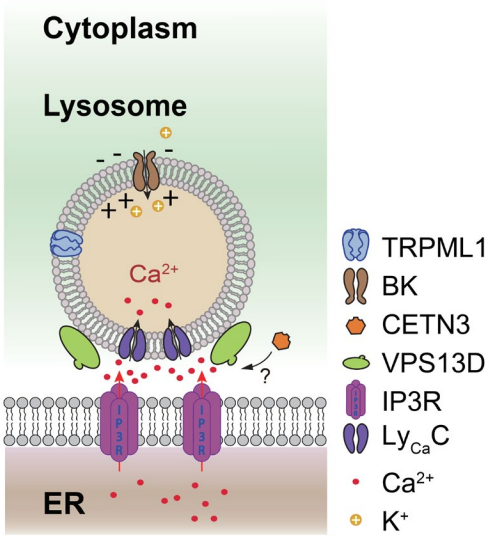

Figure 4.10 A proposed model of the roles of essential proteins in Ca^{2+} transfer from the ER to lysosomes.
Refilling of lysosomal Ca^{2+} requires the recruitment of VPS13D to the ER-LY MCSs, which functions to stabilize the ER-LY MCSs, enabling Ca^{2+} fueling from ER through IP3Rs to lysosome lumen via the lysosomal putative Ca^{2+} channel/transporter $Ly_{Ca}C$ (identity unknown). A cytosolic Ca^{2+} sensor (perhaps CETN3) is required for the process.

CHAPTER V

Conclusions and Future Directions

Conclusions

Lysosomes and lysosome-related organelles (LROs) serve as intracellular signaling centers. As stores for Ca^{2+} as well as other heavy metals, lysosomes and LROs mediate signal transduction through membrane cation channels. The tight regulation of the homeostasis of ions and the activity of the channels through which they can flow play essential roles in maintaining proper lysosomal and LRO functions.

The goal of this study was to elucidate the regulatory processes of lysosomal Ca^{2+} involved in maintaining proper cellular functions, and the mechanism of lysosomal Ca^{2+} refilling after store depletion.

The results in Chapter II and Chapter III showed two examples of the regulatory roles of TRPML1 in maintaining LRO function and cell viability. In Chapter II, TRPML1, instead of functioning in lysosomes, was discovered to also be a tubulovesicular channel. The results led to a detailed mechanism of how cAMP/PKA activation of tubulovesicular ML1 fulfills organellar functions by driving tubulovesicular membrane trafficking through Ca^{2+} release.

In Chapter III, with both *in vitro* and *in vivo* experiments, we demonstrated that upregulated TRPML1 in metastatic melanoma cells can be pharmacologically targeted by its agonists ML-SAs to cause selective cell death by inducing lysosomal Zn^{2+} release, mitochondria swelling and cellular ATP depletion. The therapeutic efficiency of ML-SAs was validated in advanced melanoma mouse models. Cancer cells store excessive Zn^{2+} in intracellular organelles such as

lysosomes as a self-protective mechanism against cytosolic Zn^{2+} induced cell death (Hwang et al., 2010). Utilizing this character, we show that over-activation of TRPML1 is sufficient to cause selective cell death of metastatic melanoma cells both. ML-SAs by artificial activation of ML1 may also serve as a potential therapeutic strategy for other types of cancers with ML1/lysosome upregulation.

Although several loss-of-function studies suggest that ML1 inhibition or knockdown may reduce cancer cell proliferation (Jung et al., 2019; Xu et al., 2019), ML1 is dispensable for cancer cell survival according to the cancer dependency map (https://depmap.org/portal/gene/MCOLN1?tab=overview). Therefore, although ML1 upregulation may act as a potential biomarker in some cancers, ML1 inhibition may not be an effective anti-cancer therapy. ML-SAs show promising therapeutic efficacy in both a cutaneous melanoma mouse model by systemical administration and a MBM mouse model by on-site delivery *in vivo*, however, it is necessary to further evaluate the blood brain barrier (BBB) permeability of ML-SAs in future work to achieve a better therapeutic efficacy.

Chapter V aimed to dissect mechanisms used to maintain lysosomal Ca^{2+} stores. We showed that ER Ca^{2+} release through IP3Rs is required for the rapid Ca^{2+} refilling of lysosomes. An increase in the number of ER-lysosome membrane contact formation was seen with ML-SA1 or GPN treatment to deplete lysosomal Ca^{2+}. Therefore, ER-lysosome MCS is likely mediating Ca^{2+} channeling, with IP3R as one of the participators on the ER side. We identified VPS13D as a functional protein on the lysosome membrane required for lysosomal Ca^{2+} refilling. Recruitment of VPS13D to the lysosome membrane is potentially required for MCS formation and stabilization. Moreover, CETN3, a cytosolic Ca^{2+} sensor, potentially triggers the refilling process through

binding para-lysosomal Ca^{2+} released followed by interacting with VPS13D to assist ER-lysosome MCSs establishment.

The trigger for Ca^{2+} refilling could either be an increase in juxta-lysosomal Ca^{2+} concentration or a decrease in lysosome luminal Ca^{2+}. Although the observation that knockdown of the cytosolic Ca^{2+} sensor CETN3 reduced refilling favors the first hypothesis, additional pathways that drive refilling when lysosomal luminal [Ca^{2+}] is low could not be ruled out based on the current data. To eliminate the possibility, refilling and MCSs formation under conditions inducing depletion of lysosomal luminal Ca^{2+} without increasing the cytosolic Ca^{2+} concentration, e.g. in the presence of BAPTA-AM, should be assessed. Using rapid Ca^{2+} chelators with high affinity is critical in this experiment. In addition, whether increase of bulk cytosolic [Ca^{2+}] without disrupting lysosomal Ca^{2+} by, for example, ATP-induced ER Ca^{2+} release, induces MCSs formation requires to be tested.

We showed that the ER regulates the acute refilling of lysosomal Ca^{2+} through IP3R-$Ly_{Ca}C$ MCSs. However, that IP3 Null HEK293 cells still have a substantial first response toward ML-SA1 indicating that the naïve Ca^{2+} stores of lysosomes must be filled by some other mechanism (Figure 4.2C). Thus, additional pathways independent of IP3R must exist to regulate the long-term maintenance of lysosomal Ca^{2+}. ER Ca^{2+} may partially involve in the naïve lysosomal Ca^{2+} store regulation, as long-term (24h) application of ER Ca^{2+} chelators resulted in a lysosome storage phenotype in cells (Garrity et al., 2016). Also, such regulation may still be Ca^{2+}-dependent since application of W-7 abolished the first naïve Ca^{2+} response (Figure 4.9A).

The presence of large Ca^{2+} stores such as the ER as well as small vesicular stores leads to the question why keeping various Ca^{2+} stores is crucial in maintaining cellular functions. Indeed, compared with the ER, which has a huge volume and thus a large Ca^{2+} store, individual vesicles

like lysosomes may only hold fewer than 100 Ca^{2+} ions, potentially allowing very fine control of the amount of Ca^{2+} released. Thus, it is of importance to understand the physiology of lysosomal Ca^{2+}. Under physiological conditions in intact cells, lysosomal Ca^{2+} channel-activating cellular signals are likely only present in a subset of lysosomes. Hence, while ER Ca^{2+} release mediates bulk $[Ca^{2+}]_{Cyt}$ increase and more general cytosolic Ca^{2+} signaling cascades, lysosomal Ca^{2+} release from individual lysosomes may not be synchronized in a manner that gives rise to global increases in $[Ca^{2+}]_{Cyt}$. Therefore, local Ca^{2+} spikes from lysosomes are more specified to regulate lysosome-specific dynamics. Notwithstanding, in some experimental settings, synchronized lysosomal Ca^{2+} release may be amplified by ER Ca^{2+} release triggering further cell signaling transduction (Kilpatrick et al., 2016b); it is not known whether such Ca^{2+}-induced Ca^{2+} release occurs under physiological conditions.

Discussion and future directions

ML1 in lysosomes and other LROs

Similar mechanisms of signal-stimulated ML1-driven exocytosis of functional vesicles may apply to granules in other secreting cells. KO of ML1 resulted in significantly enlarged Drosophila nephrocytes (data not shown), part of the Drosophila excretory system, which serves as a model for the study of the renal system. Electron micrographs of nephrocytes showed a large number of vacuoles and granules of different sizes and grades of electron densities, most likely lysosomes in different stages, some of which were filled with material containing condensed electron dense deposits (Costa-Leonardo et al., 2015). Therefore, it would be of interest to explore the role of TRPML1 in renal excretion. In addition, besides lysosomes and tubulovesicles, TRPML1 may reside on other organelles, especially those who undergo stimuli-driven membrane trafficking or exocytosis, such as melanosomes or other LROs. ML1 overexpressing $ML1^{SOX2}$

mice have grey hair comparing with their WT black siblings (data not shown), suggesting a potential role of TRPML1 in regulating melanosome secretion. The existence of ML1 on melanosomes remains untested.

The expression of ML1 on various LROs provides evidence in identifying novel physiological modulators of the channel through looking at known physiological signals modulating the organelle. In tubulovesicles we identified PKA as an activator of ML1, most likely through direct phosphorylation. As mutations on Ser557 and Ser559, the two sites previously predicted for PKA phosphorylation, did not abolish PKA activation of ML1 (data not shown) in electrophysiology, other PKA phosphorylation sites may present. With the availability of a ML1 cryo-EM structure, it should be possible to predict potential phosphorylation sites, as well as the topological mechanism of the PKA activation.

Cell-type-specific endogenous activators may exist, as examplified by the discovery of ATP as a ML1 agonist in tubulovesicles but not lysosomes, suggesting the possibility that auxiliary subunits may present in specific cells to facilitate the cell-type-specific regulation of TRPML1. Tubulovesicular ML1 pulldown followed by mass spectrometry may reveal the molecular identity under this regulation.

ML1 and Zn^{2+}

Zn^{2+} has been implicated in stroke and neurodegenerative disorders (Choi and Koh, 1998); in these situations increases in intracellular Zn^{2+} have been reported to cause massive neuronal cell death (Koh et al., 1996). A functional link between ML1 and Zn^{2+} homeostasis has been implicated in previous studies. For example, in fibroblasts from ML-IV patients, Zn^{2+} accumulation has been demonstrated in lysosomes (Eichelsdoerfer et al., 2010). Recent studies propose a role for

TRPML1 in modulating cytosolic Zn^{2+} level, most likely through lysosomal release of the ion (Cuajungco et al., 2014; Minckley et al., 2019). In the current study, we found that ML-SAs induced cell death in both melanoma cells and HEK293 cells overexpressing ML1 was sensitive to the Zn^{2+} chelator, TPEN. In addition, melanoma cells incubatd with zinc pyrithion (a zinc ionophore used to raise free zinc within cells) showed rounded-up morphological changes and rapid cell death that resembled ML-SA-induced cell death (data not shown), indicating the involvement of cellular Zn^{2+} in this cell death process. We thus hypothesize that one or more Zn^{2+}-dependent enzymes may function as part of the core cell death mechanism upon artificial activation of ML1 by ML-SAs.

The detailed mechanism of the ML-SA-induced melanoma cell death remains unclear. The physiology of the lethality driven by ML-SAs is different from previously established cell death pathways. None of the inhibitors targeting different cell death pathways, e.g. apoptosis, necroptosis and ferroptosis ablated the ML-SA-induced cell death (Figure 3.6). Meanwhile, knockdown of TFEB, or application of the autophagy inhibitor Chloroquine (CQ) or the free radical scavenger NAC (N-acetyl-L-cysteine) did not affect ML-SA-caused cell death (data not shown), excluding the possibility that it is via autophagic cell death or oxidative cell death pathways. Thus, the ML-SA-induced cell death is potentially a new mode of cell death, but the specific regulatory mechanism remains to be further established.

To delineate the mechanisms underlying lysosome-mediated cell death in melanoma, a genome-wide CRISPR/Cas9-based KO screen to identify genes required for ML-SA- or Zn^{2+}-induced cell death was performed. Several genes in Zn^{2+} binding GO pathway (GO: 0008270) showed up as top hits, including ZNF282, RFWD2, S100A8, and SUPT4H1 (data not shown). TRPML3, a TRPML family member, is also among the list. TRPML3 localizes to melanosomes,

serving as a potential melanosome Ca^{2+} regulator (Grimm et al., 2012). As TRPML3 possess gating physiology similar to TRPML1 (Cheng et al., 2010) and could potentially be activated by ML-SAs as well (data not shown), whether the ML-SA-induced melanoma cell death is specific to ML1 or there is also a contribution by melanosomal ML3 needs to be tested. In MeWo and M12 cells, lysosomes, labeled by LysoTracker which has a pKa of 5.2, appear to be the dominant Zn^{2+} store demonstrated by FluZin-3 imaging (Figure 5H), reducing the possibility that ML3 activation on melanosome membranes directly release Zn^{2+} to the bulk cytosol. The luminal pH of melanosomes is 6.8, at which ML1 activity is largely inhibited. Thus, although it seems unlikely to be directly involved in the ML1-Zn^{2+} cell death pathway, how ML3 and melanosomes participate in the process requires further investigation.

Molecular components of ER-lysosome MCS for Ca^{2+} channeling

The identity of the lysosomal membrane channel/transporter for Ca^{2+} uptake remains unrevealed. Acute inhibition of ML1 using ML-SI3 during the Tyrode's perfusion phase did not affect lysosomal Ca^{2+} refilling, suggesting that ML1 may not serve as a bidirectional Ca^{2+} channel on lysosome membrane (data not shown). Theoretically, any Ca^{2+}-permeable channel, exchanger, or pump could mediate lysosomal Ca^{2+} uptake. The slow nature of the refilling process (in minutes) suggests that it could involve either a low affinity Ca^{2+} transporter or a rectifying Ca^{2+} channel. Interestingly, low-affinity (mM range) Ca^{2+} transporters have been observed in isolated lysosomes (Lemons and Thoene, 1991). It is also possible that a putative VDAC-like channel in lysosomes might mediate the Ca^{2+} uptake (van der Kant and Neefjes, 2014).

Previous screen failed to identify the putative Ca^{2+} uptake channel. Though multiple criteria were set to select for lysosomal membrane proteins with more than one transmembrane

domain that co-evolved with LAMP1/TRPML1/IP3R (assessed by CLIME) (Li et al., 2014), or that the expression of which was significantly up/downregulated in TRPML1 OE/KO MEF (assessed by RNA-seq, data not shown), the resulting pool of candidates still exceeded 50, not to mention that current databases for lysosomal membrane proteins is incomplete, limited by the technique of lysosome isolation. Moreover, the channel may not physically interact with IP3R, making it impossible to perform mass spectrometry based on pull down assays for candidate searching. Nevertheless, a recent gene essentiality profiling approach sometimes makes it possible to identify genes of common function or cellular process with established datasets from CRISPR screens (Meyers et al., 2017; Wang et al., 2017a). Analysis for genes that are co-essential with VPS13D, IP3R and TRPML1 may conferring high-score candidates.

The putative ER protein that maintains ER-lysosome MCSs remains to be determined. The presence of a FFAT motif in the N-terminal region of the VPS13 proteins suggests their potential interaction with the ER VAP protein. Indeed, VPS13A and VPS13C were observed to accumulate over ER upon VAP co-transfection, while no longer tethered to the ER in VAP KO cells (Kumar et al., 2018). However, knockdown of VAPA showed no significant impact on lysosomal Ca^{2+} store and refilling (Figure 4.3A), indicating a different ER-binding partner of VPS13D, or that multiple ER membrane proteins are involved in the process, causing high redundancy.

In summary, we identified two regulatory pathways in which cations within lysosomes or a lysosome related organelle act to maintain cellular survival and function, and proposed a mechanism of the refilling of lysosomal Ca^{2+} stores. A critical task for future investigators is to identify the rest of the proteins essential for refilling lysosomes with Ca^{2+} and the ways these proteins interact with each other to regulate the process.

References

Al Hawas, R., Ren, Q., Ye, S., Karim, Z.A., Filipovich, A.H., and Whiteheart, S.W. (2012). Munc18b/STXBP2 is required for platelet secretion. Blood *120*, 2493-2500.

Alpy, F., Rousseau, A., Schwab, Y., Legueux, F., Stoll, I., Wendling, C., Spiegelhalter, C., Kessler, P., Mathelin, C., Rio, M.C*., et al.* (2013). STARD3 or STARD3NL and VAP form a novel molecular tether between late endosomes and the ER. J Cell Sci *126*, 5500-5512.

Amaravadi, R., Kimmelman, A.C., and White, E. (2016). Recent insights into the function of autophagy in cancer. Genes Dev *30*, 1913-1930.

Anding, A.L., Wang, C., Chang, T.K., Sliter, D.A., Powers, C.M., Hofmann, K., Youle, R.J., and Baehrecke, E.H. (2018). Vps13D Encodes a Ubiquitin-Binding Protein that Is Required for the Regulation of Mitochondrial Size and Clearance. Curr Biol *28*, 287-295 e286.

Appelqvist, H., Waster, P., Kagedal, K., and Ollinger, K. (2013). The lysosome: from waste bag to potential therapeutic target. J Mol Cell Biol *5*, 214-226.

Atakpa, P., Thillaiappan, N.B., Mataragka, S., Prole, D.L., and Taylor, C.W. (2018). IP3 Receptors Preferentially Associate with ER-Lysosome Contact Sites and Selectively Deliver Ca(2+) to Lysosomes. Cell Rep *25*, 3180-3193 e3187.

Bae, M., Patel, N., Xu, H., Lee, M., Tominaga-Yamanaka, K., Nath, A., Geiger, J., Gorospe, M., Mattson, M.P., and Haughey, N.J. (2014). Activation of TRPML1 clears intraneuronal Abeta in preclinical models of HIV infection. The Journal of neuroscience : the official journal of the Society for Neuroscience *34*, 11485-11503.

Balderhaar, H.J., and Ungermann, C. (2013). CORVET and HOPS tethering complexes - coordinators of endosome and lysosome fusion. J Cell Sci *126*, 1307-1316.

Baughman, J.M., Perocchi, F., Girgis, H.S., Plovanich, M., Belcher-Timme, C.A., Sancak, Y., Bao, X.R., Strittmatter, L., Goldberger, O., Bogorad, R.L*., et al.* (2011). Integrative genomics identifies MCU as an essential component of the mitochondrial calcium uniporter. Nature *476*, 341-345.

Bellettato, C.M., and Scarpa, M. (2010). Pathophysiology of neuropathic lysosomal storage disorders. J Inherit Metab Dis *33*, 347-362.

Berg, T.O., Stromhaug, E., Lovdal, T., Seglen, O., and Berg, T. (1994). Use of glycyl-L-phenylalanine 2-naphthylamide, a lysosome-disrupting cathepsin C substrate, to distinguish between lysosomes and prelysosomal endocytic vacuoles. The Biochemical journal *300 (Pt 1)*, 229-236.

Berridge, M.J. (2012). Calcium signalling remodelling and disease. Biochemical Society transactions *40*, 297-309.

Berridge, M.J., Lipp, P., and Bootman, M.D. (2000). The versatility and universality of calcium signalling. Nature reviews Molecular cell biology *1*, 11-21.

Blaby-Haas, C.E., and Merchant, S.S. (2014). Lysosome-related organelles as mediators of metal homeostasis. The Journal of biological chemistry *289*, 28129-28136.

Bonam, S.R., Wang, F., and Muller, S. (2019). Lysosomes as a therapeutic target. Nat Rev Drug Discov *18*, 923-948.

Bonifacino, J.S., and Traub, L.M. (2003). Signals for sorting of transmembrane proteins to endosomes and lysosomes. Annual review of biochemistry *72*, 395-447.

Booth, D.M., Enyedi, B., Geiszt, M., Varnai, P., and Hajnoczky, G. (2016). Redox Nanodomains Are Induced by and Control Calcium Signaling at the ER-Mitochondrial Interface. Mol Cell *63*, 240-248.

Bossy-Wetzel, E., Talantova, M.V., Lee, W.D., Scholzke, M.N., Harrop, A., Mathews, E., Gotz, T., Han, J., Ellisman, M.H., Perkins, G.A.*, et al.* (2004). Crosstalk between nitric oxide and zinc pathways to neuronal cell death involving mitochondrial dysfunction and p38-activated K+ channels. Neuron *41*, 351-365.

Bostanci, Z., Alam, S., Soybel, D.I., and Kelleher, S.L. (2014). Prolactin receptor attenuation induces zinc pool redistribution through ZnT2 and decreases invasion in MDA-MB-453 breast cancer cells. Experimental cell research *321*, 190-200.

Boswell, K.L., James, D.J., Esquibel, J.M., Bruinsma, S., Shirakawa, R., Horiuchi, H., and Martin, T.F. (2012). Munc13-4 reconstitutes calcium-dependent SNARE-mediated membrane fusion. J Cell Biol *197*, 301-312.

Boudewyn, L.C., and Walkley, S.U. (2018). Current concepts in the neuropathogenesis of mucolipidosis type IV. Journal of neurochemistry.

Boustany, R.M. (2013). Lysosomal storage diseases--the horizon expands. Nat Rev Neurol *9*, 583-598.

Bowman, S.L., Bi-Karchin, J., Le, L., and Marks, M.S. (2019). The road to lysosome-related organelles: Insights from Hermansky-Pudlak syndrome and other rare diseases. Traffic *20*, 404-435.

Bozym, R.A., Chimienti, F., Giblin, L.J., Gross, G.W., Korichneva, I., Li, Y., Libert, S., Maret, W., Parviz, M., Frederickson, C.J.*, et al.* (2010). Free zinc ions outside a narrow concentration range are toxic to a variety of cells in vitro. Exp Biol Med (Maywood) *235*, 741-750.

Brady, R.O. (2006). Enzyme replacement for lysosomal diseases. Annu Rev Med *57*, 283-296.

Braulke, T., and Bonifacino, J.S. (2009). Sorting of lysosomal proteins. Biochimica et biophysica acta *1793*, 605-614.

Brickner, J.H., Blanchette, J.M., Sipos, G., and Fuller, R.S. (2001). The Tlg SNARE complex is required for TGN homotypic fusion. J Cell Biol *155*, 969-978.

Burgoyne, T., Patel, S., and Eden, E.R. (2015). Calcium signaling at ER membrane contact sites. Biochimica et biophysica acta *1853*, 2012-2017.

Cang, C., Aranda, K., Seo, Y.J., Gasnier, B., and Ren, D. (2015). TMEM175 Is an Organelle K(+) Channel Regulating Lysosomal Function. Cell *162*, 1101-1112.

Cang, C., Zhou, Y., Navarro, B., Seo, Y.J., Aranda, K., Shi, L., Battaglia-Hsu, S., Nissim, I., Clapham, D.E., and Ren, D. (2013). mTOR regulates lysosomal ATP-sensitive two-pore Na(+) channels to adapt to metabolic state. Cell *152*, 778-790.

Cao, Q., Zhong, X.Z., Zou, Y., Murrell-Lagnado, R., Zhu, M.X., and Dong, X.P. (2015a). Calcium release through P2X4 activates calmodulin to promote endolysosomal membrane fusion. J Cell Biol *209*, 879-894.

Cao, Q., Zhong, Xi Z., Zou, Y., Zhang, Z., Toro, L., and Dong, X.-P. (2015b). BK Channels Alleviate Lysosomal Storage Diseases by Providing Positive Feedback Regulation of Lysosomal Ca2+ Release. Developmental cell *33*, 427-441.

Cardenas, C., Miller, R.A., Smith, I., Bui, T., Molgo, J., Muller, M., Vais, H., Cheung, K.H., Yang, J., Parker, I.*, et al.* (2010). Essential regulation of cell bioenergetics by constitutive InsP3 receptor Ca2+ transfer to mitochondria. Cell *142*, 270-283.

Castellano, B.M., Thelen, A.M., Moldavski, O., Feltes, M., van der Welle, R.E., Mydock-McGrane, L., Jiang, X., van Eijkeren, R.J., Davis, O.B., Louie, S.M.*, et al.* (2017). Lysosomal cholesterol activates mTORC1 via an SLC38A9-Niemann-Pick C1 signaling complex. Science *355*, 1306-1311.

Cerny, J., Feng, Y., Yu, A., Miyake, K., Borgonovo, B., Klumperman, J., Meldolesi, J., McNeil, P.L., and Kirchhausen, T. (2004). The small chemical vacuolin-1 inhibits Ca(2+)-dependent lysosomal exocytosis but not cell resealing. EMBO reports *5*, 883-888.

Chakraborty, K., Leung, K., and Krishnan, Y. (2017). High lumenal chloride in the lysosome is critical for lysosome function. Elife *6*, e28862.

Chandler, P., Kochupurakkal, B.S., Alam, S., Richardson, A.L., Soybel, D.I., and Kelleher, S.L. (2016). Subtype-specific accumulation of intracellular zinc pools is associated with the malignant phenotype in breast cancer. Mol Cancer *15*, 2.

Chandra, M., Zhou, H., Li, Q., Muallem, S., Hofmann, S.L., and Soyombo, A.A. (2011). A role for the Ca2+ channel TRPML1 in gastric acid secretion, based on analysis of knockout mice. Gastroenterology *140*, 857-867.

Chang, D., Nalls, M.A., Hallgrimsdottir, I.B., Hunkapiller, J., van der Brug, M., Cai, F., International Parkinson's Disease Genomics, C., andMe Research, T., Kerchner, G.A., Ayalon, G.*, et al.* (2017). A meta-analysis of genome-wide association studies identifies 17 new Parkinson's disease risk loci. Nat Genet *49*, 1511–1516.

Chen, C.S., Bach, G., and Pagano, R.E. (1998). Abnormal transport along the lysosomal pathway in mucolipidosis, type IV disease. Proceedings of the National Academy of Sciences of the United States of America *95*, 6373-6378.

Chen, Q., She, J., Zeng, W., Guo, J., Xu, H., Bai, X.C., and Jiang, Y. (2017). Structure of mammalian endolysosomal TRPML1 channel in nanodiscs. Nature *550*, 415-418.

Cheng, X., Shen, D., Samie, M., and Xu, H. (2010). Mucolipins: Intracellular TRPML1-3 channels. FEBS letters *584*, 2013-2021.

Cheng, X., Zhang, X., Gao, Q., Ali Samie, M., Azar, M., Tsang, W.L., Dong, L., Sahoo, N., Li, X., Zhuo, Y.*, et al.* (2014). The intracellular Ca(2)(+) channel MCOLN1 is required for sarcolemma repair to prevent muscular dystrophy. Nature medicine *20*, 1187-1192.

Chew, C.S., and Brown, M.R. (1986). Release of intracellular Ca2+ and elevation of inositol trisphosphate by secretagogues in parietal and chief cells isolated from rabbit gastric mucosa. Biochimica et biophysica acta *888*, 116-125.

Chew, C.S., Hersey, S.J., Sachs, G., and Berglindh, T. (1980). Histamine responsiveness of isolated gastric glands. The American journal of physiology *238*, G312-320.

Chicka, M.C., Ren, Q., Richards, D., Hellman, L.M., Zhang, J., Fried, M.G., and Whiteheart, S.W. (2016). Role of Munc13-4 as a Ca2+-dependent tether during platelet secretion. The Biochemical journal *473*, 627-639.

Cho, K.S., Yoon, Y.H., Choi, J.A., Lee, S.J., and Koh, J.Y. (2012). Induction of autophagy and cell death by tamoxifen in cultured retinal pigment epithelial and photoreceptor cells. Invest Ophthalmol Vis Sci *53*, 5344-5353.

Choi, D.W., and Koh, J.Y. (1998). Zinc and brain injury. Annu Rev Neurosci *21*, 347-375.

Christensen, K.A., Myers, J.T., and Swanson, J.A. (2002). pH-dependent regulation of lysosomal calcium in macrophages. J Cell Sci *115*, 599-607.

Chu, B.B., Liao, Y.C., Qi, W., Xie, C., Du, X., Wang, J., Yang, H., Miao, H.H., Li, B.L., and Song, B.L. (2015). Cholesterol transport through lysosome-peroxisome membrane contacts. Cell *161*, 291-306.

Chung, J., Torta, F., Masai, K., Lucast, L., Czapla, H., Tanner, L.B., Narayanaswamy, P., Wenk, M.R., Nakatsu, F., and De Camilli, P. (2015). INTRACELLULAR TRANSPORT. PI4P/phosphatidylserine countertransport at ORP5- and ORP8-mediated ER-plasma membrane contacts. Science *349*, 428-432.

Clapham, D.E. (2007). Calcium signaling. Cell *131*, 1047-1058.

Coen, K., Flannagan, R.S., Baron, S., Carraro-Lacroix, L.R., Wang, D., Vermeire, W., Michiels, C., Munck, S., Baert, V., Sugita, S.*, et al.* (2012). Lysosomal calcium homeostasis defects, not proton pump defects, cause endo-lysosomal dysfunction in PSEN-deficient cells. J Cell Biol *198*, 23-35.

Condrescu, M., Chernaya, G., Kalaria, V., and Reeves, J.P. (1997). Barium influx mediated by the cardiac sodium-calcium exchanger in transfected Chinese hamster ovary cells. The Journal of general physiology *109*, 41-51.

Costa-Leonardo, A.M., Janei, V., Laranjo, L.T., and Haifig, I. (2015). Location, morphology and function of nephrocytes in termites. Arthropod Struct Dev *44*, 346-354.

Costello, L.C., Liu, Y., Franklin, R.B., and Kennedy, M.C. (1997). Zinc inhibition of mitochondrial aconitase and its importance in citrate metabolism of prostate epithelial cells. The Journal of biological chemistry *272*, 28875-28881.

Courtois-Coutry, N., Roush, D., Rajendran, V., McCarthy, J.B., Geibel, J., Kashgarian, M., and Caplan, M.J. (1997). A tyrosine-based signal targets H/K-ATPase to a regulated compartment and is required for the cessation of gastric acid secretion. Cell *90*, 501-510.

Coutinho, M.F., Prata, M.J., and Alves, S. (2012). A shortcut to the lysosome: the mannose-6-phosphate-independent pathway. Mol Genet Metab *107*, 257-266.

Csordas, G., Varnai, P., Golenar, T., Roy, S., Purkins, G., Schneider, T.G., Balla, T., and Hajnoczky, G. (2010). Imaging interorganelle contacts and local calcium dynamics at the ER-mitochondrial interface. Mol Cell *39*, 121-132.

Cuajungco, M.P., Basilio, L.C., Silva, J., Hart, T., Tringali, J., Chen, C.C., Biel, M., and Grimm, C. (2014). Cellular zinc levels are modulated by TRPML1-TMEM163 interaction. Traffic *15*, 1247-1265.

Cui, Y., Vogt, S., Olson, N., Glass, A.G., and Rohan, T.E. (2007). Levels of zinc, selenium, calcium, and iron in benign breast tissue and risk of subsequent breast cancer. Cancer Epidemiol Biomarkers Prev *16*, 1682-1685.

Cullinane, A.R., Curry, J.A., Carmona-Rivera, C., Summers, C.G., Ciccone, C., Cardillo, N.D., Dorward, H., Hess, R.A., White, J.G., Adams, D.*, et al.* (2011). A BLOC-1 mutation screen reveals that PLDN is mutated in Hermansky-Pudlak Syndrome type 9. American journal of human genetics *88*, 778-787.

Davis, L.C., Morgan, A.J., Chen, J.L., Snead, C.M., Bloor-Young, D., Shenderov, E., Stanton-Humphreys, M.N., Conway, S.J., Churchill, G.C., Parrington, J.*, et al.* (2012). NAADP activates two-pore channels on T cell cytolytic granules to stimulate exocytosis and killing. Curr Biol *22*, 2331-2337.

de Brito, O.M., and Scorrano, L. (2008). Mitofusin 2 tethers endoplasmic reticulum to mitochondria. Nature *456*, 605-610.

De Leo, M.G., Staiano, L., Vicinanza, M., Luciani, A., Carissimo, A., Mutarelli, M., Di Campli, A., Polishchuk, E., Di Tullio, G., Morra, V.*, et al.* (2016). Autophagosome-lysosome fusion triggers a lysosomal response mediated by TLR9 and controlled by OCRL. Nature cell biology *18*, 839-850.

De, M., Oleskie, A.N., Ayyash, M., Dutta, S., Mancour, L., Abazeed, M.E., Brace, E.J., Skiniotis, G., and Fuller, R.S. (2017). The Vps13p-Cdc31p complex is directly required for TGN late endosome transport and TGN homotypic fusion. J Cell Biol *216*, 425-439.

De Stefani, D., Raffaello, A., Teardo, E., Szabo, I., and Rizzuto, R. (2011). A forty-kilodalton protein of the inner membrane is the mitochondrial calcium uniporter. Nature *476*, 336-340.

Decressac, M., Mattsson, B., Weikop, P., Lundblad, M., Jakobsson, J., and Bjorklund, A. (2013). TFEB-mediated autophagy rescues midbrain dopamine neurons from alpha-synuclein toxicity. Proc Natl Acad Sci U S A *110*, E1817-1826.

Delevoye, C., Marks, M.S., and Raposo, G. (2019). Lysosome-related organelles as functional adaptations of the endolysosomal system. Curr Opin Cell Biol *59*, 147-158.

Dell'Angelica, E.C. (2009). AP-3-dependent trafficking and disease: the first decade. Curr Opin Cell Biol *21*, 552-559.

Dell'Angelica, E.C., Shotelersuk, V., Aguilar, R.C., Gahl, W.A., and Bonifacino, J.S. (1999). Altered trafficking of lysosomal proteins in Hermansky-Pudlak syndrome due to mutations in the beta 3A subunit of the AP-3 adaptor. Mol Cell *3*, 11-21.

Dennis, M.K., Delevoye, C., Acosta-Ruiz, A., Hurbain, I., Romao, M., Hesketh, G.G., Goff, P.S., Sviderskaya, E.V., Bennett, D.C., Luzio, J.P.*, et al.* (2016). BLOC-1 and BLOC-3 regulate

VAMP7 cycling to and from melanosomes via distinct tubular transport carriers. J Cell Biol *214*, 293-308.

Dennis, M.K., Mantegazza, A.R., Snir, O.L., Tenza, D., Acosta-Ruiz, A., Delevoye, C., Zorger, R., Sitaram, A., de Jesus-Rojas, W., Ravichandran, K.*, et al.* (2015). BLOC-2 targets recycling endosomal tubules to melanosomes for cargo delivery. J Cell Biol *209*, 563-577.

Di Mattia, T., Wilhelm, L.P., Ikhlef, S., Wendling, C., Spehner, D., Nomine, Y., Giordano, F., Mathelin, C., Drin, G., Tomasetto, C.*, et al.* (2018). Identification of MOSPD2, a novel scaffold for endoplasmic reticulum membrane contact sites. EMBO reports *19*.

Di Pietro, S.M., Falcon-Perez, J.M., Tenza, D., Setty, S.R., Marks, M.S., Raposo, G., and Dell'Angelica, E.C. (2006). BLOC-1 interacts with BLOC-2 and the AP-3 complex to facilitate protein trafficking on endosomes. Molecular biology of the cell *17*, 4027-4038.

Dickson, E.J. (2017). Endoplasmic Reticulum-Plasma Membrane Contacts Regulate Cellular Excitability. Advances in experimental medicine and biology *997*, 95-109.

Dickson, E.J., Duman, J.G., Moody, M.W., Chen, L., and Hille, B. (2012). Orai-STIM-mediated Ca2+ release from secretory granules revealed by a targeted Ca2+ and pH probe. Proc Natl Acad Sci U S A *109*, E3539-3548.

Dieckmann, N.M., Hackmann, Y., Arico, M., and Griffiths, G.M. (2015). Munc18-2 is required for Syntaxin 11 Localization on the Plasma Membrane in Cytotoxic T-Lymphocytes. Traffic *16*, 1330-1341.

Dineley, K.E., Votyakova, T.V., and Reynolds, I.J. (2003). Zinc inhibition of cellular energy production: implications for mitochondria and neurodegeneration. Journal of neurochemistry *85*, 563-570.

Dong, X.P., Cheng, X., Mills, E., Delling, M., Wang, F., Kurz, T., and Xu, H. (2008). The type IV mucolipidosis-associated protein TRPML1 is an endolysosomal iron release channel. Nature *455*, 992-996.

Dong, X.P., Shen, D., Wang, X., Dawson, T., Li, X., Zhang, Q., Cheng, X., Zhang, Y., Weisman, L.S., Delling, M.*, et al.* (2010). PI(3,5)P(2) controls membrane trafficking by direct activation of mucolipin Ca(2+) release channels in the endolysosome. Nature communications *1*, 38.

Dong, X.P., Wang, X., Shen, D., Chen, S., Liu, M., Wang, Y., Mills, E., Cheng, X., Delling, M., and Xu, H. (2009). Activating mutations of the TRPML1 channel revealed by proline-scanning mutagenesis. The Journal of biological chemistry *284*, 32040-32052.

Doray, B., Ghosh, P., Griffith, J., Geuze, H.J., and Kornfeld, S. (2002). Cooperation of GGAs and AP-1 in packaging MPRs at the trans-Golgi network. Science *297*, 1700-1703.

Du, W., Seah, I., Bougazzoul, O., Choi, G., Meeth, K., Bosenberg, M.W., Wakimoto, H., Fisher, D., and Shah, K. (2017). Stem cell-released oncolytic herpes simplex virus has therapeutic efficacy in brain metastatic melanomas. Proc Natl Acad Sci U S A *114*, E6157-E6165.

Du, X., Kumar, J., Ferguson, C., Schulz, T.A., Ong, Y.S., Hong, W., Prinz, W.A., Parton, R.G., Brown, A.J., and Yang, H. (2011). A role for oxysterol-binding protein-related protein 5 in endosomal cholesterol trafficking. J Cell Biol *192*, 121-135.

Dudek, J., Rehling, P., and van der Laan, M. (2013). Mitochondrial protein import: common principles and physiological networks. Biochimica et biophysica acta *1833*, 274-285.

Duffield, A., Kamsteeg, E.J., Brown, A.N., Pagel, P., and Caplan, M.J. (2003). The tetraspanin CD63 enhances the internalization of the H,K-ATPase beta-subunit. Proc Natl Acad Sci U S A *100*, 15560-15565.

Eichelsdoerfer, J.L., Evans, J.A., Slaugenhaupt, S.A., and Cuajungco, M.P. (2010). Zinc dyshomeostasis is linked with the loss of mucolipidosis IV-associated TRPML1 ion channel. The Journal of biological chemistry *285*, 34304-34308.

Eisenberg-Bord, M., Shai, N., Schuldiner, M., and Bohnert, M. (2016). A Tether Is a Tether Is a Tether: Tethering at Membrane Contact Sites. Developmental cell *39*, 395-409.

Elstak, E.D., Neeft, M., Nehme, N.T., Voortman, J., Cheung, M., Goodarzifard, M., Gerritsen, H.C., van Bergen En Henegouwen, P.M., Callebaut, I., de Saint Basile, G.*, et al.* (2011). The munc13-4-rab27 complex is specifically required for tethering secretory lysosomes at the plasma membrane. Blood *118*, 1570-1578.

Falcon-Perez, J.M., and Dell'Angelica, E.C. (2007). Zinc transporter 2 (SLC30A2) can suppress the vesicular zinc defect of adaptor protein 3-depleted fibroblasts by promoting zinc accumulation in lysosomes. Experimental cell research *313*, 1473-1483.

Forte, J.G., and Zhu, L. (2010). Apical recycling of the gastric parietal cell H,K-ATPase. Annual review of physiology *72*, 273-296.

Franklin, R.B., and Costello, L.C. (2009). The important role of the apoptotic effects of zinc in the development of cancers. J Cell Biochem *106*, 750-757.

Friedman, J.R., Dibenedetto, J.R., West, M., Rowland, A.A., and Voeltz, G.K. (2013). ER-endosome contact increases as endosomes traffic and mature. Molecular biology of the cell.

Friedman, J.R., Lackner, L.L., West, M., DiBenedetto, J.R., Nunnari, J., and Voeltz, G.K. (2011). ER tubules mark sites of mitochondrial division. Science *334*, 358-362.

Gao, M., and Yang, H. (2018). VPS13: A lipid transfer protein making contacts at multiple cellular locations. J Cell Biol *217*, 3322-3324.

Garofalo, T., Matarrese, P., Manganelli, V., Marconi, M., Tinari, A., Gambardella, L., Faggioni, A., Misasi, R., Sorice, M., and Malorni, W. (2016). Evidence for the involvement of lipid rafts localized at the ER-mitochondria associated membranes in autophagosome formation. Autophagy *12*, 917-935.

Garrity, A.G., Wang, W., Collier, C.M., Levey, S.A., Gao, Q., and Xu, H. (2016). The endoplasmic reticulum, not the pH gradient, drives calcium refilling of lysosomes. Elife *5*, e15887.

Gatta, A.T., and Levine, T.P. (2017). Piecing Together the Patchwork of Contact Sites. Trends in cell biology *27*, 214-229.

Gerondopoulos, A., Langemeyer, L., Liang, J.R., Linford, A., and Barr, F.A. (2012). BLOC-3 mutated in Hermansky-Pudlak syndrome is a Rab32/38 guanine nucleotide exchange factor. Curr Biol *22*, 2135-2139.

Giordano, F., Saheki, Y., Idevall-Hagren, O., Colombo, S.F., Pirruccello, M., Milosevic, I., Gracheva, E.O., Bagriantsev, S.N., Borgese, N., and De Camilli, P. (2013). PI(4,5)P(2)-dependent and Ca(2+)-regulated ER-PM interactions mediated by the extended synaptotagmins. Cell *153*, 1494-1509.

Giorgi, C., Bonora, M., Sorrentino, G., Missiroli, S., Poletti, F., Suski, J.M., Galindo Ramirez, F., Rizzuto, R., Di Virgilio, F., Zito, E.*, et al.* (2015). p53 at the endoplasmic reticulum regulates apoptosis in a Ca2+-dependent manner. Proc Natl Acad Sci U S A *112*, 1779-1784.

Goldsmith, J., Levine, B., and Debnath, J. (2014). Autophagy and cancer metabolism. Methods Enzymol *542*, 25-57.

Graves, A.R., Curran, P.K., Smith, C.L., and Mindell, J.A. (2008). The Cl-/H+ antiporter ClC-7 is the primary chloride permeation pathway in lysosomes. Nature *453*, 788.

Grimm, C., Butz, E., Chen, C.C., Wahl-Schott, C., and Biel, M. (2017). From mucolipidosis type IV to Ebola: TRPML and two-pore channels at the crossroads of endo-lysosomal trafficking and disease. Cell calcium *67*, 148-155.

Grimm, C., Hassan, S., Wahl-Schott, C., and Biel, M. (2012). Role of TRPML and two-pore channels in endolysosomal cation homeostasis. J Pharmacol Exp Ther *342*, 236-244.

Groth-Pedersen, L., and Jaattela, M. (2013). Combating apoptosis and multidrug resistant cancers by targeting lysosomes. Cancer Lett *332*, 265-274.

Guo, J., Zeng, W., and Jiang, Y. (2017). Tuning the ion selectivity of two-pore channels. Proc Natl Acad Sci U S A *114*, 1009-1014.

Hamalisto, S., and Jaattela, M. (2016). Lysosomes in cancer-living on the edge (of the cell). Curr Opin Cell Biol *39*, 69-76.

Hamasaki, M., Furuta, N., Matsuda, A., Nezu, A., Yamamoto, A., Fujita, N., Oomori, H., Noda, T., Haraguchi, T., Hiraoka, Y.*, et al.* (2013). Autophagosomes form at ER-mitochondria contact sites. Nature *495*, 389-393.

Han, Y., Goldberg, J.M., Lippard, S.J., and Palmer, A.E. (2018). Superiority of SpiroZin2 Versus FluoZin-3 for monitoring vesicular Zn(2+) allows tracking of lysosomal Zn(2+) pools. Scientific reports *8*, 15034.

He, W., Liu, W., Chew, C.S., Baker, S.S., Baker, R.D., Forte, J.G., and Zhu, L. (2011). Acid secretion-associated translocation of KCNJ15 in gastric parietal cells. American journal of physiology Gastrointestinal and liver physiology *301*, G591-600.

Hersey, S.J., and Sachs, G. (1995). Gastric acid secretion. Physiological reviews *75*, 155-189.

Hirabayashi, Y., Kwon, S.K., Paek, H., Pernice, W.M., Paul, M.A., Lee, J., Erfani, P., Raczkowski, A., Petrey, D.S., Pon, L.A.*, et al.* (2017). ER-mitochondria tethering by PDZD8 regulates Ca(2+) dynamics in mammalian neurons. Science *358*, 623-630.

Hirschi, M., Herzik, M.A., Jr., Wie, J., Suo, Y., Borschel, W.F., Ren, D., Lander, G.C., and Lee, S.Y. (2017). Cryo-electron microscopy structure of the lysosomal calcium-permeable channel TRPML3. Nature *550*, 411-414.

Hockey, L.N., Kilpatrick, B.S., Eden, E.R., Lin-Moshier, Y., Brailoiu, G.C., Brailoiu, E., Futter, C.E., Schapira, A.H., Marchant, J.S., and Patel, S. (2015). Dysregulation of lysosomal morphology by pathogenic LRRK2 is corrected by TPC2 inhibition. J Cell Sci *128*, 232-238.

Hoglinger, D., Burgoyne, T., Sanchez-Heras, E., Hartwig, P., Colaco, A., Newton, J., Futter, C.E., Spiegel, S., Platt, F.M., and Eden, E.R. (2019). NPC1 regulates ER contacts with endocytic organelles to mediate cholesterol egress. Nature communications *10*, 4276.

Honscher, C., Mari, M., Auffarth, K., Bohnert, M., Griffith, J., Geerts, W., van der Laan, M., Cabrera, M., Reggiori, F., and Ungermann, C. (2014). Cellular metabolism regulates contact sites between vacuoles and mitochondria. Developmental cell *30*, 86-94.

Huang, L., and Gitschier, J. (1997). A novel gene involved in zinc transport is deficient in the lethal milk mouse. Nat Genet *17*, 292-297.

Huang, X., Jiang, C., Yu, L., and Yang, A. (2020). Current and Emerging Approaches for Studying Inter-Organelle Membrane Contact Sites. Front Cell Dev Biol *8*, 195.

Hume, A.N., Collinson, L.M., Rapak, A., Gomes, A.Q., Hopkins, C.R., and Seabra, M.C. (2001). Rab27a regulates the peripheral distribution of melanosomes in melanocytes. J Cell Biol *152*, 795-808.

Huotari, J., and Helenius, A. (2011). Endosome maturation. The EMBO journal *30*, 3481-3500.

Hwang, J.J., Kim, H.N., Kim, J., Cho, D.H., Kim, M.J., Kim, Y.S., Kim, Y., Park, S.J., and Koh, J.Y. (2010). Zinc(II) ion mediates tamoxifen-induced autophagy and cell death in MCF-7 breast cancer cell line. Biometals : an international journal on the role of metal ions in biology, biochemistry, and medicine *23*, 997-1013.

Infante, R.E., Wang, M.L., Radhakrishnan, A., Kwon, H.J., Brown, M.S., and Goldstein, J.L. (2008). NPC2 facilitates bidirectional transfer of cholesterol between NPC1 and lipid bilayers, a step in cholesterol egress from lysosomes. Proc Natl Acad Sci U S A *105*, 15287-15292.

Jentsch, T.J. (2007). Chloride and the endosomal-lysosomal pathway: emerging roles of CLC chloride transporters. Journal of Physiology-London *578*, 633-640.

Jeong, J., and Eide, D.J. (2013). The SLC39 family of zinc transporters. Mol Aspects Med *34*, 612-619.

Ji, K., Mayernik, L., Moin, K., and Sloane, B.F. (2019). Acidosis and proteolysis in the tumor microenvironment. Cancer Metastasis Rev *38*, 103-112.

Jinn, S., Drolet, R.E., Cramer, P.E., Wong, A.H., Toolan, D.M., Gretzula, C.A., Voleti, B., Vassileva, G., Disa, J., Tadin-Strapps, M*., et al.* (2017). TMEM175 deficiency impairs lysosomal and mitochondrial function and increases alpha-synuclein aggregation. Proc Natl Acad Sci U S A *114*, 2389-2394.

Johnson, B., Leek, A.N., Sole, L., Maverick, E.E., Levine, T.P., and Tamkun, M.M. (2018). Kv2 potassium channels form endoplasmic reticulum/plasma membrane junctions via interaction with VAPA and VAPB. Proc Natl Acad Sci U S A *115*, E7331-E7340.

Johnson, D.E., Ostrowski, P., Jaumouille, V., and Grinstein, S. (2016). The position of lysosomes within the cell determines their luminal pH. J Cell Biol *212*, 677-692.

Jung, J., Cho, K.J., Naji, A.K., Clemons, K.N., Wong, C.O., Villanueva, M., Gregory, S., Karagas, N.E., Tan, L., Liang, H.*, et al.* (2019). HRAS-driven cancer cells are vulnerable to TRPML1 inhibition. EMBO reports *20*.

Kalatzis, V., Cherqui, S., Antignac, C., and Gasnier, B. (2001). Cystinosin, the protein defective in cystinosis, is a H(+)-driven lysosomal cystine transporter. EMBO J *20*, 5940-5949.

Kallunki, T., Olsen, O.D., and Jaattela, M. (2013). Cancer-associated lysosomal changes: friends or foes? Oncogene *32*, 1995-2004.

Kannan, M., Lahiri, S., Liu, L.K., Choudhary, V., and Prinz, W.A. (2017). Phosphatidylserine synthesis at membrane contact sites promotes its transport out of the ER. Journal of lipid research *58*, 553-562.

Kantheti, P., Qiao, X., Diaz, M.E., Peden, A.A., Meyer, G.E., Carskadon, S.L., Kapfhamer, D., Sufalko, D., Robinson, M.S., Noebels, J.L.*, et al.* (1998). Mutation in AP-3 delta in the mocha mouse links endosomal transport to storage deficiency in platelets, melanosomes, and synaptic vesicles. Neuron *21*, 111-122.

Kasitinon, S.Y., Eskiocak, U., Martin, M., Bezwada, D., Khivansara, V., Tasdogan, A., Zhao, Z., Mathews, T., Aurora, A.B., and Morrison, S.J. (2019). TRPML1 Promotes Protein Homeostasis in Melanoma Cells by Negatively Regulating MAPK and mTORC1 Signaling. Cell Rep *28*, 2293-2305 e2299.

Kawai, A., Uchiyama, H., Takano, S., Nakamura, N., and Ohkuma, S. (2007). Autophagosome-lysosome fusion depends on the pH in acidic compartments in CHO cells. Autophagy *3*, 154-157.

Kilpatrick, B.S., Eden, E.R., Hockey, L.N., Yates, E., Futter, C.E., and Patel, S. (2017). An Endosomal NAADP-Sensitive Two-Pore Ca(2+) Channel Regulates ER-Endosome Membrane Contact Sites to Control Growth Factor Signaling. Cell Rep *18*, 1636-1645.

Kilpatrick, B.S., Magalhaes, J., Beavan, M.S., McNeill, A., Gegg, M.E., Cleeter, M.W., Bloor-Young, D., Churchill, G.C., Duchen, M.R., Schapira, A.H.*, et al.* (2016a). Endoplasmic reticulum and lysosomal Ca(2)(+) stores are remodelled in GBA1-linked Parkinson disease patient fibroblasts. Cell calcium *59*, 12-20.

Kilpatrick, B.S., Yates, E., Grimm, C., Schapira, A.H., and Patel, S. (2016b). Endo-lysosomal TRP mucolipin-1 channels trigger global ER Ca2+ release and Ca2+ influx. J Cell Sci *129*, 3859-3867.

Kilpatrick, K., Zeng, Y., Hancock, T., and Segatori, L. (2015). Genetic and chemical activation of TFEB mediates clearance of aggregated alpha-synuclein. PloS one *10*, e0120819.

Kim, Y.J., Guzman-Hernandez, M.L., and Balla, T. (2011). A highly dynamic ER-derived phosphatidylinositol-synthesizing organelle supplies phosphoinositides to cellular membranes. Developmental cell *21*, 813-824.

Kirkegaard, T., and Jaattela, M. (2009). Lysosomal involvement in cell death and cancer. Biochimica et biophysica acta *1793*, 746-754.

Kiselyov, K., Colletti, G.A., Terwilliger, A., Ketchum, K., Lyons, C.W., Quinn, J., and Muallem, S. (2011). TRPML: transporters of metals in lysosomes essential for cell survival? Cell calcium *50*, 288-294.

Kiselyov, K., Yamaguchi, S., Lyons, C.W., and Muallem, S. (2010). Aberrant Ca2+ handling in lysosomal storage disorders. Cell calcium *47*, 103-111.

Koh, J.Y., Suh, S.W., Gwag, B.J., He, Y.Y., Hsu, C.Y., and Choi, D.W. (1996). The role of zinc in selective neuronal death after transient global cerebral ischemia. Science *272*, 1013-1016.

Koivusalo, M., Steinberg, B.E., Mason, D., and Grinstein, S. (2011). In situ measurement of the electrical potential across the lysosomal membrane using FRET. Traffic *12*, 972-982.

Kolter, T., and Sandhoff, K. (2005). Principles of lysosomal membrane digestion: stimulation of sphingolipid degradation by sphingolipid activator proteins and anionic lysosomal lipids. Annual review of cell and developmental biology *21*, 81-103.

Kornfeld, S. (1992). Structure and function of the mannose 6-phosphate/insulinlike growth factor II receptors. Annual review of biochemistry *61*, 307-330.

Kornfeld, S., and Mellman, I. (1989). The biogenesis of lysosomes. Annu Rev Cell Biol *5*, 483-525.

Korolchuk, V.I., Saiki, S., Lichtenberg, M., Siddiqi, F.H., Roberts, E.A., Imarisio, S., Jahreiss, L., Sarkar, S., Futter, M., Menzies, F.M.*, et al.* (2011). Lysosomal positioning coordinates cellular nutrient responses. Nature cell biology *13*, 453-460.

Kroemer, G., and Jaattela, M. (2005). Lysosomes and autophagy in cell death control. Nat Rev Cancer *5*, 886-897.

Kukic, I., Lee, J.K., Coblentz, J., Kelleher, S.L., and Kiselyov, K. (2013). Zinc-dependent lysosomal enlargement in TRPML1-deficient cells involves MTF-1 transcription factor and ZnT4 (Slc30a4) transporter. The Biochemical journal *451*, 155-163.

Kumagai, K., and Hanada, K. (2019). Structure, functions and regulation of CERT, a lipid-transfer protein for the delivery of ceramide at the ER-Golgi membrane contact sites. FEBS letters *593*, 2366-2377.

Kumar, N., Leonzino, M., Hancock-Cerutti, W., Horenkamp, F.A., Li, P., Lees, J.A., Wheeler, H., Reinisch, K.M., and De Camilli, P. (2018). VPS13A and VPS13C are lipid transport proteins differentially localized at ER contact sites. J Cell Biol *217*, 3625-3639.

Kuznetsova, S.S., Azarkina, N.V., Vygodina, T.V., Siletsky, S.A., and Konstantinov, A.A. (2005). Zinc ions as cytochrome C oxidase inhibitors: two sites of action. Biochemistry (Mosc) *70*, 128-136.

Lackner, L.L., Ping, H., Graef, M., Murley, A., and Nunnari, J. (2013). Endoplasmic reticulum-associated mitochondria-cortex tether functions in the distribution and inheritance of mitochondria. Proc Natl Acad Sci U S A *110*, E458-467.

Lahiri, S., Toulmay, A., and Prinz, W.A. (2015). Membrane contact sites, gateways for lipid homeostasis. Curr Opin Cell Biol *33*, 82-87.

Lambrecht, N.W., Yakubov, I., Scott, D., and Sachs, G. (2005). Identification of the K efflux channel coupled to the gastric H-K-ATPase during acid secretion. Physiological genomics *21*, 81-91.

Lee, J.H., McBrayer, M.K., Wolfe, D.M., Haslett, L.J., Kumar, A., Sato, Y., Lie, P.P., Mohan, P., Coffey, E.E., Kompella, U.*, et al.* (2015). Presenilin 1 Maintains Lysosomal Ca(2+)

Homeostasis via TRPML1 by Regulating vATPase-Mediated Lysosome Acidification. Cell Rep *12*, 1430-1444.

Lee, S.J., and Koh, J.Y. (2010). Roles of zinc and metallothionein-3 in oxidative stress-induced lysosomal dysfunction, cell death, and autophagy in neurons and astrocytes. Mol Brain *3*, 30.

Lees, J.A., and Reinisch, K.M. (2020). Inter-organelle lipid transfer: a channel model for Vps13 and chorein-N motif proteins. Curr Opin Cell Biol *65*, 66-71.

Lemons, R.M., and Thoene, J.G. (1991). Mediated calcium transport by isolated human fibroblast lysosomes. The Journal of biological chemistry *266*, 14378-14382.

Li, R.J., Xu, J., Fu, C., Zhang, J., Zheng, Y.G., Jia, H., and Liu, J.O. (2016a). Regulation of mTORC1 by lysosomal calcium and calmodulin. Elife *5*, e19360.

Li, S., Sandercock, A.M., Conduit, P., Robinson, C.V., Williams, R.L., and Kilmartin, J.V. (2006). Structural role of Sfi1p-centrin filaments in budding yeast spindle pole body duplication. J Cell Biol *173*, 867-877.

Li, X., Garrity, A.G., and Xu, H. (2013a). Regulation of membrane trafficking by signalling on endosomal and lysosomal membranes. The Journal of physiology *591*, 4389-4401.

Li, X., Rydzewski, N., Hider, A., Zhang, X., Yang, J., Wang, W., Gao, Q., Cheng, X., and Xu, H. (2016b). A molecular mechanism to regulate lysosome motility for lysosome positioning and tubulation. Nature cell biology *18*, 404-417.

Li, X., Wang, X., Zhang, X., Zhao, M., Tsang, W.L., Zhang, Y., Yau, R.G., Weisman, L.S., and Xu, H. (2013b). Genetically encoded fluorescent probe to visualize intracellular phosphatidylinositol 3,5-bisphosphate localization and dynamics. Proc Natl Acad Sci U S A *110*, 21165-21170.

Li, Y., Calvo, S.E., Gutman, R., Liu, J.S., and Mootha, V.K. (2014). Expansion of biological pathways based on evolutionary inference. Cell *158*, 213-225.

Lie, P.P.Y., and Nixon, R.A. (2019). Lysosome trafficking and signaling in health and neurodegenerative diseases. Neurobiol Dis *122*, 94-105.

Lieberman, A.P., Puertollano, R., Raben, N., Slaugenhaupt, S., Walkley, S.U., and Ballabio, A. (2012). Autophagy in lysosomal storage disorders. Autophagy *8*, 719-730.

Lim, J.A., Li, L., Kakhlon, O., Myerowitz, R., and Raben, N. (2015). Defects in calcium homeostasis and mitochondria can be reversed in Pompe disease. Autophagy *11*, 385-402.

Liou, J., Kim, M.L., Heo, W.D., Jones, J.T., Myers, J.W., Ferrell, J.E., Jr., and Meyer, T. (2005). STIM is a Ca2+ sensor essential for Ca2+-store-depletion-triggered Ca2+ influx. Curr Biol *15*, 1235-1241.

Litvinov, D.Y., Savushkin, E.V., and Dergunov, A.D. (2018). Intracellular and Plasma Membrane Events in Cholesterol Transport and Homeostasis. J Lipids *2018*, 3965054.

Liu, Y., Ding, X., Wang, D., Deng, H., Feng, M., Wang, M., Yu, X., Jiang, K., Ward, T., Aikhionbare, F.*, et al.* (2007). A mechanism of Munc18b-syntaxin 3-SNAP25 complex assembly in regulated epithelial secretion. FEBS letters *581*, 4318-4324.

Lloyd-Evans, E., Morgan, A.J., He, X., Smith, D.A., Elliot-Smith, E., Sillence, D.J., Churchill, G.C., Schuchman, E.H., Galione, A., and Platt, F.M. (2008). Niemann-Pick disease type C1 is a

sphingosine storage disease that causes deregulation of lysosomal calcium. Nature medicine *14*, 1247.

Lockwood, T.D. (2013). Lysosomal metal, redox and proton cycles influencing the CysHis cathepsin reaction. Metallomics *5*, 110-124.

Lubke, T., Lobel, P., and Sleat, D.E. (2009). Proteomics of the lysosome. Biochimica et biophysica acta *1793*, 625-635.

Luzio, J.P., Bright, N.A., and Pryor, P.R. (2007a). The role of calcium and other ions in sorting and delivery in the late endocytic pathway. Biochemical Society transactions *35*, 1088-1091.

Luzio, J.P., Pryor, P.R., and Bright, N.A. (2007b). Lysosomes: fusion and function. Nature reviews Molecular cell biology *8*, 622-632.

Lynes, E.M., Bui, M., Yap, M.C., Benson, M.D., Schneider, B., Ellgaard, L., Berthiaume, L.G., and Simmen, T. (2012). Palmitoylated TMX and calnexin target to the mitochondria-associated membrane. EMBO J *31*, 457-470.

Lynes, E.M., and Simmen, T. (2011). Urban planning of the endoplasmic reticulum (ER): how diverse mechanisms segregate the many functions of the ER. Biochimica et biophysica acta *1813*, 1893-1905.

Machado, E., White-Gilbertson, S., van de Vlekkert, D., Janke, L., Moshiach, S., Campos, Y., Finkelstein, D., Gomero, E., Mosca, R., Qiu, X.*, et al.* (2015). Regulated lysosomal exocytosis mediates cancer progression. Sci Adv *1*, e1500603.

Maeda, K., Anand, K., Chiapparino, A., Kumar, A., Poletto, M., Kaksonen, M., and Gavin, A.C. (2013). Interactome map uncovers phosphatidylserine transport by oxysterol-binding proteins. Nature *501*, 257-261.

Malinowska, D.H., Sachs, G., and Cuppoletti, J. (1988). Gastric H+ secretion: histamine (cAMP-mediated) activation of protein phosphorylation. Biochimica et biophysica acta *972*, 95-109.

Manford, A.G., Stefan, C.J., Yuan, H.L., Macgurn, J.A., and Emr, S.D. (2012). ER-to-plasma membrane tethering proteins regulate cell signaling and ER morphology. Developmental cell *23*, 1129-1140.

Maret, W. (2017). Zinc in Cellular Regulation: The Nature and Significance of "Zinc Signals". Int J Mol Sci *18*.

Margalioth, E.J., Schenker, J.G., and Chevion, M. (1983). Copper and zinc levels in normal and malignant tissues. Cancer *52*, 868-872.

Marks, M.S., Heijnen, H.F., and Raposo, G. (2013). Lysosome-related organelles: unusual compartments become mainstream. Curr Opin Cell Biol *25*, 495-505.

Mauvezin, C., and Neufeld, T.P. (2015). Bafilomycin A1 disrupts autophagic flux by inhibiting both V-ATPase-dependent acidification and Ca-P60A/SERCA-dependent autophagosome-lysosome fusion. Autophagy *11*, 1437-1438.

McCartney, A.J., Zhang, Y., and Weisman, L.S. (2014). Phosphatidylinositol 3,5-bisphosphate: low abundance, high significance. Bioessays *36*, 52-64.

McCormick, N.H., and Kelleher, S.L. (2012). ZnT4 provides zinc to zinc-dependent proteins in the trans-Golgi network critical for cell function and Zn export in mammary epithelial cells. American journal of physiology Cell physiology *303*, C291-297.

McQuin, C., Goodman, A., Chernyshev, V., Kamentsky, L., Cimini, B.A., Karhohs, K.W., Doan, M., Ding, L., Rafelski, S.M., Thirstrup, D.*, et al.* (2018). CellProfiler 3.0: Next-generation image processing for biology. PLoS biology *16*, e2005970.

Medina, D.L., Di Paola, S., Peluso, I., Armani, A., De Stefani, D., Venditti, R., Montefusco, S., Scotto-Rosato, A., Prezioso, C., Forrester, A.*, et al.* (2015). Lysosomal calcium signalling regulates autophagy through calcineurin and TFEB. Nature cell biology *17*, 288.

Medina, D.L., Fraldi, A., Bouche, V., Annunziata, F., Mansueto, G., Spampanato, C., Puri, C., Pignata, A., Martina, J.A., Sardiello, M.*, et al.* (2011). Transcriptional activation of lysosomal exocytosis promotes cellular clearance. Developmental cell *21*, 421-430.

Meng, J., and Wang, J. (2015). Role of SNARE proteins in tumourigenesis and their potential as targets for novel anti-cancer therapeutics. Biochimica et biophysica acta *1856*, 1-12.

Meyers, R.M., Bryan, J.G., McFarland, J.M., Weir, B.A., Sizemore, A.E., Xu, H., Dharia, N.V., Montgomery, P.G., Cowley, G.S., Pantel, S.*, et al.* (2017). Computational correction of copy number effect improves specificity of CRISPR-Cas9 essentiality screens in cancer cells. Nat Genet *49*, 1779-1784.

Miao, Y., Li, G., Zhang, X., Xu, H., and Abraham, S.N. (2015). A TRP Channel Senses Lysosome Neutralization by Pathogens to Trigger Their Expulsion. Cell *161*, 1306-1319.

Miklavc, P., Mair, N., Wittekindt, O.H., Haller, T., Dietl, P., Felder, E., Timmler, M., and Frick, M. (2011). Fusion-activated Ca2+ entry via vesicular P2X4 receptors promotes fusion pore opening and exocytotic content release in pneumocytes. Proc Natl Acad Sci U S A *108*, 14503-14508.

Miklavc, P., Thompson, K.E., and Frick, M. (2013). A new role for P2X4 receptors as modulators of lung surfactant secretion. Front Cell Neurosci *7*, 171.

Mills, E., Dong, X.P., Wang, F., and Xu, H. (2010). Mechanisms of brain iron transport: insight into neurodegeneration and CNS disorders. Future Med Chem *2*, 51-64.

Min, S.W., Chang, W.P., and Sudhof, T.C. (2007). E-Syts, a family of membranous Ca2+-sensor proteins with multiple C2 domains. Proc Natl Acad Sci U S A *104*, 3823-3828.

Minckley, T.F., Zhang, C., Fudge, D.H., Dischler, A.M., LeJeune, K.D., Xu, H., and Qin, Y. (2019). Sub-nanomolar sensitive GZnP3 reveals TRPML1-mediated neuronal Zn(2+) signals. Nature communications *10*, 4806.

Mindell, J.A. (2012). Lysosomal acidification mechanisms. Annual review of physiology *74*, 69-86.

Miron, S., Durand, D., Chilom, C., Perez, J., and Craescu, C.T. (2011). Binding of calcium, magnesium, and target peptides to Cdc31, the centrin of yeast Saccharomyces cerevisiae. Biochemistry *50*, 6409-6422.

Morgan, A.J., Davis, L.C., and Galione, A. (2015). Imaging approaches to measuring lysosomal calcium. Methods Cell Biol *126*, 159-195.

Morgan, A.J., Platt, F.M., Lloyd-Evans, E., and Galione, A. (2011). Molecular mechanisms of endolysosomal Ca2+ signalling in health and disease. The Biochemical journal *439*, 349-374.

Mu, T.W., Fowler, D.M., and Kelly, J.W. (2008). Partial restoration of mutant enzyme homeostasis in three distinct lysosomal storage disease cell lines by altering calcium homeostasis. PLoS biology *6*, e26.

Muallem, S., Chung, W.Y., Jha, A., and Ahuja, M. (2017). Lipids at membrane contact sites: cell signaling and ion transport. EMBO reports *18*, 1893-1904.

Murakami, M., and Hirano, T. (2008). Intracellular zinc homeostasis and zinc signaling. Cancer Sci *99*, 1515-1522.

Murgia, C., Vespignani, I., Cerase, J., Nobili, F., and Perozzi, G. (1999). Cloning, expression, and vesicular localization of zinc transporter Dri 27/ZnT4 in intestinal tissue and cells. The American journal of physiology *277*, G1231-1239.

Muto, A., Ohkura, M., Abe, G., Nakai, J., and Kawakami, K. (2013). Real-time visualization of neuronal activity during perception. Curr Biol *23*, 307-311.

Muto, A., Ohkura, M., Kotani, T., Higashijima, S., Nakai, J., and Kawakami, K. (2011). Genetic visualization with an improved GCaMP calcium indicator reveals spatiotemporal activation of the spinal motor neurons in zebrafish. Proc Natl Acad Sci U S A *108*, 5425-5430.

Naegeli, K.M., Hastie, E., Garde, A., Wang, Z., Keeley, D.P., Gordon, K.L., Pani, A.M., Kelley, L.C., Morrissey, M.A., Chi, Q.*, et al.* (2017). Cell Invasion In Vivo via Rapid Exocytosis of a Transient Lysosome-Derived Membrane Domain. Developmental cell *43*, 403-417 e410.

Nagree, M.S., Scalia, S., McKillop, W.M., and Medin, J.A. (2019). An update on gene therapy for lysosomal storage disorders. Expert Opin Biol Ther *19*, 655-670.

Nakada, S.L., Crothers, J.M., Jr., Machen, T.E., and Forte, J.G. (2012). Apical vacuole formation by gastric parietal cells in primary culture: effect of low extracellular Ca2+. American journal of physiology Cell physiology *303*, C1301-1311.

Neagoe, I., Stauber, T., Fidzinski, P., Bergsdorf, E.Y., and Jentsch, T.J. (2010). The Late Endosomal ClC-6 Mediates Proton/Chloride Countertransport in Heterologous Plasma Membrane Expression. Journal of Biological Chemistry *285*, 21689-21697.

Negulescu, P.A., Reenstra, W.W., and Machen, T.E. (1989). Intracellular Ca requirements for stimulus-secretion coupling in parietal cell. The American journal of physiology *256*, C241-251.

Nguyen, T., Chin, W.C., and Verdugo, P. (1998). Role of Ca2+/K+ ion exchange in intracellular storage and release of Ca2+. Nature *395*, 908-912.

Nickerson, D.P., Brett, C.L., and Merz, A.J. (2009). Vps-C complexes: gatekeepers of endolysosomal traffic. Curr Opin Cell Biol *21*, 543-551.

Nightingale, T.D., White, I.J., Doyle, E.L., Turmaine, M., Harrison-Lavoie, K.J., Webb, K.F., Cramer, L.P., and Cutler, D.F. (2011). Actomyosin II contractility expels von Willebrand factor from Weibel-Palade bodies during exocytosis. J Cell Biol *194*, 613-629.

Nixon, R.A. (2004). Niemann-Pick Type C disease and Alzheimer's disease: the APP-endosome connection fattens up. Am J Pathol *164*, 757-761.

Nixon, R.A. (2013). The role of autophagy in neurodegenerative disease. Nature medicine *19*, 983-997.

Okamoto, C.T., Duman, J.G., Tyagarajan, K., McDonald, K.L., Jeng, Y.Y., McKinney, J., Forte, T.M., and Forte, J.G. (2000). Clathrin in gastric acid secretory (parietal) cells: biochemical characterization and subcellular localization. American journal of physiology Cell physiology *279*, C833-851.

Onyenwoke, R.U., Sexton, J.Z., Yan, F., Diaz, M.C., Forsberg, L.J., Major, M.B., and Brenman, J.E. (2015). The mucolipidosis IV Ca2+ channel TRPML1 (MCOLN1) is regulated by the TOR kinase. The Biochemical journal *470*, 331-342.

Osawa, M., Swindells, M.B., Tanikawa, J., Tanaka, T., Mase, T., Furuya, T., and Ikura, M. (1998). Solution structure of calmodulin-W-7 complex: the basis of diversity in molecular recognition. Journal of molecular biology *276*, 165-176.

Ostenfeld, M.S., Fehrenbacher, N., Hoyer-Hansen, M., Thomsen, C., Farkas, T., and Jaattela, M. (2005). Effective tumor cell death by sigma-2 receptor ligand siramesine involves lysosomal leakage and oxidative stress. Cancer Res *65*, 8975-8983.

Padman, B.S., Bach, M., Lucarelli, G., Prescott, M., and Ramm, G. (2013). The protonophore CCCP interferes with lysosomal degradation of autophagic cargo in yeast and mammalian cells. Autophagy *9*, 1862-1875.

Palmiter, R.D., Cole, T.B., and Findley, S.D. (1996). ZnT-2, a mammalian protein that confers resistance to zinc by facilitating vesicular sequestration. EMBO J *15*, 1784-1791.

Pan, Z., Choi, S., Ouadid-Ahidouch, H., Yang, J.M., Beattie, J.H., and Korichneva, I. (2017). Zinc transporters and dysregulated channels in cancers. Front Biosci (Landmark Ed) *22*, 623-643.

Parenti, G., Andria, G., and Ballabio, A. (2015). Lysosomal storage diseases: from pathophysiology to therapy. Annu Rev Med *66*, 471-486.

Park, C.Y., Hoover, P.J., Mullins, F.M., Bachhawat, P., Covington, E.D., Raunser, S., Walz, T., Garcia, K.C., Dolmetsch, R.E., and Lewis, R.S. (2009). STIM1 clusters and activates CRAC channels via direct binding of a cytosolic domain to Orai1. Cell *136*, 876-890.

Parkinson-Lawrence, E.J., Shandala, T., Prodoehl, M., Plew, R., Borlace, G.N., and Brooks, D.A. (2010). Lysosomal storage disease: revealing lysosomal function and physiology. Physiology *25*, 102-115.

Pasham, V., Rotte, A., Mia, S., Alesutan, I., Chatterjee, S., Hosseinzadeh, Z., Bhandaru, M., Noegel, A.A., and Lang, F. (2013). Annexin 7 in the regulation of gastric acid secretion. Cellular physiology and biochemistry : international journal of experimental cellular physiology, biochemistry, and pharmacology *32*, 1643-1654.

Peplowska, K., Markgraf, D.F., Ostrowicz, C.W., Bange, G., and Ungermann, C. (2007). The CORVET tethering complex interacts with the yeast Rab5 homolog Vps21 and is involved in endo-lysosomal biogenesis. Developmental cell *12*, 739-750.

Perera, R.M., and Zoncu, R. (2016). The Lysosome as a Regulatory Hub. Annual review of cell and developmental biology *32*, 223-253.

Petersen, N.H., Olsen, O.D., Groth-Pedersen, L., Ellegaard, A.M., Bilgin, M., Redmer, S., Ostenfeld, M.S., Ulanet, D., Dovmark, T.H., Lonborg, A.*, et al.* (2013). Transformation-associated changes in sphingolipid metabolism sensitize cells to lysosomal cell death induced by inhibitors of acid sphingomyelinase. Cancer Cell *24*, 379-393.

Phillips, M.J., and Voeltz, G.K. (2016). Structure and function of ER membrane contact sites with other organelles. Nature reviews Molecular cell biology *17*, 69-82.

Piao, S., and Amaravadi, R.K. (2016). Targeting the lysosome in cancer. Annals of the New York Academy of Sciences *1371*, 45-54.

Ping, H.A., Kraft, L.M., Chen, W., Nilles, A.E., and Lackner, L.L. (2016). Num1 anchors mitochondria to the plasma membrane via two domains with different lipid binding specificities. J Cell Biol *213*, 513-524.

Pizzo, P., Lissandron, V., Capitanio, P., and Pozzan, T. (2011). Ca(2+) signalling in the Golgi apparatus. Cell calcium *50*, 184-192.

Platt, F.M., and Lachmann, R.H. (2009). Treating lysosomal storage disorders: current practice and future prospects. Biochimica et biophysica acta *1793*, 737-745.

Pohlmann, R., Boeker, M.W., and von Figura, K. (1995). The two mannose 6-phosphate receptors transport distinct complements of lysosomal proteins. The Journal of biological chemistry *270*, 27311-27318.

Polito, V.A., Li, H., Martini-Stoica, H., Wang, B., Yang, L., Xu, Y., Swartzlander, D.B., Palmieri, M., di Ronza, A., Lee, V.M.*, et al.* (2014). Selective clearance of aberrant tau proteins and rescue of neurotoxicity by transcription factor EB. EMBO Mol Med *6*, 1142-1160.

Pols, M.S., ten Brink, C., Gosavi, P., Oorschot, V., and Klumperman, J. (2013a). The HOPS proteins hVps41 and hVps39 are required for homotypic and heterotypic late endosome fusion. Traffic *14*, 219-232.

Pols, M.S., van Meel, E., Oorschot, V., ten Brink, C., Fukuda, M., Swetha, M.G., Mayor, S., and Klumperman, J. (2013b). hVps41 and VAMP7 function in direct TGN to late endosome transport of lysosomal membrane proteins. Nature communications *4*, 1361.

Poston, C.N., Duong, E., Cao, Y., and Bazemore-Walker, C.R. (2011). Proteomic analysis of lipid raft-enriched membranes isolated from internal organelles. Biochemical and biophysical research communications *415*, 355-360.

Prakriya, M., Feske, S., Gwack, Y., Srikanth, S., Rao, A., and Hogan, P.G. (2006). Orai1 is an essential pore subunit of the CRAC channel. Nature *443*, 230-233.

Prakriya, M., and Lewis, R.S. (2015). Store-Operated Calcium Channels. Physiological reviews *95*, 1383-1436.

Prinz, W.A., Toulmay, A., and Balla, T. (2020). The functional universe of membrane contact sites. Nature reviews Molecular cell biology *21*, 7-24.

Pryor, P.R., Reimann, F., Gribble, F.M., and Luzio, J.P. (2006). Mucolipin-1 is a lysosomal membrane protein required for intracellular lactosylceramide traffic. Traffic *7*, 1388-1398.

Rahman, N., Ramos-Espiritu, L., Milner, T.A., Buck, J., and Levin, L.R. (2016). Soluble adenylyl cyclase is essential for proper lysosomal acidification. The Journal of general physiology *148*, 325-339.

Raiborg, C., Wenzel, E.M., Pedersen, N.M., Olsvik, H., Schink, K.O., Schultz, S.W., Vietri, M., Nisi, V., Bucci, C., Brech, A.*, et al.* (2015). Repeated ER-endosome contacts promote endosome translocation and neurite outgrowth. Nature *520*, 234-238.

Raposo, G., and Marks, M.S. (2007). Melanosomes--dark organelles enlighten endosomal membrane transport. Nature reviews Molecular cell biology *8*, 786-797.

Ravi, S., Pena, K.A., Chu, C.T., and Kiselyov, K. (2016). Biphasic regulation of lysosomal exocytosis by oxidative stress. Cell calcium *60*, 356-362.

Reaves, S.K., Fanzo, J.C., Arima, K., Wu, J.Y., Wang, Y.R., and Lei, K.Y. (2000). Expression of the p53 tumor suppressor gene is up-regulated by depletion of intracellular zinc in HepG2 cells. J Nutr *130*, 1688-1694.

Rijnboutt, S., Aerts, H.M., Geuze, H.J., Tager, J.M., and Strous, G.J. (1991a). Mannose 6-phosphate-independent membrane association of cathepsin D, glucocerebrosidase, and sphingolipid-activating protein in HepG2 cells. The Journal of biological chemistry *266*, 4862-4868.

Rijnboutt, S., Kal, A.J., Geuze, H.J., Aerts, H., and Strous, G.J. (1991b). Mannose 6-phosphate-independent targeting of cathepsin D to lysosomes in HepG2 cells. The Journal of biological chemistry *266*, 23586-23592.

Rizzuto, R., Pinton, P., Carrington, W., Fay, F.S., Fogarty, K.E., Lifshitz, L.M., Tuft, R.A., and Pozzan, T. (1998). Close contacts with the endoplasmic reticulum as determinants of mitochondrial Ca2+ responses. Science *280*, 1763-1766.

Rocha, N., Kuijl, C., van der Kant, R., Janssen, L., Houben, D., Janssen, H., Zwart, W., and Neefjes, J. (2009). Cholesterol sensor ORP1L contacts the ER protein VAP to control Rab7-RILP-p150 Glued and late endosome positioning. J Cell Biol *185*, 1209-1225.

Ronco, V., Potenza, D.M., Denti, F., Vullo, S., Gagliano, G., Tognolina, M., Guerra, G., Pinton, P., Genazzani, A.A., Mapelli, L.*, et al.* (2015). A novel Ca(2)(+)-mediated cross-talk between endoplasmic reticulum and acidic organelles: implications for NAADP-dependent Ca(2)(+) signalling. Cell calcium *57*, 89-100.

Rong, Y., Liu, M., Ma, L., Du, W., Zhang, H., Tian, Y., Cao, Z., Li, Y., Ren, H., Zhang, C.*, et al.* (2012). Clathrin and phosphatidylinositol-4,5-bisphosphate regulate autophagic lysosome reformation. Nature cell biology *14*, 924-934.

Rowland, A.A., Chitwood, P.J., Phillips, M.J., and Voeltz, G.K. (2014). ER contact sites define the position and timing of endosome fission. Cell *159*, 1027-1041.

Sachse, M., Urbe, S., Oorschot, V., Strous, G.J., and Klumperman, J. (2002). Bilayered clathrin coats on endosomal vacuoles are involved in protein sorting toward lysosomes. Molecular biology of the cell *13*, 1313-1328.

Saftig, P., and Klumperman, J. (2009). Lysosome biogenesis and lysosomal membrane proteins: trafficking meets function. Nature reviews Molecular cell biology *10*, 623-635.

Saheki, Y., and De Camilli, P. (2017). Endoplasmic Reticulum-Plasma Membrane Contact Sites. Annual review of biochemistry *86*, 659-684.

Sahoo, N., Gu, M., Zhang, X., Raval, N., Yang, J., Bekier, M., Calvo, R., Patnaik, S., Wang, W., King, G.*, et al.* (2017). Gastric Acid Secretion from Parietal Cells Is Mediated by a Ca2+ Efflux Channel in the Tubulovesicle. Developmental cell *41*, 262-273 e266.

Samie, M., Wang, X., Zhang, X., Goschka, A., Li, X., Cheng, X., Gregg, E., Azar, M., Zhuo, Y., Garrity, A.G.*, et al.* (2013). A TRP channel in the lysosome regulates large particle phagocytosis via focal exocytosis. Developmental cell *26*, 511-524.

Schiffmann, R., Dwyer, N.K., Lubensky, I.A., Tsokos, M., Sutliff, V.E., Latimer, J.S., Frei, K.P., Brady, R.O., Barton, N.W., Blanchette-Mackie, E.J.*, et al.* (1998). Constitutive achlorhydria in mucolipidosis type IV. Proc Natl Acad Sci U S A *95*, 1207-1212.

Schissel, S.L., Keesler, G.A., Schuchman, E.H., Williams, K.J., and Tabas, I. (1998). The cellular trafficking and zinc dependence of secretory and lysosomal sphingomyelinase, two products of the acid sphingomyelinase gene. The Journal of biological chemistry *273*, 18250-18259.

Schmiege, P., Fine, M., Blobel, G., and Li, X. (2017). Human TRPML1 channel structures in open and closed conformations. Nature *550*, 366-370.

Schrader, M., King, S.J., Stroh, T.A., and Schroer, T.A. (2000). Real time imaging reveals a peroxisomal reticulum in living cells. J Cell Sci *113 (Pt 20)*, 3663-3671.

Schroder, B., Wrocklage, C., Pan, C., Jager, R., Kosters, B., Schafer, H., Elsasser, H.P., Mann, M., and Hasilik, A. (2007). Integral and associated lysosomal membrane proteins. Traffic *8*, 1676-1686.

Schulze, H., and Sandhoff, K. (2011). Lysosomal lipid storage diseases. Cold Spring Harbor perspectives in biology *3*.

Schwake, M., Schroder, B., and Saftig, P. (2013). Lysosomal membrane proteins and their central role in physiology. Traffic *14*, 739-748.

Scorrano, L., De Matteis, M.A., Emr, S., Giordano, F., Hajnoczky, G., Kornmann, B., Lackner, L.L., Levine, T.P., Pellegrini, L., Reinisch, K.*, et al.* (2019). Coming together to define membrane contact sites. Nature communications *10*, 1287.

Serra, M., Columbano, A., Ammarah, U., Mazzone, M., and Menga, A. (2020). Understanding Metal Dynamics Between Cancer Cells and Macrophages: Competition or Synergism? Front Oncol *10*, 646.

Serrano-Puebla, A., and Boya, P. (2016). Lysosomal membrane permeabilization in cell death: new evidence and implications for health and disease. Annals of the New York Academy of Sciences *1371*, 30-44.

Settembre, C., Di Malta, C., Polito, V.A., Garcia Arencibia, M., Vetrini, F., Erdin, S., Erdin, S.U., Huynh, T., Medina, D., Colella, P.*, et al.* (2011). TFEB links autophagy to lysosomal biogenesis. Science *332*, 1429-1433.

Setty, S.R., Tenza, D., Sviderskaya, E.V., Bennett, D.C., Raposo, G., and Marks, M.S. (2008). Cell-specific ATP7A transport sustains copper-dependent tyrosinase activity in melanosomes. Nature *454*, 1142-1146.

Setty, S.R., Tenza, D., Truschel, S.T., Chou, E., Sviderskaya, E.V., Theos, A.C., Lamoreux, M.L., Di Pietro, S.M., Starcevic, M., Bennett, D.C.*, et al.* (2007). BLOC-1 is required for cargo-specific sorting from vacuolar early endosomes toward lysosome-related organelles. Molecular biology of the cell *18*, 768-780.

Shai, N., Yifrach, E., van Roermund, C.W.T., Cohen, N., Bibi, C., L, I.J., Cavellini, L., Meurisse, J., Schuster, R., Zada, L.*, et al.* (2018). Systematic mapping of contact sites reveals tethers and a function for the peroxisome-mitochondria contact. Nature communications *9*, 1761.

Sheftel, A.D., Zhang, A.S., Brown, C., Shirihai, O.S., and Ponka, P. (2007). Direct interorganellar transfer of iron from endosome to mitochondrion. Blood *110*, 125-132.

Sheline, C.T., Behrens, M.M., and Choi, D.W. (2000). Zinc-induced cortical neuronal death: contribution of energy failure attributable to loss of NAD(+) and inhibition of glycolysis. The Journal of neuroscience : the official journal of the Society for Neuroscience *20*, 3139-3146.

Shen, D., Wang, X., Li, X., Zhang, X., Yao, Z., Dibble, S., Dong, X.P., Yu, T., Lieberman, A.P., Showalter, H.D.*, et al.* (2012). Lipid storage disorders block lysosomal trafficking by inhibiting a TRP channel and lysosomal calcium release. Nature communications *3*, 731.

Shibata, Y., Voss, C., Rist, J.M., Hu, J., Rapoport, T.A., Prinz, W.A., and Voeltz, G.K. (2008). The reticulon and DP1/Yop1p proteins form immobile oligomers in the tubular endoplasmic reticulum. The Journal of biological chemistry *283*, 18892-18904.

Shirane, M., and Nakayama, K.I. (2006). Protrudin induces neurite formation by directional membrane trafficking. Science *314*, 818-821.

Skulachev, V.P., Chistyakov, V.V., Jasaitis, A.A., and Smirnova, E.G. (1967). Inhibition of the respiratory chain by zinc ions. Biochemical and biophysical research communications *26*, 1-6.

Sohar, I., Sleat, D., Gong Liu, C., Ludwig, T., and Lobel, P. (1998). Mouse mutants lacking the cation-independent mannose 6-phosphate/insulin-like growth factor II receptor are impaired in lysosomal enzyme transport: comparison of cation-independent and cation-dependent mannose 6-phosphate receptor-deficient mice. The Biochemical journal *330 (Pt 2)*, 903-908.

Spessott, W.A., Sanmillan, M.L., McCormick, M.E., Kulkarni, V.V., and Giraudo, C.G. (2017). SM protein Munc18-2 facilitates transition of Syntaxin 11-mediated lipid mixing to complete fusion for T-lymphocyte cytotoxicity. Proc Natl Acad Sci U S A *114*, E2176-E2185.

Stathopulos, P.B., and Ikura, M. (2017). Store operated calcium entry: From concept to structural mechanisms. Cell calcium *63*, 3-7.

Stathopulos, P.B., Zheng, L., Li, G.Y., Plevin, M.J., and Ikura, M. (2008). Structural and mechanistic insights into STIM1-mediated initiation of store-operated calcium entry. Cell *135*, 110-122.

Stauber, T., and Jentsch, T.J. (2013). Chloride in vesicular trafficking and function. Annual review of physiology *75*, 453-477.

Suchanek, M., Hynynen, R., Wohlfahrt, G., Lehto, M., Johansson, M., Saarinen, H., Radzikowska, A., Thiele, C., and Olkkonen, V.M. (2007). The mammalian oxysterol-binding protein-related proteins (ORPs) bind 25-hydroxycholesterol in an evolutionarily conserved pocket. The Biochemical journal *405*, 473-480.

Suda, J., Zhu, L., Okamoto, C.T., and Karvar, S. (2011). Rab27b localizes to the tubulovesicle membranes of gastric parietal cells and regulates acid secretion. Gastroenterology *140*, 868-878.

Sumner, J.P., Aylott, J.W., Monson, E., and Kopelman, R. (2002). A fluorescent PEBBLE nanosensor for intracellular free zinc. Analyst *127*, 11-16.

Sun, X., Yang, Y., Zhong, X.Z., Cao, Q., Zhu, X.H., Zhu, X., and Dong, X.P. (2018). A negative feedback regulation of MTORC1 activity by the lysosomal Ca(2+) channel MCOLN1 (mucolipin 1) using a CALM (calmodulin)-dependent mechanism. Autophagy *14*, 38-52.

Syder, A.J., Karam, S.M., Mills, J.C., Ippolito, J.E., Ansari, H.R., Farook, V., and Gordon, J.I. (2004). A transgenic mouse model of metastatic carcinoma involving transdifferentiation of a gastric epithelial lineage progenitor to a neuroendocrine phenotype. Proc Natl Acad Sci U S A *101*, 4471-4476.

Szabadkai, G., Bianchi, K., Varnai, P., De Stefani, D., Wieckowski, M.R., Cavagna, D., Nagy, A.I., Balla, T., and Rizzuto, R. (2006). Chaperone-mediated coupling of endoplasmic reticulum and mitochondrial Ca2+ channels. J Cell Biol *175*, 901-911.

Thompson, E.G., Schaheen, L., Dang, H., and Fares, H. (2007). Lysosomal trafficking functions of mucolipin-1 in murine macrophages. BMC Cell Biol *8*, 54.

Thorn, P., Zorec, R., Rettig, J., and Keating, D.J. (2016). Exocytosis in non-neuronal cells. Journal of neurochemistry.

Trivedi, P.C., Bartlett, J.J., and Pulinilkunnil, T. (2020). Lysosomal Biology and Function: Modern View of Cellular Debris Bin. Cells *9*.

Tsunemi, T., Ashe, T.D., Morrison, B.E., Soriano, K.R., Au, J., Roque, R.A., Lazarowski, E.R., Damian, V.A., Masliah, E., and La Spada, A.R. (2012). PGC-1alpha rescues Huntington's disease proteotoxicity by preventing oxidative stress and promoting TFEB function. Sci Transl Med *4*, 142ra197.

Tsunoda, Y., Takeda, H., Otaki, T., Asaka, M., Nakagaki, I., and Sasaki, S. (1988). Intracellular Ca2+ shift and signal transduction from the tubulovesicular portion of gastric parietal cells during gastrin stimulation or Ca2+ ionophore treatment: comparison between luminescent and fluorescent probes, and electron probe X-ray microanalyzer. Biochemistry and cell biology = Biochimie et biologie cellulaire *66*, 279-287.

Valm, A.M., Cohen, S., Legant, W.R., Melunis, J., Hershberg, U., Wait, E., Cohen, A.R., Davidson, M.W., Betzig, E., and Lippincott-Schwartz, J. (2017). Applying systems-level spectral imaging and analysis to reveal the organelle interactome. Nature *546*, 162-167.

van der Kant, R., and Neefjes, J. (2014). Small regulators, major consequences - Ca(2)(+) and cholesterol at the endosome-ER interface. J Cell Sci *127*, 929-938.

Venkatachalam, K., Long, A.A., Elsaesser, R., Nikolaeva, D., Broadie, K., and Montell, C. (2008). Motor deficit in a Drosophila model of mucolipidosis type IV due to defective clearance of apoptotic cells. Cell *135*, 838-851.

Venugopal, B., Browning, M.F., Curcio-Morelli, C., Varro, A., Michaud, N., Nanthakumar, N., Walkley, S.U., Pickel, J., and Slaugenhaupt, S.A. (2007). Neurologic, gastric, and opthalmologic pathologies in a murine model of mucolipidosis type IV. American journal of human genetics *81*, 1070-1083.

Vergarajauregui, S., Martina, J.A., and Puertollano, R. (2009). Identification of the penta-EF-hand protein ALG-2 as a Ca2+-dependent interactor of mucolipin-1. The Journal of biological chemistry *284*, 36357-36366.

Vergarajauregui, S., Oberdick, R., Kiselyov, K., and Puertollano, R. (2008a). Mucolipin 1 channel activity is regulated by protein kinase A-mediated phosphorylation. The Biochemical journal *410*, 417-425.

Vergarajauregui, S., Oberdick, R., Kiselyov, K., and Puertollano, R. (2008b). Mucolipin 1 channel activity is regulated by protein kinase A-mediated phosphorylation. Biochemical Journal *410*, 417-425.

Vitner, E.B., Platt, F.M., and Futerman, A.H. (2010). Common and uncommon pathogenic cascades in lysosomal storage diseases. The Journal of biological chemistry *285*, 20423-20427.

Viviano, J., Krishnan, A., Wu, H., and Venkataraman, V. (2016). Electrophoretic mobility shift in native gels indicates calcium-dependent structural changes of neuronal calcium sensor proteins. Anal Biochem *494*, 93-100.

Walkley, S.U., and Vanier, M.T. (2009). Secondary lipid accumulation in lysosomal disease. Biochimica et biophysica acta *1793*, 726-736.

Wang, S., Tukachinsky, H., Romano, F.B., and Rapoport, T.A. (2016). Cooperation of the ER-shaping proteins atlastin, lunapark, and reticulons to generate a tubular membrane network. Elife *5*.

Wang, T., Yu, H., Hughes, N.W., Liu, B., Kendirli, A., Klein, K., Chen, W.W., Lander, E.S., and Sabatini, D.M. (2017a). Gene Essentiality Profiling Reveals Gene Networks and Synthetic Lethal Interactions with Oncogenic Ras. Cell *168*, 890-903 e815.

Wang, W., Zhang, X., Gao, Q., Lawas, M., Yu, L., Cheng, X., Gu, M., Sahoo, N., Li, X., Li, P.*, et al.* (2017b). A voltage-dependent K(+) channel in the lysosome is required for refilling lysosomal Ca(2+) stores. J Cell Biol *216*, 1715-1730.

Wang, X., Zhang, X., Dong, X.P., Samie, M., Li, X., Cheng, X., Goschka, A., Shen, D., Zhou, Y., Harlow, J.*, et al.* (2012). TPC proteins are phosphoinositide- activated sodium-selective ion channels in endosomes and lysosomes. Cell *151*, 372-383.

Wong, C.O., Li, R., Montell, C., and Venkatachalam, K. (2012). Drosophila TRPML is required for TORC1 activation. Curr Biol *22*, 1616-1621.

Wong, L.H., Gatta, A.T., and Levine, T.P. (2019). Lipid transfer proteins: the lipid commute via shuttles, bridges and tubes. Nature reviews Molecular cell biology *20*, 85-101.

Wong, Y.C., Ysselstein, D., and Krainc, D. (2018). Mitochondria-lysosome contacts regulate mitochondrial fission via RAB7 GTP hydrolysis. Nature *554*, 382-386.

Wu, H., Carvalho, P., and Voeltz, G.K. (2018). Here, there, and everywhere: The importance of ER membrane contact sites. Science *361*.

Wu, X., Rao, K., Bowers, M.B., Copeland, N.G., Jenkins, N.A., and Hammer, J.A., 3rd (2001). Rab27a enables myosin Va-dependent melanosome capture by recruiting the myosin to the organelle. J Cell Sci *114*, 1091-1100.

Wu, X.S., Rao, K., Zhang, H., Wang, F., Sellers, J.R., Matesic, L.E., Copeland, N.G., Jenkins, N.A., and Hammer, J.A., 3rd (2002). Identification of an organelle receptor for myosin-Va. Nature cell biology *4*, 271-278.

Wyant, G.A., Abu-Remaileh, M., Frenkel, E.M., Laqtom, N.N., Dharamdasani, V., Lewis, C.A., Chan, S.H., Heinze, I., Ori, A., and Sabatini, D.M. (2018). NUFIP1 is a ribosome receptor for starvation-induced ribophagy. Science *360*, 751-758.

Wyant, G.A., Abu-Remaileh, M., Wolfson, R.L., Chen, W.W., Freinkman, E., Danai, L.V., Vander Heiden, M.G., and Sabatini, D.M. (2017). mTORC1 Activator SLC38A9 Is Required to Efflux Essential Amino Acids from Lysosomes and Use Protein as a Nutrient. Cell *171*, 642-654 e612.

Xiao, Q., Yan, P., Ma, X., Liu, H., Perez, R., Zhu, A., Gonzales, E., Burchett, J.M., Schuler, D.R., Cirrito, J.R.*, et al.* (2014). Enhancing astrocytic lysosome biogenesis facilitates Abeta clearance and attenuates amyloid plaque pathogenesis. The Journal of neuroscience : the official journal of the Society for Neuroscience *34*, 9607-9620.

Xiong, J., and Zhu, M.X. (2016). Regulation of lysosomal ion homeostasis by channels and transporters. Science China Life sciences *59*, 777-791.

Xu, H., Martinoia, E., and Szabo, I. (2015). Organellar channels and transporters. Cell calcium *58*, 1-10.

Xu, H., and Ren, D. (2015). Lysosomal physiology. Annual review of physiology *77*, 57-80.

Xu, M., Almasi, S., Yang, Y., Yan, C., Sterea, A.M., Rizvi Syeda, A.K., Shen, B., Richard Derek, C., Huang, P., Gujar, S.*, et al.* (2019). The lysosomal TRPML1 channel regulates triple negative breast cancer development by promoting mTORC1 and purinergic signaling pathways. Cell calcium *79*, 80-88.

Yang, J., Zhao, Z., Gu, M., Feng, X., and Xu, H. (2018). Release and uptake mechanisms of vesicular Ca(2+) stores. Protein Cell *10*, 8-19.

Yao, X., and Forte, J.G. (2003). Cell biology of acid secretion by the parietal cell. Annual review of physiology *65*, 103-131.

Ye, S., Karim, Z.A., Al Hawas, R., Pessin, J.E., Filipovich, A.H., and Whiteheart, S.W. (2012). Syntaxin-11, but not syntaxin-2 or syntaxin-4, is required for platelet secretion. Blood *120*, 2484-2492.

Yoboue, E.D., Sitia, R., and Simmen, T. (2018). Redox crosstalk at endoplasmic reticulum (ER) membrane contact sites (MCS) uses toxic waste to deliver messages. Cell Death Dis *9*, 331.

Yu, L., Zhang, X., Yang, Y., Li, D., Tang, K., Zhao, Z., He, W., Wang, C., Sahoo, N., Converso-Baran, K.*, et al.* (2020). Small-molecule activation of lysosomal TRP channels ameliorates Duchenne muscular dystrophy in mouse models. Sci Adv *6*, eaaz2736.

Yu, T., Chung, C., Shen, D., Xu, H., and Lieberman, A.P. (2012). Ryanodine receptor antagonists adapt NPC1 proteostasis to ameliorate lipid storage in Niemann-Pick type C disease fibroblasts. Hum Mol Genet *21*, 3205-3214.

Zaar, K., Hartig, F., Fahimi, H.D., and Gorgas, K. (1984). Peroxisomal aggregates forming large stacks in the lipid segment of the canine kidney. Acta Histochem Suppl *29*, 165-168.

Zhang, X., Cheng, X., Yu, L., Yang, J., Calvo, R., Patnaik, S., Hu, X., Gao, Q., Yang, M., Lawas, M.*, et al.* (2016). MCOLN1 is a ROS sensor in lysosomes that regulates autophagy. Nature communications *7*, 12109.

Zhang, X., Li, X., and Xu, H. (2012). Phosphoinositide isoforms determine compartment-specific ion channel activity. Proceedings of the National Academy of Sciences *109*, 11384-11389.

Zhao, K., and Ridgway, N.D. (2017). Oxysterol-Binding Protein-Related Protein 1L Regulates Cholesterol Egress from the Endo-Lysosomal System. Cell Rep *19*, 1807-1818.

Zhitomirsky, B., and Assaraf, Y.G. (2016). Lysosomes as mediators of drug resistance in cancer. Drug Resist Updat *24*, 23-33.

Zhong, X.Z., Zou, Y., Sun, X., Dong, G., Cao, Q., Pandey, A., Rainey, J.K., Zhu, X., and Dong, X.P. (2017). Inhibition of Transient Receptor Potential Channel Mucolipin-1 (TRPML1) by Lysosomal Adenosine Involved in Severe Combined Immunodeficiency Diseases. The Journal of biological chemistry *292*, 3445-3455.

Zhou, Y., Srinivasan, P., Razavi, S., Seymour, S., Meraner, P., Gudlur, A., Stathopulos, P.B., Ikura, M., Rao, A., and Hogan, P.G. (2013). Initial activation of STIM1, the regulator of store-operated calcium entry. Nature structural & molecular biology *20*, 973-981.

Zhou, Y., Wong, C.O., Cho, K.J., van der Hoeven, D., Liang, H., Thakur, D.P., Luo, J., Babic, M., Zinsmaier, K.E., Zhu, M.X.*, et al.* (2015). SIGNAL TRANSDUCTION. Membrane potential modulates plasma membrane phospholipid dynamics and K-Ras signaling. Science *349*, 873-876.

Zolov, S.N., Bridges, D., Zhang, Y., Lee, W.W., Riehle, E., Verma, R., Lenk, G.M., Converso-Baran, K., Weide, T., Albin, R.L.*, et al.* (2012). In vivo, Pikfyve generates PI(3,5)P2, which serves as both a signaling lipid and the major precursor for PI5P. Proc Natl Acad Sci U S A *109*, 17472-17477.

Zou, J., Hu, B., Arpag, S., Yan, Q., Hamilton, A., Zeng, Y.S., Vanoye, C.G., and Li, J. (2015). Reactivation of Lysosomal Ca2+ Efflux Rescues Abnormal Lysosomal Storage in FIG4-Deficient Cells. The Journal of neuroscience : the official journal of the Society for Neuroscience *35*, 6801-6812.